学位論文

Star formation in the outer Galaxy

（銀河系外縁部における星生成）

平成 27 年 12 月博士（理学）申請

東京大学大学院理学系研究科

天文学専攻

泉　奈都子

ABSTRACT

In the past decades, detailed star-formation processes have been extensively studied mostly for nearby star-forming regions at distances less than 1 kpc, such as the Orion and Taurus star-forming regions. As a result, the star-formation mechanism in the "present-day Galaxy" have been well explained. However, many questions still remain for the star-formation mechanisms in the "early-phase of the formation of the Galaxy" (e.g. Krumholz, 2014), which is very important to understand the galaxy formation processes. In a primordial environment with low-gas density and low-metallicity, such as in the early phase of the formation of the Galaxy, the star-formation rate (SFR) and star-formation efficiency (SFE) in a global scale are known to decrease significantly (e.g. Kennicutt & Evans, 2012; Shi et al., 2014). However, the mechanisms for this qualitative change of star formation have not been understood, because observations of the detailed star-formation processes have been impossible even for nearby galaxies and, not to mention, for high-z galaxies. Thus I pay attention to the outer Galaxy, where the environment that existed during the formation of the Galaxy is still preserved. The H I density and H I surface density in the Galaxy starts to decrease sharply at Galactocentic radius (R_{G}) $\sim$ 13.5 kpc, and these values go down to about 1/10 of those in the solar neighborhood at $R_{\mathrm{G}} \sim$ 18 kpc (e.g. Nakanishi & Sofue, 2003). The metallicity in the Galaxy also decreases with increasing R_{G}, and is about 1/3 to 1/10 of that in the solar neighborhood at R_{G} = 13.5 – 18 kpc. Therefore, the outer Galaxy is considered to have similar characteristics as that in the early phase of Galaxy formation, in particular, in the Thick disk formation (Ferguson et al., 1998; Kobayashi et al., 2008). It is theoretically suggested that star-formation processes in low-gas density and low-metallicity environment, such as in the outer Galaxy, is different from those in high-gas density and high-metallicity environment, such as in the inner Galaxy (e.g. Krumholz, 2014). The outer Galaxy serves as an excellent laboratory for studying star-forming processes in low-gas density and low-

metallicity environments because we could directly observe detail of the galaxy formation processes in unprecedented detail at a much closer distance than distant galaxies and also because there is no complex star formation history and not much large number of field stars as in the inner Galaxy. Such regions have been recognized as being identical to XUV (Extended UV) region, which ubiquitously exists in the outskirt of disk galaxies (e.g. Thilker et al., 2007). In this thesis, I investigate properties of star formation at smaller scale ($\sim$ pc scale), as oppose to past studies with galaxy- or sub-galaxy scale, by making use of the advantage of the outer Galaxy region.

As a pilot study, we investigated a very distant molecular cloud Digel Cloud 1 (R_G = 22 kpc; Digel et al., 1994) with ^{12}CO(1-0) lines using the Nobeyama 45 m radio telescope as well as with near-infrared (NIR) wavelength using the Subaru 8.2 m telescope. As a result, I discovered two embedded clusters at two CO peaks of Cloud 1. Based on K-band (2.2 μm) luminosity function (KLF) and disk fraction, I have estimated the age of the clusters to be less than 1 Myr. I also estimated the photometric distance of the clusters with KLF to be $D \geq 12$ kpc ($R_G \geq 19$ kpc), which is consistent with the kinematic distance (D = 16 kpc). Using these parameters, I estimated the SFEs of Cloud 1 clusters to be 5 – 20 %, which is consistent with that in the solar neighborhood (2.3 – 57 %; Yasui et al., 2008). Based on the latest HI survey data, I have suggested that the impact of High-velocity clouds (HVCs) onto the outer part of the Galactic disk could be major trigger of Cloud 1 formation as well as star formation in Cloud 1. HVCs are known to interact with the Galaxy, and suggested to affect the Galaxy evolution. Triggered star formation by such interaction is predicted to major mode of star formation in the early phase of the Galaxy formation. Cloud 1 suggests the existence of such mode and could be a valuable target for revealing the detailed processes of such triggered formation. From those lines of study, I confirmed that star formation processes at the scale of molecular cloud ($\sim$ pc scale) in very distant star-forming regions can be investigated with the same quality as in the solar neighborhood, using large telescopes and large-scale survey data.

To clarify the global nature of star-formation activity, we need a statistical number of sample star-forming regions. However, the outer Galaxy has never been comprehensively surveyed because of lack of infrared survey data deep enough for large distances, and only about 30 star-forming regions are known so far. Therefore, I pay attention to the WISE (Wide-Field Infrared Survey Explorer) mid infrared (MIR) all sky survey data. *WISE* has archived a great increase in sensitivity, about 100 times more sensitive than IRAS (Infrared Astronomical Satellite), and therefore, the *WISE* data has a high potential in searching for distant star-forming regions. I therefore developed a simple identification criteria of star-forming regions with *WISE* colors, which can effectively pick up star-forming regions by combining with recently available CO survey data in the outer Galaxy. Using the criteria, I searched for star-forming regions within the area of 320 deg^2 to discover 711 new candidates of star-forming regions, which enable the statistical study of star-formation activity in the outer Galaxy for the first time.

From the distribution of newly discovered star-forming regions, I confirmed perhaps a new arm structure beyond the outer arm. I also investigated the properties of molecular clouds with and without star-forming regions to find clear differences between them: 1) slope of mass spectrum for clouds with star-forming regions (-1.41 ± 0.12) is less steeper than clouds without star-forming regions (-1.87 ± 0.11), 2) clouds with star-forming regions are about 2-times more massive than those without star-forming regions, and 3) line-widths of clouds with star-forming regions are widely spread at $0.5 \leq \Delta v \leq 5$ km s^{-1}, while those of clouds without star-forming regions are concentrated at smaller range ($0.5 \leq \Delta v \leq 3$ km s^{-1}). Furthermore, I investigated the relation between cloud virial mass (M_{vir}) and cloud mass from CO intensity (M_{CO}) using Galactic average mass calibration rate N(H$_2$)/I_{CO} (2.0×10^{20} cm^{-2}(K km s^{-1})$^{-1}$; e.g. Bolatto et al., 2013). As a result, I found that most massive clouds ($\geq 10^3\ M_{\odot}$) follow the $M_{\mathrm{vir}} = M_{\mathrm{CO}}$ relation, which suggests that the mass calibration rate in the outer Galaxy is same as that in the solar neighborhood. I also confirmed that almost all clouds with star-forming regions are virialized while almost all unvirialized clouds do not have star-forming regions.

Using the newly identified star-forming regions, I studied SFE of each molecular cloud as apposed to global SFE used for constructing Kennicutt-Schmidt law. I developed two SFE-indices, 1) the number ratio of clouds with star-forming region to all clouds, and 2) MIR luminosities per cloud mass, to examine variation of these indices with Galactocentric radius. Although star-formation processes are predicted to change with environment, I found that those indices do not significantly vary at R_{G} = 13.5 – 20 kpc. This results suggest that the star formation processes inside molecular cloud do not heavily depend on the environmental parameters, such as metallicity, and the low SFE found in the outer regions of disk galaxies (e.g. Bigiel et al., 2010) simply reflect the smaller number of molecular clouds in such region. SFE in the inner galaxies, where the interstellar medium (ISM) is dominated by H_2 molecular gas, is suggested to depend only on the amount of H_2 gas, but not of HI gas. The above results suggest that SFE in the outer galaxy, where the ISM is dominated by HI gas, also simply depend on the amount of H_2 gas as in the inner galaxy.

Contents

List of Figures

List of Tables

Chapter 1

Introduction

1.1 Outer Galaxy

In the past decades, detailed star-formation processes have been extensively studied mostly for nearby star-forming regions at distances less than 1 kpc, such as the Orion and Taurus star-forming regions. As a result, the star-formation mechanisms in the "present-day Galaxy" have been well explained. However, many questions still remain for the star-formation mechanisms in the "early phase of the formation of the Galaxy" (e.g. Krumholz, 2014). In such a primordial environment with low-gas density and low-metallicity, the star-formation rate (SFR) and star-formation efficiency (SFE), in Galactic scale to ~ 100 pc scale, are known to decrease significantly (e.g. Kennicutt & Evans, 2012; Shi et al., 2014). The mechanisms for such qualitative change of star formation have not been understood, because observations of the detailed star-formation processes have been impossible even for relatively nearby galaxies and, not to mention, for high-z galaxies. One possible approach is to study distant forming galaxies in high-resolution with large telescope. However, even with the cutting-edge facilities, it is difficult to study the star formation in extragalactic objects with the same quality as for the star-forming regions in the solar neighborhood. Another potentially very interesting approach is to study Galactic star-forming regions that may preserve the environment that existed during the formation of the Galaxy. It is like studying "living fossil" as apposed to Galactic archaeology (e.g. Freeman & Bland-Hawthorn, 2002), which studies old stars as fossil of the formation of the Galaxy.

The outer Galaxy may offer such possibility because it has a significant difference from the solar neighborhood, for example, lower gas density, lower metallicity, and the interstellar medium (ISM) completely dominated by HI so that H_2 fractions are extremely small (e.g. Wouterloot et al., 1990; Kalberla & Dedes, 2008; Wolfire et al., 2003; Rudolph et al., 2006; Smartt & Rolleston, 1997). The HI surface, total (HI + H_2) gas surface, and HI density start to decrease at Galactocentric radius (R_G) $\sim$ 13.5 kpc, and at $R_G \sim 18$ kpc, these values are down to about $1/10$ of those in the solar neighborhood (Figure 1.1, 1.2, and 1.3). The region with $R_G \geq 13.5$ kpc is defined as "Far Outer Galaxy" (FOG; Snell et al., 2002), and the region with $R_G \geq 18$ kpc is defined as "Extreme Outer Galaxy" (EOG; Kobayashi et al., 2008). The metallicity in the Galaxy also decrease with increasing R_G, and is down to about $1/3$ and $1/10$ of that in the solar neighborhood at FOG and EOG, respectively (Figure 1.4). Such environments may have similar characteristics as dwarf galaxies and that existed in the early phase of Galaxy formation, in particular, in the Thick disk formation (Figure 1.5, Ferguson et al., 1998; Kobayashi et al., 2008). We could directly observe detail of the galaxy formation processes in unprecedented detail at a much closer distance than distant galaxies. The outer Galaxy serves as an excellent laboratory for studying star-forming processes also because there is no complex star formation history and not much large number of field stars as in the inner Galaxy.

Such outer part of disk galaxies are gaining signifiant attentions after the discovery of UV bright stellar complexes in the extreme outer disk (Extended UV disk: XUV disk) in extensive samples of GALEX (Galaxy Evolution Explore)-surveyed galaxies (Thilker et al., 2005; Gil de Paz et al., 2005). XUV disks are typically associated with largely extended HI disk beyond the galactocentric radii at which molecular gas has yet been detected (see Figure 1.6 for the case of M83; Thilker et al., 2005). Figure 1.7 shows the radial profiles of HI, H_2, Hα, and FUV/NUV surface brightness for the prototypical XUV galaxy M83 (Thilker et al., 2005). Note the remarkable difference between the Hα and UV profiles at galactocentric radii > 5 kpc. After the extensive GALEX survey, XUV disk is known to ubiquitously exist in disk galaxies (detailed is more than 20 % of GALEX-observed disk galaxies Thilker et al., 2007). The understanding of this site may give us clues of star formation parameters in forming galaxies, such as Initial mass function (IMF) in low gas densities (e.g. Pflamm-Altenburg & Kroupa, 2008)

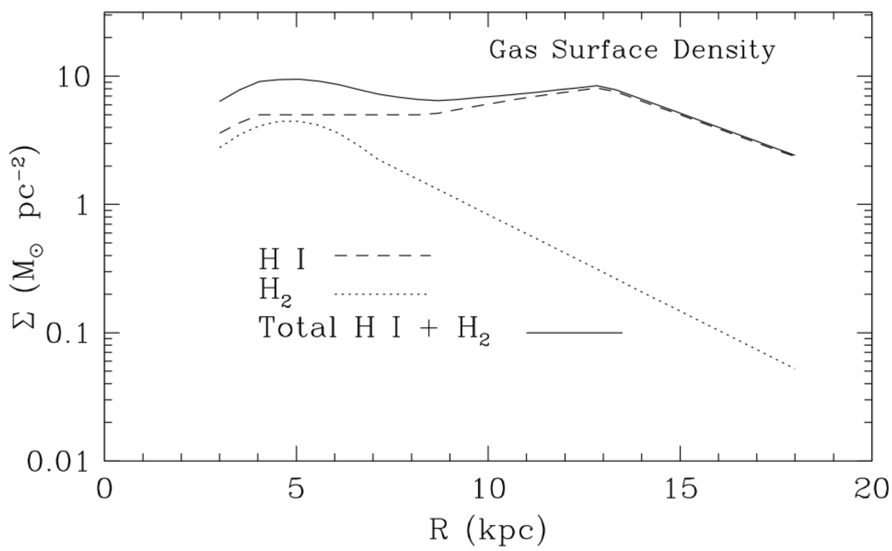

Figure 1.1: Variations of azimuthally averaged gas surface densities with Galactocentric radius *R*. The dashed curve, dotted curve, and solid curve show HI (Σ_{HI}), H_2 (Σ_{H2}), and total (Σ_{HI+H2}) gas surface density, respectively. This figure is reproduced from Wolfire et al. (2003)

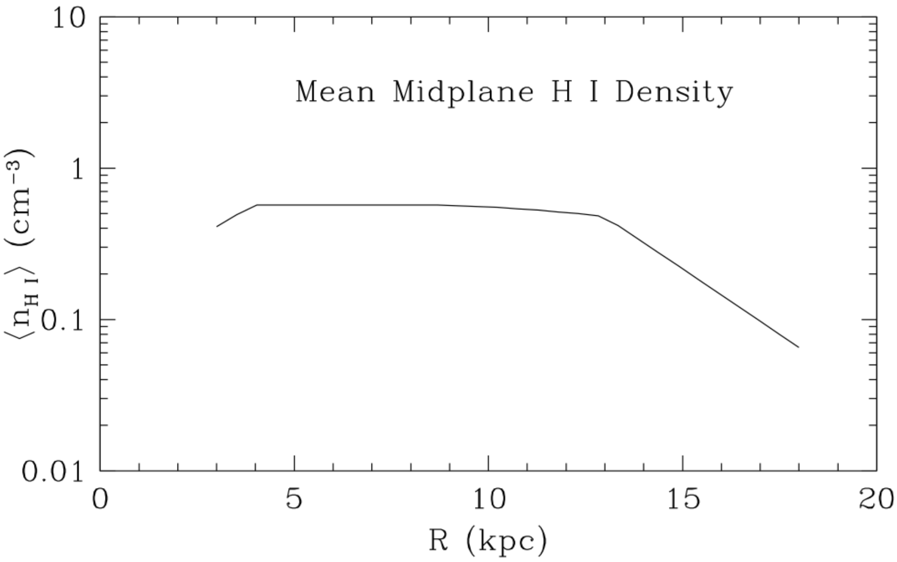

Figure 1.2: Mean midplane HI density variation with Galactocentric radius *R*. This figure is reproduced from Wolfire et al. (2003).

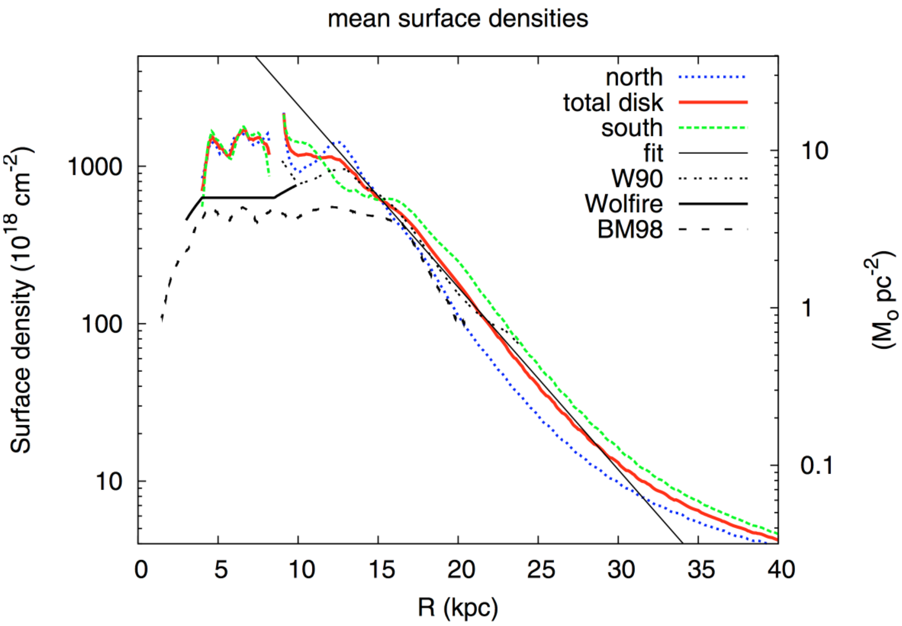

Figure 1.3: Variations of HI gas surface densities with Galactocentric radius up to R_G = 40 kpc. The dotted blue, dotted green, and solid red line show N_H in the northern part, the southern part, and total of the Galaxy. This figure is reproduced from Kalberla & Dedes (2008).

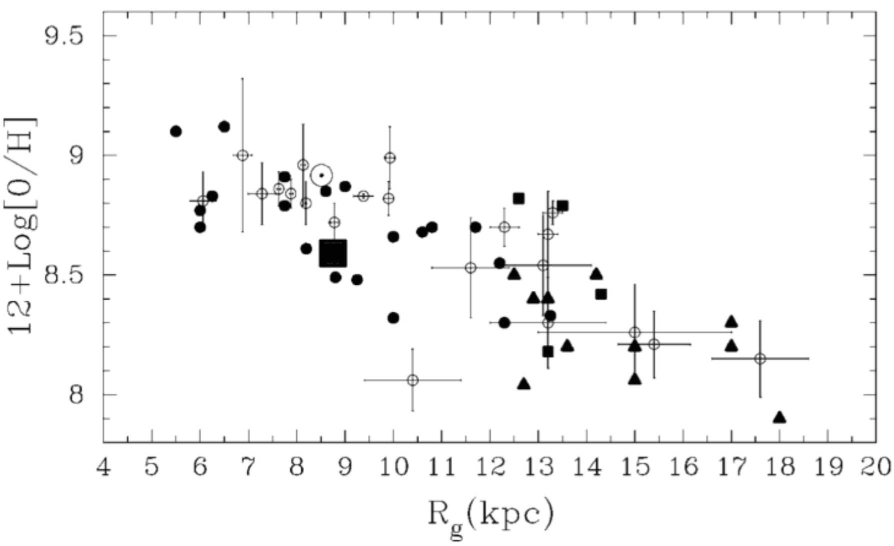

Figure 1.4: Oxygen abundance variation with Galactocentric radius. The open circles and filled symbols show abundance for B-type stars and HII regions, respectively. This figure is reproduced from Smartt & Rolleston (1997).

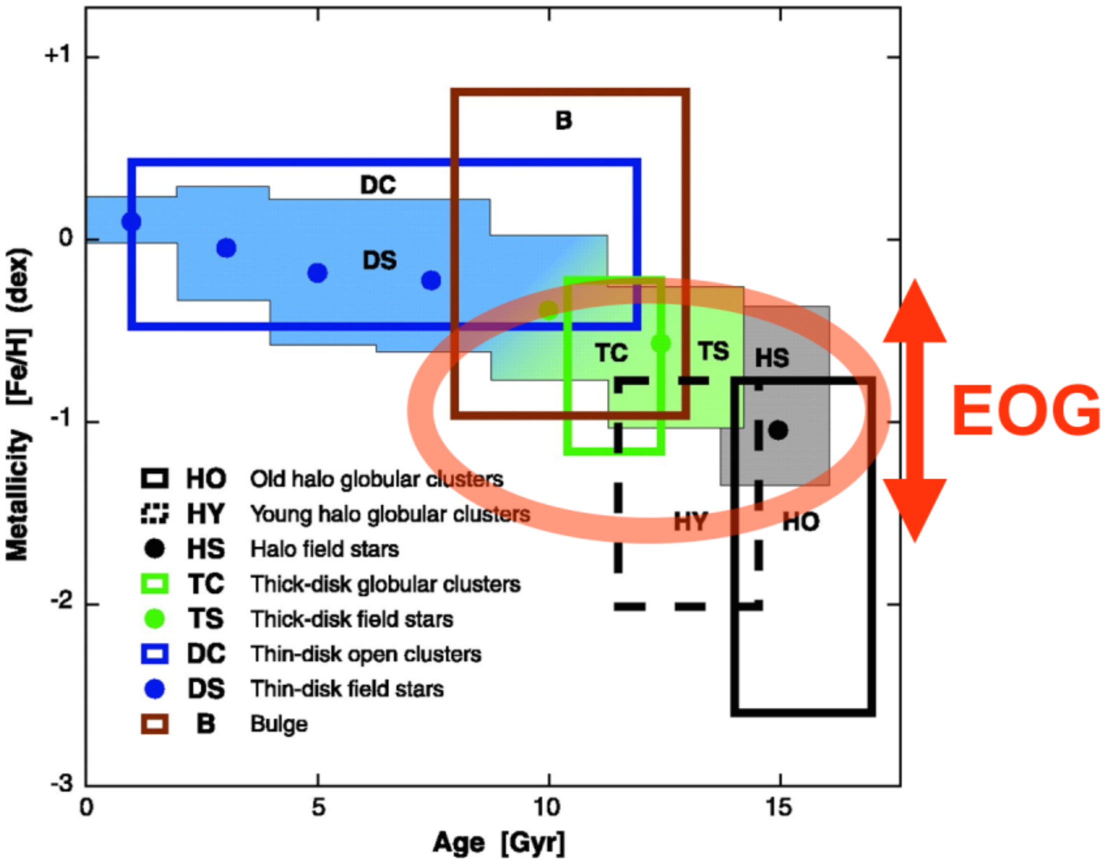

Figure 1.5: The age-metallicity relation of stars in the Galaxy. The EOG (Extreme outer Galaxy) is being found to have similar characteristics that existed in the phase of thick-disk formation. This figure is reproduced from Buser (2000).

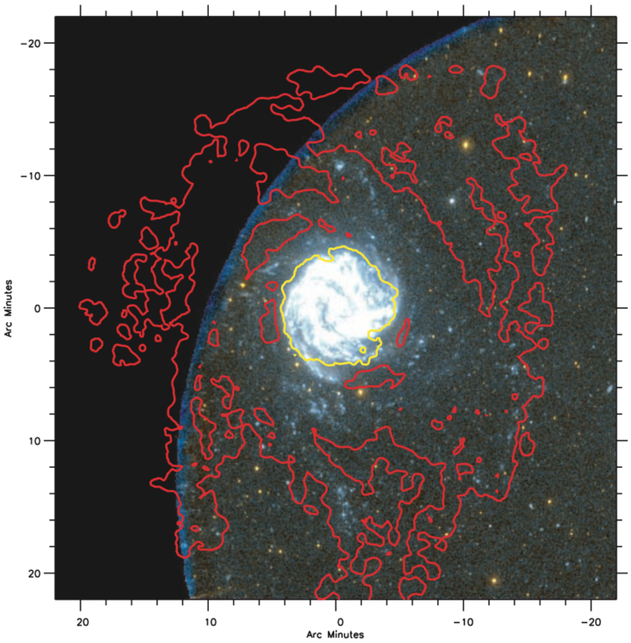

Figure 1.6: FUV (*blue*) and NUV (*orange*) color-composite image of M83 from *GALEX* data. The red contour shows HI distribution by Tilanus & Allen (1993), and is drawn at 1.8×10^{20} cm^{-2} (~ 0.4 $M_{\odot}$pc^{-2}). The yellow contour shows total neutral gas surface density of 10 $M_{\odot}$ pc^{-2} by Crosthwaite et al. (2002). This figure is reproduced from Thilker et al. (2005).

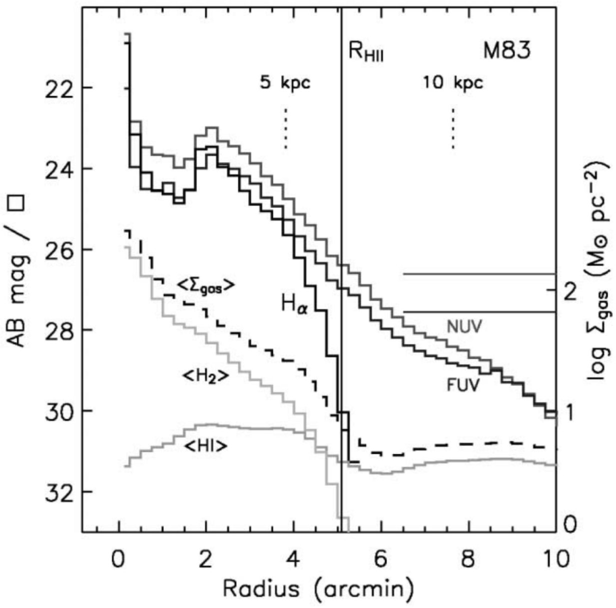

Figure 1.7: Radial profiles of the median FUV, NUV, and Hα surface brightness and average HI, CO and total gas surface densities in M83. The UV profiles are presented in absolute units, while the Hα profile is arbitrarily normalized. The vertical and horizontal lines indicate radius of inner disk (R_{HII}) and UV sky background, respectively. This figure is reproduced from Thilker et al. (2005).

1.2 Star formation law in outer region of galaxies

Figure 1.8 shows the relation between the gas surface densities ($\Sigma_{\mathrm{HI+H2}}$) and SFR surface densities, so-called "Kennicutt-Schmidt law (K-S law)", for nearby galaxies. The plot shows a complex star formation law, with at least three distinct regimes: 1) *the region within* $\Sigma_{\mathrm{HI+H2}} < 200\ M_{\odot}\ \mathrm{pc}^{-2}$, which is mainly composed of starburst galaxies, 2) *the region within* $10 < \Sigma_{\mathrm{HI+H2}} \leq 200\ M_{\odot}\ \mathrm{pc}^{-2}$, which is mainly composed of inner part of spiral galaxies, 3) *the region within* $\Sigma_{\mathrm{HI+H2}} \leq 10\ M_{\odot}\ \mathrm{pc}^{-2}$, which is mainly composed of outer part of spiral galaxies and low surface brightness galaxies. Thus, from the point-of-view of star formation law, inner and outer regions of spiral galaxies are distinctly different. The threshold surface density of K-S law ($\Sigma_{\mathrm{gas}} \sim 10\ M_{\odot}\ \mathrm{pc}^{-2}$) corresponds to that of FOG at $R_{\mathrm{G}} \sim 13.5$ kpc (See Figure 1.1). Compared to the inner Galaxy, the star formation process in the our Galaxy are predicted to start changing at FOG, then completely change in EOG (See Figure 1.8).

Recent studies show that, in inner region of galaxies, SFR correlates well with H_2 surface density while the correlation in weaker for HI (e.g. Figure 1.9, Schruba et al., 2011). Instead, the HI surface density distribution is found to saturate maximum values regardless SFR (e.g. Bigiel et al., 2008; Krumholz, 2013). Krumholz et al. (2008, 2009a,b) and McKee & Krumholz (2010) explained that the saturation is due to shielding effect: a certain column density of HI is required to block out the photodissociating effects of the interstellar radiation field and to allow a transition to H_2 (Krumholz, 2013). Therefore, SFR is likely to be determined simply by the amount of H_2 gas, suggesting the star formation process from molecular clouds to stars are the same.

However, the situation is quite different in outer region of galaxies and in dwarf galaxies, where the ISM is dominated by HI. Bigiel et al. (2010) and Bolatto et al. (2011) suggest that SFR begins to correlate with the total HI density, as the surface gas density goes down below $\Sigma_{\mathrm{gas}} \sim 3\ M_{\odot}\ \mathrm{pc}^{-2}$ (See Figure 1.8). The depletion time (τ_{dp}) of the star formation correlated with H_2 is ~ 2 Gyr, while that correlated with HI is significantly longer up to ~ 100 Gyr (Krumholz, 2013, ; See also Figure 1.8). Shi et al. (2014) also shows that extremely metal poor galaxies (dwarf galaxies) have longer depletion time, in other words, smaller constant star formation efficiency ($1/\tau_{\mathrm{dp}}$) than that in the metal-rich galaxies (Figure 1.10). Krumholz et al. (2008, 2009a,b); Krumholz (2012, 2013) and Ostriker et al. (2010) propose theoretical models to explain the star formation law in such metal-poor environments. For example, Krumholz (2012) shows that star formation occur in a cold atomic phase of the ISM rather than a molecular phase at extremely low metallicity region, Krumholz (2013) shows that H_2 fraction $f_{H2} = \Sigma_{H2} / (\Sigma_{HI} + \Sigma_{H2})$ decrease significantly at HI rich region (green solid line in Figure 1.10), and Ostriker et al. (2010) shows that SFR corresponds to Σ_{HI+H2} and midplane density of stars + dark matter in low SFR region (green dashed line in Figure 1.10). However, star-formation processes in the outer Galaxy are still not well understood, – *which model is best fitted for the observational result?* Therefore, it is very important to compare their models and observation results.

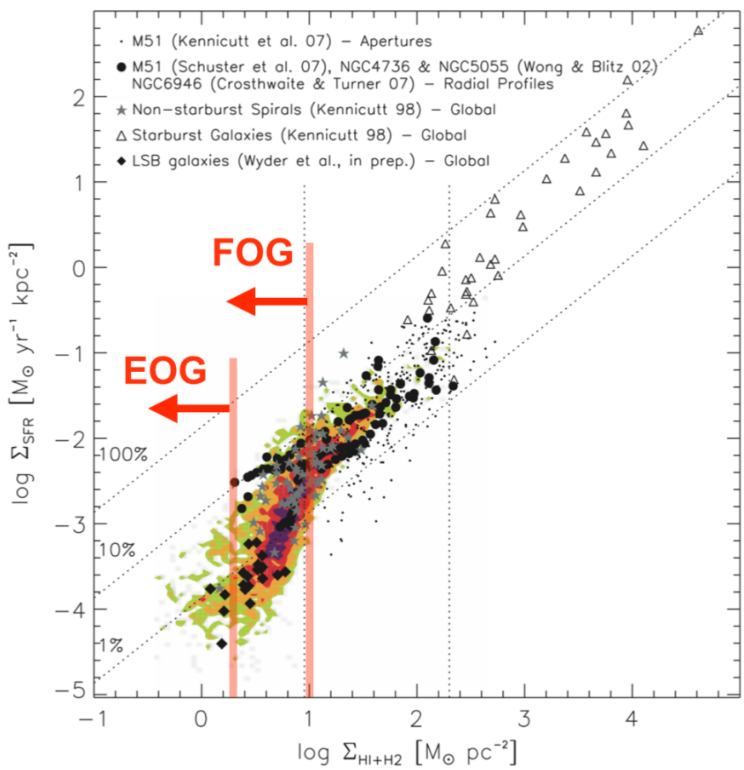

Figure 1.8: Relation between SFR surface densities (Σ_{SFR}) and total (atomic and molecular) gas surface densities (Σ_{HI+H2}) for various set of measurements. The diagonal dotted lines indicate constant SFE. This intensive plot indicates three distinctly different regions (separated by two vertical dotted-lines) for the SF law. This figure is reproduced from Bigiel et al. (2008) and slightly modified to show Σ_{HI+H2} range for FOG/EOG.

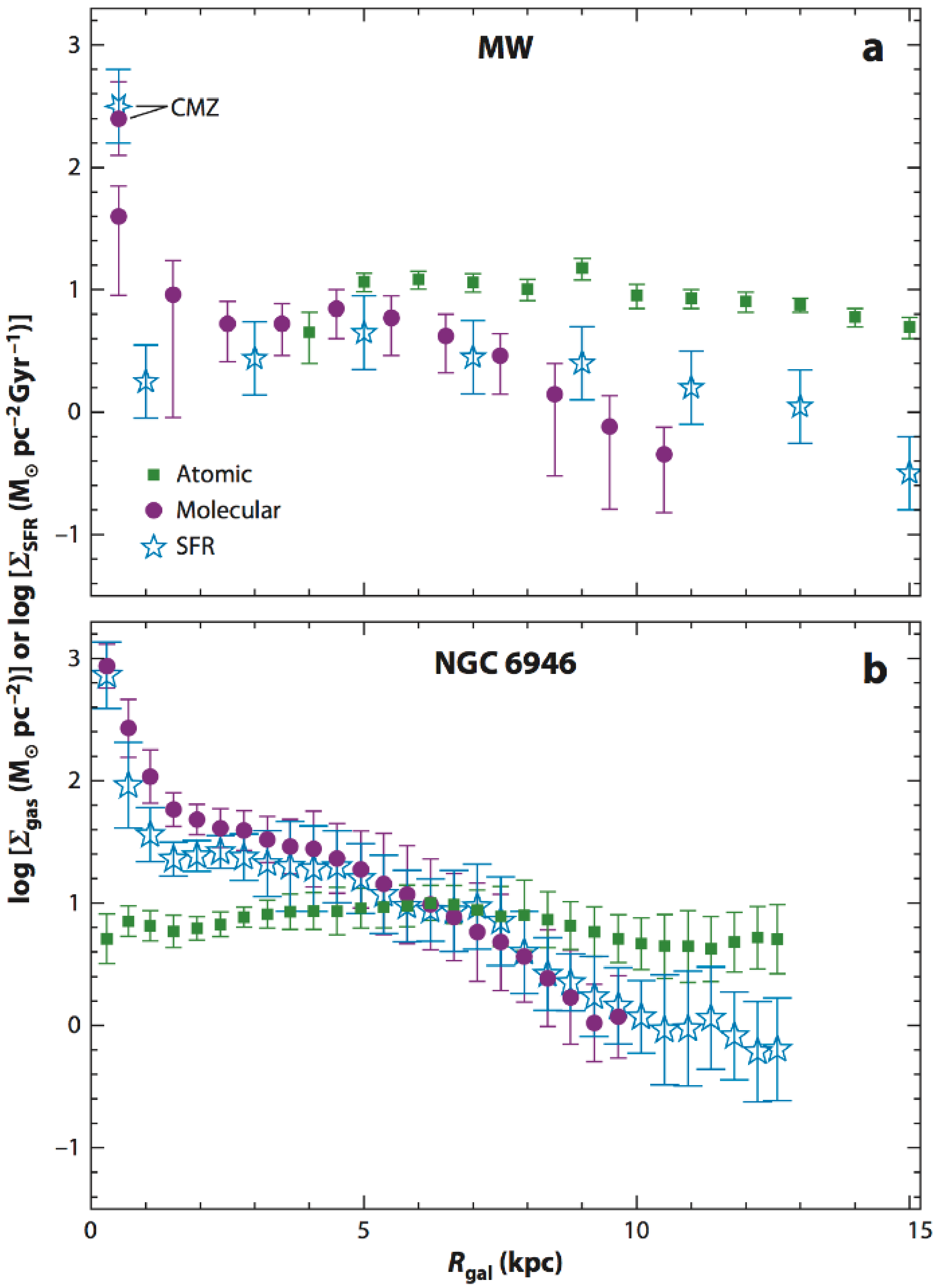

Figure 1.9: *Top*: The radial distribution of surface densities of atomic gas, molecular gas, and SFR for the Galaxy. *Bottom*: Same as top panel for NGC 6946, based on a figure in Schruba et al. (2011). This figure is reproduced from Kennicutt & Evans (2012).

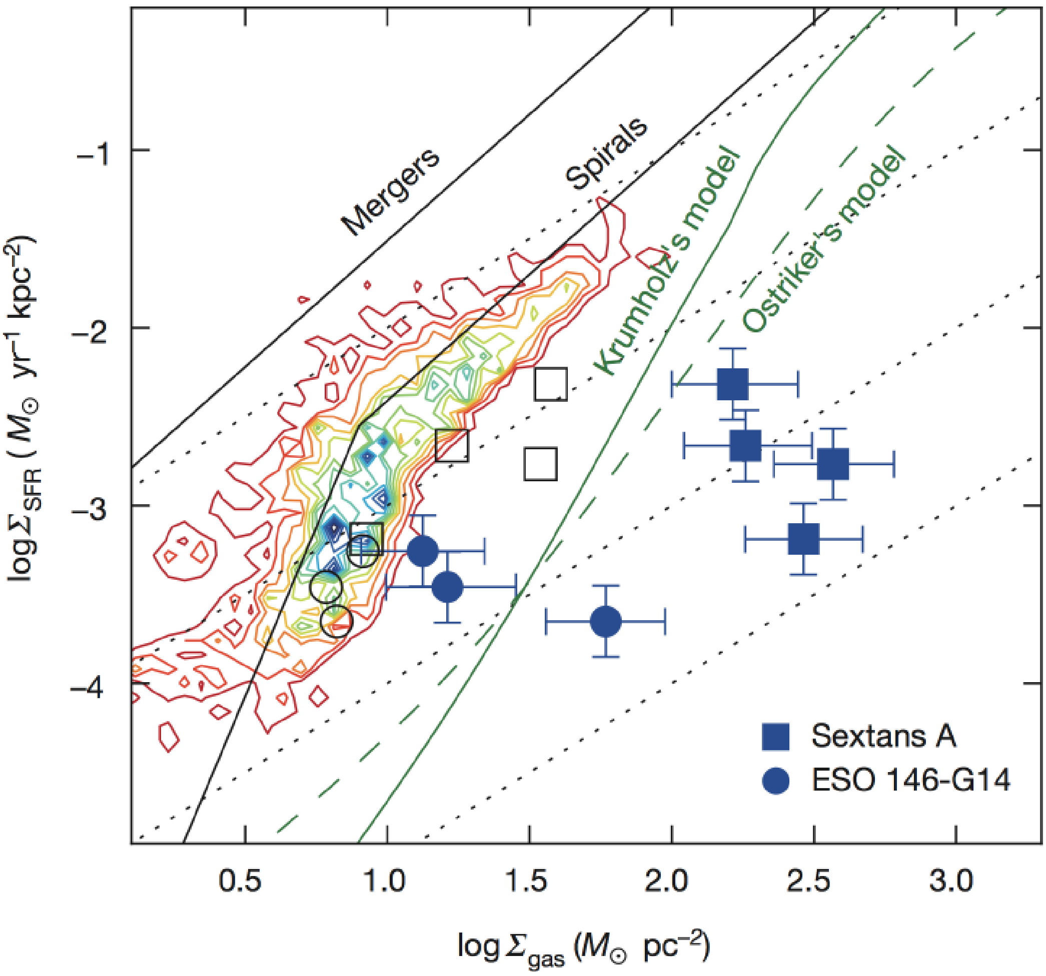

Figure 1.10: SFR versus gas surface densities for seven metal poor star-forming clumps in dwarf galaxies. Filled symbols for dust-based total gas mass, while open symbols are for atomic gas only. Data for spiral disk at sub-kpc scales (color contours; Bigiel et al., 2008), and integrated spirals and mergers (black lines; Daddi et al., 2010) are shown for comparison. The green solid and dashed lines show the models by Krumholz (2013) at 8% solar metallicity and a clumping factor 1, and by Bolatto et al. (2011) at 8% solar metallicity, respectively. Dotted lines indicate constant SFEs (in yr^{-1}) of, from top to bottom, 10^{-9}, 10^{-10}, 10^{-11}, 10^{-12}. This figure is reprinted by permission from Macmillan Publishers Ltd: Nature. Shi et al., Nature, 514, 335 (2014), copyright 2006.

1.3 Trigger of molecular cloud/star formation in the outer Galaxy

Because of the low gas density, trigger of star formation (including molecular cloud formation) is of strong concern in the outer Galaxy (e.g. Brand & Wouterloot, 2007). Low gas density naturally leads to triggered formation as opposed to spontaneous formation as a major mode of star formation in an environment (e.g. Rubio et al., 2015; Elmegreen, 1998, 2012). One clear example was provided by Yasui et al. (2006) and Kobayashi et al. (2008), who found that star formation in the Digel Cloud 2 (Digel et al., 1994), which is located at R_G = 19 kpc, are triggered by expansion of supernova remnant (SNR) shell. However, supernovae require the progenitor stars, whose origin again will be questioned. Although infalling dwarf galaxies in the halo of our Galaxy could be a source of the progenitor stars, density of such stars would be very low to ensure SNRs as major star-formation trigger.

Another possible trigger is infalling of HI clouds onto the outer Galaxy (e.g. Mirabel & Morras, 1990). Our Galaxy has a population of HI gas clouds moving at high velocities relative to the Local Standard of Rest (LSR), so-called High-Velocity Clouds (HVCs). HVCs are widely distributed in the halo (Figure 1.11) but the origin of HVCs is still controversial (e.g. Wakker & van Woerden, 1991). Recent high-sensitive HI observations finally found HVCs in other large spiral galaxies (Westmeier et al., 2008; Miller et al., 2009) and the Local Group galaxies (Adams et al., 2013). HVCs are suggested to affect galaxy evolution by bringing a large amount of gas ($M > 10^6\ M_\odot$) that can be used for a significant amount of star formation (Putman, 2006; Lehner & Howk, 2011; Putman et al., 2012; Fox et al., 2014). HVCs can also initiate star formation (Tenorio-Tagle, 1981; Lepine & Duvert, 1994) upon the impact with the disk. In fact, the head-tail structures of several HVCs (e.g. Putman et al., 2011; McClure-Griffiths et al., 2008) are considered to be the evidence of such interaction with our Galaxy. Recently, Complex GPC, called as Smith Cloud (Smith, 1963; Wakker & van Woerden, 1997), is paid a significant attention because it is suggested to be on the way fallings onto the Galactic disk (e.g. Lockman et al., 2008). Another type of halo clouds called IVCs (Intermediate-Velocity Clouds) are also focused as a major sources of interaction with the Galactic disk (Figure 1.12; Marasco et al., 2013). The origin of them are relatively clear and being explained by so-called fountain model (Norman & Ikeuchi, 1989).

Therefore, infalling HVCs could be a ubiquitous mechanism for triggering star formation in all kinds of disk galaxies. Because infalling of gas clouds must have been major events during the formation phase of galaxies (Figure 1.13; Dekel et al., 2009), study of such events in the outer Galaxy "at present time" is of strong interest in connection to the star formation in the early phase of the formation of the Galaxy.

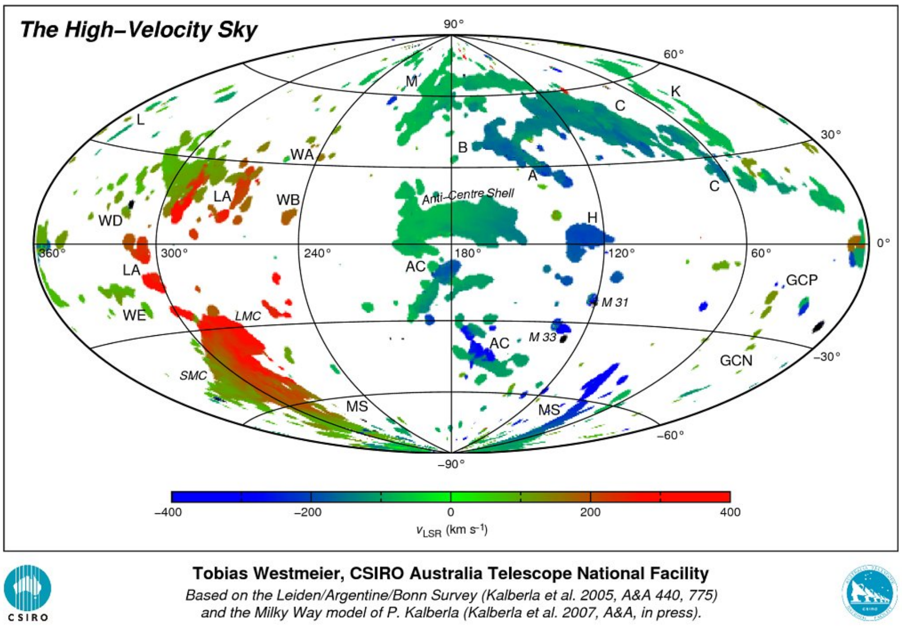

Figure 1.11: All-sky map of High-velocity clouds around the Galaxy. This figure is reproduced from `http://www.atnf.csiro.au/people/Tobias.Westmeier/research_hvcsky.php`.

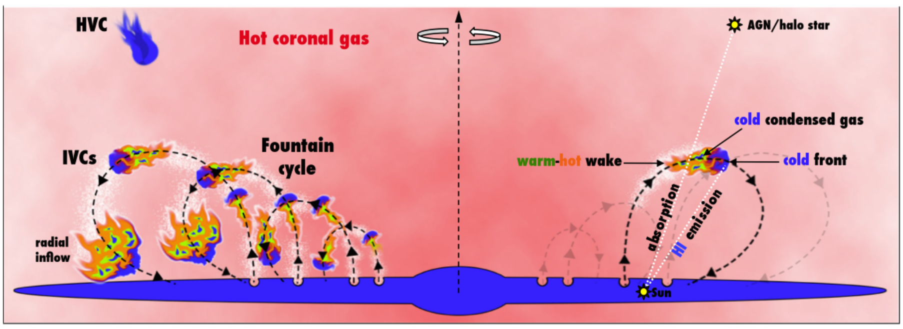

Figure 1.12: Image for Galactic fountain model. This figure is reproduced from Marasco et al. (2013).

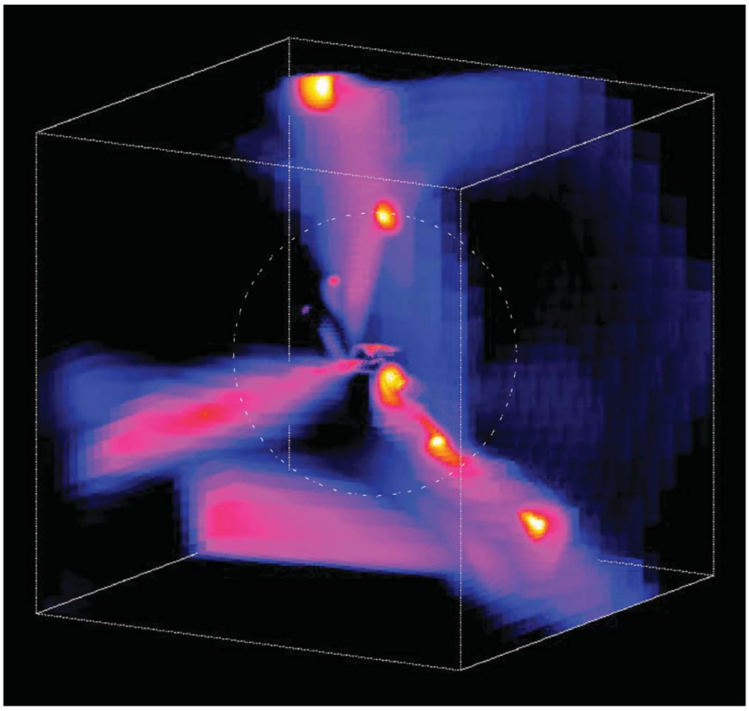

Figure 1.13: Simulated three dimentional image of cold streams penetrating hot haloes at high-z galaxy. This figure is reprinted by permission from Macmillan Publishers Ltd: Nature. Dekel et al., Nature, 457, 451 (2009), copyright 2009.

1.4 Past study of star-formation activity in the outer Galaxy

To date, a moderate number of molecular clouds have been recognized in the outer Galaxy up to R_G $\sim$ 22 kpc (Top panel of Figure 1.14). However, star-forming regions in the outer Galaxy have never been comprehensively surveyed and listed because of a lack of infrared survey data deep enough for large distance. Only about 30 star-forming regions are known so far (Bottom panel of Figure 1.14; e.g. Snell et al., 2002; Brand & Wouterloot, 2007).

In the classical work by Fich et al. (1990), they identified several HII regions in the FOG with Fabry-Perot spectroscopy in Hα. Since then, the outer Galaxy had not been exploited until de Geus et al. (1993) found an Hα emission in a very distant molecular cloud at the kinematic distance of D = 21 kpc (R_G = 28 kpc), Digel Cloud 2, which was found in the course of EOG cloud survey by

Digel et al. (1994). Subsequently, Kobayashi & Tokunaga (2000) discovered Young stellar objects (YSOs) in Cloud 2 with near-infrared (NIR) imaging, confirming it is surely a star-forming region in the EOG. Snell et al. (2002) performed K'- band (2.1 μm) imaging of 10 *IRAS* point sources associated with the FOG clouds to detect 11 stellar clusters within R_{G} = 13.5 – 17.3 kpc. They studied the star formation activity of all sample clouds using the ratio of far-infrared (FIR) luminosity to molecular cloud mass as an index of SFE. As a result, they found no-clear difference of star formation compared with molecular clouds in the W3/W4/W5 region of the Perseus spiral arm or in the inner Galaxy, despite the large difference of environment. The star formation processing in the FOG may really equal to that in the inner Galaxy, but the number of samples is not enough for any conclusive results. Also more details should be investigated to study the metallicity dependances of each star formation processes.

In the EOG, Kobayashi et al. (2008); Yasui et al. (2008) discovered star-forming clusters in Digel Cloud 2 (R_{G} = 19 kpc: Digel et al., 1994; Yasui et al., 2006). From fitting of the model K-band luminosity function (KLF) to the observed KLF, Yasui et al. (2008) suggest that the IMF in the Cloud 2 is not significantly different from the "universal" IMF. Yasui et al. (2010) also found that disk fraction of clusters with low-metallicity declines rapidly, which is much faster than the typical values for the solar-metallicity clusters. They recently found possible increase of disk fraction in the higher metallicity region in the inner most Galaxy (Yasui et al., 2016). All there result suggest that disk lifetime shortens with decreasing metallicity possibly with an $\sim 10^{\mathrm{Z}}$ dependence. Recently, Brand & Wouterloot (2007) discovered stellar cluster at direction of IRAS 06145+1455 (WB89-789), which associates with molecular clouds with kinematic distance of D = 11.9 kpc ($R_{\mathrm{G}} \sim$ 20.2 kpc). From such detailed study of star-forming regions, the star formation processes in the outer Galaxy are gradually cultivated.

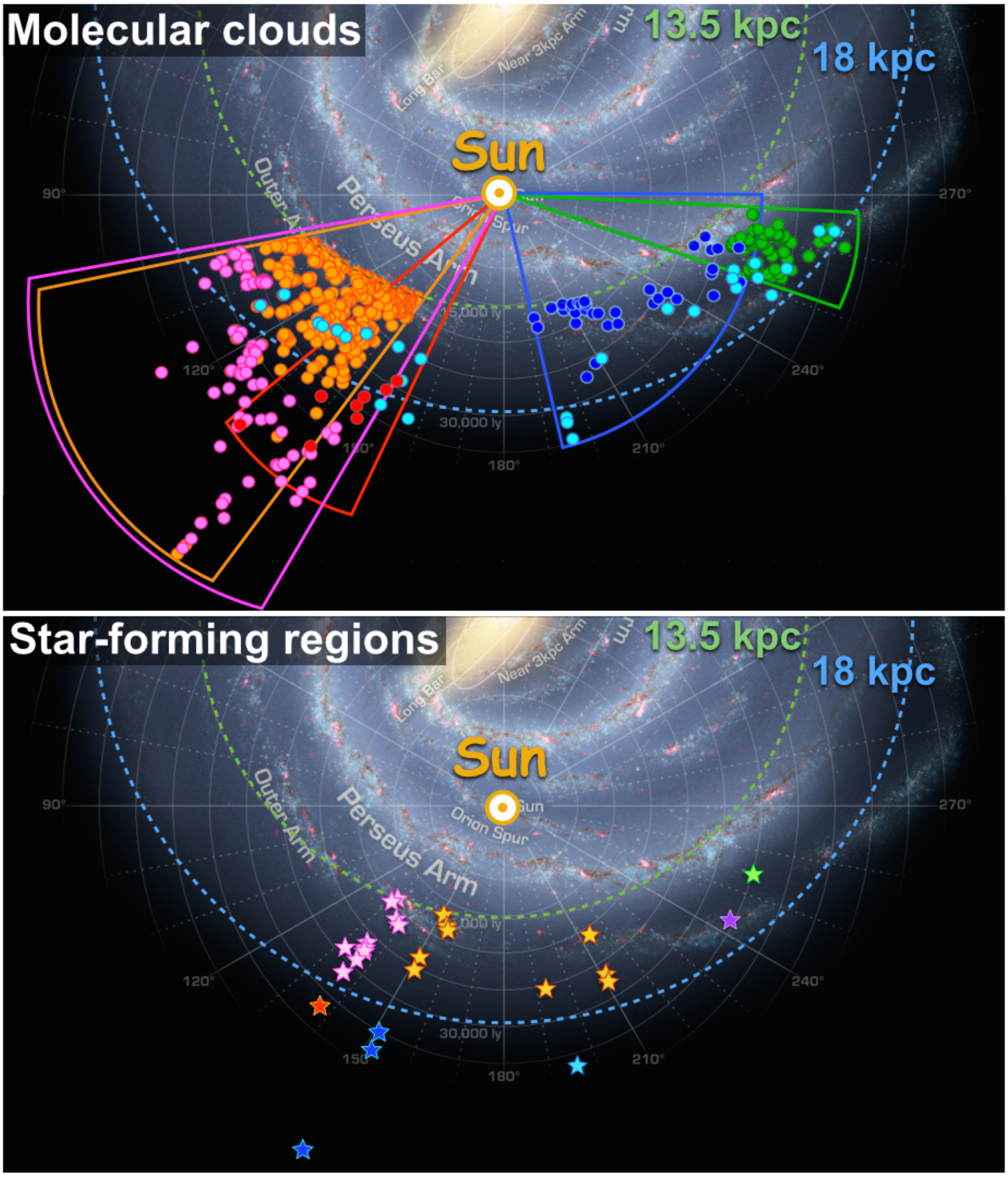

Figure 1.14: Distribution of known molecular clouds and star-forming regions in the Galaxy at $R_{\rm G} \geq 13.5$ kpc (rearranged the image of Milky Way Galaxy from NASA's Spitzer Space Telescope by NASA/JPL-Caltech). *Top*: Distribution of molecular clouds discovered by representative surveys at second and third quadrants (Orange: Brunt et al. (2003), Magenta: Sun et al. (2015), Red: Digel et al. (1994), Cyan: Brand & Wouterloot (1994), Blue: May et al. (1997), Green: Nakagawa et al. (2005)). Fan-shaped regions show each survey area, corresponding to the circles of the same color. Note that Brand & Wouterloot (1994) did not set survey area, but searched for molecular clouds based on *IRAS* sources in the second and third quadrants. *Bottom*: Distribution of star-forming regions in second and third quadrants (Magenta: Snell et al. (2002), Red: Yasui et al. (2006), Yellow: Brand & Blitz (1993), Green: Yun et al. (2015), Cyan:Brand & Wouterloot (2007), Blue:Anderson et al. (2015), Purple: Yadav et al. (2015)).

1.5 The purpose of this thesis

In this thesis, I present a study of global properties of star-formation activities in the outer Galaxy ($R_{\mathrm{G}} \geq 13.5$ kpc) in the scale of molecular cloud. First, I study the very distant molecular cloud Digel Cloud 1 (R_{G} = 22 kpc; Digel et al., 1994) with ^{12}CO(1-0) lines using the Nobeyama 45 m radio telescope as well as with NIR wavelength using the Subaru 8.2 m telescope, as a pilot study of star-formation in the outer Galaxy (Chaper 2). Next, I conducted a survey of star-forming regions at R_{G} $\geq$ 13.5 kpc in the 2nd Galactic quadrant with WISE (Wide-field Infrared Survey Explorer), which can effectively pick up star-forming regions by combining with recently available CO survey data in the outer Galaxy (Chapter 3). Using the newly identified star-forming regions from the survey, I discuss the distribution of star-forming region/molecular clouds in the Galactic disk (Chapter 4) and the properties of molecular clouds and star-forming regions in the outer Galaxy (Chapter 5). Finally, I discuss the variation of star-formation activities across Galactocentric radius. At R_{G} = 20 kpc, HI gas density and metallicity go down to less than half of those at R_{G} = 13.5 kpc. Thus, using only newly identified star-forming regions, the environmental dependence of star-forming activities can be investigated. While star formation consists of two basic processes, converting HI gas to H_2 gas, then converting H_2 gas to stars, my study focuses on the latter processes, as a first step to such a unique environment (Chapter 6). In Chapter 7, the summary of this thesis and the future prospect are presented.

Chapter 2

Star formation in Digel Cloud 1

In this Chapter, I report the properties of star-formation activity in a very distant molecular cloud in the EOG, as a pilot study of star-formation in the outer Galaxy. We performed high-sensitivity ^{12}CO mapping with the Nobeyama 45 m radio telescope and deep NIR imaging with the Subaru 8.2 m telescope to find two young embedded clusters at two CO peaks of Digel Cloud 1 at the kinematic distance of D = 16 kpc (R_G = 22 kpc). The contents in this chapter is already published as "Discovery of Star Formation in the Extreme Outer Galaxy Possibly Induced by a High-velocity Cloud Impact" (Izumi et al., 2014).

2.1 Digel Cloud 1

Based on CO observation of distant HI peaks in the Maryland-Green Bank survey (Westerhout & Wendlandt, 1982), Digel et al. (1994) discovered eight molecular clouds in the EOG (Digel Cloud 1-8, red filled circles in top panel of Figure 1.14). These clouds are a very valuable sample because the expected number of molecular clodus in such a low-density region is very small (Snell et al., 2002). A star-forming region has been identified in Cloud 2 (de Geus et al., 1993; Kobayashi & Tokunaga, 2000; Yasui et al., 2006, 2008), which has the highest CO luminosity among all Digel Clouds. While Cloud 1 has the largest dynamical mass, $M_{\mathrm{vir}} = 6 \times 10^4\ M_\odot$, among all Digel Clouds and it shows a relatively strong ^{13}CO line, no star-forming activity has been reported so far because of the very large distance with the largest Galactocentric radius (R_G = 22 kpc) among all Digel Clouds[1].

2.2 Observation and Data reduction

We observed Cloud 1 with deep NIR imaging by the Subaru 8.2 m telescope and high-sensitivity CO mapping by the Nobeyama (NRO) 45 m telescope (Figure 2.1). The left panel of Figure 2.2 shows the field of vied of the Subaru observation and mapping size of the NRO obeservation.

2.2.1 Subaru MOIRCS Imaging

We obtained J (1.25 μm)-, H (1.65 μm)-, and K_S (2.15 μm)-band deep images of the two CO peaks of Cloud 1 (Cloud 1a and Cloud 1b, left panel of Figure 2.2). The observations were conducted on 2006 September 2 UT with a wide-field near-infrared (NIR) camera, MOIRCS (Ichikawa et al., 2006) on the Subaru 8.2 m telescope. It provides a $4' \times 7'$ field of view with a $0''.117$ pixel^{-1} scale and employs the Mauna Kea Observatory (MKO) NIR photometric filters (Tokunaga et al., 2002). The total integration time was ∼700, 600, and 600 s for J, H, and K_S bands, respectively. The observing condition was photometric and the seeing was excellent ($\sim 0''.4$) throughout the observing period.

All of the data for each band were reduced with IRAF ver 2.14 with standard procedures: dark subtraction, flat fielding, bad-pixel correction, median-sky subtraction, image shifts with dithering offsets, and combining. The stellar FWHM in final images of the J, H, and K_S bands are $0''.45$, $0''.43$, and $0''.40$, respectively. JHK_S photometry has been performed using the IRAF APPHOT package, with aperture diameters of $1''.17$ (10 pixels). The aperture sizes were chosen to achieve high signal-to-noise ratio (S/N) and sufficient flux count from the stellar objects. Photometric calibration was done using the standard star Persson9166 (GSPC P330-E; J = 11.772, H = 11.455, K = 11.419; Leggett et al., 2006). The resultant 10σ limiting magnitudes in the J, H, and K_S bands were estimated at 21.0, 20.5, and 19.5 mag, respectively.

[1]Although the kinematic distance of Cloud 2 is larger than that of Cloud 1 in Digel et al.'s (1994) original list, the photometric distance of Cloud 2 is found to be smaller than the kinematic distance (R_G = 19 kpc). See Chapter 2.4 for more detail.

2.2.2 CO Data with the Nobeyama Radio Observatory (NRO) 45 m Telescope

We have performed observations of Cloud 1 in the CO (J= 1–0; 115.271 GHz) line with the NRO 45 m telescope[2] in 2007 December. We used the 25-BEam Array Recceiver System (BEARS) in the double-side band mode, which has 5 $\times$ 5 beams separated by 41$''$.1 on the plane of the sky (Sunada et al., 2000; Yamaguchi et al., 2000). The telescope beamwidth and the main beam efficiency at 115 GHz was 14$''$.5 and 0.39, respectively. As a backend, the autocorrelator was adopted, and the typical noise level was 0.40 K in $T_{\rm A}^*$ with 0.25 km s^{-1} resolution in CO.

We employed an on-the-fly mode developed for the NRO 45 m telescope (Sawada et al., 2008). The data sampling interval of the R.A. or decl. scans is $\sim$ 1$''$, and the separation between the each scans is 5$''$.1. After subtracting linear baselines, the data were convolved with a Gaussian-tapered Bessel function whose FWHM was 14$''$ and resampled onto a 6$''$ grid. Since the telescope beam is a Gaussian with an FWHM of 14$''$.5–14$''$.8, and effective FWHM resolution of $\sim$17$''$. Finally, to reduce the "scanning effect", where some of the conditions outlined above have not been adequately satisfied, resulting in an effective noise level on the final map higher than the theoretical value, we combine the two maps scanned R.A. and decl. directions using the basket-weaving method (Emerson & Graeve, 1988). We mapped an area of 15$'$ $\times$ 16$'$ in CO to cover the entire Cloud 1 (Figure 2.2).

The atmospheric corrected temperature scale $T_{\rm A}^*$ is obtained with the chopper wheel method. During the observation, the typical system noise temperature of BEARS in the double-side band was 400 K at CO frequencies. The telescope pointing was checked about every 90 minutes by five-point scans of the SiO maser source S-Per [R.A. = 02$^{\rm h}$ 22$^{\rm m}$ 51$^{\rm s}$.713, decl. = 58° 35$'$ 11$''$. 50 (J2000)] with SIS 49 GHz receiver (S40). The measured pointing errors ranged from 1$''$.5 to 6$''$.0 during the observing run.

2.2.3 Previous Observations

In addition to the our NIR and CO observation, I used archived data from previous observations "the Canadian Galactic Plane Survey (CGPS)"(Taylor et al., 2003), "the FCRAO outer Galaxy Survey" (Heyer et al., 1998), "the Leiden/Argentine/Bonn (LAB) Survey of Galactic HI"(Kalberla et al.,

[2]The Nobeyama Radio Observatory is a branch of the National Astronomical Observatory of Japan, National Institutes of Natural Sciences.

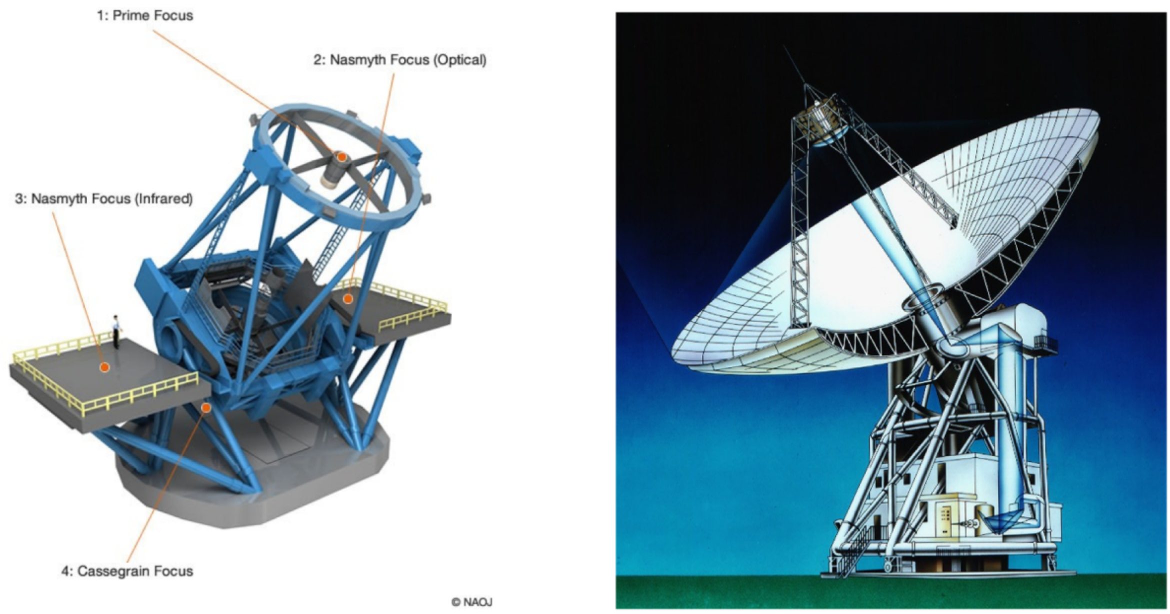

Figure 2.1: *Left*: Image of the Subaru 8.2 m telescope. This figure is reproduced from `http://subarutelescope.org/Introduction/telescope.html`. *Right*: Image of the Nobeyama 45 m radio telescope. This figure is reproduced from `http://www.nro.nao.ac.jp/~nro45mrt/html/pictures/illust/index-e.html`.

2005), "the *Wide-field Infrared Survey Explorer* (*WISE*) all-sky survey" (Wright et al., 2010), and "the INT/WFC Photometric Hα Survey (IPHAS)" (Drew et al., 2005). I summarize the observation I used to study Cloud 1in this thesis in Table 2.1. Note that the FCRAO outer Galaxy Survey and *WISE* all-sky survey are described in more detail in Chapter 3 for other studies in this thesis.

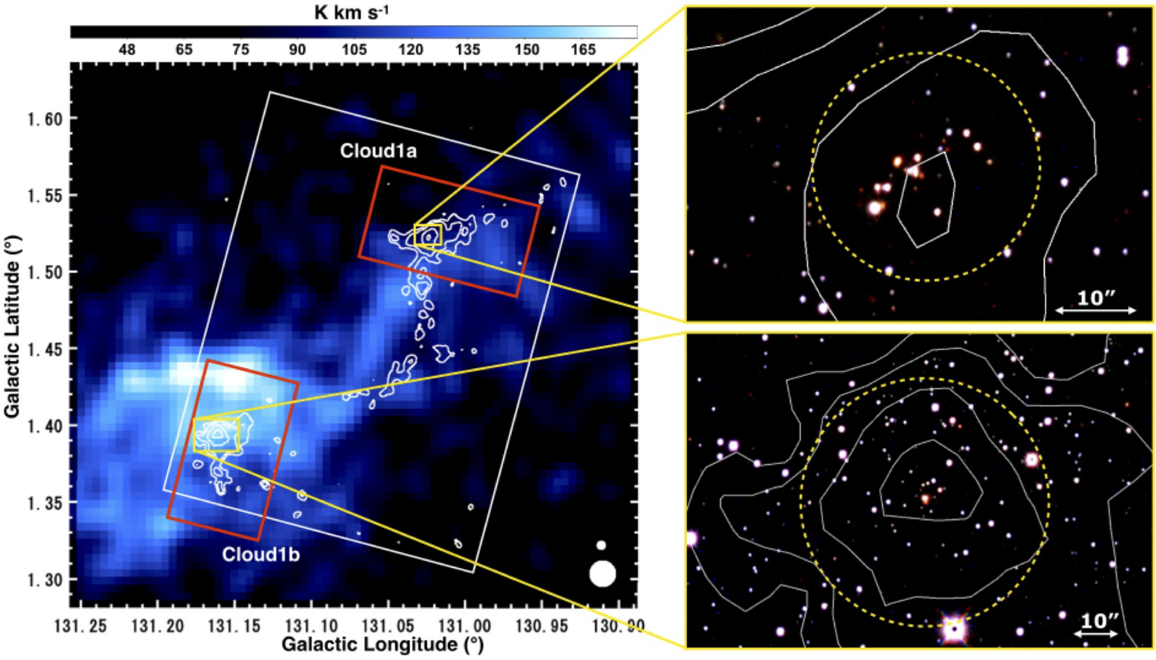

Figure 2.2: *Left*: HI map around Cloud 1 (from CGPS data : $v_{\rm LSR} = -104.5 \sim -99.6$ km s^{-1}). The white contours show the integrated ^{12}CO (1–0) map of Cloud 1 (from our NRO 45 m telescope data: $v_{\rm LSR} = -104.1 \sim -99.1$ km s^{-1}), and contour levels are at 2σ, 3σ, 5σ, 7σ (1σ = 0.5 K km s $^{-1}$). The white and red boxes show the mapping size of the NRO 45 m observation and the field of view of the Subaru MOIRCS ($4' \times 7'$), respectively. The large and small white filled circles at the lower right corner show the beam sizes of the DRAO ($\sim$58″) and NRO 45 m telescope ($\sim$17″), respectively. *Right*: *JHK* pseudo-color images of the Cloud 1 clusters from our Subaru MOIRCS data. The white contours show the same as the ^{12}CO map as in the left panel. The yellow dotted circles show the defined cluster regions (radius of Cloud 1a circle : 14″, Cloud 1b : 28″).

Table 2.1: Parameters of the Observations Containing the Region Cloud 1 or Complex H

Project	Telescope	Wavelength	Coverage	Velocity Range (km s^{-1})	Velocity Resolution (km s^{-1})	Resolution[a]
CGPS	DRAO	21.1 cm (HI)	$74^\circ.2 < l < 147^\circ.3$	-150 to 50	1.32	$58'' \times 58''$cosecδ
	Synthesis Telescope		$-3^\circ.6 < b < +5^\circ.6$			
LAB survey	Villa Elisa	21.1 cm (HI)	$0^\circ < l < 360^\circ$	-450 to 450	1.27	$30'.0$
	30 m		$-90^\circ < b < -25^\circ$			
	Dwingeloo	21.1 cm (HI)	$0^\circ < l < 360^\circ$	-450 to 450	1.25	$35'.7$
	25 m		$-30^\circ < b < +90^\circ$			
FCRAO outer	FCRAO	2.6 mm (^{12}CO)	$102^\circ.49 < l < 141^\circ.54$	-153 to 40	0.98	$45''$
Galaxy Survey	14 m		$-3^\circ.03 < b < +5^\circ.41$			
WISE	*WISE*	3.4 μm	All-sky	···	···	$6''.1$
	satellite	4.6 μm	All-sky	···	···	$6''.4$
		12 μm	All-sky	···	···	$6''.5$
		22 μm	All-sky	···	···	$12''.0$
IPHAS	Issac Newton 2.5 m	656.8 nm (Hα)	$29^\circ < l < 215^\circ$	···	···	$0''.333$ pixel^{-1}
	(Wide Field Camera)		$-5^\circ < b < +5^\circ$			
This thesis	Subaru 8.2 m	1.25 μm (J)	$4' \times 7' \times 2$	···	···	$0''.112$ pixel^{-1}
	(MOIRCS)	1.65 μm (H)	$4' \times 7' \times 2$	···	···	$0''.112$ pixel^{-1}
		2.15 μm (K_S)	$4' \times 7' \times 2$	···	···	$0''.112$ pixel^{-1}
	NRO45 m	2.6 mm (^{12}CO)	$15' \times 16'$	-110 to -90	0.25	$\sim 17''$

[a] The meaning of the resolution with the IPHAS and Subaru 8.2 m observation is pixel size, and others is diffraction limited resolution.

2.3 Results

2.3.1 Detection of Star-forming Regions in Cloud 1

The right panel of Figure 2.2 shows JHK pseudo-color images from our Subaru MOIRCS data at two CO peaks of Cloud 1a and 1b (Digel et al., 1994, left panel of Figure 2.2). I found two star clusters of reddened stars, in the vicinity of the two CO peaks. I examined the positional relationship between clusters, Cloud 1, and the other foreground molecular clouds on the sky to confirm that Cloud 1 is the only molecular cloud positionally coincident with the clusters. Therefore, I concluded that these clusters are embedded clusters associated with Cloud 1. In view of the location of the clusters in the molecular clouds, near the peak of the dense CO core, these clusters are likely to be younger than $\sim$ 3 Myr (Lada & Lada, 2003).

In order to define the extent of the clusters, I derived the stellar number density distribution around the CO peaks (Figure 2.3). As a result, I defined the radius of the Cloud 1a and 1b cluster region to be $14''$ and $28''$, respectively.

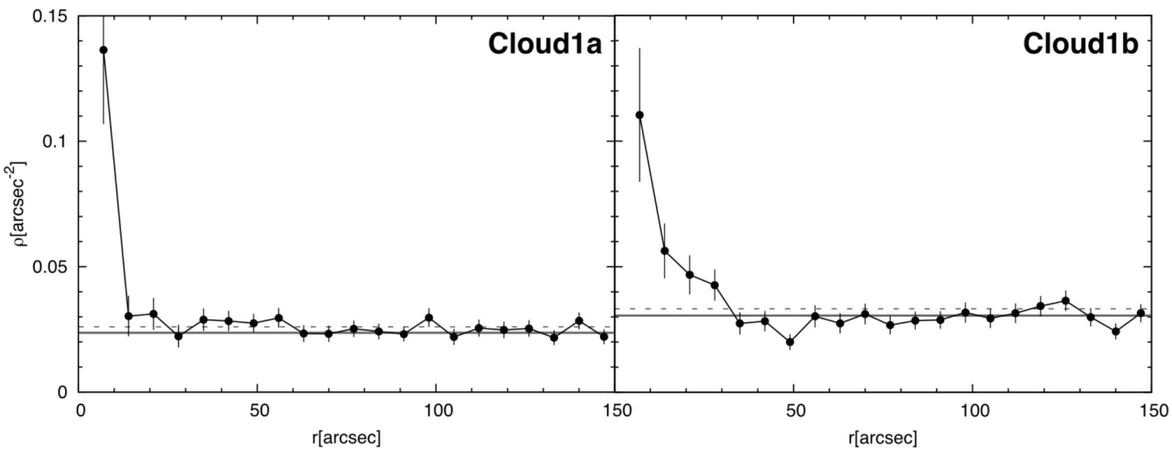

Figure 2.3: Radial variation of the projected stellar number density of stars around the center of the CO peaks (left: Cloud 1a, right: Cloud 1b). The center position of Clouds 1a and 1b are (l,b)=(131°.02, 1°.52) and (131°.16, 1°.39), respectively. The error bars represent Poisson errors (1σ). The horizontal solid lines and horizontal dashed lines indicate the average density of stars outside the Cloud 1 clouds and the Poisson errors (1σ), respectively.

2.3.2 Identification of Cluster Members

I identified cluster members using the $J - K_S$ versus J color-magnitude diagram of all the detected sources with S/N $> 5\sigma$ in all three bands (Figure 2.4) following the method used in Yasui et al. (2006, 2008). On the color-magnitude diagram, we estimated the nominal extinction (A_V) of all the detected sources by measuring the distance along the reddening vector (Rieke & Lebofsky, 1985) from a reference isochrone of an assumed age of 1 Myr and a kinematic distance of D = 16 kpc (see Figure 2.4). I found that stars with large extinction, $A_V \geq 4$ mag and 3 mag are concentrated on the Cloud 1a and Cloud 1b cluster area, respectively, while stars with small extinction ($A_V = 0$–2 mag) are uniformly distributed over the observed field (see insets in Figure 2.4). Therefore, I identified the cluster members with the following criteria: (1) distributed in the regions of Cloud 1a and Cloud 1b cluster region (see Figure 2.2) and (2) $A_V \geq 4$ and 3 mag for Cloud 1a and Cloud 1b, respectively. With this 2nd criterion, the contamination of field stars is estimated to be only 2 % (1a) and 10 % (1b), which is almost negligible. The number of resultant cluster members of Cloud 1a and Cloud 1b are 18 and 45, respectively (Figure 2.5). The radii of the defined cluster region in Cloud 1a and Cloud 1b are 1.1 pc (14″) and 2.2 pc (28″), respectively (see Figure 2.2). Therefore, the estimated stellar densities of the clusters are 5 pc^{-2} and 3 pc^{-2}, respectively. The achieved limiting magnitudes correspond to the mass-detection limit of $< 1\ M_\odot$ for the kinematic distance (D = 16 kpc).

Figure 2.6 shows the K-band luminosity functions (KLFs), which are the number of stars as a function of K-band magnitude, for the member of two Cloud 1 clusters. The estimated completeness limit of Cloud 1 data is about K_S = 20 mag. I estimated the detection completeness by the number of field stars, which rapidly decrease at $K_S > 20$ mag. The KLF of the Cloud 1a cluster shows a rather stochastic curve probably because of the small number of detected members due to the large differential extinction, or the truly small number of members. Therefore, I use the KLF of the Cloud 1b cluster for the present study assuming that the Cloud 1a and 1b clusters have similar properties.

2.3.3 Molecular Clouds Distribution in Cloud 1

In the CO distribution of Cloud 1 (Figure 2.7), I detected two CO peaks (Cloud 1a and Cloud 1b) at $v_{\rm LSR} \sim 100$ km s^{-1} and a newly found bridge structure, which connects the two peaks. To estimate the

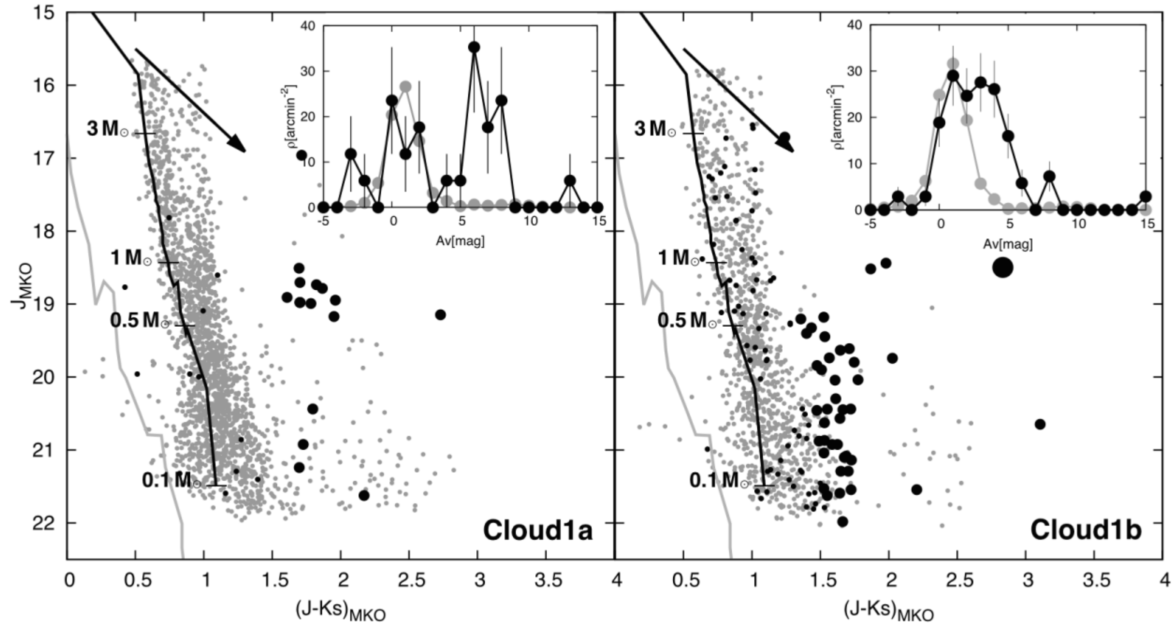

Figure 2.4: $(J - K_S)$ vs. J color-magnitude diagram for the Cloud 1 clusters in the MKO system (left: Cloud 1a, right: Cloud 1b). The top-right inset of each panel shows A_V distributions of stars in the cluster regions (black filled circles and lines) and in the field (gray filled circles and lines). The error bars show the uncertainties assuming Poisson statistics. The gray lines show dwarf tracks (Bessell & Brett, 1988), while the black lines show isochrone models (1.0 Myr; Siess et al., 2000). The black arrows show the redding vectors of A_V = 5 mag. The filled circles show stars in the cluster regions of Cloud 1a and Cloud 1b, respectively, small circles show field stars in the cluster regions, large circles show identified cluster members, and the very large circle shows the most luminous dereddened source. The gray dots show field stars in the field of view.

masses of these clouds from the CO intensity I_{CO}, I used the same mass-calibration ratio $N(H_2)/I_{CO}$ as Digel et al. (1994) (2.3×10^{20} cm^{-2} (K km s^{-1})$^{-1}$; the Galactic average value). The estimated masses of Cloud 1a, Cloud 1b, and the bridge are 3.0×10^3, 3.5×10^3, and 4.5×10^3 $M_\odot$, respectively. The estimated velocity width of Cloud 1a, Cloud 1b, and the bridge are 2.2, 2.4, and 1.9 km s^{-1}, respectively. The estimated radii of Cloud 1a and Cloud 1b are 5.6 and 4.2 pc, respectively, and the length of the bridge is 42 pc. The parameters for Cloud 1a and Cloud 1b are consistent with the results of Digel et al. (1994).

Figure 2.7 also shows MIR pseudo-color images from the *WISE* data around Cloud 1. I confirmed that the Cloud 1 clusters are also detected in the MIR images as groups of compact reddened stellar objects. I found some other compact reddened stellar objects around the two CO peaks and in the

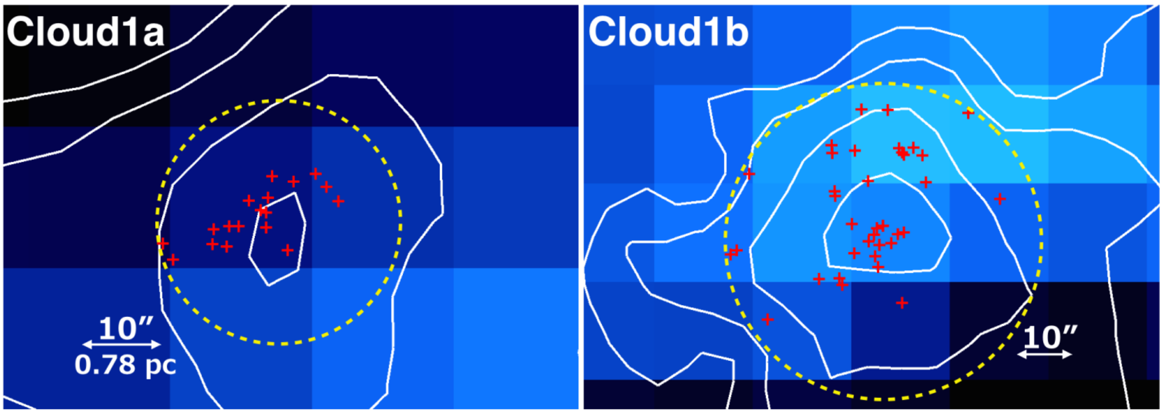

Figure 2.5: Distribution of cluster members in Cloud 1 clusters (Left: Cloud 1a, Right: Cloud 1b). The red crosses show position of cluster members. Blue-scale backgrounds show HI distribution from CGPS data, which are same as left panel of Figure 2.2. The white contours show the integrated ^{12}CO (1–0) map of Cloud 1 from our NRO 45 m telescope data, which are same as Figure 2.2. The yellow dotted circles show the defined cluster regions, which are same as right panel of Figure 2.2 (radius of Cloud 1a circle : 14″, Cloud 1b : 28″).

bridge, which also appear to be associated with Cloud 1. The large diffuse reddened (12 μm) structures are considered to be the Galactic cirrus (Meisner & Finkbeiner, 2014) in the foreground. The compact reddened stellar objects are discussed in detail in Chapter 3 for other studies in this thesis.

2.3.4 Extinction Inside Cloud 1

I compared the extinction of the Cloud 1 clusters from our NIR data to that from the ^{13}CO column density in the literature. Ruffle (2006) estimated the ^{13}CO column density of Cloud 1a to be N(^{13}CO) = $2.09 \pm 0.32 \times 10^{15}$ cm^{-2}, but no estimate was made for Cloud 1b. From this column density, I estimated the extinction of Cloud 1a to be $A_V = 4.4$ mag, assuming the same dust-to-gas ratio and ^{13}CO fractional abundance as the solar neighborhood (e.g., Frerking et al., 1982). The total extinction of Cloud 1a from our data is $A_V = 5 \sim 8$ mag (see the top right inset of Figure 2.4), and the extinction by foreground interstellar clouds at $R_G < 20$ kpc is estimated to be $A_V = 3 \sim 4$ mag (e.g., Amôres & Lépine, 2005). Therefore, the extinction of the Cloud 1a clusters contributed from only the molecular cloud is estimated to be $A_V = 1 \sim 5$ mag. In view of the systematic uncertainties of related parameters, this value is roughly consistent with the extinction derived from the ^{13}CO data. Although the dust-to-gas ratio in such low-metallicity environment compared to the solar neighborhood is of great interest,

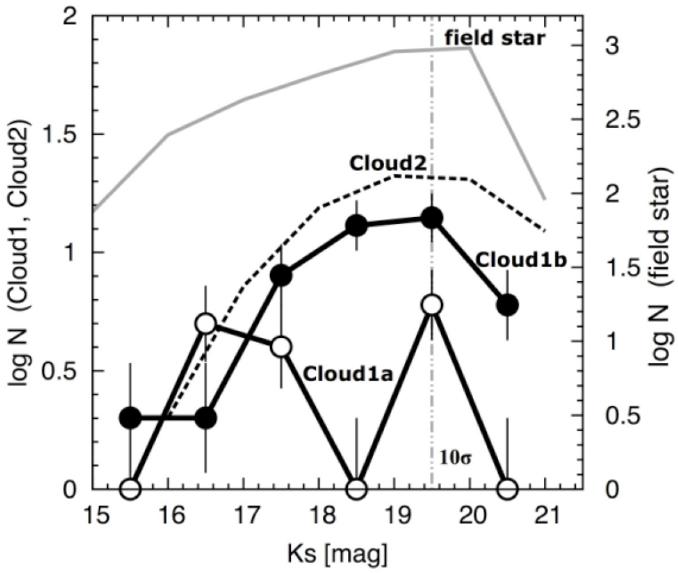

Figure 2.6: *K*-band luminosity function (KLF) of Cloud 1a (open circle), Cloud 1b (filled circle), and Cloud 2 (dashed line) clusters. The KLF for Cloud 2 is from the left panel of Figure 10 in Yasui et al. (2008). The error bars show the uncertainties assuming Poisson statistics. The gray line shows all of the field stars in the MOIRCS images of Cloud 1. The vertical dotted line shows the estimated completeness limit of Cloud 1 data (note that the completeness limit for Cloud 2 is about 20 mag).

it is hard to discuss the possible difference without other independent data.

2.3.5 HI Distribution around Cloud 1

The large-scale HI distribution around Cloud 1 (Figure 2.8) shows that there is an HI peak of the HVC Complex H (HVC 131+1-200) close to Cloud 1 on the sky with a separation of only $\sim 0.5°$, though they are about 100 km s^{-1} apart from each other in the line-of-sight velocities. Furthermore, there is a large HI shell at $v_{\rm LSR} \sim -100$ km s^{-1}, which was originally identified by Heiles (1979). Cloud 1 overlaps in position with part of the shell, at around $l \sim 131^\circ.1, b \sim 1^\circ.5$, and also in the line-of-sight velocity (Morras et al., 1998). The shell is elongated along the Galactic plane and its size is about $7° \times 3.5°$, approximately constant in the size and position within the $v_{\rm LSR}$ velocity range of –109 to –98 km s^{-1}, suggesting that the cavity surrounded by the shell has a cylindrical shape (Morras et al., 1998).

The high-resolution HI map around Cloud 1 from the CGPS data (see Figure 2.2) shows that

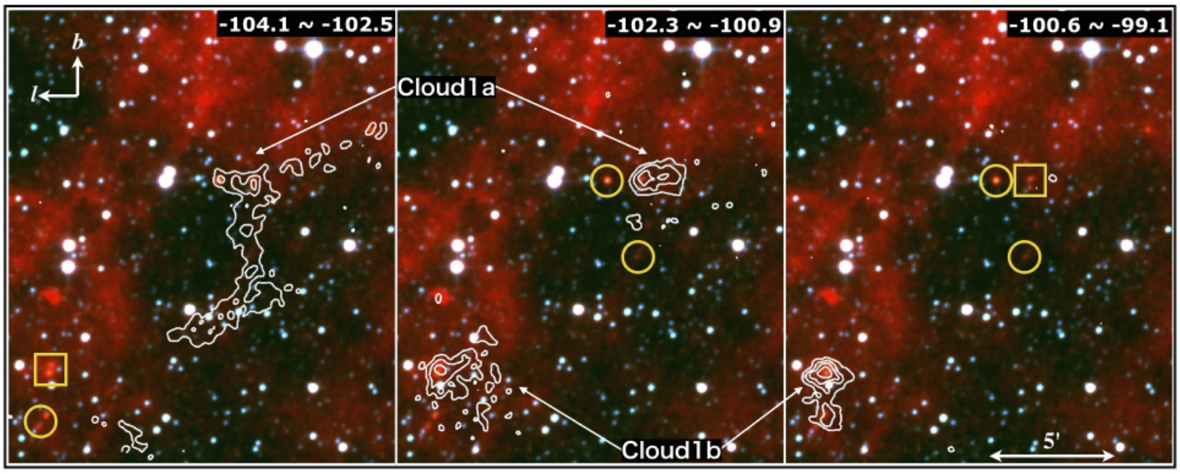

Figure 2.7: ^{12}CO velocity channel maps for three consecutive line-of-sight velocity ranges in km s $^{-1}$ (from NRO 45 m telescope data) and mid-infrared pseudo color image around Cloud 1. The color images are produced by combining the 3.4, 4.6, and 12 μm images from the *WISE* data. The yellow circles show compact reddened stellar objects in Cloud 1, and the yellow boxes show the Cloud 1a and 1b clusters, which are detected by the 8.2 m Subaru telescope. The contour interval is 0.46 K km s^{-1} and range is from 0.46 to 1.82 K km s^{-1}.

Cloud 1 is associated with an elongated HI distribution in the same velocity range. I estimated the HI column density, radius, mass, and velocity width of the HI cloud as 3.6×10^{20} cm^{-2}, 67 pc, 4.1×10^4 $M_\odot$, and 9.1 km s^{-1}, respectively.

2.4 Properties of Cloud 1 clusters

Because the slope and peak magnitude of KLF vary with age and distance (Muench et al., 2000), I estimate those parameters of the Cloud 1 clusters by comparing the observed KLF with that of the young (0.5–1 Myr) embedded cluster in the EOG, the Digel Cloud 2 clusters (Yasui et al., 2006, 2008). The photometric distance of Cloud 2 has been estimated to be R_G = 15–19 kpc (D = 8–12 kpc) by high-resolution optical spectroscopy of a B-type star MR1 (Smartt et al., 1996), which is apparently associated with Cloud 2 (de Geus et al., 1993); the shortest and longest distances are based on LTE and nonLTE model stellar atmospheres, respectively. Each producing errors are less than 15% (D = 8±1–12±2, R_G = 15±1–19±2). In this thesis, I adopt R_G = 19 kpc (D = 12 kpc) because the nonLTE model is more likely to be accurate for stars in the effective temperature regime of MR-1 (Smartt et

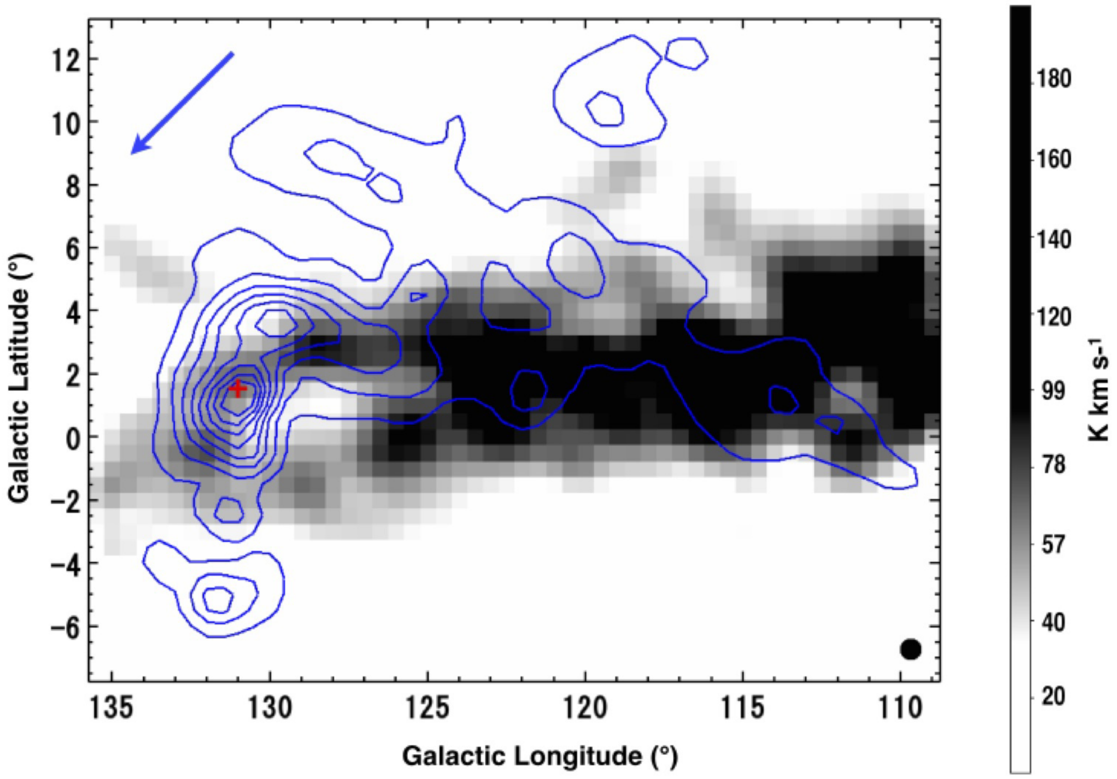

Figure 2.8: HI clouds in the extreme outer Galactic disk and HVC Complex H seen in a wide field from LAB data. While the blue contours show Complex H ($v_{\rm LSR}$ = –229.8 $\sim$ –150.5 km s^{-1}), the grayscale HI map shows the Galactic disk at $v_{\rm LSR}$ = –104.1 $\sim$ –98.9 km s^{-1}. The red cross marks the position of Cloud 1 in the Galactic disk ($v_{\rm LSR}$ $\sim$ –101 km s^{-1}). The contour interval is 10.8 K km s^{-1} (20σ) and the range is from 8.5 to 73.1 K km s^{-1} (15σ to 135σ). The blue arrow shows the direction of Complex H's motion (Lockman, 2003). The black filled circle shows the beam size of the LAB data ($\sim$ 35′).

al., 1996; Kobayashi et al., 2008) and also because $R_{\rm G}$ = 15 kpc has too much large discrepancy with $R_{\rm G}$ = 22 kpc from the kinematic distance. In Table 2.2, the properties of the Cloud 1 and 2 clusters are listed.

2.4.1 Age

I estimated the age using the slope of KLF, which is modeled to vary with age (Muench et al., 2000) and the slope becomes steeper with older age. Yasui et al. (2006, 2008) discussed the age of the Cloud 2 clusters by comparing observed KLF and model KLFs of various ages. They used model KLF based on Trapezium IMF (Muench et al., 2002). Trapezium is consisted of about 10^3 cluster members, and therefore, IMF of the cluster is the most reliable IMF for young clusters (e.g. Lada & Lada, 2003). Clusters with $10^1 \sim 10^3$ cluster members are empirically known to have same IMF (e.g. Lada & Lada, 2003; Yasui et al., 2006). Thus, Trapezium IMF is of good use for small clusters ($\sim 10^1$ cluster members), such as Cloud 1 and 2 clusters. They estimated the ages of Cloud 2 clusters to be 0.5 – 1 Myr, because the model KLF of 0.1 Myr and 2 Myr have gentler and steeper slopes, respectively, than the observed KLF of the Cloud 2 clusters (see Figures 7 and 10 in Yasui et al. 2006 and 2008, respectively). To check the possible large difference of IMF from the typical IMFs because of the special environment of the EOG, they tried to fit the observed KLF assuming the fixed age of 2 Myr. As a result, they found that the necessary IMF has a very unrealistic slope (See Figure 6 in Yasui et al., 2006), and concluded that the age of the Cloud 2 clusters to be 0.5–1 Myr, and 2 Myr at most. Figure 2.6 shows that the KLF of the Cloud 1b and Cloud 2 clusters have a very similar slope between K_S = 16 to 19 mag, and therefore, I estimated the age of the Cloud 1 clusters to be similar to the Cloud 2 clusters (0.5 – 1 Myr, and 2 Myr at most).

As an additional check of the age, I derived the disk fraction (DF) of the clusters, which is the percentage of cluster members with a optically thick circumstellar dust disk. Because the DF is known to decrease with increasing age up to 10 Myr (e.g., Lada, 1999; Haisch et al., 2001; Hernández et al., 2007; Yasui et al., 2010), it is sometimes used for the estimate of the cluster age. Following the description in Yasui et al. (2009, 2010), I derived the DF of the Cloud 1 clusters using the H–K_S versus J–H color-color (CC) diagram. The resulting DF of 24 $\pm$ 8% (9/37) for detected sources with S/N $> 10\sigma$ suggests that the age of the Cloud 1 clusters is less than 1 Myr assuming the rapidly decaying DF curve in the low-metallicity environment (Figure 1 in Yasui et al., 2010). Because the ages estimated from both KLF and DF are consistent, I conclude that the age of the Cloud 1 clusters is less than 1 Myr, suggesting that these clusters are truly young embedded clusters.

2.4.2 Photometric Distance

The peak magnitude of KLF is sensitive to age and distance of the cluster. For older age and larger distance, the peak magnitude becomes fainter. Figure 2.6 shows that the peak magnitude of the Cloud 1b cluster is similar to or fainter than, that of the Cloud 2 cluster. In view of the similarity of the age of the Cloud 2 cluster (see Chapter 2.4.1), the Cloud 1 clusters are expected to have the same or larger distance than the Cloud 2 cluster. Therefore, the distance to the Cloud 1 clusters with R_G is suggested to be more than 19 kpc ($D \geq 12$ kpc), which is consistent with the kinematic distance (R_G = 22 kpc; Digel et al., 1994). In addition, I tried to estimate the distance to the Cloud1 clusters, assuming that the most luminous star in the cluster is Herbig Ae/Be star of 3–5 $M_\odot$, which is suggested for such small clusters (Testi et al., 1999; Weidner & Kroupa, 2006). The resultant distance is 8 kpc $\leq D \leq$ 21 kpc (15 kpc $\leq R_G \leq$ 27 kpc), which is consistent with the estimated distance by KLF and kinematic distance. Therefore, we suggest that the Cloud 1 clusters are located in the EOG region.

2.4.3 Star formation efficiency

Using the properties of Cloud1, I estimated the Star formation efficiency (SFE) of Cloud 1 clusters: $M_{\rm stars}/(M_{\rm gas}+M_{\rm stars})$, where $M_{\rm gas}$ is cluster forming core mass and $M_{\rm stars}$ is total stellar mass in the clusters. First, I derived $M_{\rm stars}$ for Cloud 1 clusters using isochrone model by Siess et al. (2000) with D = 16 kpc, Age = 1 Myr, Av = 3 – 5 mag, and metallicity (Z) = 0.02 (solar metallicity). The mass limit is set at $\sim$ 0.2 $M_\odot$ (K_S = 19.5 mag). The resulting $M_{\rm stars}$ value of Cloud 1a and b are 27 and 28 $M_\odot$, respectively. Next, I derived $M_{\rm gas}$ of Cloud 1 from ^{12}CO intensity within the cluster region (radius of cluster region in Cloud 1a and b are 1.1 pc and 2.2 pc, respectively; see Section 2.3.2) with the Galactic average mass-calibration ratio N(H_2)/$I_{\rm CO}$ =2.0 $\times$ 10^{20} cm^{-2} (K km s^{-1}) (e.g. Bolatto et al., 2013) and the correction for the abundance of helium (1.36; Dickman, 1978). The resulting $M_{\rm gas}$ of Cloud 1a and b are 1.5 $\times$ 10^2 $M_\odot$ and 5.8 $\times$ 10^2 $M_\odot$, respectively. As a results, the SFEs of Cloud 1a and 1b are 18% and 4.8% respectively. These values are consistent with that of Cloud 2 clusters (12 – 13 %; Yasui et al., 2008) and clusters in the solar neighborhood (2.3% to 57% with an median of 15 %; Yasui et al., 2008). However, we should be careful in comparing SFEs for Cloud 1 clusters with the others, because $M_{\rm gas}$ for the other clusters are derived from ^{13}CO or C^{18}O, and also the mass detection limits of the other clusters are less than 0.2 $M_\odot$.

To check the uncertainty of $M_{\rm stars}$, I examined the isochrone model (Siess et al., 2000) with the range of D = 12 – 16 kpc, Age = 0.5 – 2 Myr, Av = 3 – 5 mag, and Z = 0.02 – 0.01 (See Figure 2.9). The masses of the most luminous stars in the cluster (K_S $\sim$ 15.5 mag), which are dominant on total stellar mass in the clusters, change from 3 to 5 $M_\odot$, and thus the $M_{\rm stars}$ change only by 20 % at most within the range of those parameters. However, the uncertainty of $M_{\rm gas}$ appears to be much larger than that of M_{stars}. There are at least two main parameters of M_{gas}: 1) size of core region, and 2) mass-calibration ratio N(H_2)/I_{CO}. First, M_{gas} varies from 10^2 $M_\odot$ to 10^3 $M_\odot$ by changing the size of core region from the cluster area to the cloud area (within 3σ). Next, the mass-calibration ratio could be larger in low-metallicity environment, such as outer Galaxy, than Galactic average ratio (e.g. Bolatto et al., 2013). In fact, the ratio in the Small Magellanic cloud, which has about 1/5 solar metallicity, is suggested to be about 10 times of Galactic average ratio (Leroy et al., 2011). In addition, M_{gas} values derived with ^{12}CO and other optically thinner lines (such as ^{13}CO and C^{18}O) may be different. In view of the potentially large uncertainty of M_{gas}, the estimated SFEs should be taken as preliminary values.

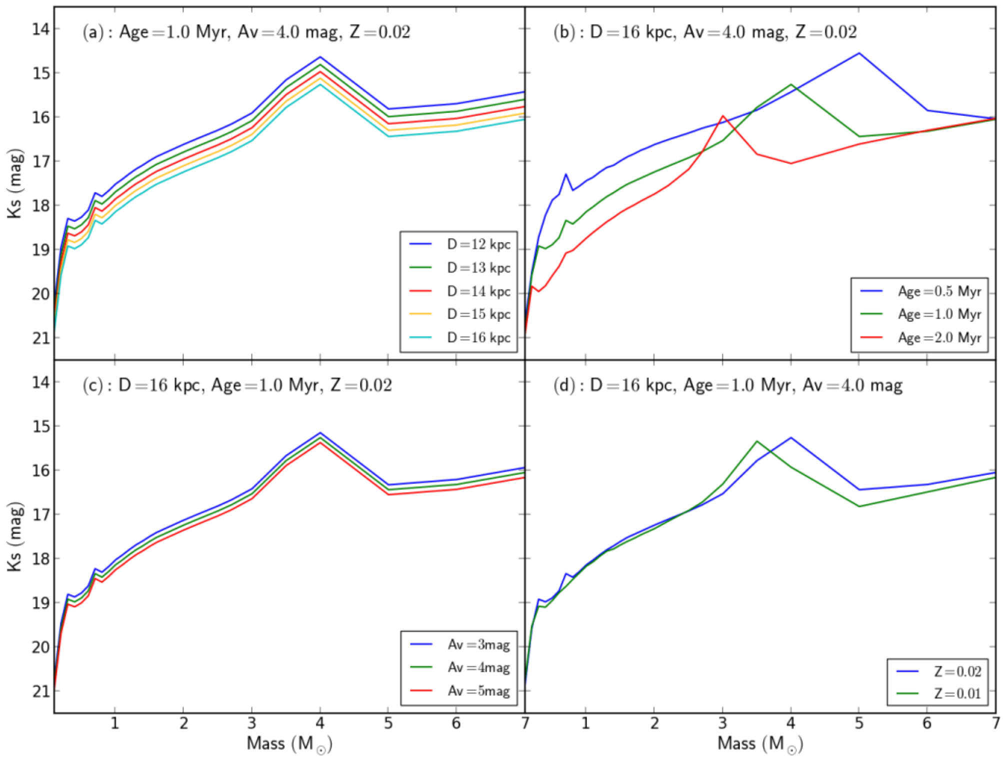

Figure 2.9: Variation of Isochrone model with parameters (Siess et al., 2000). (a) Variations of Isochrone model with distances. (b) Variations of Isochrone model with ages. (c) Variations of Isochrone model with extinctions (Av). (d) Variations of Isochrone model with metallicities (Z).

Table 2.2: Properties of Cloud 1 and Cloud 2

Cloud	Cloud Mass ($10^3 M_\odot$)	Number of Stars	Disk Fraction (%)	Age (Myr)	R_G (kinematic) (kpc)	R_G (photometric) (kpc)	SFE (%)
Cloud 1a	3.0	18	14 ± 10 (2/14)	<1	22	≥ 19	18
Cloud 1b	3.5	45	24 ± 8 (9/37)	<1	22	≥ 19	4.8
Bridge	4.5	···	···	···	22	···	···
Cloud 2-S[a]	8.5	66	27 ± 7 (16/59)	0.5–1.0	23.6	19	13
Cloud 2-N[a]	14	72	9 ± 4 (5/52)	0.5–1.0	23.6	19	12

[a] The mass, kinematic distance, photometric distance of Cloud 2 clouds are from Digel et al. (1994), Stil & Irwin (2001), Kobayashi et al. (2008), respectively. Other parameters of Cloud 2 are estimated by Yasui et al. (2006, 2008, 2010).

2.5 Possible triggered cloud/star formation in Cloud 1

Here, I discuss the triggered Cloud/star formation in Cloud1. Because of the low-density, triggered formation as opposed to spontaneous formation may play a crucial role in such a low-density environment (Elmegreen, 2011, 2012). Triggered star formation on the scale of a molecular cloud is nominally described as follows (Elmegreen, 1998, 2011), (1) stellar pressure (including expansion of HII region and supernova remnant (SNR) shell), and (2) collision and collapse between two clouds (cloud-cloud collision). In the following I introduce the unique environment of Cloud 1 to discuss the possibility that a *large-scale* cloud-cloud collision, which was originally proposed by Morras et al. (1998), is the trigger of cloud/star formation of Cloud 1.

2.5.1 Large HI Shell

Cloud 1 is located on a large HI shell with a size of 0.8 kpc $\times$ 0.9 kpc at the kinematic distance of R_G= 22 kpc (Figure 2.8, see also Chapter 2.3.5). Therefore, the star-formation mechanism is primarily suggested to be connected to the shell formation. In fact, such a large-scale triggered star formation by a super bubble or a super shell is reported for several regions in the Local arm (e.g., Lee & Chen, 2009), the Perseus arm (e.g., Sakai et al., 2014; Lee & Lim, 2008), and the EOG (Kobayashi et al., 2008). In addition to Cloud 1, I noticed several more molecular clouds, which are associated with the shell, from the list of molecular clouds identified in the FCRAO data (Brunt et al., 2003). Because no molecular cloud is found inside or outside the shell (see Figure 2.10), I suggest that all those clouds are related to the shell formation.

2.5.2 Stellar Feedback?

First, I discuss the possibility that the shell formation was triggered by stellar feedback. Morras et al. (1998) estimated the energy required to produce the large HI shell by a sudden explosion is of the order of $\sim 10^{53}$ erg, which requires the combined action of stellar winds and supernova explosions. However, a large OB association, which can make such a large shell, has not been detected near Cloud1 (Morras et al., 1998). To confirm this idea, I reexamined the presence of any prominent sources of stellar pressure inside the HI shell, using the latest archival data compiled after Morras's work : Hα images (IPHAS), MIR images (*WISE*), and HI data (LAB and CGPS). However, I could not identify any source and/or structure that traces an OB association or an SNR.

2.5.3 HVC Impacting on the Galactic Disk?

Next, I pay attention to the interaction between Complex H and the Galactic disk, which was first noted by Morras et al. (1998) and later discussed by others (e.g., Blitz et al., 1999; Lockman, 2003; Simon et al., 2006), to discuss if it can cause the HI shell formation as well as the molecular cloud/star formation. Based on HI data with the Effelsberg 100 m Radio Telescope, Morras et al. (1998) suggested the impact of an HVC on the outer Galactic disk, which resulted in the presently observed Complex H and the large HI shell. Based on highly sensitive data with the Green Bank Telescope, Lockman (2003) paid attention to the "tail" structure between Complex H and the Galactic disk in a position-velocity (PV) map, and suggested that the Complex H is more like a satellite of the Galaxy in an inclined retrograde orbit, whose outermost layers are currently being stripped away in its encounter with the Galaxy. However, in a PV map made from the LAB data (Figure 2.11), we have noticed that some intermediate velocity structures of the "spur" and "bridge", which connect the Complex H to the Galactic disk, in addition to the "tail" structure, and that Cloud 1 appears to be located at the edge of such structures. Although the large-scale tail structure is likely to be formed by tidal force, the existence of the bridge and spur structures in the PV diagrams as well as the HI shell structure (Chapter 2.5.1) support the Morras et al. (1998)'s impacting idea because such structures are predicted by the simulation of cloud-cloud collision (e.g., Figure 2 in Comeron & Torra, 1992).

Blitz et al. (1999) posed a major objection to the Morras et al. (1998)'s impacting idea because there is no trace of an impact, such as Hα and X ray emission from a strong shock, suggesting that Complex H is an extragalactic HI cloud. Simon et al. (2006) followed the Blitz et al. (1999)'s extragalactic idea to present the argument that Complex H is either a dark galaxy in the Local Group, or an example of a cold accretion flow onto the Galaxy. However, a similar case of an HI cloud impacting on the Galactic disk, which does not show any detectable Hα or soft X-ray emission, is reported for HVC 306-2+230 by McClure-Griffiths et al. (2008), who argue that such emissions from associated ionized gas are absorbed by foreground dust and gas in the Galactic plane. The Complex H is also located at low-galactic latitude, and moderately high extinction is measured for the large distance. Therefore, the lack of Hα and X ray emission does not appear to be strong evidence against Morras et al. (1998)' impacting idea.

I also considered the timescale of the collision (impact) in relation to the cloud/star formation in Cloud 1. Assuming that the HI peak of the Complex H has a spherical shape with a radius of $R \sim$1.4 kpc (5° at R_G= 22 kpc) and the relative velocity of $\Delta v \sim$ 100 km s^{-1}, the estimated dynamical timescale of the collision is $R/\Delta v \sim$ 10 Myr. The typical timescale for formation of a molecular cloud is considered to be $\sim$ 10 Myr (Ballesteros-Paredes et al., 2007; Gratier et al., 2012). The lifetime of a molecular cloud as well as the timescale of star formation is also considered as $\sim$ 10 Myr (Mouschovias et al., 2006). All of these timescales are not longer than the estimated collision timescale. In fact, the ages of Cloud 1 clusters are estimated to be $<$1 Myr (see Chapter 2.4.1). In all possible cases in which the impact triggered (1) both molecular cloud and star formation, (2) only molecular cloud formation, or (3) only star formation in Cloud 1, the collision timescale does not conflict with the timescales of subsequent processes.

Therefore, I suggest a possibility that the formation of the Cloud 1 clusters and Cloud 1 itself was triggered by the impact of Complex H on the Galactic disk at $R_G \sim$ 22 kpc. Further study of this cloud will be very important for revealing the dynamical processes of such triggered formation.

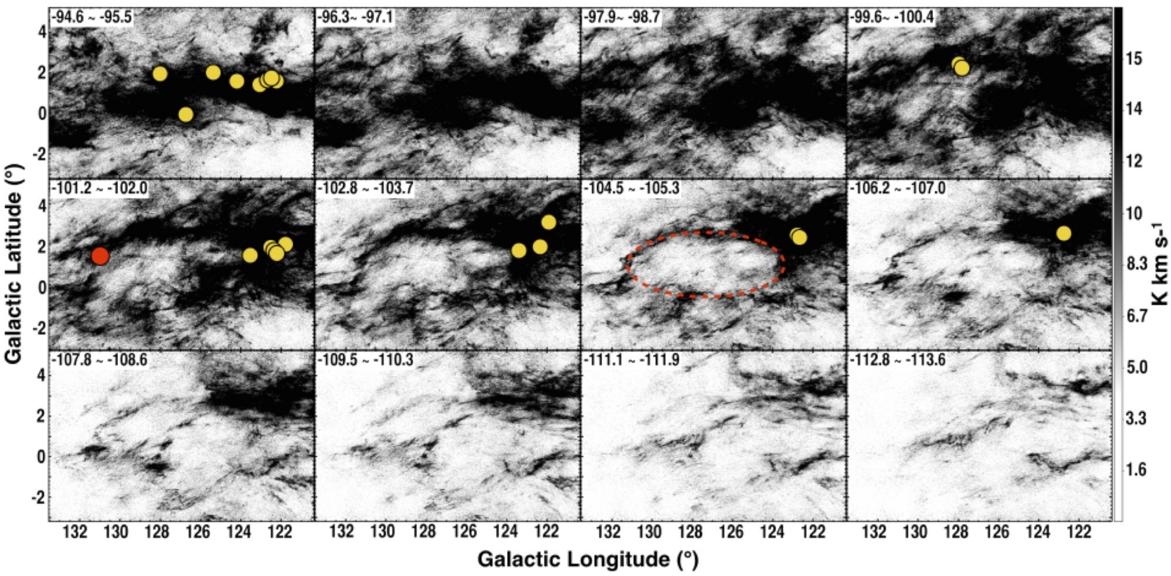

Figure 2.10: HI channel map from the CGPS data. Every other channel between –94 and –113 km s^{-1} is shown. The red filled circle shows the position of Cloud 1, and the dotted red line traces the large shell structure (see Chapter 2.3.4, Chapter 2.5.1). The yellow filled circles show the positions of the molecular clouds, which are identified in the FCRAO data (see Chapter 2.5.1 for detail).

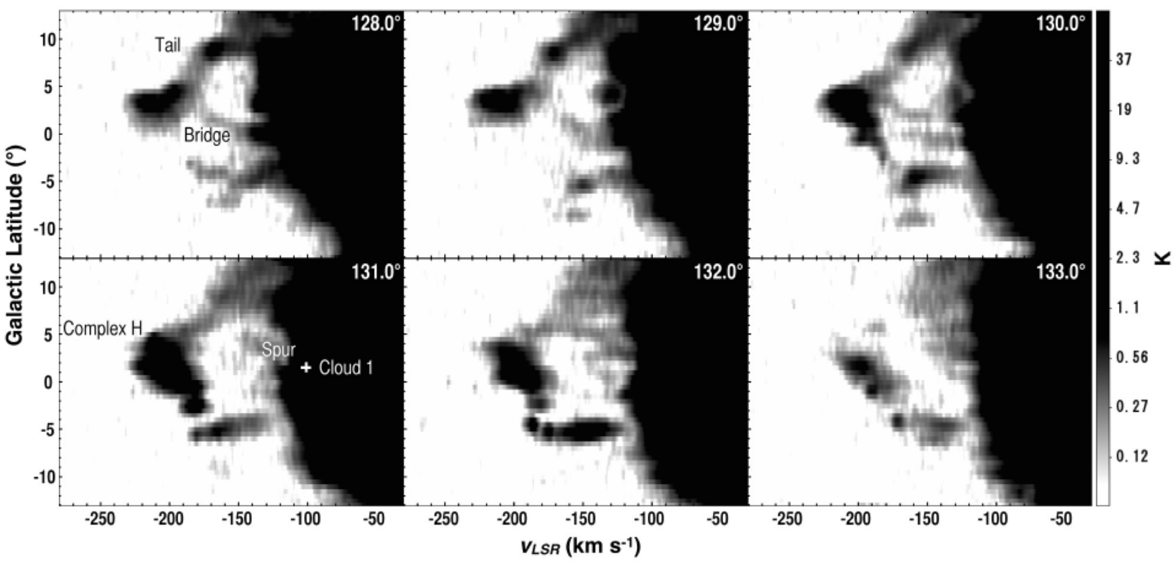

Figure 2.11: HI velocity-latitude cut through Cloud 1 from l = 128°.0 to 133°.0 made from the LAB data. The white cross shows the position of Cloud 1. Besides the probable tidal-interaction "tail" (Lockman, 2003), some other "bridge" or "spur" features are seen in between the Complex H ($v_{LSR} \sim$ –200 km s^{-1}) and the Galactic disk ($v_{LSR} \leq -100$ km s^{-1}).

Chapter 3

A new survey of star-forming regions in the outer Galaxy

In the previous Chapter, I studied the detail of very distant star-forming region in the EOG as an extreme case. To clarify the global nature of star-formation activity in the outer Galaxy, we need a statistical number of sample star-forming regions in the outer Galaxy. However, the outer Galaxy has never been comprehensively surveyed because of lack of infrared (IR) survey data deep enough for large distances. Thus, as a next step of my research, I conducted a survey of star-forming regions at $R_{\rm G} \geq 13.5$ kpc in the 2nd Galactic quadrant with WISE (Wide-field Infrared Survey Explorer), which can effectively pick up star-forming regions by combining with recently available CO survey data in the outer Galaxy.

3.1 Strategy

For statistical study of star formation in the outer Galaxy, it is crucial to establish a path for efficient detection and identification of candidate of star-forming regions in the outer Galaxy. Search for star-forming regions has been traditionally conduced with *Infrared Astronomical Satellite* (*IRAS*; Neugebauer et al., 1984; Beichman et al., 1988) utilizing all sky infrared survey data (e.g. Kerton & Brunt, 2003; Hughes & MacLeod, 1989), but the sensitivity was quite limited. The recent mid-infrared (MIR) all-sky survey explorer "*Wide-field Infrared Survey Explore* (*WISE*; Wright et al., 2010; Jarrett et al., 2011, Figure3.1) " has archived a great increase in sensitivity, about 100 times more sensitive than *IRAS* (Figure 3.2, Fabinsky, 2006; Wright et al., 2010), and therefore, the *WISE* data has a high potential in searching for distant star-forming regions. In past study, *WISE* magnitudes and colors of individual young stellar objects (YSOs) in the solar neighborhood ($D \leq 2$ kpc) have been established (e.g. Koenig et al., 2012; Koenig & Leisawitz, 2014) by comparing with the well-established data from *Spitzer Space Telescope* (Werner et al., 2004). However, *WISE* data have never been applied to distant star-forming regions.

In view of the typical distance between YSOs in young clusters ($2'$ - $3'$ for Taurus star-forming region at $D \sim 150$ pc), we cannot resolve clusters beyond $D \sim 4$ kpc into individual stars with the resolution of $WISE$ (~ 6 - $12''$), which is demonstrated in Figure 3.3. Because we can utilize only integrated MIR magnitudes and colors of star-forming regions, we investigated the $WISE$ colors of known star-forming regions in the outer Galaxy as a sample to construct criteria for identifying distant and unresolved star-forming regions. Furthermore, we chose CO molecular clouds from a number of surveys as the base of our study, because our target, young star-forming regions with embedded clusters (Age < 3 Myr), should accompany their parental molecular clouds (Lada & Lada, 2003). Using the criteria, I perform a new survey of star-forming regions in the outer Galaxy combining with recently available CO survey.

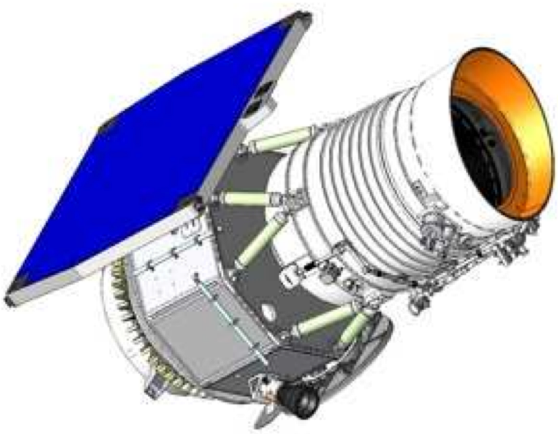

Figure 3.1: Diagram of the $WISE$ satellite in survey mode. This figure is reproduced from Wright et al. (2010).

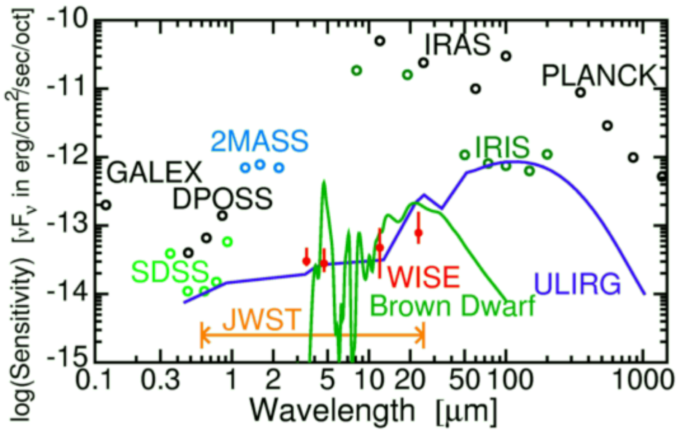

Figure 3.2: *WISE* 5 sigma point source sensitivities versus that of the other surveys. This figure is reproduced from Fabinsky (2006).

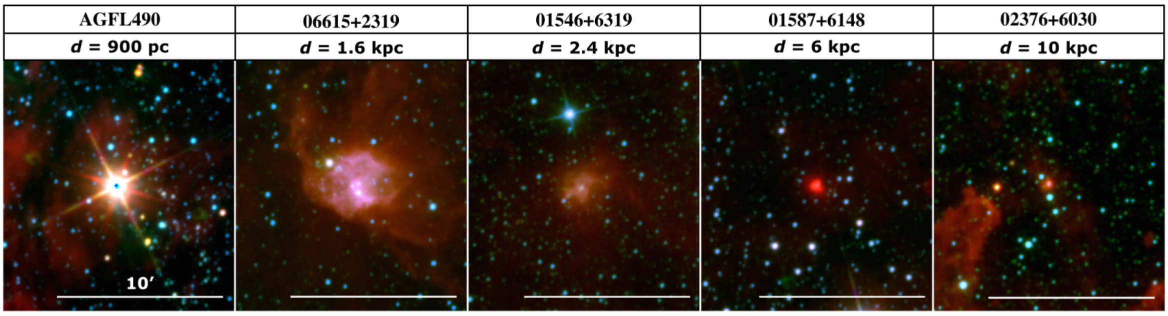

Figure 3.3: *WISE* 3.4, 4.6, 12 μm pseudo-color images of known low-mass clusters ($\sim 10^2\ M_\odot$) in the Galaxy: AGFL490, 06615+2319, and 01546+6219 (Lada & Lada, 2003), 01587+6148 and 02367+6030 (Snell et al., 2002). The white lines indicate 10 arcmin. These clusters look smaller and fainter with increasing distance, and appear to be unresolved beyond d = 4 kpc.

3.2 WISE and AllWISE catalogue

WISE mapped at least eight-times on over 99 % of the sky with four MIR bands centered at 3.4, 4.6, 12, and 22μm in a 6 month survey at 2010 (Figure 3.4). *WISE* has achieved 5σ point-source sensitivities of detecting sources fainter than 16.5, 15.5, 11.2, and 7.9 mag (Vega) at 3.4, 4.6, 12, and 22 μm bands, respectively, in regions observed in eight or more times (Wright et al., 2010). In contrast to the high sensitivity, the angular resolutions are limited to $6''.1$, $6''.4$, $6''.5$, and $12''.0$ at 3.4, 4.6, 12, and 22 μ m bands, respectively (Wright et al., 2010), due to the relatively small telescope aperture (40 cm) destined for space survey telescopes. From model Spectral Energy Distribution (SED) of galaxies (e.g. da Cunha et al., 2008), 3.4 and 4.6 μm show information mainly from stars while 12 and 22 μm

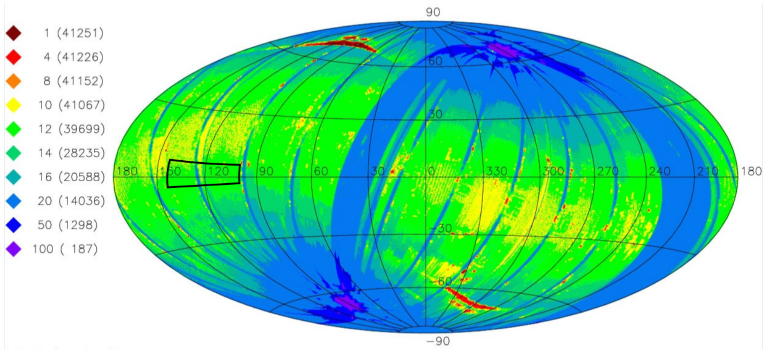

Figure 3.4: Survey map of the WISE All-Sky Release Atlas and Catalog in equatorial Aitoff projection. The color show the average number of individual 7.7 sec (3.4 and 4.6 μm) and 8.8 sec (12 and 22 μm) exposure frames. The region within the black lines shows the our survey region. This figure is reproduced from `http://wise2.ipac.caltech.edu/docs/release/allsky/`

show information mainly from circumstellar dust.

I used AllWISE Source Catalog[1] to investigate the *WISE* magnitudes and colors of the sample star-forming regions. AllWISE Source Catalog contains astrometry and photometry for 747,634,026 objects detected on the deep AllWISE Atlas Intensity Images[2]. In addition to the catalogued position and photometric information, we also used measurement quality and source reliability information, in particular, contamination and confusion flag (*cc_flags*) to reject false sources. The *cc_flags* show that the source may be a spurious of a diffraction spike (D), short-term latent image (P), scattered light halo (H), or optical ghost image (O).

3.3 Sample star-forming regions

For the sample star-forming regions, we selected 13 known distant star-forming molecular clouds in the outer Galaxy at $R_G \geq 13.5$ kpc: three in the EOG ($R_G \geq 18$ kpc) and ten in the FOG ($13.5 \leq R_G < 18$ kpc). They are listed in Table 3.1, and their locations in the Galactic plane are shown in Figure 3.5.

[1] `http://wise2.ipac.caltech.edu/docs/release/allwise/expsup/sec1_3.html#src_cat`

[2] Detailed information is listed in the following site: `http://wise2.ipac.caltech.edu/docs/release/allwise/expsup/`

Table 3.1: Sample star-forming molecular clouds in the outer Galaxy

Region	Star-forming [a] molecular cloud	Galactic coordinate l	b	V_{LSR} [km s^{-1}]	D [kpc]	R_G [kpc]	Age [Myr]	References [b]
EOG	Digel Cloud 1	131°.05	1°.45	-101.8	16	22	< 1	1,2
	Digel Cloud 2	137°.75	-1°.00	-102.4	12	19	0.5 – 1.0	1,3,4
	WB89-789 (IRAS0615+1455)	195°.82	-0°.57	34.01	11.9	20.2	-	5,6
FOG	01537+6154	130°.539	0°.263	-62.0	6.5	13.6	-	7,8
	01587+6148	131°.145	0°.312	-61.0	6.3	13.5	-	7,8
	02071+6235	131°.856	1°.332	-78.3	9.4	16.4	-	7,8
	02376+6030	135°.988	0°.672	-78.1	10.2	17.4	-	7,8
	02383+6241	135°.182	2°.694	-71.8	8.5	15.7	-	7,8
	02395+6244	135°.278	2°.797	-71.6	8.8	16.0	-	7,8
	02407+6029b	136°.347	0°.817	-74.4	9.4	16.8	-	7,8
	02413+6037	136°.357	0°.958	-61.6	6.9	14.3	-	7,8
	02421+6233	135°.627	2°.765	-72.4	8.9	16.1	-	7,8
	02598+6008	138°.618	1°.562	-59.6	7.0	14.5	-	7,8

[a]: Name of star-forming regions in the FOG indicate name of IRAS sources.
[b]: References. (1) Digel et al. (1994); (2) Chapter 2 in this thesis; (3) Kobayashi et al. (2008); (4) Yasui et al. (2008); (5) Brand & Wouterloot (1994); (6) Brand & Wouterloot (2007); (7) Heyer et al. (1998); (8) Snell et al. (2002)

3.3.1 Sample details

In the EOG ($R_G \geq 18$ kpc), only three confirmed star-forming molecular clouds are known: Digel Cloud 1 (See Chapter 2), Cloud 2 (Kobayashi & Tokunaga, 2000; Yasui et al., 2006, 2008; Kobayashi et al., 2008), and WB-89-789 (Brand & Wouterloot, 2007). Among all, star-forming regions in Digel Clouds 1 and 2 were thoroughly studied by a complete set of data, such as high-resolution ^{12}CO maps with Nobeyama 45 m radio telescope, deep NIR images of embedded clusters with MOIRCS on the Subaru 8.2 m telescope (Yasui et al., 2008, Chapter 2), and wide-field NIR images of Cloud 2 with QUIRC on the University of Hawaii 2.2 m telescope (Kobayashi et al., 2008). Both Clouds 1 and 2 have two CO peaks, and embedded clusters were detected in all four CO peaks with Subaru NIR images (Figure 2.2 in Chapter 2.3.1 and Figure 3.6). Cloud 1 is perhaps the most distant star-forming cloud in the outer Galaxy at R_G = 22 kpc (Digel et al., 1994, Chapter 2). Besides the star-forming regions (embedded clusters/stellar aggregates) already listed in our previous papers (e.g. Kobayashi & Tokunaga, 2000; Kobayashi et al., 2008), we identified new 13 stellar aggregates (two in Cloud 1 and eleven in Cloud 2) in and near the CO peaks or ridges as reddened stellar associations in the NIR images (Izumi et al. in prep). Another star-forming region in the EOG, WB89-789 (IRAS 0615+1455), was identified by Brand & Wouterloot (2007) at the probable distance of D = 11.9 kpc

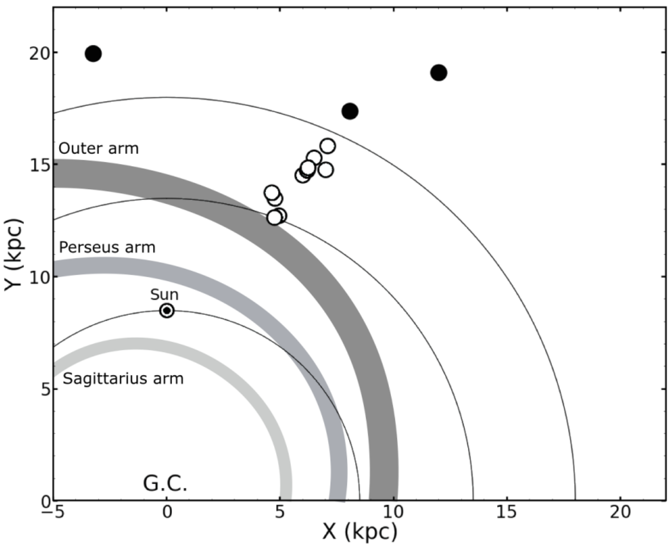

Figure 3.5: Locations of the sample star-forming molecular clouds at $R_G \geq 13.5$ kpc on the Galactic plane. Filled and open circles show clouds in the EOG and FOG, respectively. The three grey curves indicate approximate locations of the three major spiral arms by Reid et al. (2014). The locations of those clouds are also tabulated in Table 3.1

($R_G \sim 20.2$ kpc). They performed a complete set of observations from NIR (J, H, K) to mm-wave molecular-lines, and dust continuum to investigate the star formation activity (Figure 3.7).

In the FOG ($13.5 \leq R_G < 18$ kpc), a number of star-forming clouds have been reported (e.g. Snell et al., 2002; Yun et al., 2015; Brand & Wouterloot, 1994). Among all, we picked up star-forming clouds identified by Snell et al. (2002), because they present relatively large number of samples and performed systematic studies. Among FOG clouds found by FCRAO ^{12}CO survey of the Outer Galaxy (Heyer et al., 1998, 2001), Snell et al. (2002) identified 10 star-forming clouds by associating *IRAS* sources that show the colors of star-forming regions. They performed K'- band imaging of the 10 *IRAS* sources using QUIRC NIR imager on the University of Hawaii 2.2 m telescope to detect 11 embedded clusters, thus confirmed star-forming regions. Among them, three were found to be associated with HII regions (see Table 3.2), which should be produced by OB stars (Rudolph et al., 1996; Snell et al., 2002). NIR images of those sample star-forming regions are shown in Figure 3.8.

3.3.2 WISE images

Figure 3.9 shows the whole view of the sample star-forming clouds in the EOG, Clouds 1 and 2, in ^{12}CO (left) and *WISE* color (3.4, 4.6, and 12 μm bands; right). Figure 3.10 shows the blow-up images of each star-forming regions in the clouds. Almost all the confirmed star-forming regions but one are clearly detected as compact *WISE* sources. Only Cloud 2N cluster is detected as diffuse *WISE* sources. This appears to reflect the low-stellar density of the Cloud 2N cluster (Yasui et al., 2008), which is similar to that for the Taurus star-forming association. Figure 3.11 shows another star-forming region in the EOG, WB89-789 (Brand & Wouterloot, 2007) in C^{18}O (2-1) and K-band (left) and *WISE* color (right). We did not plot CO distribution on *WISE* image of WB89-789, because we do not have CO molecular data.

Figure 3.12 shows *WISE* images of sample star-forming clouds in the FOG (Snell et al., 2002). The star-forming regions (embedded clusters) identified by Snell et al. (2002) with NIR images are also clearly detected as compact or diffuse sources in the *WISE* images.

3.3.3 WISE sources

For all the sample star-forming regions, I searched for corresponding *WISE* sources in AllWISE source catalog with the signal-to-noise (S/N) of more than 5 at all 3.4, 4.6, and 12 μm bands, which are critical for source classification of YSOs in the solar neighborhood (see Figure 10 in Koenig & Leisawitz, 2014). I do not use the 22 μm data because *WISE* has the lowest spatial resolution and sensitivity at this wavelength (Wright et al., 2010). I selected associated sources within a few arcseconds ($< 3''$) from each star-forming region. All the identified *WISE* sources are listed in Table 3.2. I rejected *WISE* sources with cc_flags (see Chapter 3.2). For example, all the sources in and around the star-forming cloud 02395+6244 in the FOG, are rejected, because they have D flags due to a very bright $WISE$ source in the CO peak (see Figure 3.12). For Cloud 2 in the EOG, a significant number of *WISE* sources in the northern half of the cloud, including some obvious star-forming regions, are found to be catalogued with R flags with unknown reason (see Figure 3.13). However, I did not reject all these sources, because we suspect that *WISE* catalog identified the extended photo-dissociation regions in the northern cloud (Kobayashi et al., 2008) as a latent feature. In the next step, we may need source-by-source checking of the flagged sources to increase the accuracy of the identification.

Koenig & Leisawitz (2014) reported the existence of *WISE* sources with fake photometry in nearby star-forming regions by comparing with *Spitzer* data. They showed that many sources with low S/N and high reduced chi-square (χ^2) of profile-fit photometry, which means extended, are fake (e.g. Figure 1 in Koenig & Leisawitz, 2014). However, we cannot reject the sources with high χ^2, because virtually all of the distant star-forming regions are identified as extended sources (high χ^2) in the *WISE* images.

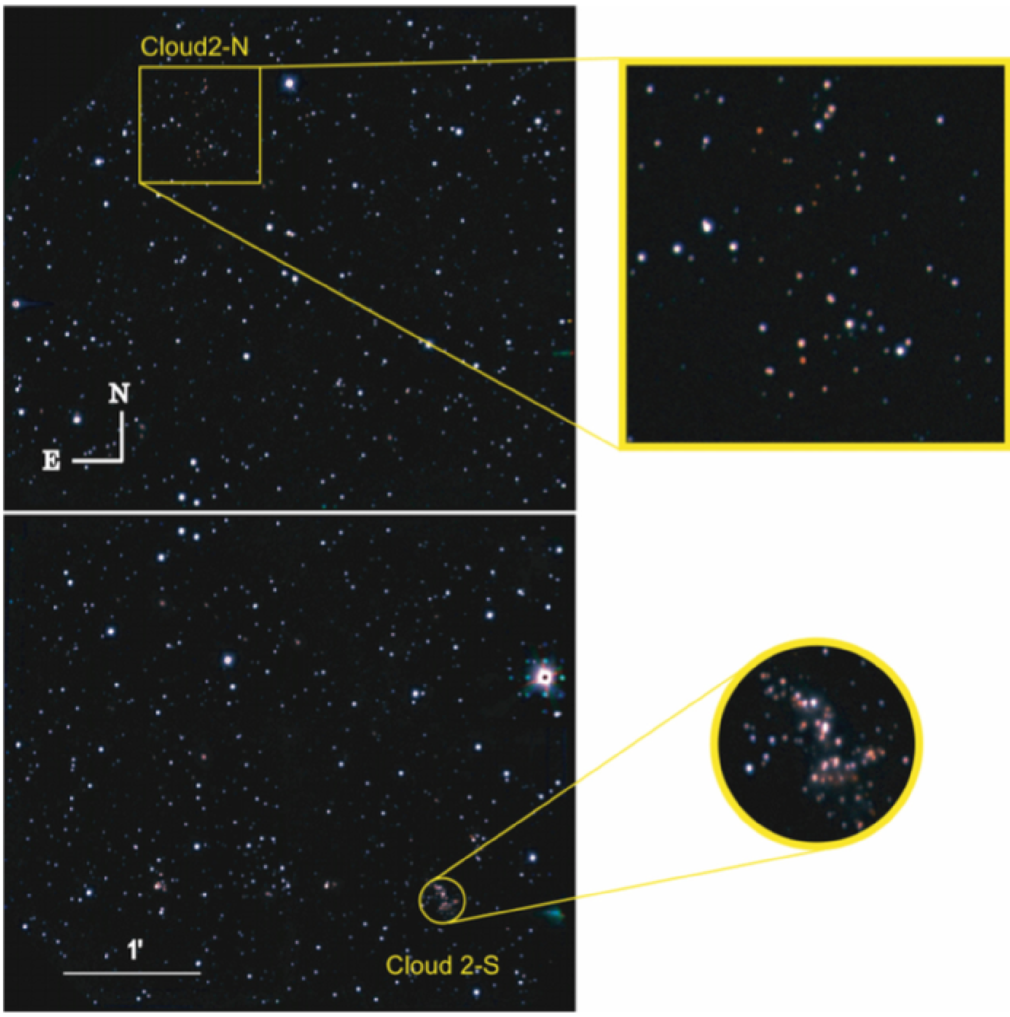

Figure 3.6: NIR pseudo-color images (J = blue, H = green, K_S = red) of the Cloud 2 clusters obtained with Subaru MOIRCS (Top: Cloud 2-N, bottom: Cloud 2-S). The field of view of both images is $\sim 3.'5 \times 4'$. The yellow box and the circle mark the locations of the clusters, with close-ups shown on the right. This figure is reproduced from Yasui et al. (2009).

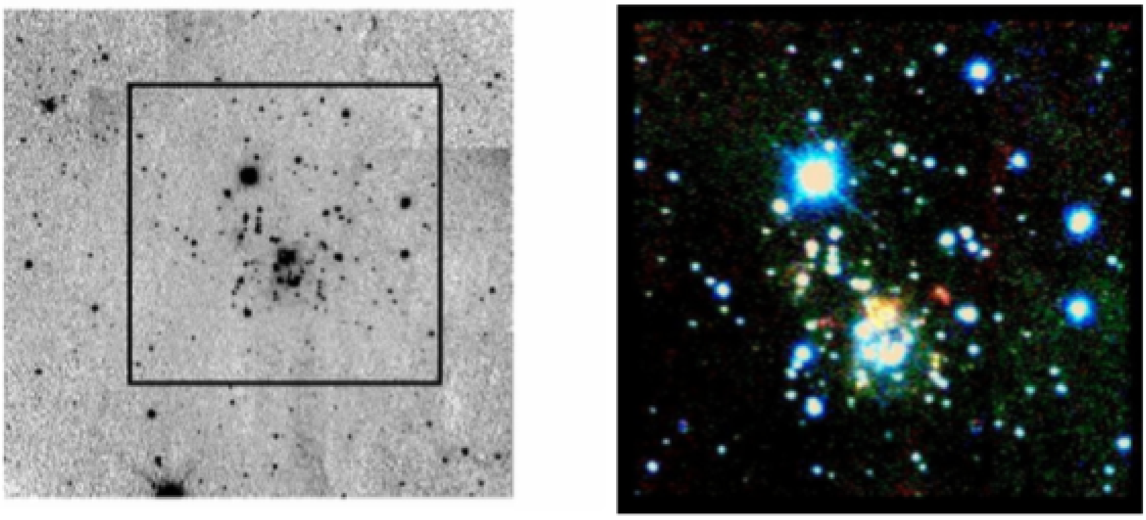

Figure 3.7: *Left*: *K*- band image of the region around WB89-789 (IRAS 06145+1455). The area of sky visible here is $\sim$3 $\times$ 3 arcmin^2. The region outlined by the black box has a size of $\sim$ 1.7 $\times$ 1.7 arcmin^2, and is shown on the right. North is up, East is left. *Right*: NIR pseudo-color image (J = blue, H = green, K = red) of a $\sim$ 1.7 $\times$ 1.7 arcmin^2 region around WB89-789. This figure is reproduced from Brand & Wouterloot (2007).

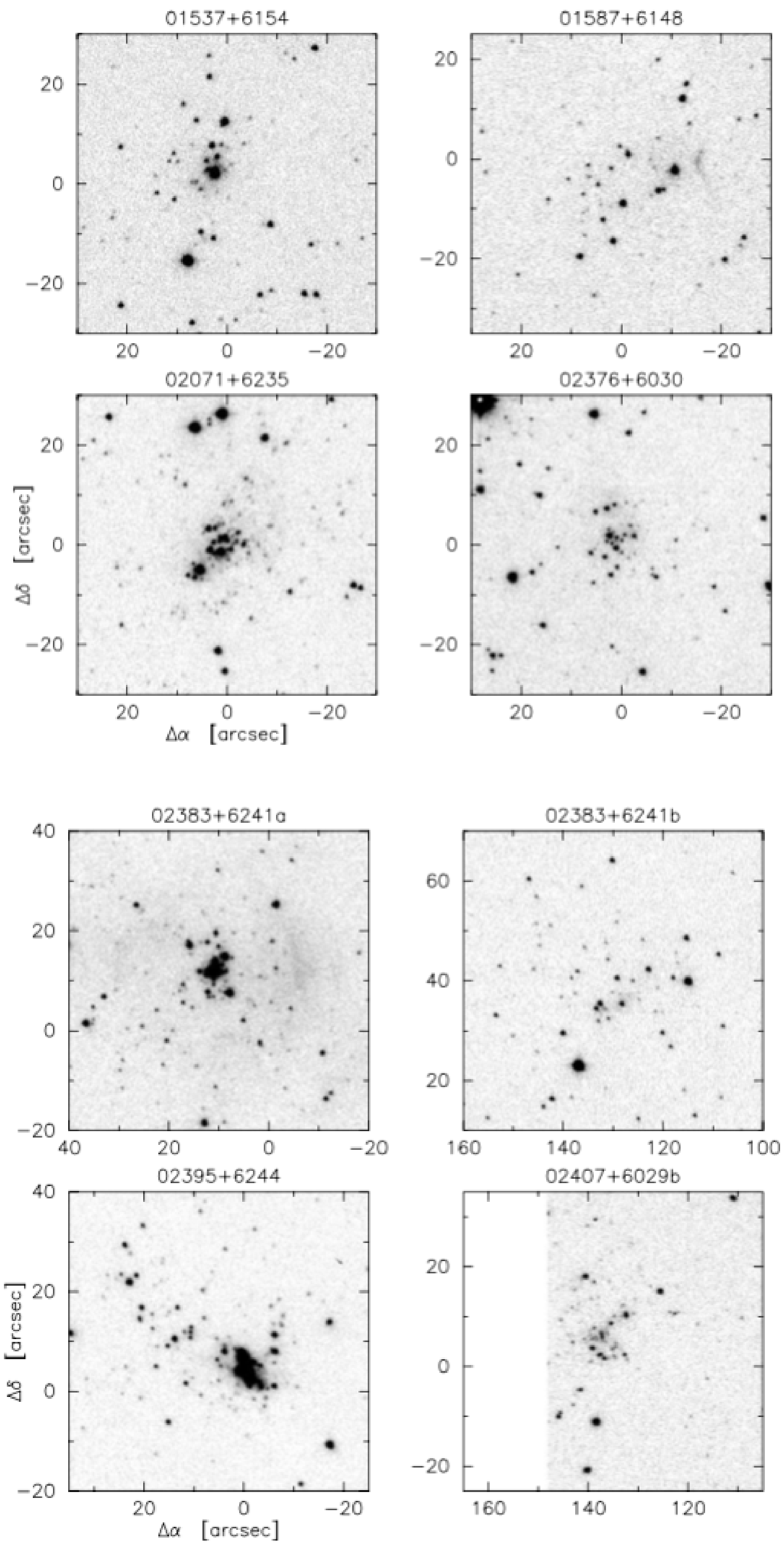

Figure 3.8: K'- band image of 11 stellar clusters detected by QUIRC NIR imager on the University of Hawaii 2.2 m telescope. This figure is reproduced from Snell et al. (2002).

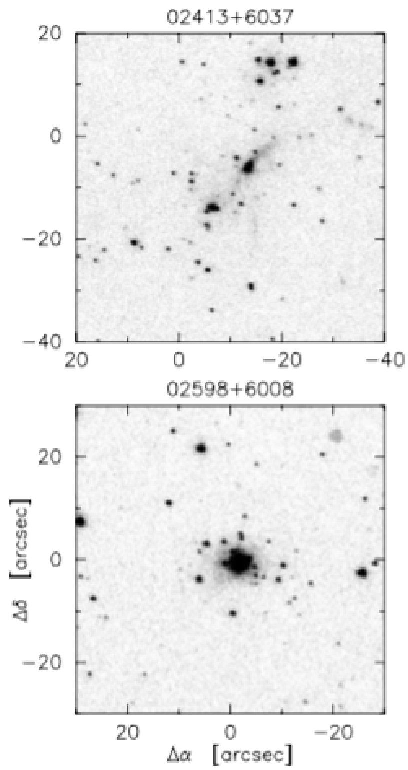

Figure 3.8 *Continued*

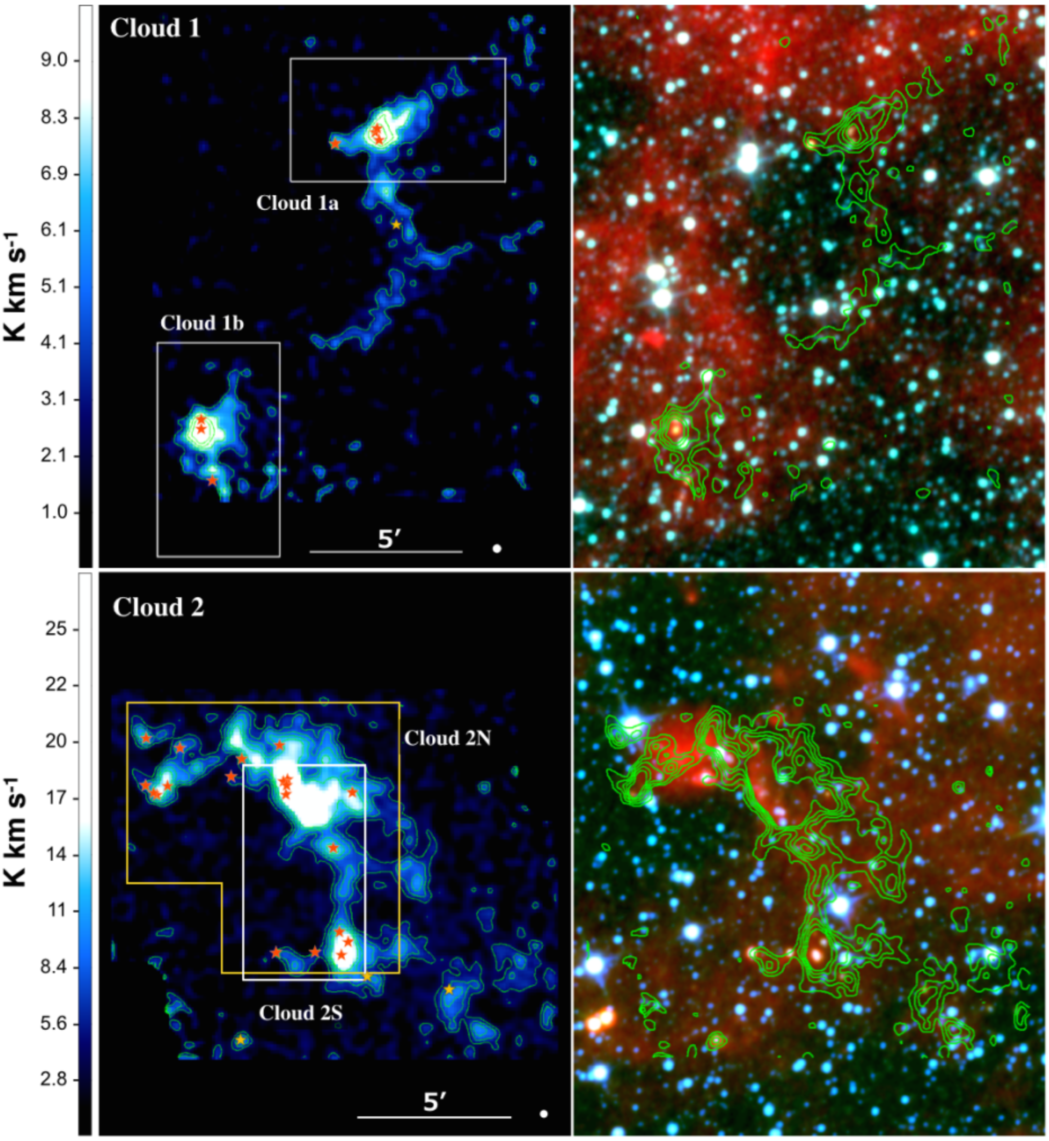

Figure 3.9: *Left*: ^{12}CO(1-0) distribution of the four CO peaks in the EOG star-forming clouds (from our NRO 45 m telescope data, Cloud 1: $v_{\rm LSR}$ = -105.4 $\sim$ -98.9 km s^{-1}, Cloud 2 : $v_{\rm LSR}$ = -106.1 $\sim$ -99.1 km s^{-1}). The green contours show the ^{12}CO (1-0) distribution with contour levels of 3σ, 5σ, 7σ, 9σ, 11σ (Cloud 1: 1σ = 0.85 K km s^{-1}, Cloud 2: 1σ = 1.2 K km s^{-1}). White filled circles show the beam size of the NRO 45 m telescope ($\sim$ 15″). The red star marks show the location of star-forming regions (embedded clusters/stellar aggregates) identified with our deep NIR images (Kobayashi et al., 2008; Yasui et al., 2008, Chapter 2, Izumi et al, imprep). The yellow star marks show the location of candidates of star-forming region newly identified with *WISE* data. The white boxes and yellow lines show the field of view of the Subaru MOIRCS (4′ × 7′) and UH QUIRC (3.2′ × 3.2′), respectively. *Right*: *WISE* 3.4 μm (blue), 4.6 μm (green), and 12 μm (red) band pseudo-color images of the same area. The green contours show the same as the ^{12}CO map as in the left panel.

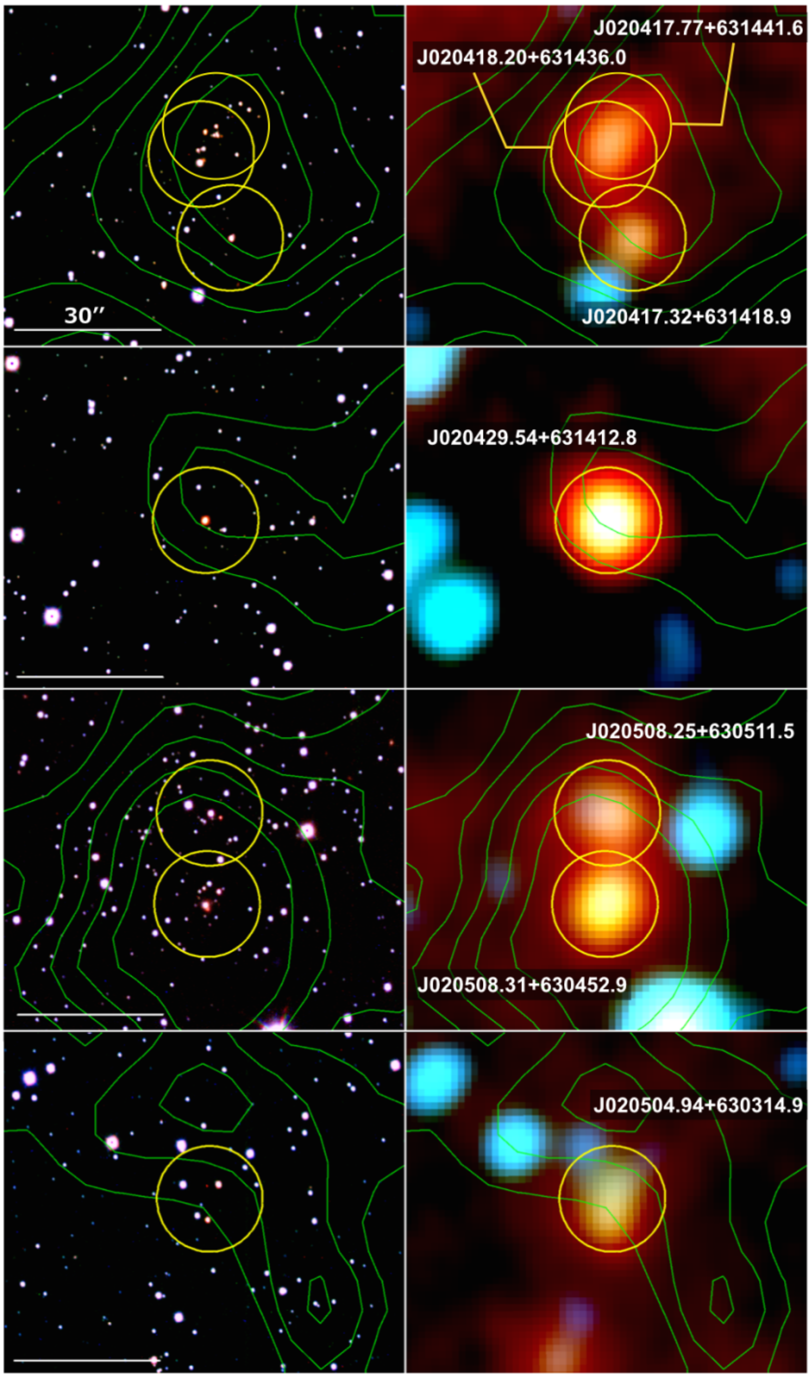

Figure 3.10: Subaru and QUIRC JHK_S (Left) and *WISE* 3.4, 4.6, 12 μm (Right) pseudo-color image of known star-forming regions in the EOG. The green contours show the ^{12}CO (1-0) distribution from the NRO 45 m telescope with contour levels of 3σ, 5σ, 7σ, 9σ, 11σ. The yellow circles show the location of star-forming regions.

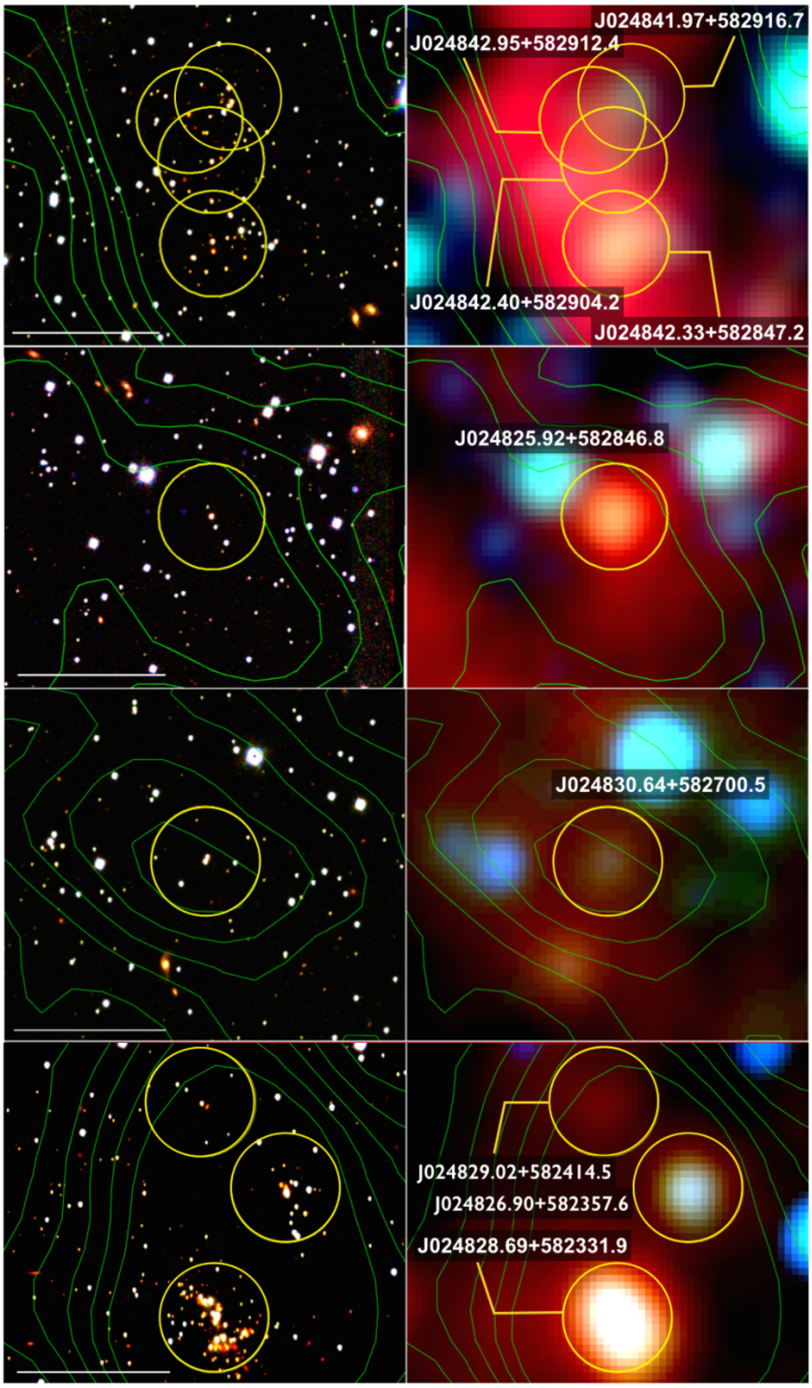

Figure 3.10 *Continued*

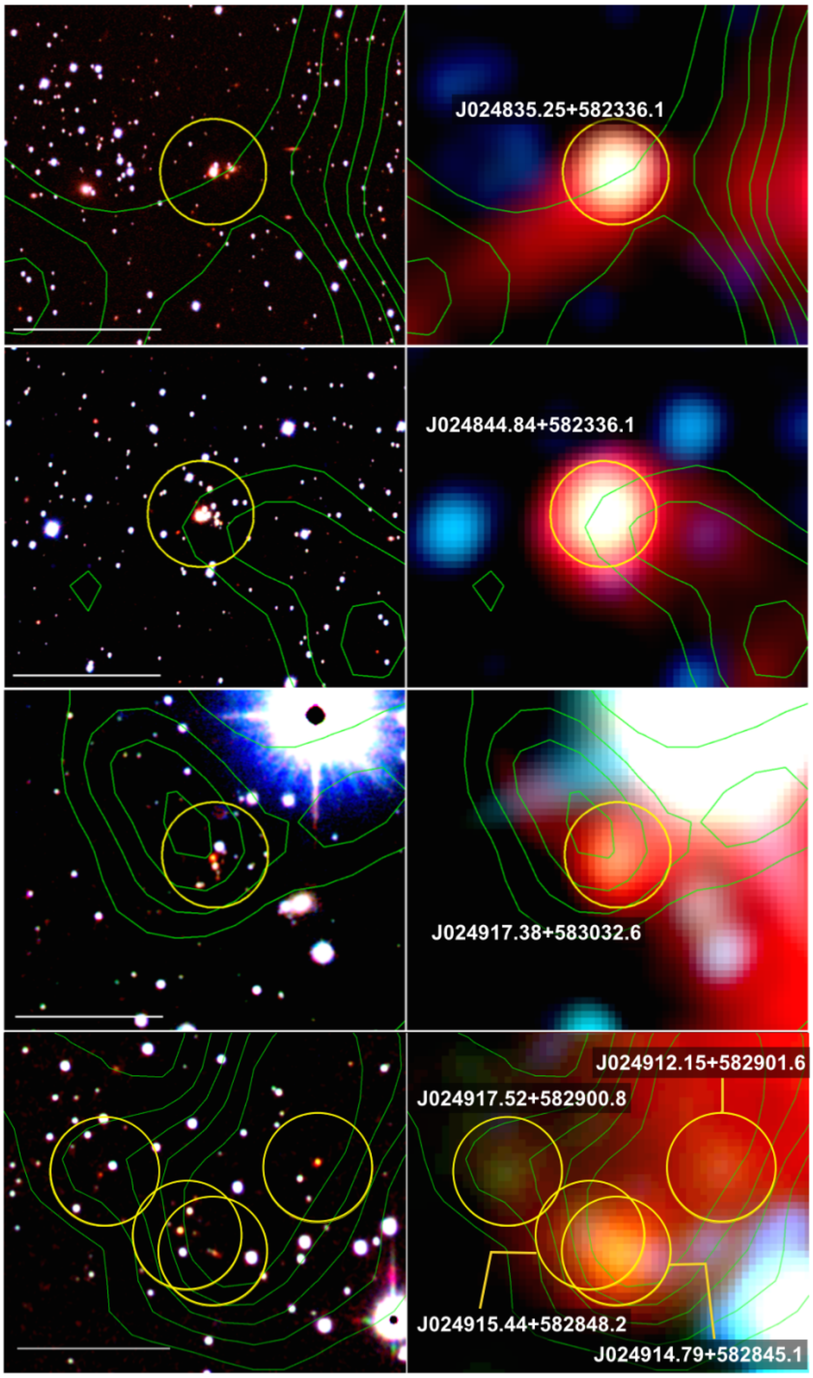

Figure 3.10 *Continued*

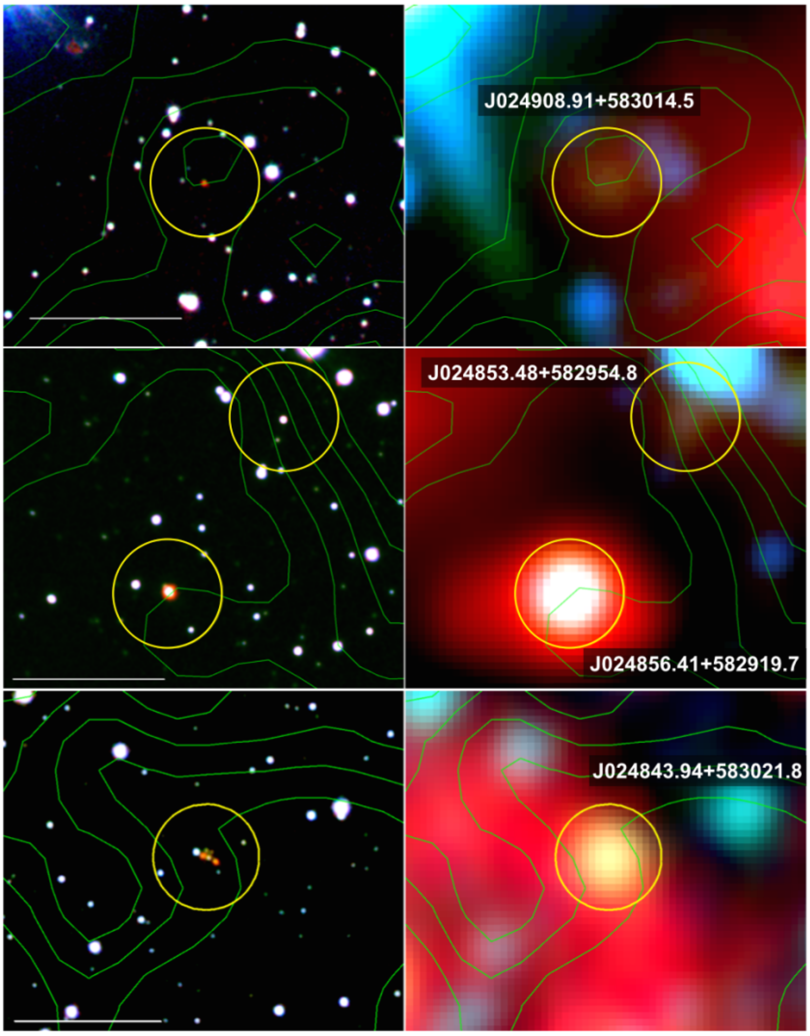

Figure 3.10 *Continued*

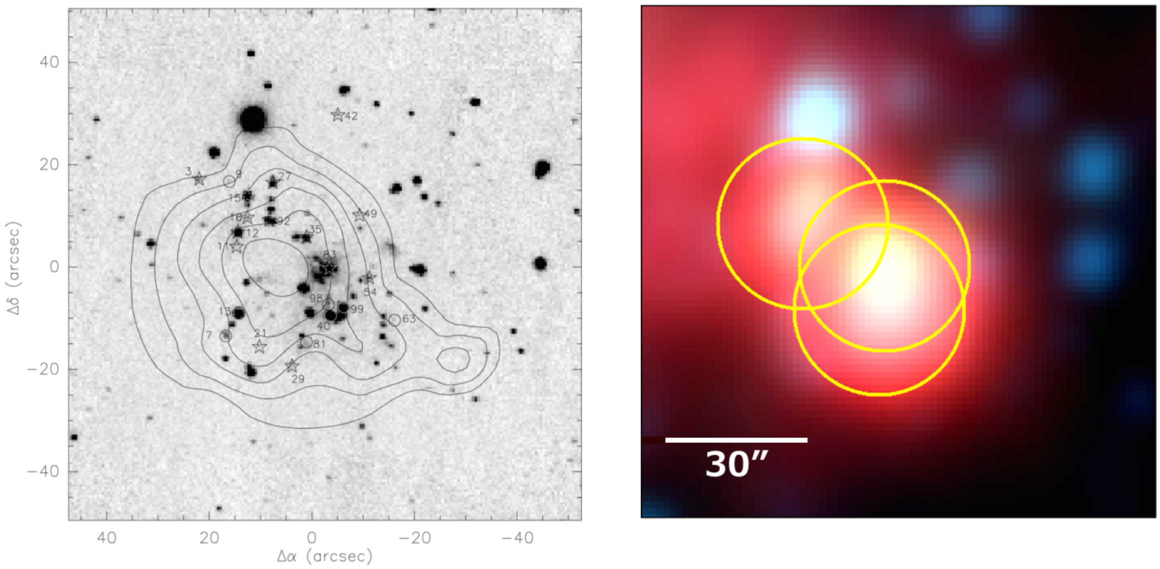

Figure 3.11: *Left*: *K*- band image of the WB89-789 region, with contours of the integrated $C^{18}O$(2-1) emission superimposed. The IRAS source (0615+1455) is positioned at (0,0). The asterisks indicate the star with NIR-excess, and circles indicate star with anomalous colors (Figure 6 in Brand & Wouterloot, 2007). *Right*: *WISE* 3.4, 4.6, and 12 μm pseudo color images of WB89-789. The yellow circles show the locations of the *WISE* sources for embedded clusters identified by Brand & Wouterloot (2007).

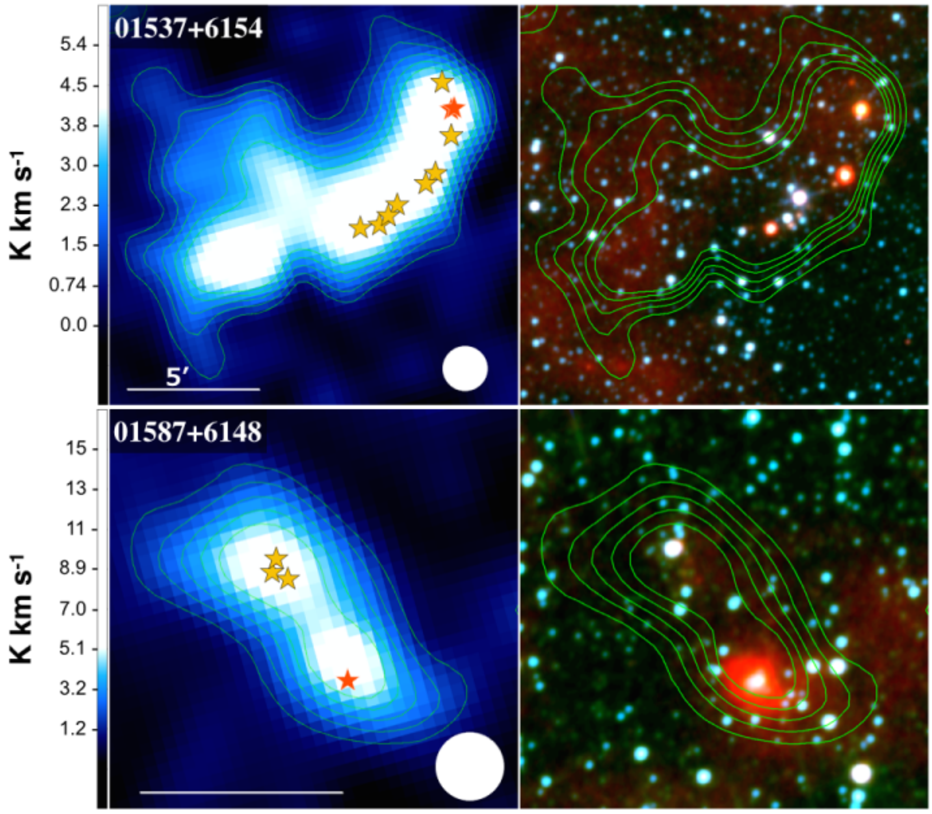

Figure 3.12: *Left*: ^{12}CO(1-0) distribution of the four CO peaks in the FCRAO star-forming clouds in the FOG (from FCRAO 14 m telescope ^{12}CO outer Galaxy survey data reprocessed by Brunt et al. (2003), 01537+6154 : $v_{\rm LSR}$ = -59.2 $\sim$ -63.3 km s^{-1}, 01587+6148 : $v_{\rm LSR}$ = -57.5 $\sim$ -64.9 km s^{-1}, 02071+6235 : $v_{\rm LSR}$ = -76.5 $\sim$ -80.6 km s^{-1}, 02376+6030 : $v_{\rm LSR}$ = -74.0 $\sim$ -79.8 km s^{-1}, 02383+6241 : $v_{\rm LSR}$ = -69.9 $\sim$ -74.0 km s^{-1}, 02393+6244 : $v_{\rm LSR}$ = -69.1 $\sim$ -75.7 km s^{-1}, 02407+6029 : $v_{\rm LSR}$ = -72.4 $\sim$ -78.1 km s^{-1}, 02413+6037 : $v_{\rm LSR}$ = -59.2 $\sim$ -64.1 km s^{-1}, 02421+6233 : $v_{\rm LSR}$ = -69.9 $\sim$ -74.8 km s^{-1}, 02593+6008 : $v_{\rm LSR}$ = -57.5 $\sim$ -61.6 km s^{-1}). The green contours show the ^{12}CO (1-0) distribution with contour levels of 3σ, 5σ, 7σ, 9σ, 11σ (01537+6154 : 1 σ = 0.29 K km s^{-1}, 01587+6148 : 1 σ = 0.40 K km s^{-1}, 02071+6235 : 1 σ = 0.29 K km s^{-1}, 02376+6030 : 1 σ = 0.35 K km s^{-1}, 02383+6241 : 1 σ = 0.29 K km s^{-1}, 02393+6244 : 1 σ = 0.37 K km s^{-1}, 02407+6029 : 1 σ = 0.35 K km s^{-1}, 02413+6037 : 1 σ = 0.32 K km s^{-1}, 02421+6233 : 1 σ = 0.32 K km s^{-1}, 02593+6008 : 1 σ = 0.29 K km s^{-1}). White filled circles show the spatial resolution of the FCRAO data (100.″88) reprocessed by Brunt et al. (2003). The red star marks show the location of star-forming regions (embedded clusters) identified by Snell et al. (2002). The yellow star marks show the location of candidates of star-forming region newly identified with *WISE* data. The blue star mark shows the location of the known embedded cluster in 02395+6244, but could not be used in this study because of false flags (see Chapter 3.3.3). *Right*: *WISE* 3.4, 4.6, and 12 μm pseudo-color images of FCRAO star-forming regions in the FOG. The green contours show the same ^{12}CO map as in the left panel.

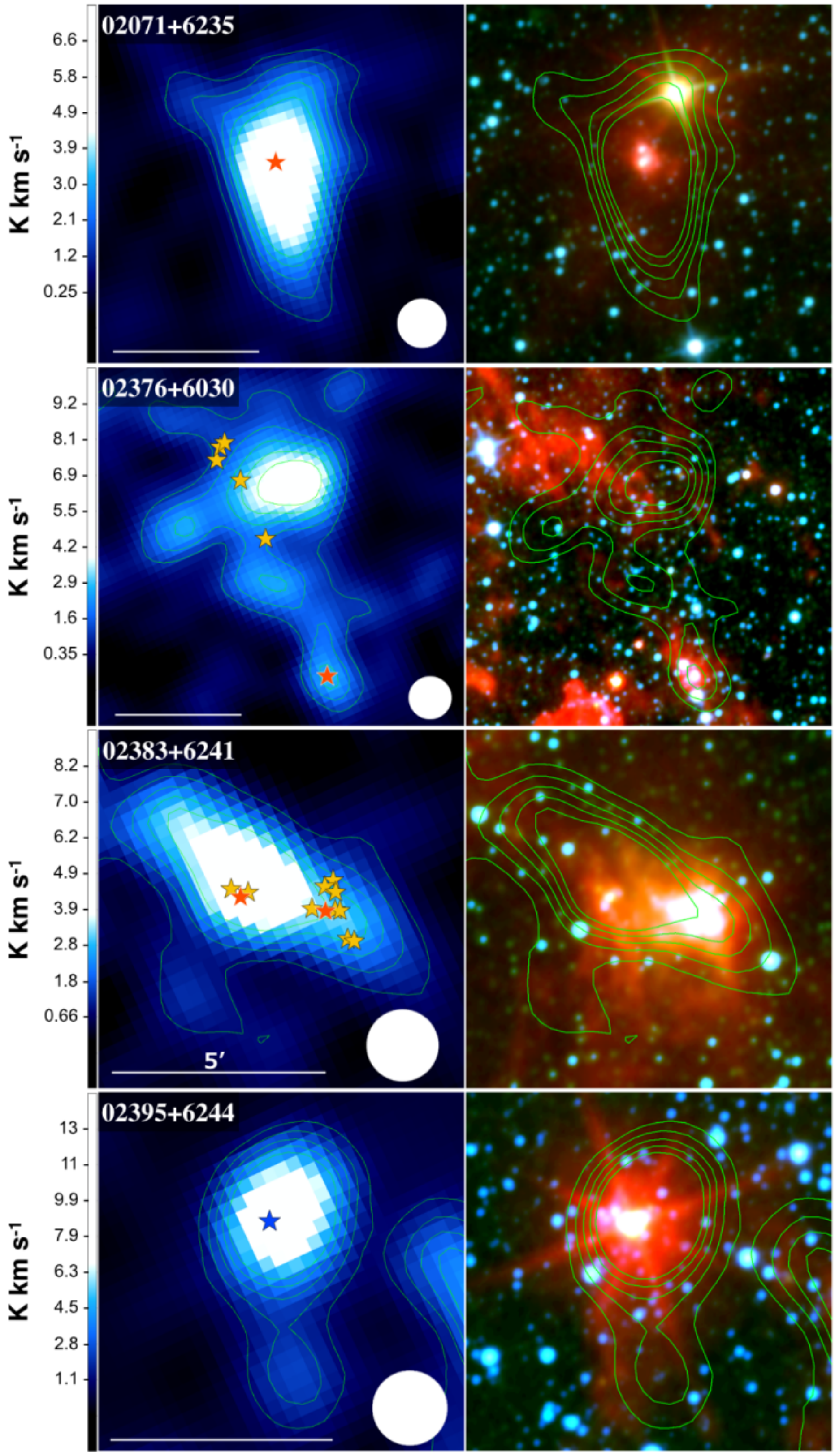

Figure 3.12 *Continued*

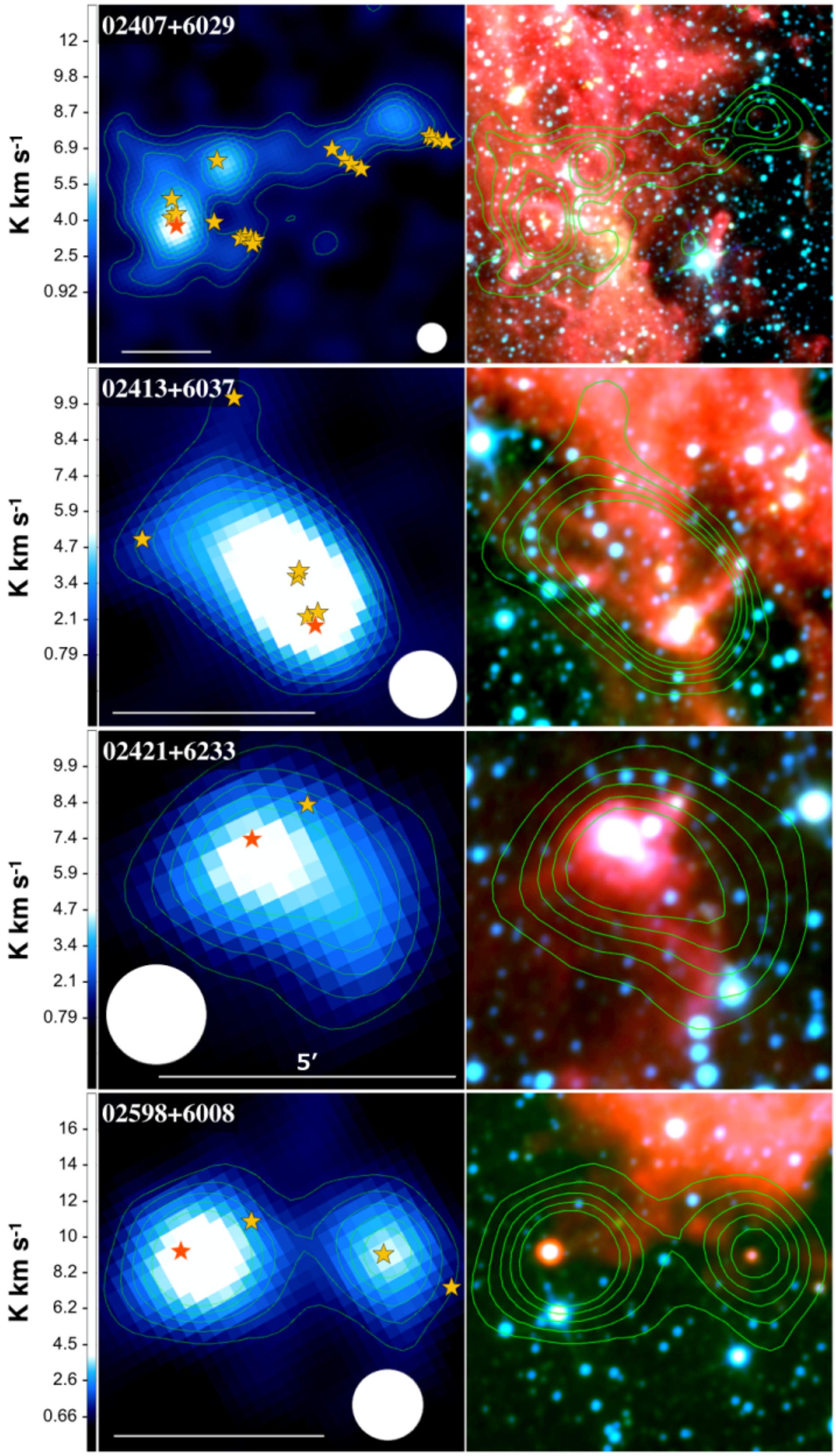

Figure 3.12 *Continued*

Table 3.2: Samples and candidate of star-forming regions and *WISE* sources in the outer Galaxy

Region	Star-forming molecular cloud	Star-forming [a] region	Type [b]	AllWISE source	Coordinate l	b	3.4 μm [mag]	$\sigma_{3.4}$ [mag]	4.6 μm [mag]	$\sigma_{4.6}$ [mag]	12 μm [mag]	σ_{12} [mag]	22 μm [mag]	σ_{22} [mag]
EOG	Digel Cloud 1	CAN	-	J020411.94+631135.7	131.028	1.471	15.328	0.044	13.679	0.035	10.939	0.103	8.476	0.354
		Q	A	J020429.54+631412.8	131.047	1.522	13.059	0.025	11.901	0.022	9.156	0.035	6.704	0.074
		Cloud 1a	EC	J020417.32+631418.9	131.025	1.517	14.053	0.027	13.195	0.029	10.718	0.096	7.885	0.223
		Cloud 1a	EC	J020418.20+631436.0	131.025	1.522	14.310	0.037	13.559	0.044	10.948	0.142	7.711	0.270
		Cloud 1a	EC	J020417.77+631441.6	131.024	1.524	14.444	0.040	13.592	0.046	11.160	0.174	8.082	null
		Cloud 1b	EC	J020508.31+630452.9	131.161	1.393	13.781	0.030	12.462	0.027	9.475	0.044	6.297	0.065
		Cloud 1b	EC	J020508.25+630511.5	131.160	1.398	13.692	0.026	12.997	0.029	9.904	0.050	7.505	0.139
		Q	A	J020504.94+630314.9	131.163	1.365	13.830	0.030	12.895	0.028	10.340	0.069	7.650	0.168
	Digel Cloud 2	Cloud 2-N	EC	J024842.33+582847.2	137.766	-0.973	13.997	0.030	13.118	0.029	9.601	0.048	6.757	0.078
		Q	A	J024912.15+582901.6	137.823	-0.941	15.288	0.049	14.764	0.073	10.592	0.119	8.000	0.225
		Q	A	J024915.44+582848.2	137.831	-0.942	15.004	0.051	14.147	0.046	10.285	0.082	7.091	0.113
		Q	A	J024917.52+582900.8	137.833	-0.936	15.535	0.042	14.788	0.058	11.284	0.172	8.280	null
		Q	A	J024914.79+582845.1	137.830	-0.943	15.225	0.050	13.561	0.035	9.540	0.061	6.719	0.094
		Q	A	J024853.48+582954.8	137.780	-0.946	13.860	0.034	13.233	0.030	9.869	0.065	7.285	0.125
		Q	A	J024908.91+583014.5	137.807	-0.926	15.431	0.047	14.462	0.050	10.243	0.103	7.646	0.230
		IRS 1	A	J024856.41+582919.7	137.790	-0.952	11.713	0.023	11.001	0.020	7.374	0.018	5.365	0.050
		Q	A	J024917.38+583032.6	137.822	-0.914	13.729	0.028	13.126	0.030	10.539	0.130	8.390	0.328
		Cloud 2-N	EC	J024842.95+582912.4	137.764	-0.966	15.546	0.055	14.646	0.063	10.554	0.127	7.539	0.146
		Cloud 2-N	EC	J024841.97+582916.7	137.762	-0.966	14.707	0.037	14.090	0.045	11.071	0.194	8.718	0.423
		Cloud 2-N	EC	J024842.40+582904.2	137.764	-0.969	15.278	0.049	14.404	0.053	10.539	0.120	7.537	0.158
		Q	A	J024825.92+582846.8	137.734	-0.989	14.539	0.033	13.228	0.030	9.903	0.056	7.629	0.139
		Q	A	J024843.94+583021.8	137.758	-0.948	14.190	0.030	12.980	0.028	10.328	0.087	7.501	0.128
		CAN	-	J024801.66+582222.8	137.732	-1.108	14.423	0.030	13.028	0.028	9.707	0.042	7.472	0.129
		CAN	-	J024853.76+582046.1	137.847	-1.083	13.742	0.042	12.739	0.036	9.156	0.068	6.975	0.152
		Q	A	J024830.64+582700.5	137.756	-1.011	14.859	0.040	14.356	0.050	10.871	0.110	8.271	0.222
		IRS 3	A	J024826.90+582357.6	137.771	-1.060	13.571	0.033	12.424	0.028	9.812	0.061	7.182	0.155
		Cloud 2-S	EC	J024828.69+582331.9	137.777	-1.065	12.686	0.023	11.495	0.021	8.358	0.026	5.042	0.034
		IRS 5	A	J024844.84+582336.1	137.809	-1.049	12.076	0.023	11.062	0.020	8.240	0.022	5.856	0.046
		IRS 4	A	J024835.25+582336.1	137.790	-1.058	12.626	0.025	11.611	0.022	9.124	0.038	6.767	0.085
		Q	A	J024829.02+582414.5	137.773	-1.054	15.489	0.068	14.590	0.052	10.719	0.110	7.624	0.133
		CAN	-	J024822.19+582249.7	137.770	-1.082	14.037	0.028	12.966	0.027	10.166	0.063	7.960	0.214
	WB89-789	-	EC	J061724.10+145431.6	195.823	-0.569	10.588	0.020	9.948	0.020	4.746	0.011	1.834	0.031
		-	EC	J061724.02+145440.7	195.821	-0.568	10.313	0.026	8.804	0.020	4.944	0.020	1.706	0.027
		-	EC	J061725.21+145449.6	195.821	-0.563	11.268	0.058	10.231	0.028	5.045	0.015	1.924	0.020
FOG	01537+6154	CAN	-	J015724.02+620703.1	130.560	0.227	9.537	0.023	8.333	0.021	5.166	0.016	2.981	0.023
		01537+6154	EC	J015719.28+620914.7	130.542	0.260	11.764	0.023	11.203	0.022	9.205	0.037	4.560	0.034
		CAN	-	J015718.83+620832.0	130.544	0.248	14.399	0.029	13.758	0.032	11.294	0.185	8.089	0.249

Table 3.2 (Continued.)

Region	Star-forming molecular cloud	Star-forming region [a]	Type [b]	AllWISE source	Coordinate l	Coordinate b	3.4 μm [mag]	$\sigma_{3.4}$ [mag]	4.6 μm [mag]	$\sigma_{4.6}$ [mag]	12 μm [mag]	σ_{12} [mag]	22 μm [mag]	σ_{22} [mag]
		01537+6154	EC	J015718.61+620931.3	130.540	0.264	9.801	0.023	7.651	0.020	5.538	0.013	2.729	0.016
		CAN	-	J015721.61+621033.4	130.541	0.282	15.445	0.041	13.453	0.029	9.897	0.046	6.550	0.063
		CAN	-	J015736.47+620554.3	130.589	0.214	13.845	0.028	13.288	0.029	10.966	0.142	8.062	0.221
		CAN	-	J015727.30+620644.2	130.568	0.223	13.537	0.028	12.468	0.028	9.598	0.049	6.504	0.076
		CAN	-	J015741.70+620511.2	130.602	0.205	12.432	0.024	11.651	0.022	9.357	0.037	7.128	0.099
		CAN	-	J015738.91+620533.1	130.595	0.210	12.321	0.048	11.720	0.022	9.619	0.047	7.318	0.126
		CAN	-	J015748.03+620503.9	130.614	0.207	9.818	0.022	9.072	0.021	6.861	0.017	5.003	0.033
	01587+6148	CAN	-	J020239.51+620525.3	131.161	0.362	14.789	0.033	13.923	0.038	11.324	0.173	8.290	0.282
		CAN	-	J020238.68+620543.8	131.158	0.367	15.452	0.070	14.775	0.071	11.362	0.184	8.130	0.233
		CAN	-	J020236.09+620513.8	131.156	0.357	17.110	0.118	15.782	0.115	11.072	0.142	7.114	0.103
		01587+6148	EC	J020223.40+620245.3	131.143	0.311	11.472	0.023	10.891	0.021	5.935	0.014	3.726	0.020
	02071+6235	02071+6235	EC w/ HII	J021049.90+624910.4	131.857	1.333	9.774	0.020	8.923	0.015	4.537	0.014	1.098	0.013
	02376+6030	02376+6030	EC	J024129.21+604327.8	135.988	0.673	10.677	0.022	10.159	0.020	5.148	0.015	2.779	0.018
		CAN	-	J024156.78+605113.4	135.986	0.814	15.289	0.051	14.023	0.044	10.714	0.134	8.412	0.336
		CAN	-	J024202.34+605240.4	135.986	0.841	15.990	0.094	15.428	0.107	10.233	0.116	8.264	0.279
		CAN	-	J024202.89+605232.2	135.988	0.839	16.101	0.105	15.390	0.110	10.490	0.143	8.193	0.263
		CAN	-	J024204.42+605202.2	135.995	0.833	16.339	0.191	15.470	0.115	9.944	0.117	8.167	0.250
		CAN	-	J024148.47+604853.0	135.987	0.772	15.820	0.052	14.573	0.054	11.229	0.162	8.374	null
	02383+6241	CAN	-	J024241.28+625436.3	135.213	2.722	13.539	0.027	12.843	0.030	8.172	0.040	5.197	0.042
		CAN	-	J024218.97+625405.0	135.178	2.697	10.779	0.027	10.148	0.024	4.700	0.015	1.179	0.034
		CAN	-	J024224.73+625407.2	135.188	2.702	11.196	0.021	10.637	0.021	5.297	0.012	1.596	0.020
		CAN	-	J024220.30+625447.2	135.176	2.708	13.346	0.026	12.741	0.025	7.580	0.018	3.090	0.008
		CAN	-	J024219.76+625430.3	135.177	2.704	11.636	0.016	11.042	0.014	5.957	0.006	1.138	0.004
		CAN	-	J024222.00+625438.4	135.180	2.707	13.455	0.019	12.914	0.026	7.249	0.015	1.960	0.006
		02383+6241a	EC w/ HII	J024221.73+625403.6	135.183	2.698	9.942	0.025	9.344	0.021	4.601	0.016	0.384	0.018
		CAN	-	J024219.87+625404.0	135.180	2.697	10.650	0.029	9.917	0.027	4.705	0.019	0.871	0.029
		CAN	-	J024238.04+625430.8	135.208	2.718	12.918	0.034	12.414	0.037	7.502	0.026	4.628	0.032
		02383+6241b	EC	J024239.14+625425.3	135.211	2.718	12.029	0.028	10.790	0.022	7.045	0.022	4.247	0.037
		CAN	-	J024216.31+625322.9	135.179	2.684	13.519	0.016	12.852	0.014	7.245	0.005	4.223	0.018
		CAN	-	J024217.33+625324.8	135.180	2.685	13.283	0.026	12.582	0.025	6.782	0.014	3.904	0.021
	02407+6029b	CAN	-	J024459.59+604345.7	136.376	0.857	13.900	0.035	12.879	0.032	9.912	0.083	6.904	0.090
		CAN	-	J024422.18+604114.4	136.324	0.786	14.434	0.089	13.479	0.139	8.852	0.093	4.591	0.036
		CAN	-	J024422.36+604133.8	136.322	0.791	14.265	0.033	13.072	0.035	8.978	0.078	5.286	0.032
		CAN	-	J024421.32+604127.5	136.321	0.789	14.220	0.047	13.569	0.048	8.659	0.077	5.123	0.045
		CAN	-	J024425.77+604143.5	136.328	0.797	14.457	0.160	13.205	0.139	9.536	0.202	6.264	0.155
		CAN	-	J024427.51+604136.2	136.332	0.796	14.218	0.088	12.995	0.070	8.704	0.060	5.711	0.099
		CAN	-	J024458.97+604250.7	136.381	0.842	12.726	0.026	11.505	0.026	8.368	0.029	5.431	0.049
		CAN	-	J024458.20+604259.7	136.379	0.844	13.688	0.037	12.936	0.049	8.816	0.033	5.776	0.052

Table 3.2 (Continued.)

Region	Star-forming molecular cloud	Star-forming region [a]	Type [b]	AllWISE source	Coordinate l	Coordinate b	3.4 μm [mag]	$\sigma_{3.4}$ [mag]	4.6 μm [mag]	$\sigma_{4.6}$ [mag]	12 μm [mag]	σ_{12} [mag]	22 μm [mag]	σ_{22} [mag]
		02407+6029b	EC	J024457.48+604225.6	136.381	0.835	12.032	0.025	10.310	0.022	7.717	0.026	4.069	0.031
		CAN	-	J024440.19+604230.6	136.349	0.821	10.755	0.025	10.139	0.021	4.591	0.016	1.142	0.017
		CAN	-	J024332.92+604537.3	136.203	0.810	16.483	0.162	15.535	0.130	9.988	0.103	8.747	0.372
		CAN	-	J024259.82+604713.3	136.130	0.807	15.010	0.038	14.414	0.051	9.834	0.061	6.244	0.065
		CAN	-	J024300.53+604720.4	136.131	0.809	15.095	0.063	14.530	0.055	9.977	0.063	6.843	0.082
		CAN	-	J024253.79+604703.0	136.120	0.799	15.143	0.058	14.534	0.061	9.316	0.047	5.646	0.044
		CAN	-	J024256.29+604704.5	136.125	0.801	14.615	0.038	13.912	0.040	8.934	0.038	5.817	0.064
		CAN	-	J024438.68+604603.1	136.321	0.873	12.806	0.034	11.636	0.026	9.280	0.068	6.596	0.100
		CAN	-	J024336.65+604551.4	136.208	0.817	16.550	0.172	15.844	0.153	10.065	0.149	8.579	null
		CAN	-	J024339.81+604601.4	136.213	0.822	16.615	0.168	15.492	0.123	10.071	0.113	8.329	null
		CAN	-	J024346.10+604637.8	136.220	0.837	15.895	0.067	15.227	0.091	10.130	0.188	8.802	0.526
	02413+6037	CAN	-	J024512.35+604951.0	136.356	0.959	9.945	0.163	9.368	0.099	5.615	0.082	2.540	0.030
		CAN	-	J024514.20+605059.1	136.352	0.978	11.808	0.025	10.998	0.022	7.252	0.033	4.747	0.035
		CAN	-	J024514.44+605050.7	136.353	0.976	11.918	0.027	11.315	0.026	6.741	0.027	4.667	0.039
		CAN	-	J024545.93+605141.7	136.405	1.016	14.924	0.075	13.897	0.052	10.519	0.178	7.722	0.314
		CAN	-	J024527.40+605513.5	136.346	1.054	14.674	0.136	14.052	0.129	8.558	0.212	6.046	0.172
		CAN	-	J024510.24+604956.4	136.352	0.959	10.572	0.023	9.502	0.021	5.327	0.017	0.425	0.008
		02413+6037	EC	J024510.79+604937.1	136.355	0.955	9.941	0.024	7.435	0.020	3.379	0.014	-0.009	0.015
	02421+6233	02421+6233	EC w/ HII	J024607.12+624630.3	135.626	2.765	9.447	0.022	8.817	0.020	3.721	0.014	0.474	0.016
		CAN	-	J024558.90+624708.0	135.607	2.767	12.086	0.023	11.316	0.021	7.805	0.021	5.131	0.036
	02598+6008	CAN	-	J030311.26+602007.6	138.548	1.521	12.065	0.024	11.302	0.024	7.219	0.023	5.658	0.041
		CAN	-	J030258.27+601920.8	138.531	1.497	11.484	0.024	10.787	0.021	7.898	0.061	6.088	0.113
		CAN	-	J030336.77+602055.1	138.588	1.558	15.035	0.050	11.792	0.023	9.228	0.117	5.419	0.078
		02598+6008	EC	J030350.14+602013.2	138.618	1.562	9.211	0.023	7.760	0.020	4.075	0.014	1.167	0.011

[a]: Q: Star-forming regions (stellar aggregates) unpublished but separately identified from our Subaru and QUIRC data (Izumi et al. in prep),
CAN: Candidate of star-forming regions newly identified with *WISE* data (See Chapter 3.5.3).
Others: ID of star-forming regions in the leteratures (Kobayashi et al., 2008; Yasui et al., 2008; Snell et al., 2002) and Chapter 2.

[b]: A: Aggregate, EC: Embedded cluster, EC w/ HII: Embedded cluster with HII region

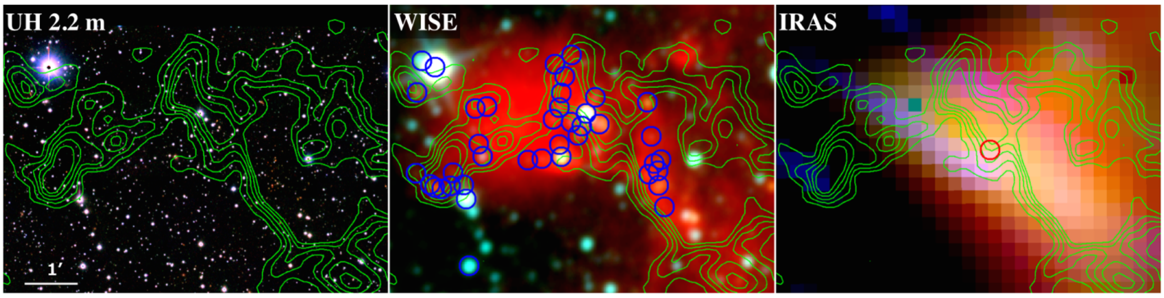

Figure 3.13: QUIRC *JHK* (Left), *WISE* 3.4, 4.6, 12 μm (Middle), and *IRAS* 25, 60, 100 μm (Right) pseudo color image of Cloud 2. The green contours show the ^{12}CO (1-0) distribution from the NRO 45 m telescope with contour levels of 3σ, 5σ, 7σ, 9σ, 11σ. The blue circles show the AllWISE sources with P (latent) flag, while red circles show the *IRAS* point sources in the *IRAS* Point Source Catalog version 2.1. Many *WISE* sources with P flags are clearly detected as *real* sources in the NIR image or with *IRAS*.

3.4 WISE color of distant star-forming regions

I set $1^\circ \times 1^\circ$ area around all the sample star-forming clouds, and divided all the AllWISE sources in the area into (1) sources associated with the sample star-forming regions (embedded clusters or stellar aggregates) and (2) the others sources, presumably the background and foreground objects (Figure 3.14). Subsequently, I investigated the colors and magnitudes of all sources in the regions.

3.4.1 Color-magnitude diagram

Figure 3.15 shows the [3.4] versus [3.4] − [4.6] color-magnitude diagram of all the *WISE* sources in the sample fields. While most field sources are distributed at around [3.4] − [4.6] = 0, all star-forming regions are distributed at [3.4] − [4.6] $\geq$ 0.5. This color corresponds to $A_r > 10$ mag (Davenport et al., 2014), some of which could be attributed to the foreground extinction in view of the large distances of star-forming regions, as well as to the intra-cluster extinction since they are embedded clusters. Among all, five star-forming region show even redder colors of [3.4] − [4.6] = 1.5 – 2.5 (equivalent extinction; A_r = 40 – 60 mag), which may be largely originated from infrared excess of circumstellar disks or envelopes besides the extinction.

Figure 3.15 also shows that the distributions of star-forming regions in the FOG and EOG are roughly separated in the vertical ([3.4] magnitude) direction: star-forming regions in the FOG are in

[3.4] = 9 – 12 mag range, while those in the EOG are in [3.4] = 11 – 16 mag range. If star-forming regions in the FOG and EOG have similar intrinsic luminosity, those in the EOG are expected to be about 2 mag fainter, because the distances to the star-forming regions in the FOG and EOG are D = 6.5 – 10 kpc and D = 12 – 16 kpc, respectively. The above-mentioned distributions are consistent with this expectation. Note that some of the EOG star-forming regions are even fainter by another 2 mag. Most of them are faint-end star-forming regions (stellar aggregate) that are found by very deep NIR imaging of Cloud 1 and 2 (see Table 3.2). In view of the [3.4] limiting magnitude, which is fainter than 16.5 mag (Wright et al., 2010), *WISE* is confirmed to have enough sensitivity to detect all kinds of star-forming regions up to the edge of the Galaxy.

3.4.2 Color-color diagram

Figure 3.16 shows the [3.4] - [4.6] versus [4.6] - [12] color-color diagram of all the *WISE* sources in the sample fields. I compared the *WISE* colors of the star-forming regions with those of individual YSOs in the solar neighborhood by Koenig & Leisawitz (2014) to confirm that the star-forming regions are primarily distributed in the YSO area defined by Koenig & Leisawitz (2014) on the diagram (see the black dashed lines in Figure 3.16). In particular, many of the star-forming regions are found to be distributed in the Class I YSOs area (e.g. Figure 5 in the Koenig & Leisawitz, 2014). This may be a natural consequence because our targets are basically embedded. However, several star-forming regions are found to be located outside the YSO area, to the lower right in the diagram (Figure 3.16). This is probably because a significant amount of polycyclic aromatic hydrocarbon (PAH) emission, which is known to be strong at [12] and, to lesser degree, at [3.4] (Wright et al., 2010), is present in star-forming regions with OB stars, whose UV flux induce the PAH emission. All the FOG star-forming regions that are known to have OB stars are, in fact, found to be in this PAH excess region (see star marks in Figure 3.16), supporting the PAH interpretation.

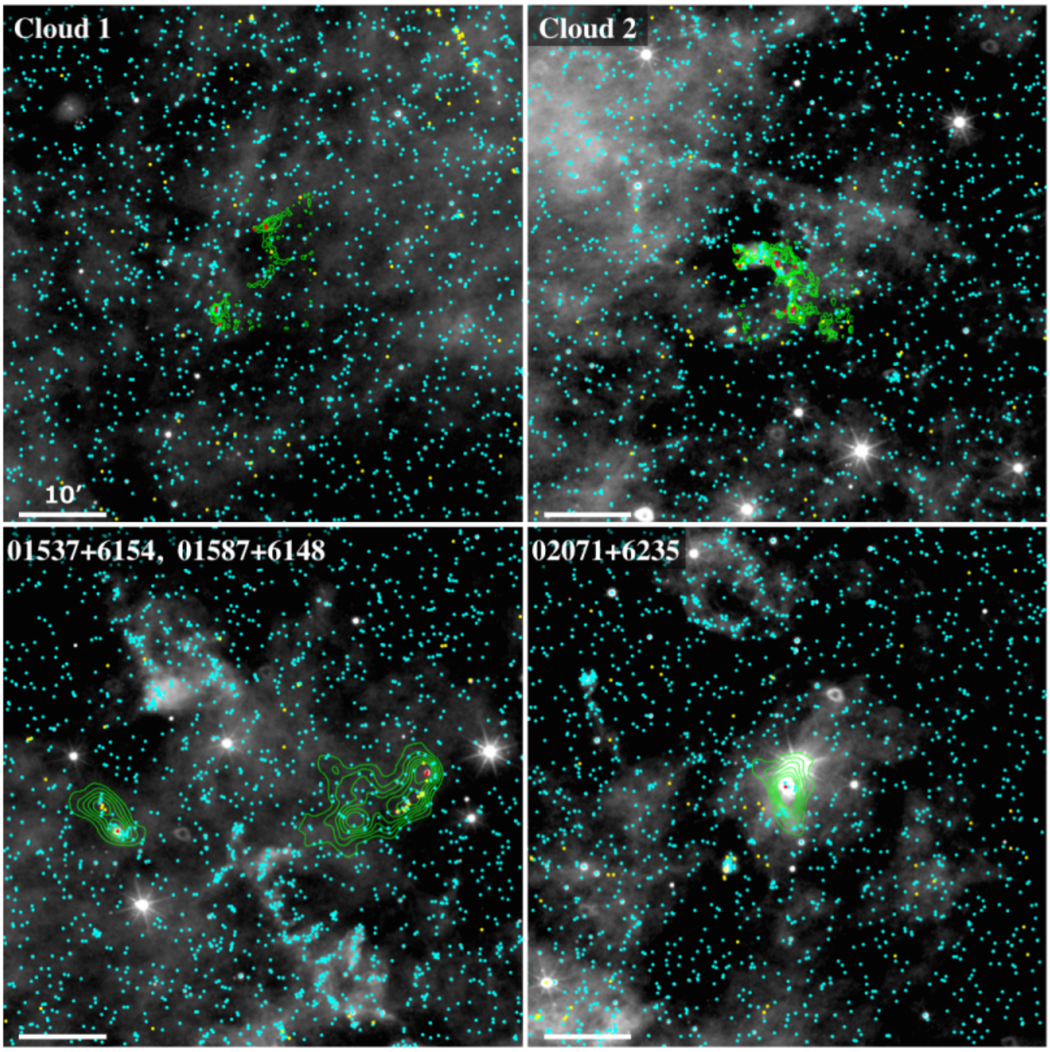

Figure 3.14: *WISE* sources in 1° × 1° fields in and around the sample star-forming molecular clouds in the EOG and FOG (except for WB89-789), plotted on *WISE* 12 μm gray-scale images. The red points show known star-forming regions, the yellow points show candidates of star-forming region, newly identified with *WISE* data and the cyan points show all the other sources in the fields. The green contours show the ^{12}CO (1-0) distribution from the FCRAO data with contour levels of 3σ, 5σ, 7σ, 9σ, 11σ, which are same as Figure 3.9 (Cloud 1, 2) and Figure 2.3 (the other clouds).

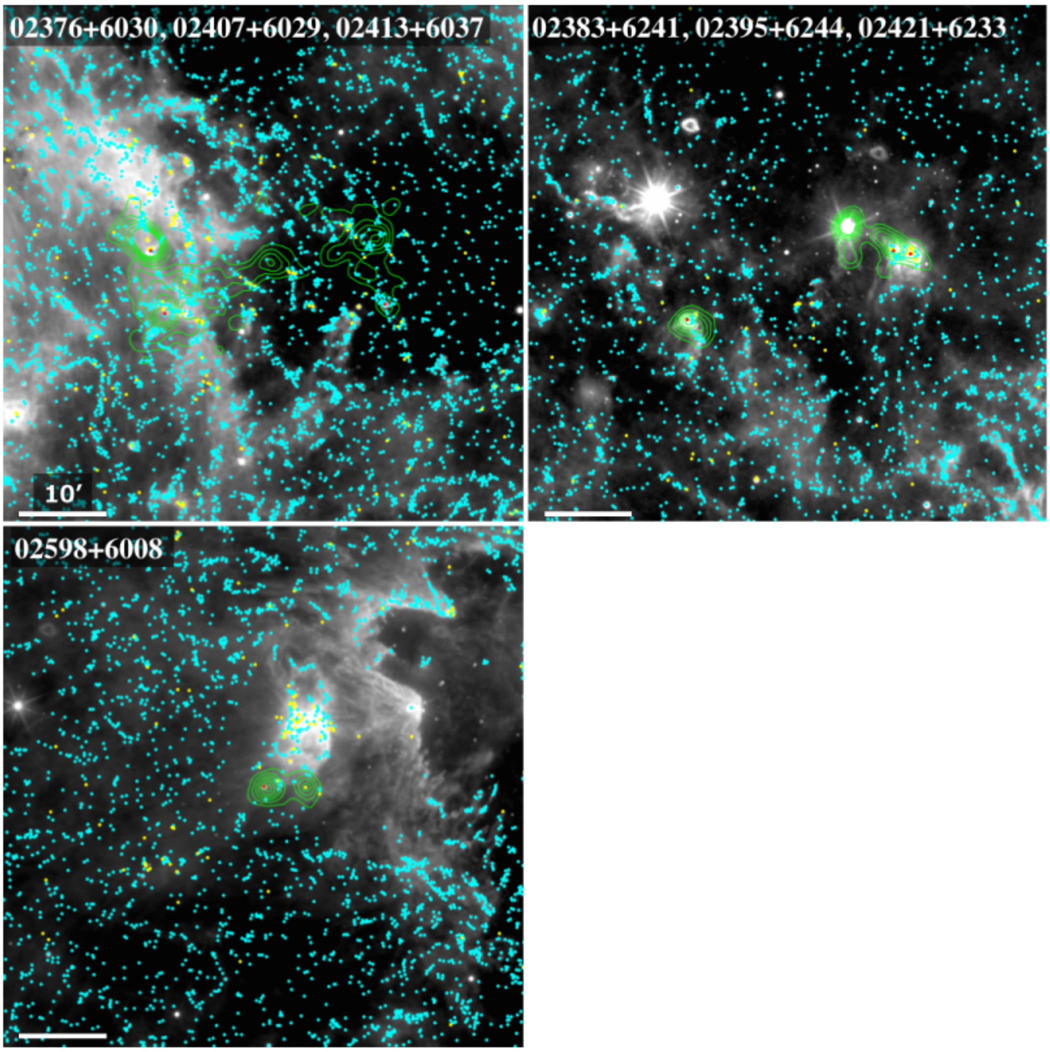

Figure 3.14 *Continued*

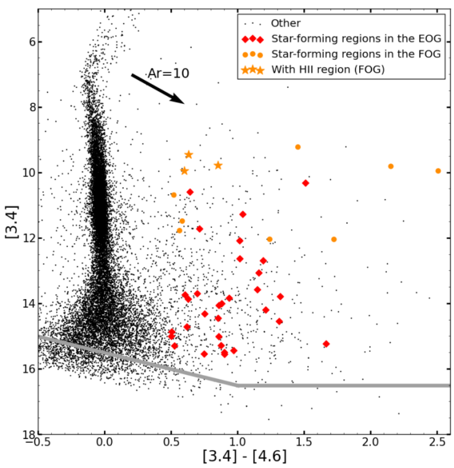

Figure 3.15: Color-Magnitude diagram of the AllWISE catalogue sources in 1° × 1° fields in and around the sample star-forming clouds in the EOG and FOG. The red and orange marks show the known star-forming regions in the EOG and FOG, respectively. The star marks show star-forming regions known to accompany OB stars. The black points show all the other sources in the fields. The grey line shows the average detection-limit for the minimum integration with eight frames (16.5 mag for 3.4 μm and 15.5 mag for 4.6 μm; Wright et al., 2010). The black arrow shows extinction vectors of A_r = 10 mag (Davenport et al., 2014).

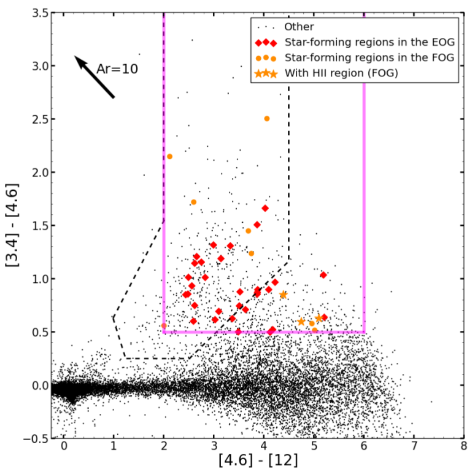

Figure 3.16: Color-Color diagram of the AllWISE catalogue sources in 1° × 1° fields in and around sample star-forming clouds in the EOG and FOG. The red and orange marks show the known star-forming regions in the EOG and FOG, respectively. Note that star mark show the star-forming regions known to accompany OB stars. The black points show all the other sources in the fields. The black arrow shows extinction vectors of A_r = 10 mag (Davenport et al., 2014). The black dashed lines show the division for individual YSOs from Koenig & Leisawitz (2014). The magenta lines show our defined division for distant star-forming regions.

3.5 Identification criteria of distant star-forming regions

3.5.1 Criteria

In Figure 3.16, the area of star-forming regions is empirically defined by a square determined by three lines, [3.4] $-$ [4.6] $\geq$ 0.5, [4.6] $-$ [12] $\geq$ 2.0, and [4.6] $-$ [12] $\leq$ 6.0. Compared to the YSO area in Koenig & Leisawitz (2014) (the black dashed lines in Figure 3.16), the newly defined area dose not included the sub area by the color ranges [3.4] $-$ [4.6] = 0.25 – 1.5 and [4.6] $-$ [12] = 1.0 – 3.0 because this region is dominated by Class II YSOs (Koenig & Leisawitz, 2014) and I wanted to avoid contamination from Class III YSOs distribution in the foreground star-forming regoins. Because our samples are embedded clusters and virtually all of them are affected by significant infrared excess from circumstellar disks and envelopes of Class I sources or compact HII regions as seen in Chapter 3.4.2, the drawback by the elimination of this area is likely to be quite limited. On the other hand, the newly identified area includes an additional area defined by [3.4] $-$ [4.6] $\geq$ 0.5 and [4.6] $-$ [12] = 2.5 – 6.0, which is outside the YSO area by Koenig & Leisawitz (2014), in order to pick up star-forming regions with OB stars with possible PAH emission at [3.4] and [12] bands as seen in Chapter 3.4.2. Because the probability of contaminations by planetary nebulae and background AGNs (e.g. Koenig & Leisawitz, 2014; Wright et al., 2010) significantly increases at bluer [3.4] - [4.6] color, I set the lower-side of the additional area at [3.4] - [4.6] = 0.5. I may be able to set more accurate shape of the area for distant unresolved star-forming regions by increasing the number of the samples star-forming regions in the near future.

3.5.2 Possible contamination problems

Here I discuss the possible contamination by foreground or background objects in the candidates of star-forming regions selected with color-color diagram. The defined area for star-forming regions is contaminated by foreground/background planetary nebulae (PNe) and by background AGNs (e.g. Koenig & Leisawitz, 2014; Wright et al., 2010). I found three clear contaminations by possible AGNs in the CO peaks of Cloud 2 (see Figure 3.17). Although the *WISE* sources show the color of star-forming regions, the corresponding objects are recognized as three galaxies with symmetric disk in the high-resolution Subaru NIR images (FWHM $\sim$ 0.3$''$ – 0.35$''$), and also the bright point-like cores in all galaxies suggest their AGN nature. However, our targets star-forming regions (embedded clusters/stellar aggregates) accompany their parental molecular clouds, and the probability of contamination by PNes or AGNs is likely to be quite low in view of the small extent of the distant molecular clouds on the sky. The number density of QSOs and AGNs are roughly estimated to be about 15 (/degree^2) from Figure 16 in Wright et al. (2010), while the number density of candidate of star-forming regions around sample star-forming molecular clouds are about 40 $\sim$ 170 (/degree^2). Furthermore, the number density of QSOs and AGNs is predicted to down to at Galactic plane because of the large extinction. We could not confirm any other clear contamination for Cloud 1 and Cloud 2, for which we have Subaru high-resolution NIR images that cover most of the cloud extention. The probability of contamination by foreground star-forming regions may be also insignificant for the same reason.

To estimate the total contamination rate quantitatively, we compared the number of candidates of star-forming region within the molecular clouds (3σ contour, $N_{\rm MC}$) to those in the field ($1^\circ \times 1^\circ$-field around 3σ contour, $N_{\rm F}$). Figure 3.14 shows the distribution of sample star-forming regions (red) that are used to construct the criteria, candidates of star-forming regions (yellow), and the other *WISE* sources in and around star-forming molecular clouds (cyan). First, I calculated the number densities of sample/candidate of star-forming regions in the cloud ($n_{\rm MC}$) and in the field ($n_{\rm F}$) using $N_{\rm MC}$, $N_{\rm F}$, and the area of the cloud with 3 σ contour, which was manually estimated on the display to avoid picking up noisy features. Then, I estimated the contamination rate as ($n_{\rm F}/n_{\rm MC}$).

Table 3.3 lists the contamination rates for all sample star-forming molecular clouds except WB89-789 [3]. I found that the median contamination rate is about 16 %, suggesting roughly one contamination source is present in each star-forming molecular clouds. This contamination rate highly depends on the environment around the star-forming clouds. For instance, the areas in and around star-forming molecular clouds 02376+6030, 02407+6029, and 02413+6037, which appear to be behind foreground star-forming regions, show much larger contamination rates than the other region ($\sim$ 20 – 60 %). On the other hand, the rate is only 3% in low contamination regions, such as Cloud 2. Figure 3.18 shows distribution of foreground molecular clouds in and around two representative regions. The amount of foreground molecular clouds appears to increase with increasing the contamination rate. Therefore, I

[3] I did not estimate the contamination rate for WB89-789, because we do not have ^{12}CO molecular data of WB89-789.

suspect that the main contamination source is likely to be YSOs associated with foreground molecular clouds. Furthermore, the contamination rates also depend on the spatial-resolution of the CO map. For example, contamination rate of Cloud 1 decreases from 9% to 6% when using ^{12}CO map from our NRO 45 m data (resolution $\sim 17''$) compared to the FCRAO 14 m data (resolution $\sim 100''$) due to the decrease of the identified cloud area. It would be useful to keep compiling high-resolution CO data of those distant molecular clouds for better identification. In view of the above results, this identification criteria appear to be effectively picking-up distant star-forming region.

Table 3.3: Contamination rate for the sample star-forming molecular clouds

Region	Star-forming molecular cloud	Number of candidate/known star-forming regions in the cloud ($N_{\rm MC}$)	Cloud area [arcmin^2]	Number densities of candidate/known star-forming regions in the cloud ($n_{\rm MC}$) [/ arcmin^2]	Number of Candidates in the field ($N_{\rm F}$)	Contamination Density ($n_{\rm F}$) [/ arcmin^2]	Contamination rate [%]
EOG	Digel Cloud 1	8	24 (NRO)	3.3×10^{-1}	68	1.9×10^{-2}	6
		8	39 (FCRAO)	2.1×10^{-1}	68	1.9×10^{-2}	9
	Digel Cloud 2	25	46 (NRO)	5.4×10^{-1}	51	1.4×10^{-2}	3
		25	56 (FCRAO)	4.5×10^{-1}	51	1.4×10^{-2}	3
	WB89-789	—	—	—	—	—	—
FOG	01537+6154	10	127.5	7.8×10^{-2}	27	0.8×10^{-2}	10
	01587+6148	4	36	1.1×10^{-1}	33	0.9×10^{-2}	8
	02071+6235	1	40.5	2.5×10^{-2}	54	1.5×10^{-2}	61
	02376+6030	6	72	8.3×10^{-2}	169	4.8×10^{-2}	57
	02383+6241	12	28	4.3×10^{-1}	53	1.5×10^{-2}	3
	02395+6244	0	21	—	63	1.8×10^{-2}	—
	02407+6029b	19	133	1.4×10^{-1}	156	4.5×10^{-2}	31
	02413+6037	7	31.5	2.2×10^{-1}	168	4.7×10^{-2}	21
	02421+6233	2	18	1.1×10^{-1}	63	1.8×10^{-2}	16
	02598+6008	4	28	1.4×10^{-1}	97	2.7×10^{-2}	19

3.5.3 New candidates of star-forming regions in the sample clouds

Using the identification criteria, I searched for new candidate of star-forming regions in all samples star-forming molecular clouds in the field of view, where NIR images are not available. As a result, I identified 58 new candidates located within the 3 σ contours of molecular clouds (Table 3.2, Figure 3.9 and 3.12). These new objects data will be subject to future follow-up studies.

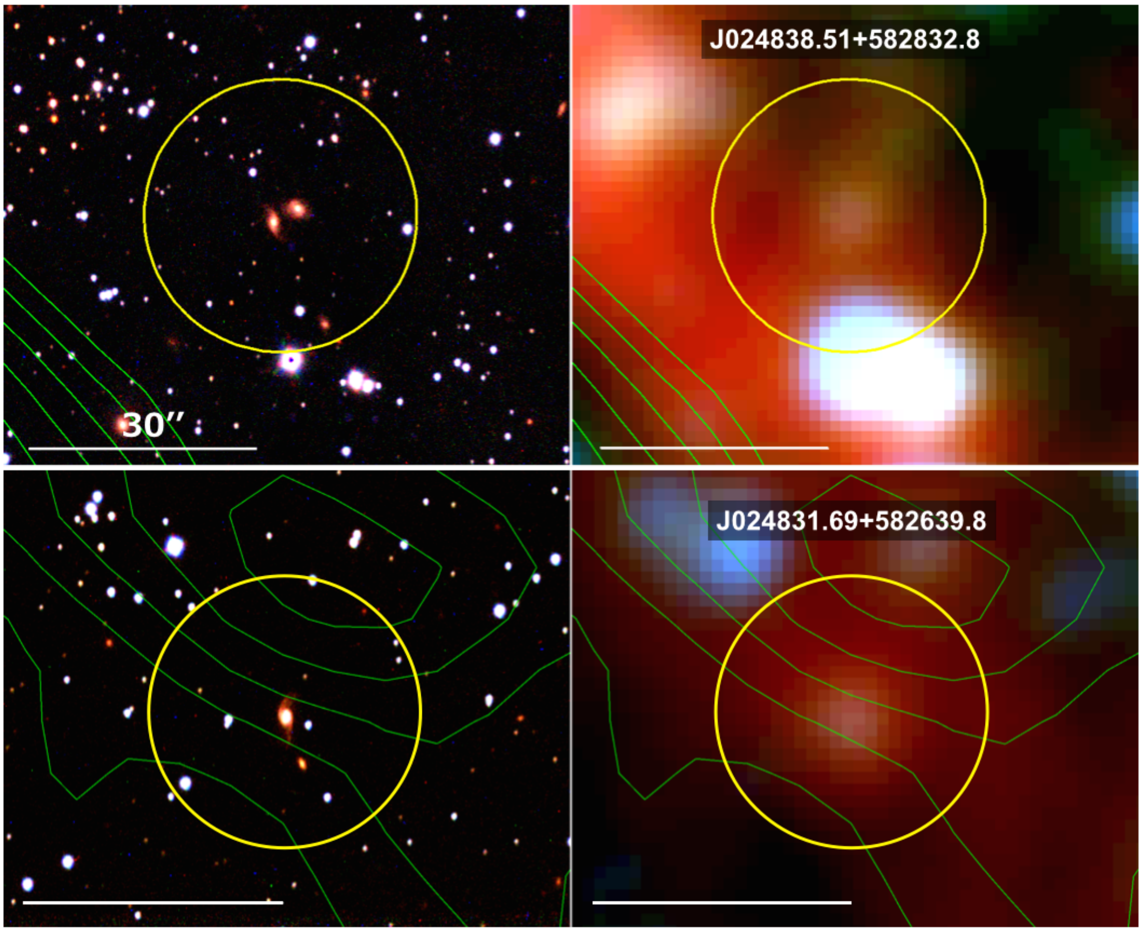

Figure 3.17: Subaru *JHK* (Left) and *WISE* 3.4 (blue), 4.6 (green), and 12 (red) μm band pseudo-color images showing an example contamination by three galaxies (possible AGNs) in the CO core of Cloud 2 in the EOG. The green contours show the ^{12}CO (1-0) distribution from the NRO 45 m telescope with contour levels of 3σ, 5σ, 7σ, 9σ, 11σ. The yellow circles show the location of a candidate of star-forming regions, which was turned out to be galaxy in the Subaru NIR image (Top: l = 137°.760, b = -0°.981, Bottom: l = 137°.761, b = -1°.015).

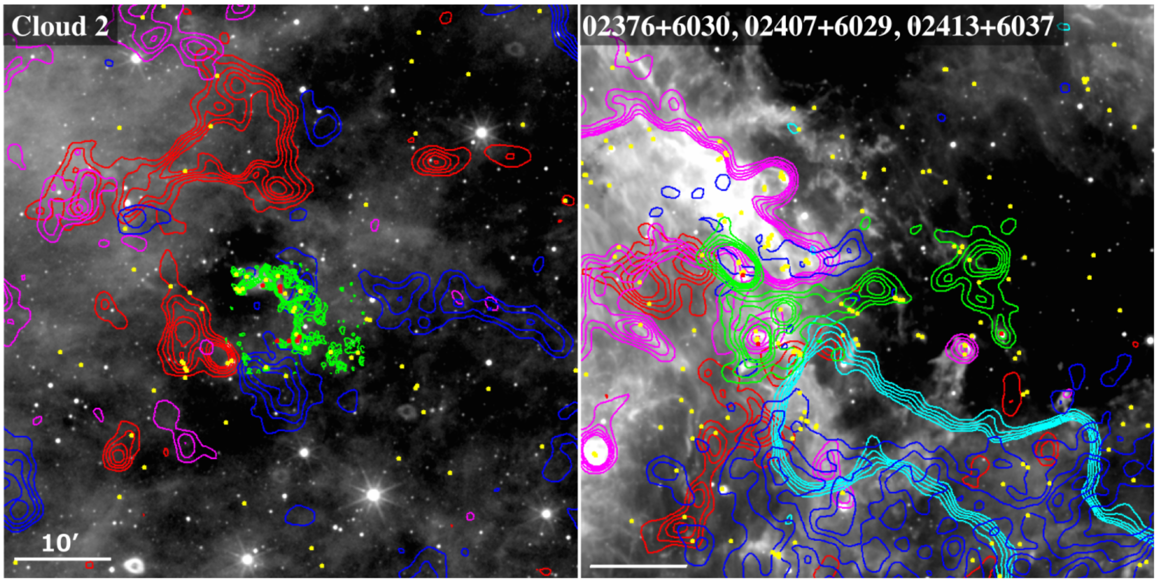

Figure 3.18: *Left* : Distribution of foreground molecular clouds in and around Digel Cloud 2. The gray-scale background image shows the *WISE* 12 μm image. The green contours show the ^{12}CO (1-0) distribution from the NRO 45 m telescope with contour levels of 3σ, 5σ, 7σ, 9σ, 11σ (same as Figure 3.9) . The red, magenta, and blue contours show the ^{12}CO (1-0) distribution of foreground molecular clouds from the FCRAO data with contour levels of 3σ, 5σ, 7σ, 9σ, 11σ (red : $v_{\rm LSR}$ = -43.5 ∼ -47.6 km s^{-1}, 1 σ = 0.42 K km s^{-1}, magenta : $v_{\rm LSR}$ = -35.3 ∼ -38.6 km s^{-1}, 1 σ = 0.25 K km s^{-1}, blue : $v_{\rm LSR}$ = -0.6 ∼ -8.9 km s^{-1}, 1 σ = 0.29 K km s^{-1}). *Right* : Distribution of foreground molecular clouds in and around 02376+6030, 02407+6029, and 02413+6037. The gray-scale background image shows the *WISE* 12 μm image. The green contours show the ^{12}CO (1-0) distribution from the FCRAO data with contour levels of 3σ, 5σ, 7σ, 9σ, 11σ (same as Figure 2.3). The red, magenta, cyan, and blue contours show the ^{12}CO (1-0) distribution of foreground molecular clouds from the FCRAO data with contour levels of 3σ, 5σ, 7σ, 9σ, 11σ (red : $v_{\rm LSR}$ = -49.3 ∼ -55.9 km s^{-1}, 1 σ = 0.42 K km s^{-1}, magenta : $v_{\rm LSR}$ = -32.0 ∼ -46.0 km s^{-1}, 1 σ = 0.42 K km s^{-1}, cyan : $v_{\rm LSR}$ = -8.1 ∼ -16.3 km s^{-1}, 1 σ = 0.35 K km s^{-1}, blue : $v_{\rm LSR}$ = 5.13 ∼ -3.11 km s^{-1}, 1 σ = 0.37 K km s^{-1}).

3.6 A new survey of star-forming regions in the outer Galaxy

By making use of the methods in Chapter 3.5, I systematically searched for new star-forming regions in a large number of molecular clouds in the outer Galaxy to study statistical properties of star-formation activities in low gas density and low metallicity environment.

3.6.1 BKP clouds

First I constructed a set of sample molecular clouds from the FCRAO ^{12}CO survey data of the Outer Galaxy (Heyer et al., 1998). This survey has achieved the best combination of large area-coverage and high sensitivity among all available outer Galaxy surveys. The FCRAO survey covers $102^\circ.49 \leq l \leq 141^\circ.54$ and $-3^\circ.03 \leq b \leq 5^\circ.41$ with the total area of about 320 deg^2 (Heyer et al., 1998). The median main beam sensitivity (1 σ) per channel is $\sim$ 0.9 K with a spatial resolution of $45''$ (Heyer et al., 1998, 2001). The v_{LSR} range covers $-153 \leq v_{\rm LSR} \leq +40$ km s^{-1} with the velocity resolution of 0.98 km s^{-1} (Heyer et al., 1998). Heyer et al. (2001) identified 10,156 clouds in the whole parameter space of the survey. To make use of the sensitive survey data, Brunt et al. (2000) reprocessed the data to remove correlated noise induced by reference-sharing and contaminating emission present in the reference positions (Brunt et al., 2000). The data was also convolved to $100''.44$ spatial resolution to be incorporated into the the Canadian Galactic Plane Survey (Taylor et al., 2003). As the result of the reprocess and the convolution, the typical sensitivity of the data was improved to 0.17 K. I confirmed the sensitivity by checking noise level of the archived data. Owing to the better sensitivity, Brunt et al. (2003) (hereafter, BKP2003) identified 14,592 clouds in the whole survey area, which is about 1.5-times that of the original survey despite the smaller velocity range of $-120 \leq v_{LSR} \leq +20.8$ km s^{-1}.

In this thesis, I employed the molecular cloud catalogue by BKP2003 (hereafter, BKP catalogue) to make use of the larger number of clouds compared to the original Heyer et al. (2001)'s catalogue. The high-sensitivity BKP catalogue is essential to study distant star-forming regions in the outer Galaxy. Using the Galactic (l,b) coordinates and $v_{\rm LSR}$ of the clouds in the BKP catalogue, I derived kinematic distances[4] of all the catalogued clouds (hereafter, BKP clouds) to pick up 466 clouds in the

[4] I assumed that the rotation speed of the Sun and all objects in the catalogue is 220 km s^{-1} and the Galactocentric distance of the Sun is 8.5 kpc.

outer Galaxy ($R_G \geq 13.5$ kpc) out of 14,592 clouds.

3.6.2 Basic properties of BKP clouds

Here, I summarize the estimated physical properties of BKP clouds (mass, size, area, and velocity width) to discuss their properties in the following chapters (Chapter 4, 5, 6, 7).

Mass– I estimated the masses of the BKP clouds from CO intensity I_{CO} ($\int T_B dv$) with the Galactic average mass-calibration ratio N(H$_2$)/I_{CO} (2.0×10^{20} cm^{-2} (K km s^{-1})$^{-1}$; e.g. Bolatto et al., 2013) and the correction for the abundance of helium (1.36; Dickman, 1978). I examined the cloud mass (luminosity) variation with the Galactocentric radius (Figure 3.19) to check the mass-completeness limits in the outer Galaxy ($R_G \geq 13.5$ kpc). Around the boundary of EOG ($R_G \sim 18$ kpc), the data set of clouds is found to be roughly complete for cloud mass larger than $10^2\ M_\odot$. At more distant region ($R_G \sim 19 - 23$ kpc), the mass-completeness limit becomes slightly larger ($\sim 2 \times 10^2\ M_\odot$). This result is consistent with the lower-limit of cloud mass at $D = 12$ kpc ($R_G \sim 18$ kpc), which was estimated as 75 $M_\odot$ from the following parameters: $T_B = 0.51$ K (3σ), $\Delta v = 0.98$ km s^{-1} (velocity resolution), $r = 100''.44$ (spatial resolution).

Figure 3.19 also shows that massive molecular clouds with $M \geq 10^4\ M_\odot$ are detected only at $R_G < 17$ kpc. Considering the completeness limit of $M = 10^2\ M_\odot$ at $R_G \leq 18 \sim 19$ kpc, this trend should reflect the real distribution of molecular clouds in the outer Galaxy, which is consistent with the surface density distributions of atomic and molecular gas in the outer Galaxy wherein the densities decrease with increasing R_G (e.g. Nakanishi & Sofue, 2006; Wolfire et al., 2003).

Size(Radius)– I estimated the cloud size from cloud diameters (FWHM) in major and minor axes, which were derived from 2D elliptical gaussian fit in BKP2003. Among all 466 clouds, the fitting failed to converge or was not attempted for 86 clouds because the size of those clouds are too small (BKP2003). For those "cloudlets", we estimated the size (S) from the number of spatial pixels in cloud (N_S) from BKP2003 using a S - N_S relation that was estimated by least-square fitting for clouds with $0 < N_S \leq 100$ (see Figure 3.20). In this fitting range, S variation is smaller than 2 arcmin, and the total number of clouds is 359, which is 94 % of the 380 clouds (= 466 - 86). The results of the fitting is $S = 0.25\ (\pm\ 0.0065)\ \sqrt{N_S} + 0.079\ (\pm\ 0.0029)$. In Figure 3.20, the fitted curve appears to be good in the whole fitting range. The size at $N_S = 0$ of the fitting curve is only 0.079 arcmin, which is much smaller than the pixel scale (0.837 arcmin), thus negligible; this assures the validity of the fitting.

Area− I estimated the area of each cloud using the number of spatial pixels (N_S) from BKP2003 and the pixel scale of 0.837 arcmin.

Velocity width− In the BKP catalogue, the velocity width of each cloud was derived from gaussian fit of each spectrum. However, the fitting failed to converge, or was not attempted for 277 clouds out of 466 clouds because their velocity widths are too small (BKP2003). For those 277 clouds, I set the upper-limit of the line widths as the velocity resolution of the FCRAO survey (0.98 km s^{-1} ; Heyer et al., 1998).

Virial mass− I estimated virial masses of BKP clouds from velocity width and size: M_{vir} = 210 $\times$ r Δv^2, assuming that the density distribution is constant (MacLaren et al., 1988). Note that I could estimate virial masses of only 189 clouds out of 466 clouds because velocity width of other 277 clouds are not derived successfully.

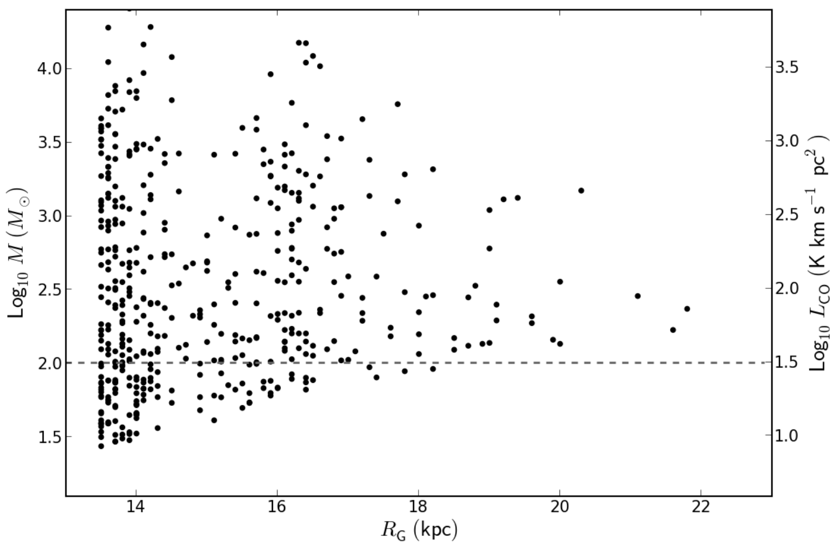

Figure 3.19: Cloud mass (luminosity) variation with Galactocentric radius for all BKP clouds (466 clouds) in the outer Galaxy ($R_G \geq 13.5$ kpc). The gray dotted line shows the cloud mass of 10^2 $M_\odot$.

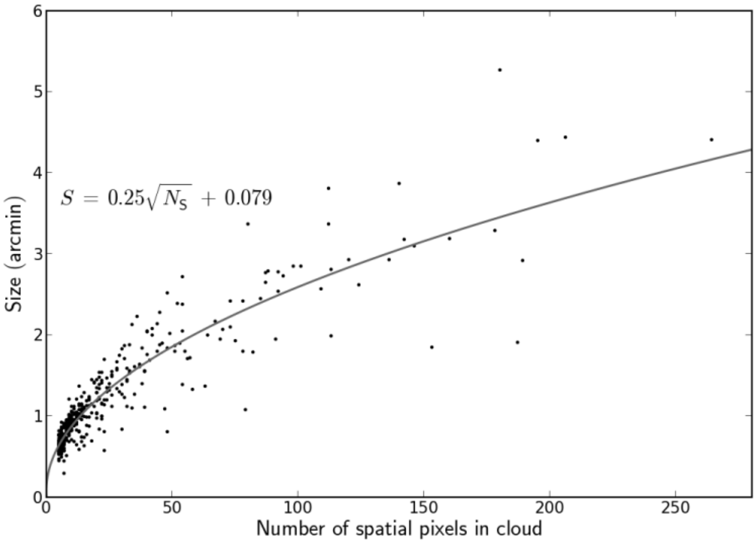

Figure 3.20: Relation between Number of spatial pixel in cloud (N_S) and size (S) of clouds in the BKP catalogue. The black line shows the result of least-square fitting ($S = 0.25\sqrt{N_S} + 0.079$) for clouds with $0 < N_S \leq 100$.

3.6.3 Search for new candidates of star-forming regions

I searched for candidates of star-forming regions with *WISE* for 466 clouds using our developed identification criteria (Chapter 3.5.1). As a result, I found 778 *WISE* sources from the AllWISE Source Catalog within 3σ contours of all 466 clouds. Those new candidates of star-forming regions are found in 252 clouds, which are about half of the whole set of 466 clouds. Among all, 67 *WISE* sources in 12 clouds are already found in the previous section (Table 3.2, Figure 3.9 and 3.12). Note that 13 sources out of all 778 *WISE* sources are contained in two different clouds at different velocities. All the *WISE* sources and BKP clouds with star-forming regions are listed in Appendix of this thesis.

3.6.4 Contamination rate

To confirm the reliability of the candidates, I estimated contamination rate (see Chapter 3.5.2) for all 252 clouds with star-forming regions by rationing the number density of candidates of star-forming regions in the cloud area to that in each $1^\circ \times 1^\circ$-field around the cloud area . Note that I searched candidates of star-forming regions within the 3 σ contours while BKP2003 identified molecular clouds using threshold of 4.7 σ and the cloud area derived at Chapter 3.6.2 is the area within the 4.7 σ contours. I preferred the lower contours (3 σ) to pick up star-forming regions as many as possible since star-forming regions are sometimes located near the edge of cloud (in the vicinity of 3 σ contours; e.g. Figure 3.9). Thus, the absolute value of the contamination rate for the cloud area within 3 σ contours should be slightly larger than the above-estimated contamination rates, but the difference should be insignificant in view of the small area difference of 3 σ to 4.7 σ.

The contamination rate distribution (Figure 3.21) shows that the number of molecular clouds sharply drops at the contamination rate of 20 $\sim$ 30 % and most clouds have lower contamination rate. Therefore, I set the contamination threshold at 30 %, and the candidates with contamination rate less than 30 % (211 clouds out of 252 clouds) are regarded as high-reliability candidates. Thus, I could identify enough number of molecular clouds with star-forming regions for statistically studying star-formation activity in the outer Galaxy.

3.6.5 Survey results

Figure 3.22 shows the [3.4] - [4.6] versus [4.6] - [12] color-color diagram for all the *WISE* sources in the survey area of FCRAO outer Galaxy survey ($102^\circ.49 \leq l \leq 141^\circ.54$ and $-3^\circ.03 \leq b \leq 5^\circ.41$). There are 926,132 *WISE* sources with S/N of more than 5 at all 3.4, 4.6, and 12 μm bands and without confusion flags (see Chapter 3.2). The black points in the left panel and black contours in the right panel show the distribution of all 926,132 sources in the area. The 26 % (204/778) of candidate of star-forming regions are located outside the YSO area by Koenig & Leisawitz (2014). These “outsiders” could be relatively massive star-forming regions (including OB stars; see Chapter 3.4.2).

Figure 3.23 shows the [3.4] versus [3.4] - [4.6] color-magnitude diagram of all the *WISE* sources in the survey area of FCRAO outer Galaxy survey. The distribution of star-forming regions are apparently different from the distribution of all “*WISE*” sources in the area (see the colored points and black contours in the right panel of Figure 3.23) The star-forming regions show much redder [3.4] - [4.6] colors than field objects, probably due to both larger extinction and infrared excess. As for the apparent magnitude, the star-forming regions spread widely at [3.4] = 8 – 17 mag, while star-forming regions with contamination rate of larger than 30 % are distributed at slightly fainter magnitudes of [3.4] = 12 – 17 mag. This may suggest that some of them are, in fact, background PNe, AGNs or low-mass YSOs in the foreground star-forming regions.

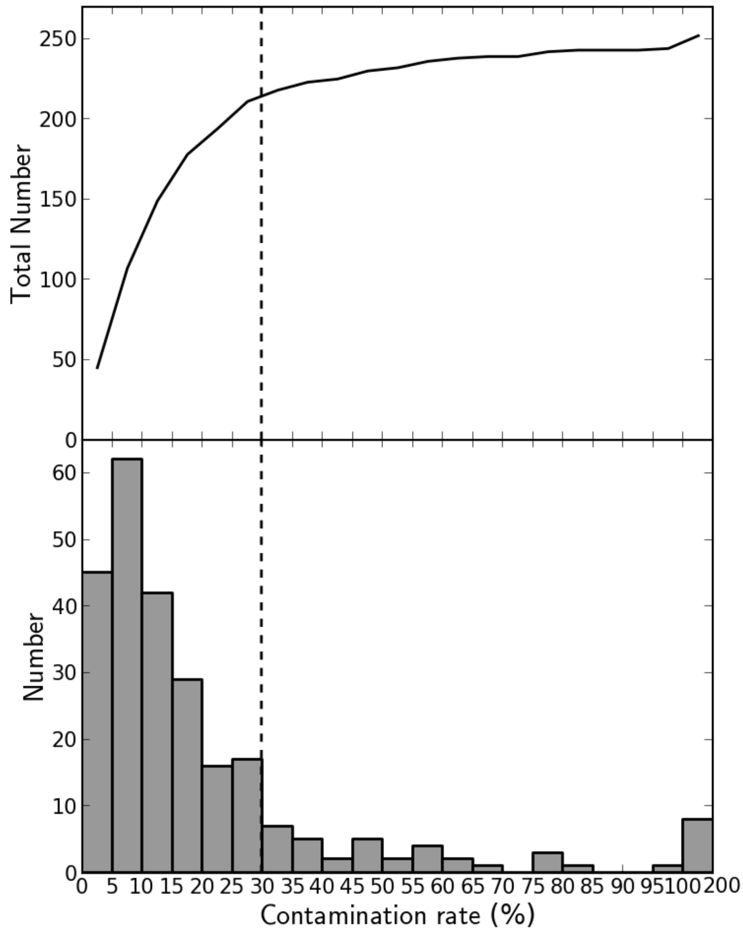

Figure 3.21: Distribution of contamination rate for all 252 molecular clouds with candidate of star-forming region. *Top*: The cumulative number of molecular clouds. *Bottom*: The number of molecular clouds per contamination rate of 5% bin. The dotted black line shows the contamination threshold of 30 %. Clouds with contamination rate less than 30 % (211 clouds) are regarded as high reliability candidates.

The left panel of Figure 3.24 shows the variation of apparent magnitude with kinematic distance in all four bands. I use kinematic distance of their parental clouds. The ranges of the magnitudes are about 8 – 10 magnitudes in all four bands. In this plot, the magnitude of the brightest star-forming region becomes fainter with increasing distance. The magnitude difference of the brightest star-forming regions around D = 6 kpc and D = 15 kpc is about 2 mag, which can be attributed to simply the distance: $\Delta m = 5 \times \log_{10} (15/6) = 2$, assuming that the absolute magnitude of the brightest star-forming regions is constant. The star-forming regions with contamination rate of larger than 30 % are concentrated at $6 \leq D \leq 8$ kpc, suggesting that the major factor of contamination rate is the apparent size of cloud, which becomes larger with decreasing the distance.

The right panel of Figure 3.24 shows the variation of the absolute magnitude with kinematic distance in all four bands. I calculated the absolute magnitude from the *WISE* magnitude in the AllWISE catalogue using the kinematic distance D of their parental clouds. At the most distant region ($D \sim 15$ kpc) the data set of *WISE* sources is found to be complete for sources with brighter than about 1.0 mag, 0.0 mag, -4.0 mag, and -7.0 mag at 3.4 μm, 4.6 μm, 12 μm, and 22 μm, respectively. These magnitudes are roughly consistent with the average detection limit for the minimum integration with eight frames (16.5 mag for 3.4 μm, 15.5 mag for 4.6 μm, 11.2 mag for 12 μm, and 7.9 mag for 22 μm; Wright et al., 2010, and see gray dotted lines and curves in Figure 3.24). I note that the setting these thresholds still remain a matter of debates, because my targets are not necessarily become fainter with increasing their distances. My targets are whole star-forming regions or some parts of star-forming regions, and therefore, I may detect different objects between D = 6 kpc and 16 kpc.

Figure 3.25 shows the variation of the flux densities with kinematic distance in all four bands. I calculated the flux from *WISE* magnitude in the AllWISE catalogue using the conversion with flux zeropoints: $F_{\nu\,3.4\mu\mathrm{m}}$ = 309.540 Jy, $F_{\nu\,4.6\mu\mathrm{m}}$ = 171.787 Jy, $F_{\nu\,12\mu\mathrm{m}}$ = 31.674 Jy, $F_{\nu\,22\mu\mathrm{m}}$ = 8.363 Jy (Jarrett et al., 2011). In Figure 3.25, I also show the flux densities of A0 and B0 stars in the main sequence for all four bands (Cyan and blue curves: calculated with Table 7.5 and 15.7 in Cox, 2000). Note that I used intrinsic colors of V-L and V-band magnitude of $M(V)$ for calculating the flux densities for all four bands, since infrared colors, such as [3.4] - [22] are negligible for those early-type stars. I also calculated the 22 μm flux density for HII regions ionized by B0 star (Blue dotted curve in Figure 3.25) using the parameters in Anderson et al. (2014). At 3.4 and 4.6 μm, the flux densities of *WISE* sources reasonably correspond to OB association and stellar aggregates (single A-type star + T Tauri Stars), while that at 12 and 22 μm show much smaller flux. This results suggest that $F_{3.4\mu\mathrm{m}}$ and $F_{4.6\mu\mathrm{m}}$ are dominated by stars wile $F_{12\mu\mathrm{m}}$ and $F_{22\mu\mathrm{m}}$ are dominated by dust emission from circumstellar dust and/or free-free emission (+ PAH emission) from HII regions. This is consistent with well-known spectral energy distribution (SED) of star-forming regions, and support the idea that $F_{3.4\mu\mathrm{m}}$ and $F_{4.6\mu\mathrm{m}}$ can be used as an indicator of total mass of the stars in the star-forming region.

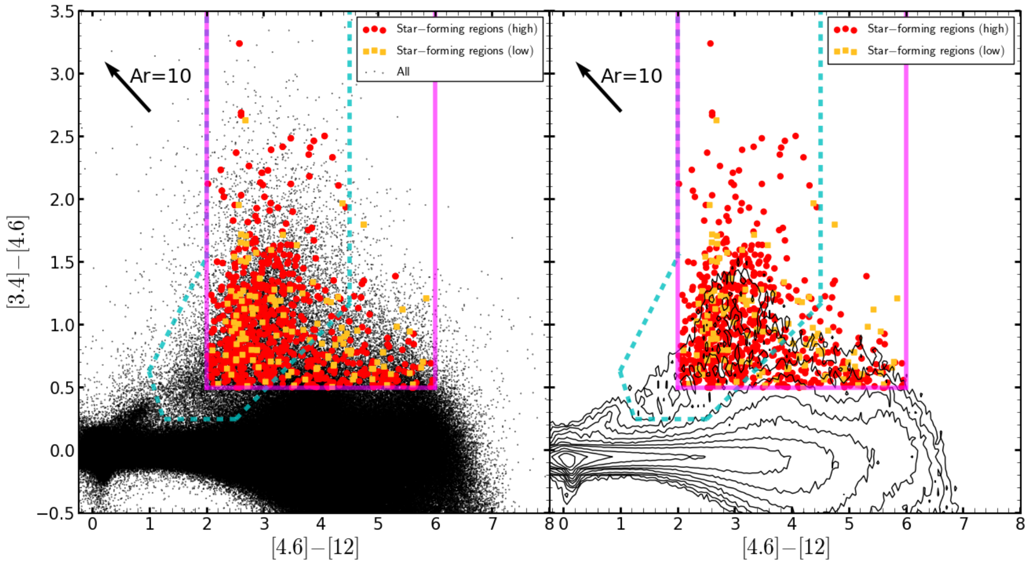

Figure 3.22: Color-Color diagram of all the AllWISE catalog sources in the FCRAO outer Galaxy survey area (102°.49 $\leq l \leq$ 141°.54 and -3°.03 $\leq b \leq$ 5°.41) . I selected the sources with the signal-to-noise (S/N) of more than 5 at all 3.4, 4.6, and 12 μm bands (926132 sources in the area). The red circles and yellow squares show the candidates of star-forming regions with Contamination rate < 30 % (red circle) and $\geq$ 30 % (yellow square). The black points in the left panel show all sources in the area. The black contours in the right panel show the distribution of all sources in the area (10, 20, 40, 80, 160, 320, 640, 1280, and 2560 independent data points per 0.05 cell). The black arrow shows the extinction of A_r = 10 mag (Davenport et al., 2014). The magenta lines show our defined division for distant star-forming regions.

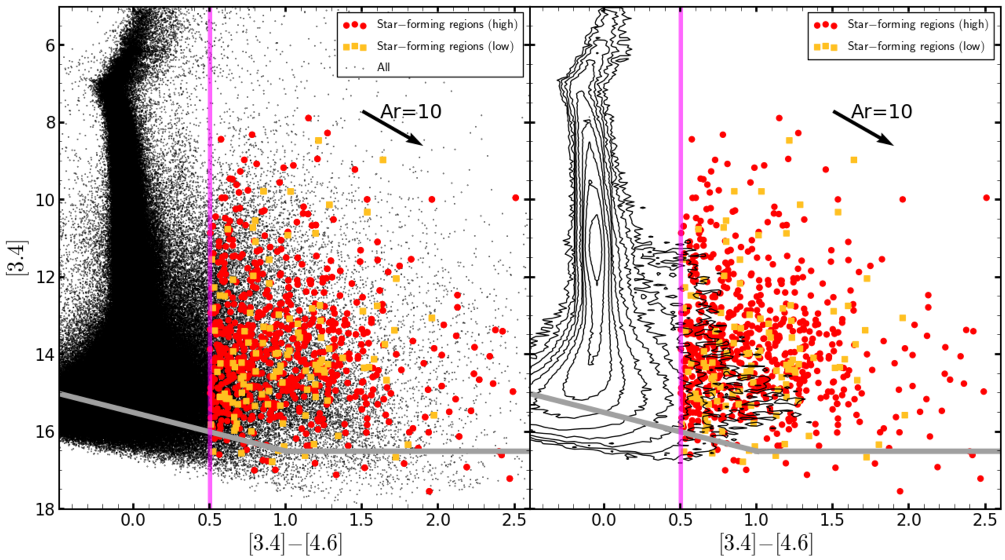

Figure 3.23: Color-Magnitude diagram of all the AllWISE catalog sources in the FCRAO outer Galaxy survey area ($102^\circ.49 \leq l \leq 141^\circ.54$ and $-3^\circ.03 \leq b \leq 5^\circ.41$) . I selected the sources with the signal-to-noise (S/N) of more than 5 at all 3.4, 4.6, and 12 μm bands (926132 sources in the area). The red circles and yellow squares show the candidates of star-forming regions with Contamination rate < 30 % (red circle) and ≥ 30 % (yellow square). The black points in the left panel show all sources in the area. The black contours in the right panel show the distribution of all sources in the area (10, 20, 40, 80, 160, 320, 640, 1280, and 2560 independent data points per 0.05 cell). The grey line shows the average detection-limit for the minimum integration with eight frames (16.5 mag for 3.4 μm and 15.5 mag for 4.6 μm; Wright et al., 2010). The black arrow shows the extinction of A_r = 10 mag (Davenport et al., 2014). The magenta line shows our defined division for distant star-forming regions.

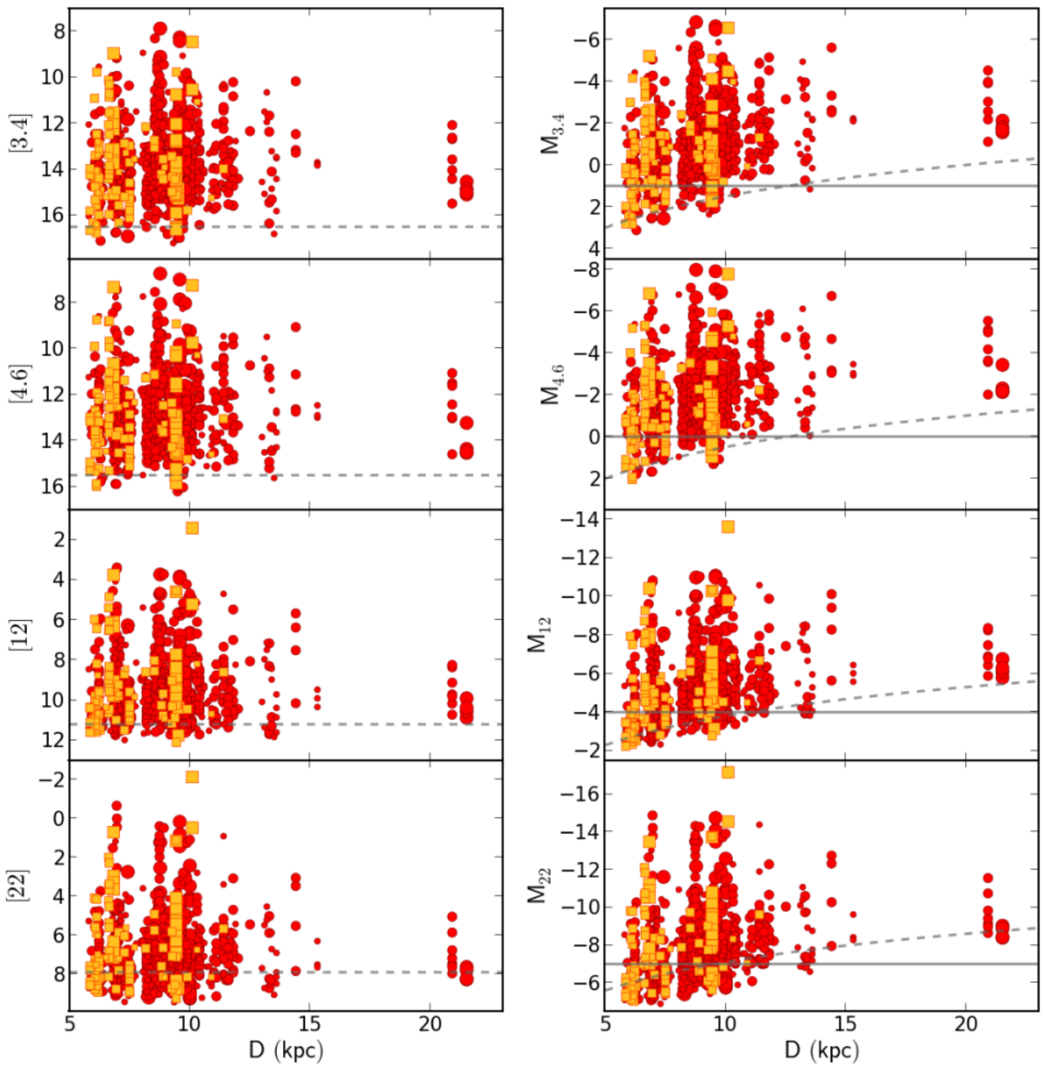

Figure 3.24: *Left*: Apparent magnitude variation with kinematic distance for newly identified star-forming regions. Red circles show the star-forming regions with Contamination rate < 30 %, while yellow squares show the star-forming regions with Contamination rate ≥ 30 %. The size of these markers indicate the mass of their parental molecular clouds (small: $10^2\ M_\odot \leq M_{\rm cloud} < 10^3\ M_\odot$, middle: $10^3\ M_\odot \leq M_{\rm cloud} < 10^4\ M_\odot$, large: $10^4\ M_\odot \leq M_{\rm cloud}$). The gray dotted lines show the average detection limit for the minimum integration with eight frames (16.5 mag for 3.4 μm, 15.5 mag for 4.6 μm, 11.2 mag for 12 μm, and 7.9 mag for 22 μm; Wright et al., 2010). *Right*: Absolute magnitude variation with kinematic distance for newly identified star-forming regions. The notation is the same as the left panel. The gray lines show the completeness limit set for our analysis with luminosity-limited samples.

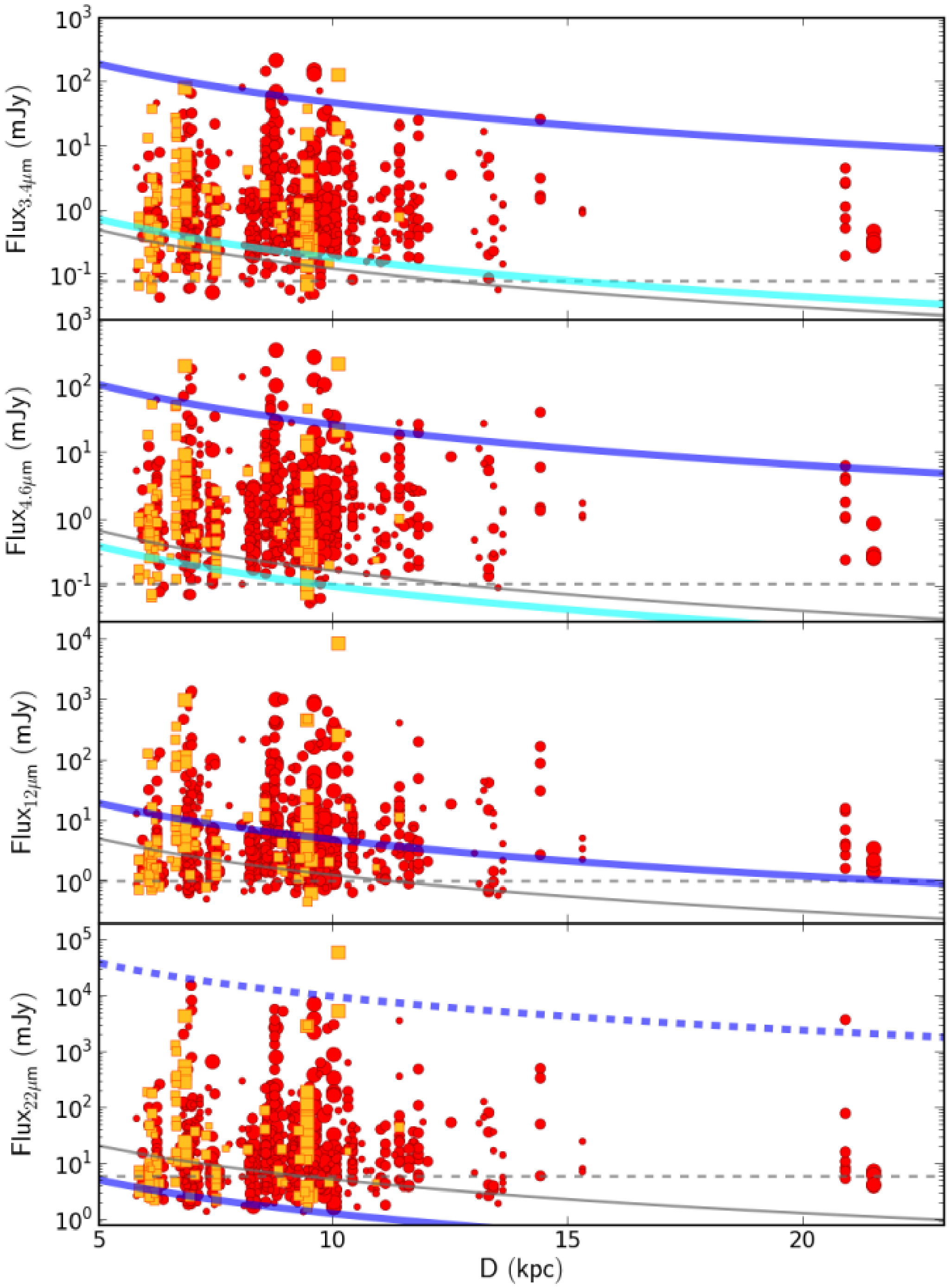

Figure 3.25: Flux density variation with kinematic distance for newly identified star-forming regions. Red circles show the star-forming regions with Contamination rate < 30 %, while the yellow squares show the star-forming regions with Contamination rate ≥ 30 %. The size of these markers indicate the mass of their parental molecular clouds (small: $10^2\ M_\odot \leq M_{\rm cloud} < 10^3\ M_\odot$, middle: $10^3\ M_\odot \leq M_{\rm cloud} < 10^4\ M_\odot$, large: $10^4\ M_\odot \leq M_{\rm cloud}$). The gray dotted lines show the average detection limit for the minimum integration with eight frames (0.08 mJy for 3.4 μm, 0.11 mJy for 4.6 μm, 1 mJy for 12 μm, and 6 mJy for 22 μm; Wright et al., 2010). The gray lines show the completeness limit set for our analysis with luminosity-limited samples. The cyan and blue curves show the flux densities of the A0 and B0 stars in the main sequence (Cox, 2000). The blue dotted curve shows the 22 μm flux density for the HII regions ionized by B0 star (Anderson et al., 2014).

Chapter 4

Spatial distribution of star-forming regions in the outer Galaxy

In Chapter 3, I report a new survey of star-forming regions in the outer Galaxy with *WISE* MIR data and CO survey data. In this Chapter, I discuss the distribution of the newly identified star-forming regions/molecular clouds with our survey. From the spiral distribution of star-forming regions, I confirmed perhaps a new arm structure beyond the outer arm.

4.1 Disk structure

4.1.1 Spiral structure of our Galaxy

Figure 4.1 shows the image of Galactic spiral structure, constrained by currently available data including the stellar data from Spitzer GLIMPSE (Galactic Legacy Infrared Mid-Plane Survey Extraordinaire; Benjamin et al., 2003) survey, HI Galactic plane surveys, and CO surveys. Our galaxy is known to be a two-armed barred Galaxy with several secondary arms. The main arms are called as Scutum-Centaurus and Peruseus arms and secondary arms are called as Sagittarius, the outer (Norma), and the 3 kpc expanding arm (See Figure 4.1). Starting with the seminal study of HII regions by Georgelin & Georgelin (1976), there have been many proposed model of spiral structures (e.g. Vallée, 2008; Hou & Han, 2014). However, still we do not know the precise structure of spiral structures, even basic ones such as the number and position of spiral arms. Observation of a large number of reliable spiral tracers and determination of their distance as accurately as possible are very important for understanding the structure.

In the outer part of the Galaxy, Hachisuka et al. (2015) performed VLBA (Very Long Baseline Array) parallax and proper motion observations of H_2O masers source in the Outer arm. As a result, they found that the Galactocentric radius of the outer arm is 14.1 ± 0.6 kpc in the direction of the anticenter. While Strasser et al. (2007) found a spiral arm structure that roughly follows R_G = 18 kpc, thus possibly beyond the Outer arm, from HI emission/absorption pairs toward continuum background sources in the northern and southern Galactic plane. Sun et al. (2015) also identified a new segment of a possible spiral arm at $R = 15 \sim 18$ kpc by HI data from CGPS survey (Taylor et al., 2003) and CO data from the Chinese MWISP (Milky Way Imaging Scroll Painting project; http://www.radioast.nsdc.cn/yhhjindex.php) project. However, only a few stellar component, which is known to be good tracers of the spiral structures, have been detected in the new arm structures (Anderson et al., 2015), and the arm structures beyond the Outer arm is still in fluid. Therefore, I investigate these structures in the outer Galaxy with our newly identified star-forming regions/molecular clouds (see Chapter 3).

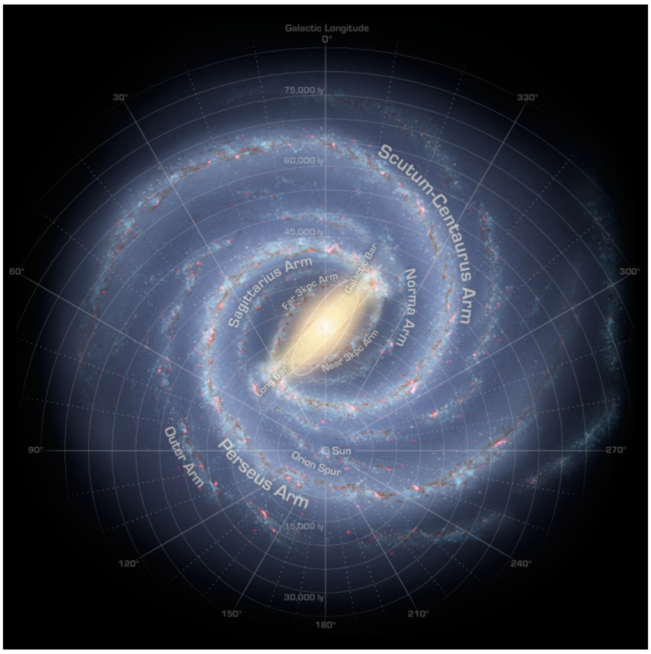

Figure 4.1: The image of the spiral disk of our Galaxy (Churchwell et al., 2009, NASA/JPL-Caltech). This image was made by Robert Hurt of the Spitzer Science Center in consultation with Robert Benjamin at the University of Wisconsin-Whitewater.

4.1.2 Distribution of newly identified star-forming regions/molecular clouds on the Galactic plane

Figure 4.2 shows the location of molecular clouds w/ and w/o star-forming region at $R_G \geq 13.5$ kpc on the Galactic plane. A gap of cloud distribution is seen at $R_G \sim 15$ kpc and two separate groups of molecular clouds appears to be present at $R_G \sim 14$ and 16 – 17 kpc (Figure 4.2a). This structure is clearer for the distribution of only clouds w/ star-forming regions (Figure 4.2b and 4.2c). Figure 4.3 shows the masses of molecular clouds and magnitudes of all star-forming regions as a function of R_G. This figure also shows that molecular clouds and star-forming regions are concentrated at $R_G \sim$ 14 and 16 – 17 kpc, in particular, the massive and the brighter ones. The former group is likely to be associated with the outer arm at $R_G \sim 14$ kpc in the direction of anticenter (e.g. Hachisuka et al., 2015) and the latter group appear to form a new arm beyond the outer arm. This new arm has slightly smaller R_G ($\sim$ 16 – 17 kpc), than R_G of the suggested new arm by Strasser et al. (2007) and Sun et al. (2015). Sun et al. (2015) proposed that their new arm is connected to the Scutum-Centaurus arm (yellow curve in Figure 4.2d). Our data shows a number of star-forming regions on the trail of Sun et al. (2015)'s proposed new arm but it is not clear if they form a part of an arm. Our new arm may be the one connected the Scutum-Centaurus arm, but could be branched from the Outer arm (cyan dotted and solid curves in 4.2d). Obviously, surveys of star-forming regions at l = 60 $\sim$ 100° will be very important for understanding these arm structures clearly.

4.2 Distribution on the sky

Figure 4.4 shows the locations on the l-b map of the clouds w/ and w/o star-forming regions and molecular clouds detected by Sun et al. (2015) at -109.5 km s^{-1} $\leq v_{LSR} \leq$ -50.9 km s^{-1}. All clouds are associated with high-intensity HI region. At -109.5 km s^{-1} $\leq v_{LSR} \leq$ -100.4 km s^{-1}, a large HI shell centered at (l, b) = (127°,1°) is clearly identified , and molecular clouds are found to be tightly tracing the shell (see Chapter 2). Figure 4.5 shows the locations on the $v_{\rm LSR}$-b map of the clouds w/ and w/o star-forming regions at 100°.0 $\leq l \leq$144°.5. The number of clouds at 100°.0 $\leq l \leq$104°.5 (Top panel of Figure 4.5) and 140°.0 $\leq l \leq$144°.5 (Bottom panel of Figure 4.5) are smaller than other panels because the survey area is limited to 102°.49 $\leq l \leq$141°.54. As in Figure 4.4 and 4.5, all clouds are associated with high specific-intensity HI regions. Those figures do not show any clear difference between distribution of clouds w/ and w/o star-forming regions. The HI cloud distributions in this v_{LSR}-b map also show the gap structure discussed at Chapter 4.1.2. The arm structures is clearly seen as cross-sections with clouds w/ star-forming regions (red and magenta crosses in Figure 4.5), in particular in the three panels $125^\circ.0 \leq l \leq 139^\circ.5$. Many of them are located at $b \geq 1^\circ$, which is expected from warping in this quadrant of the Galaxy (e.g. Nakanishi & Sofue, 2003).

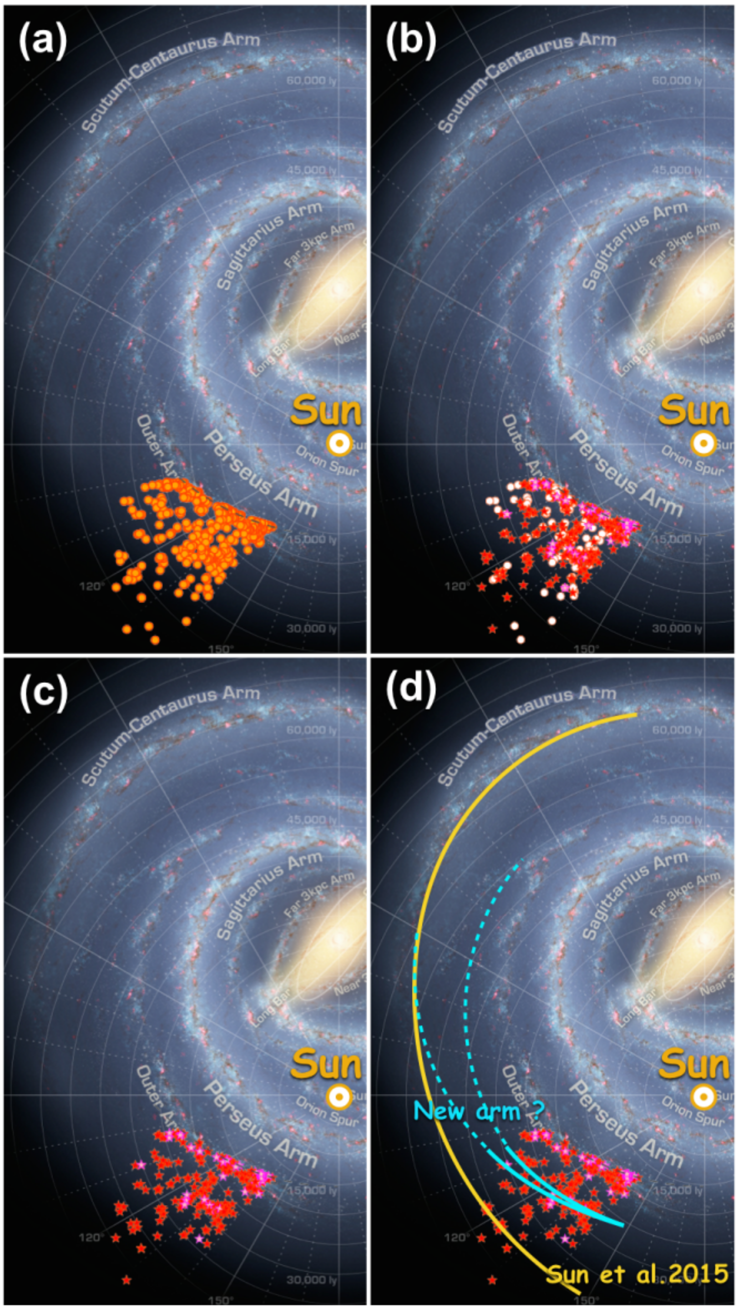

Figure 4.2: Distribution of molecular clouds in the outer Galaxy (rearranged the image of Milky Way Galaxy from NASA's Spitzer Space Telescope by NASA/JPL-Caltech). (a): Distribution of BKP clouds at $R_G \geq 13.5$ kpc. (b): Distribution of molecular clouds w/ and w/o star forming regions at $R_G \geq 13.5$ kpc (white circle: clouds w/o star-forming regions, magenta star: clouds w/ star-forming regions with Contamination rate ≥ 30 %, red star: clouds w/ star-forming regions with Contamination rate < 30 %) (c): Distribution of molecular clouds w/ star forming regions only (d): Same as (c), but with possible arm location curves The dotted and solid cyan curves shows the location of our proposing new arm. The yellow solid curve shows another arm suggested by Sun et al. (2015).

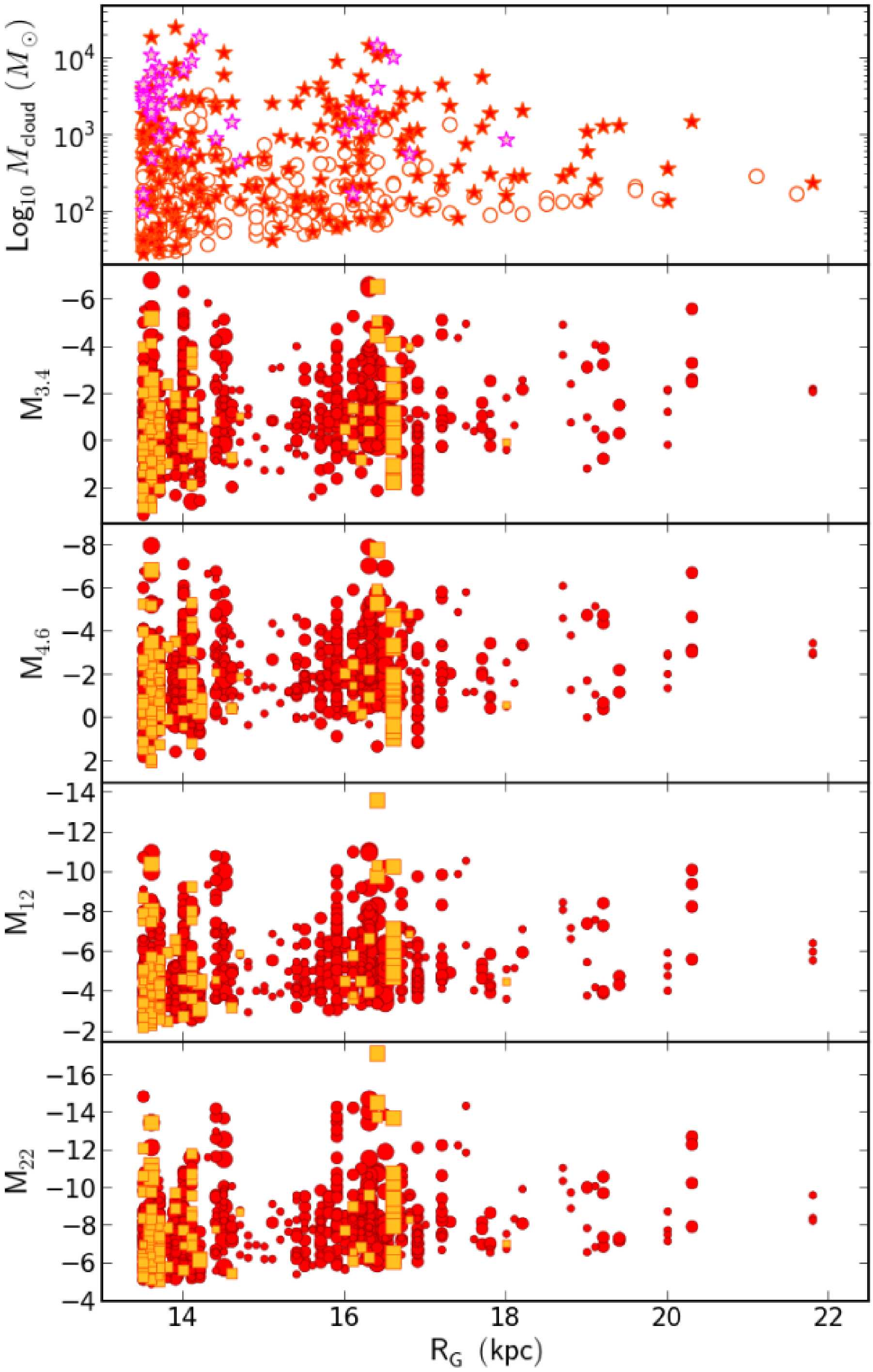

Figure 4.3: *Top*: Cloud mass variation with Galactocentric radius for clouds at $13.5 \leq R_{\mathrm{G}} \leq 22.5$ kpc. The white circles show clouds w/o star-forming regions. Red and magenta star marks show clouds w/ star-forming regions with contamination rate $<$ and ≥ 30 %, respectively. *Others*: Absolute magnitude variation with Galactocentric radius for star-forming regions at $13.5 \leq R_{\mathrm{G}} \leq 22.5$ kpc. Red circles and yellow squares show the star-forming regions with contamination rate $<$ and ≥ 30 %, respectively. The size of these markers indicate the mass of their parental molecular clouds (small: $10^2\ M_\odot \leq M_{\mathrm{cloud}} < 10^3\ M_\odot$, middle: $10^3\ M_\odot \leq M_{\mathrm{cloud}} < 10^4\ M_\odot$, large: $10^4\ M_\odot \leq M_{\mathrm{cloud}}$).

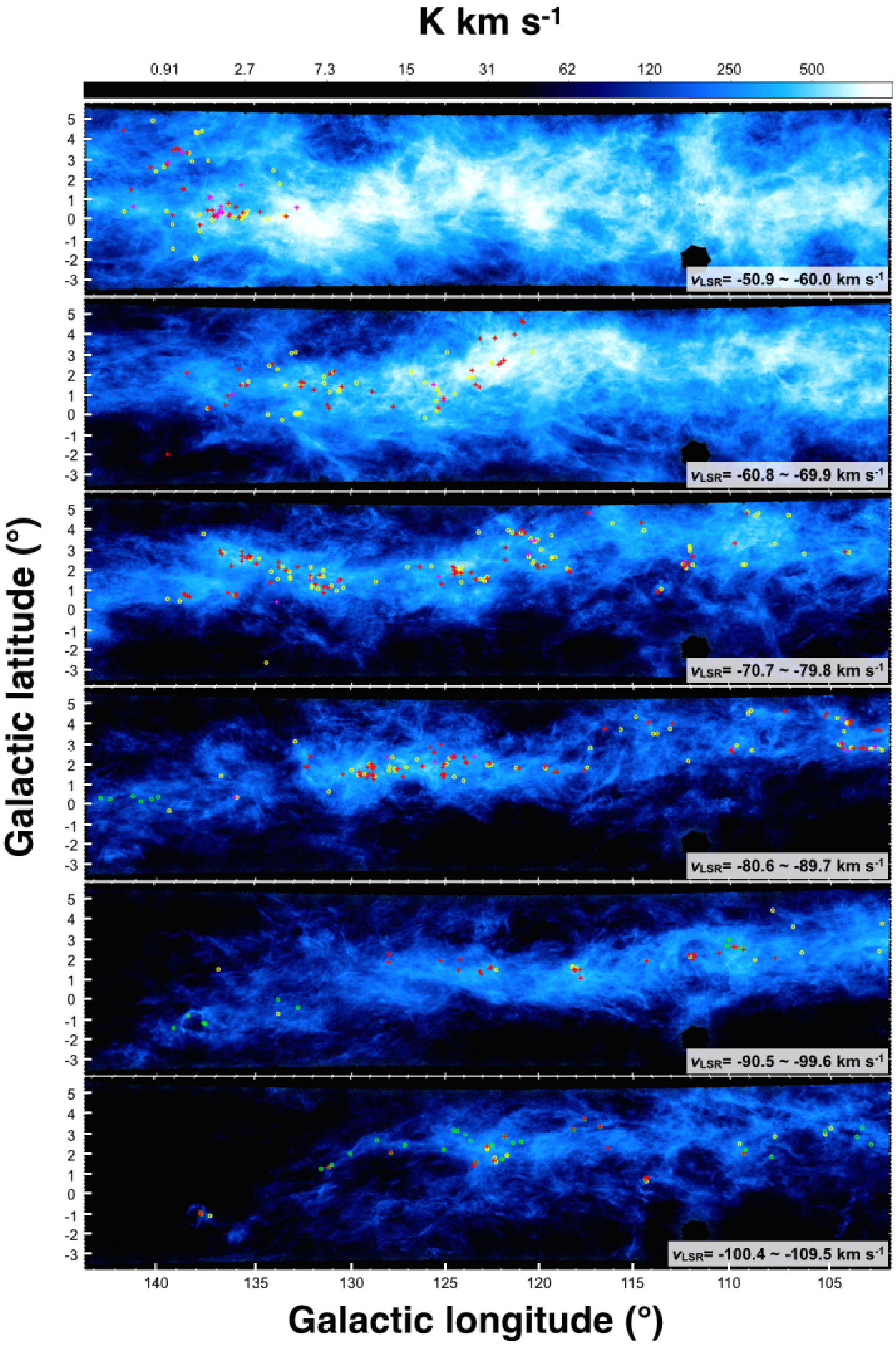

Figure 4.4: Location of molecular clouds plotted on HI channel map from the CGPS data. Every other channel between -50.9 and -109.5 km s^{-1} is shown. The red crosses show the clouds w/ star-forming regions with contamination rate < 30 %, the magenta crosses show the clouds w/ star-forming regions with contamination rate ≥ 30 %, and the yellow circles show the clouds w/o star-forming regions. The green circles show the molecular clouds detected by Sun et al. (2015).

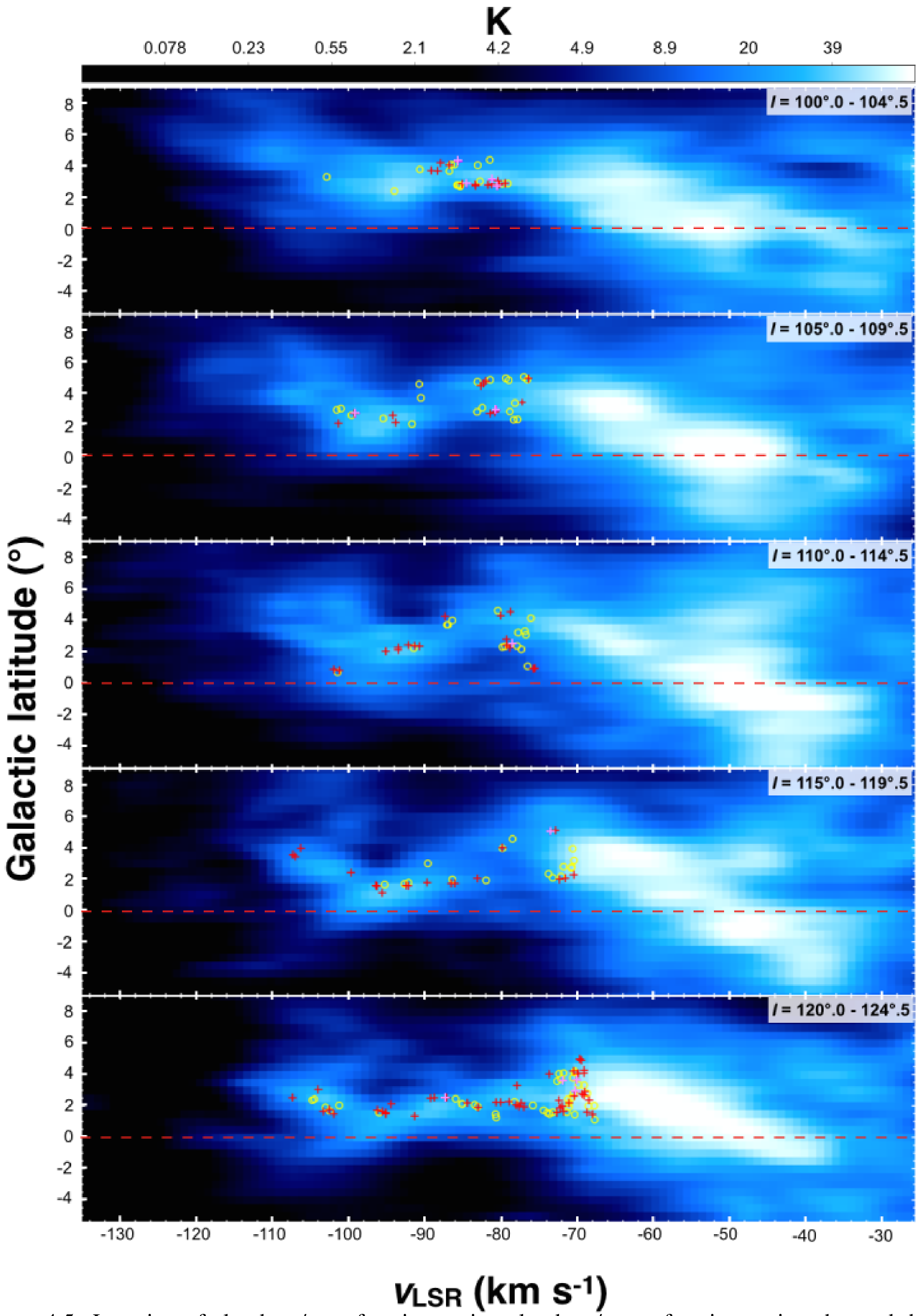

Figure 4.5: Location of clouds w/ star-forming region clouds w/o star-forming regions beyond the outer Arm. The red crosses show the clouds w/ star-forming regions with contamination rate < 30 %, the magenta crosses show the clouds w/ star-forming regions with contamination rate ≥ 30 %, and the yellow circles show the clouds w/o star-forming regions. The blue-scale backgrounds show HI velocity-latitude map from l = 100°.0 to 144°.5 made from the Leiden/Argentine/Bonn (LAB) Survey of Galactic HI data (Kalberla et al., 2005). The red dotted lines show the galactic latitude of 0°.0.

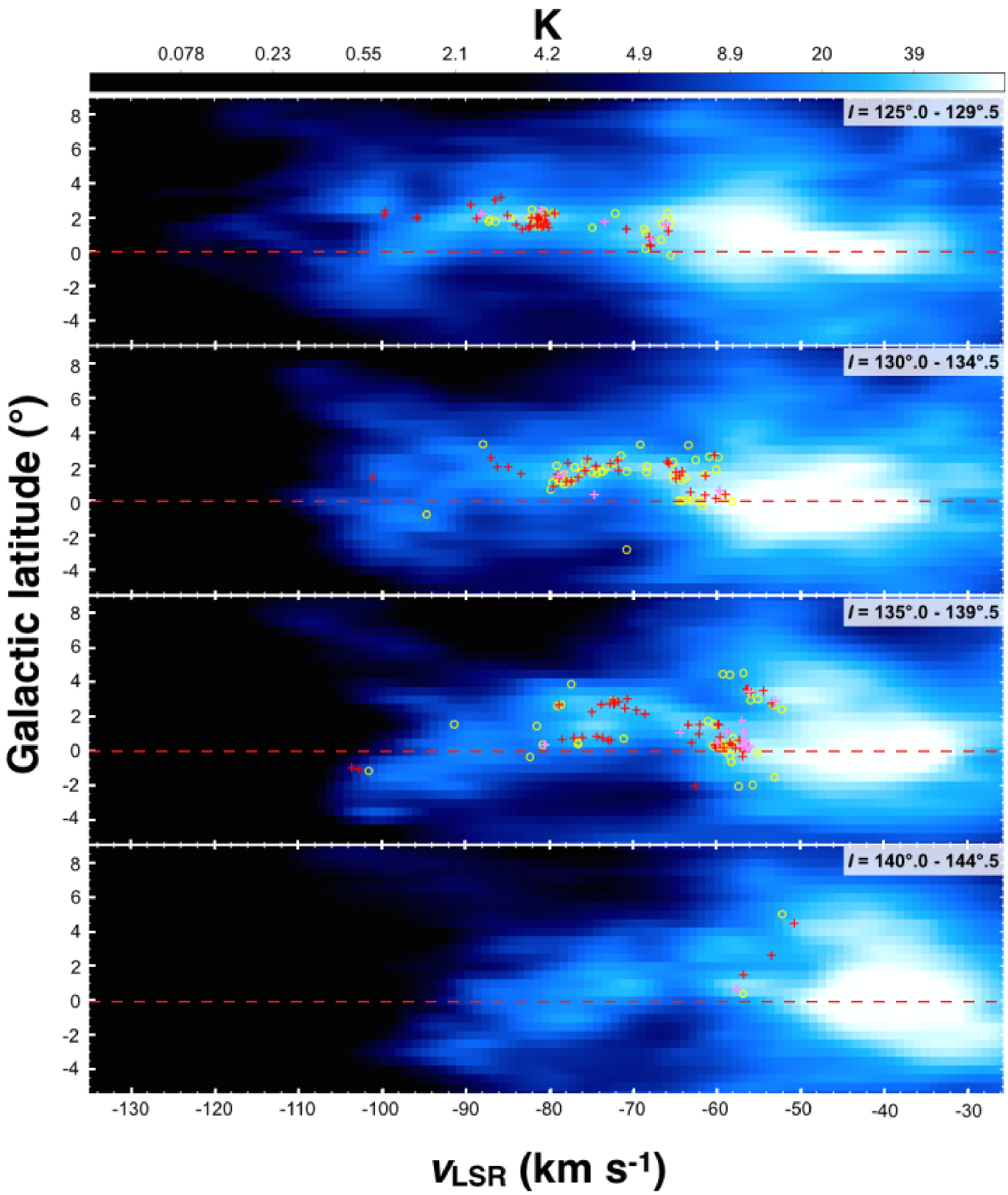

Figure 4.5 *Continued*

Chapter 5

Properties of star-forming regions in the outer Galaxy

In Chapter 4, I report a distribution of the newly identified star-forming regions/molecular clouds in the outer Galaxy. As a next step, I discuss the properties of molecular clouds and star-forming regions in the outer Galaxy based on the statistics of the BKP clouds and newly identified star-forming regions. To compare molecular clouds and star-forming regions at various distances, I set completeness limits of cloud mass and *WISE* absolute luminosities (see Chapter 3).

5.1 Molecular clouds

5.1.1 Mass distribution

The left panel of Figure 5.1 shows mass distribution for all BKP clouds at $R_{\rm G} \geq 13.5$ kpc, and the right panel of Figure 5.1 shows mass distribution for clouds w/ and w/o star-forming regions. Each spectrum has been fitted by power law at $M \geq 10^2\ M_{\odot}$. The slope for all clouds is -1.63 $\pm$ 0.10. The slopes for clouds w/ star-forming region with contamination rate $<$ 30% and all clouds w/ star-forming regions are -1.38 $\pm$ 0.13, -1.41 $\pm$ 0.12, respectively, while the slope for clouds w/o star-forming regions is -1.87 $\pm$ 0.11. The slope for clouds w/ star-forming regions is steeper than that of clouds w/o star-forming regions, indicating that high mass clouds ($M \geq 10^3\ M_{\odot}$) are dominant on cloud w/ star-forming regions while low mass clouds ($M < 10^3\ M_{\odot}$) are dominant on cloud w/o star-forming regions. This trend is also clearly shown in the number distribution of cloud mass (Figure 5.2).

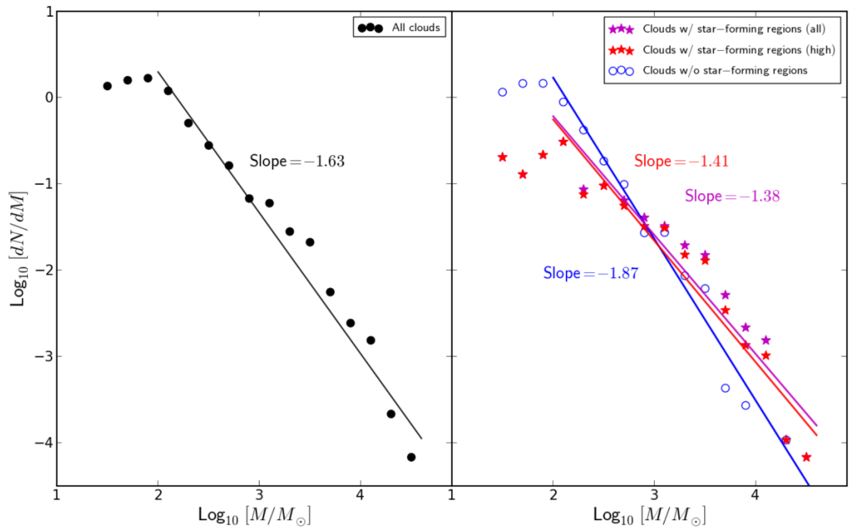

Figure 5.1: *Left*: Cloud mass distribution of whole 466 molecular clouds in the outer Galaxy. The black line shows the fitted slope for clouds with $M \geq 10^2\ M_\odot$. *Right*: Cloud mass distribution of clouds w/ and w/o star-forming regions. Red star marks and purple star marks show clouds w/ star-forming regions (with contamination rate less than 30 %) and all clouds w/ star-forming regions, respectively. Blue open circles show clouds w/o star-forming regions, The red, purple, and blue lines show the fitted power-low curves clouds w/ star-forming regions (with contamination rate less than 30 %), all clouds w/ star-forming regions, and all clouds w/o star-forming regions, respectively, for clouds with $M \geq 10^2\ M_\odot$.

5.1.2 Virial mass - CO mass relation

Figure 5.3 shows the relation between virial mass ($M_{\rm vir}$) and mass derived from CO intensity ($M_{\rm CO}$). Note that this figure shows only 189 clouds out of 466 clouds because velocity width of other 277 clouds are not derived sucessfully in BKP 2003 (see Chapter 3.6.2). Clouds with $M_{\rm CO} \geq 10^3\ M_\odot$ roughly follow the line of $M_{\rm vir} = M_{\rm CO}$, while clouds with $M_{\rm CO} < 10^3\ M_\odot$ are concentrated at the region of $M_{\rm vir} > M_{\rm CO}$. The former group is mainly composed of clouds w/ star-forming regions and the latter group is mainly composed of clouds w/o star-forming regions. This result indicates that almost all clouds w/ star-forming regions are virialized while many of the clouds w/o star-forming regions are not virialized. This trend is also clearly shown in the relation between $M_{\rm vir}/M_{\rm CO}$ ratio and $M_{\rm CO}$ (Figure 5.4) and number distribution of $M_{\rm vir}/M_{\rm CO}$ ratio (Figure 5.5). I checked high mass clouds

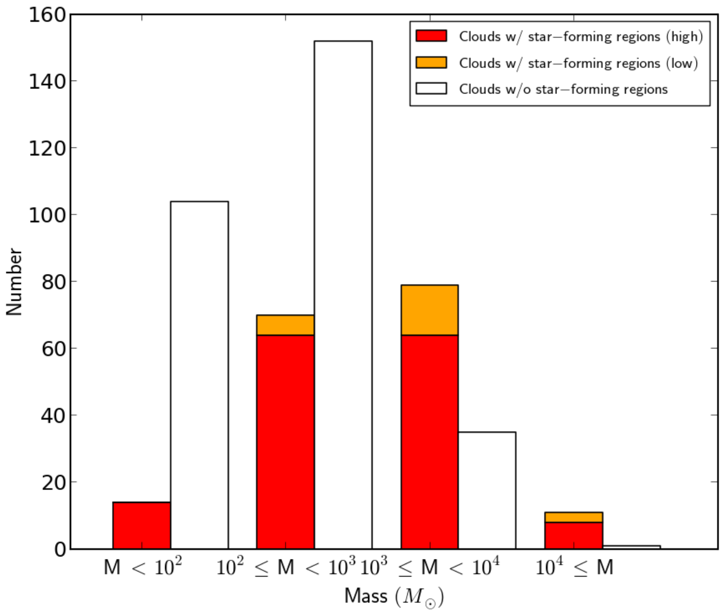

Figure 5.2: Number distribution of cloud mass. The red and orange bars show the number of clouds w/ star-forming regions with contamination rate of $<$ and $\geq$ 30 %, respectively. The white bars show the number of clouds w/o star-forming regions

($\geq 10^3$ $M_\odot$) w/o star-forming region to find that many of them have faint star-forming regions with their absolute luminosities of less than completeness limit. Thus, I suggest that the other virialized clouds w/o star-forming region also have faint star-forming regions, which are too faint to detect with *WISE*.

These results also suggest that mass calibration rate N(H_2)/I_{CO} in the outer Galaxy (R_G = 13.5 – 20 kpc) is similar to that in the solar neighborhood, although the metallicity in the outer Galaxy is less than 1/3 of that in the solar neighborhood. To detect a clearly differences of the mass calibration rate from solar neighborhood, I may need to detect enough number of molecular clouds at $R_G \geq 18$ kpc, where the metallicity is less than 1/10 of that in the solar neighborhood.

5.1.3 Size-mass relation

Figure 5.6 shows the size-mass relation of whole 466 BKP clouds at $R_G \geq 13.5$ kpc. Clouds w/ star-forming regions spread widely at $0.6 \leq r \leq 16$ pc and at 2×10^1 $M_\odot \leq M \leq 2 \times 10^4$ $M_\odot$, while clouds w/o star-forming regions are concentrated at smaller region at $1 \leq r \leq 5$ pc and $2 \times 10 \leq$

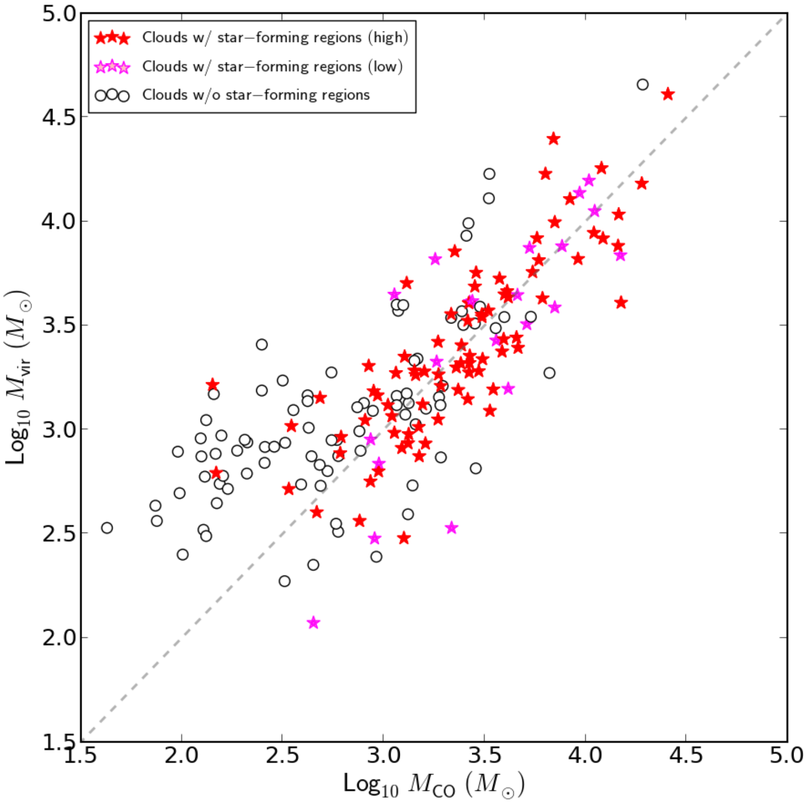

Figure 5.3: Relation between virial mass ($M_{\rm vir}$) and mass derived from CO intensity ($M_{\rm CO}$). Red and magenta star marks show clouds w/ star-forming regions with contamination rate $<$ and $\geq$ 30 %, respectively. Black open circles show clouds w/o star-forming regions. The gray dotted line shows the $M_{\rm vir} = M_{\rm CO}$ relation.

$M \leq 4 \times 10^3\ M_\odot$. This trend is also clearly shown in the number distribution of cloud size (Figure 5.7) cloud mass (Figure 5.2). The least-square fit was performed for clouds with $M \geq 10^2\ M_\odot$. The results are $M = 10^{(1.97\pm0.08)}\ r^{(2.07\pm0.14)}$, $M = 10^{(2.00\pm0.07)}\ r^{(2.06\pm0.13)}$, and $M = 10^{(1.76\pm0.06)}\ r^{(2.06\pm0.13)}$ for clouds w/ star-forming region with contamination rate $<$ 30 %, all clouds w/ star-forming regions, and clouds w/o star-forming region, respectively. This result suggests that cloud mass is basically in proportion to square of cloud size , but clouds w/ star-forming regions are about 2-times more massive than clouds w/o star-forming regions.

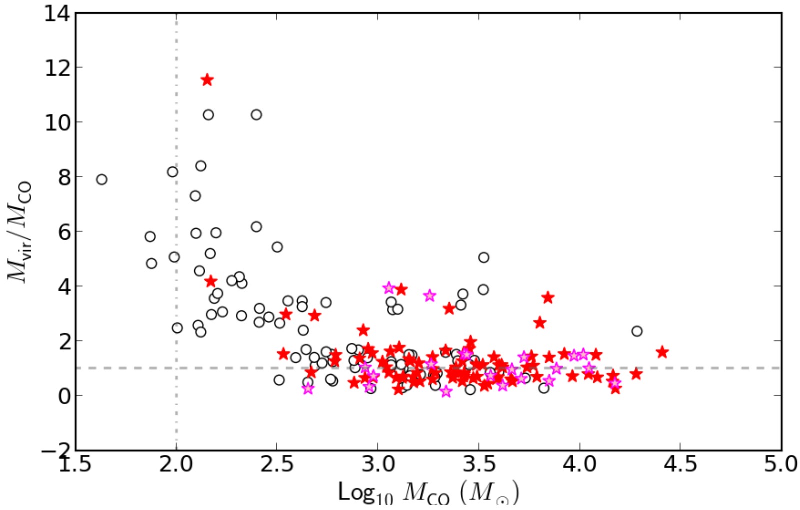

Figure 5.4: Relation between M_{vir}/M_{CO} ratio and M_{CO}. Red and magenta star marks show clouds w/ star-forming regions with contamination rate $<$ and $\geq$ 30 %, respectively. Black open circles show clouds w/o star-forming regions. The gray dotted line shows the relation of M_{vir} = M_{CO}. The gray dot-dashed line shows the detection limit of cloud (100 $M_{\odot}$).

5.1.4 Size-linewidth relation

Figure 5.8 shows the size-linewidth relation of whole 466 BKP clouds at $R_G \geq 13.5$ kpc. Clouds w/ star-forming regions spread widely at $0.6 \leq r \leq 16$ pc and $0.5 \leq \Delta v \leq 5$ km s^{-1}, while clouds w/o star-forming regions are concentrated at slightly smaller region at $1 \leq r \leq 5$ pc and $0.6 \leq \Delta v \leq 3$ km s^{-1}. This trend is also clearly shown in the number distribution of cloud size (Figure 5.7) linewidth (Figure 5.9). Although a broad tendency of larger linewidth for clouds w/ star-forming regions was expected, no obvious difference between clouds w/ star-forming regions and w/o star-forming regions is seen in this plot. I compared the distribution with the least-square fit through the outer Galaxy data from Brand & Wouterloot (1995): Δv = (0.95 $\pm$ 0.08) $r^{0.53\pm0.03}$ to confirmed that linewidth of those clouds is roughly in proportion to the one-half power of cloud size.

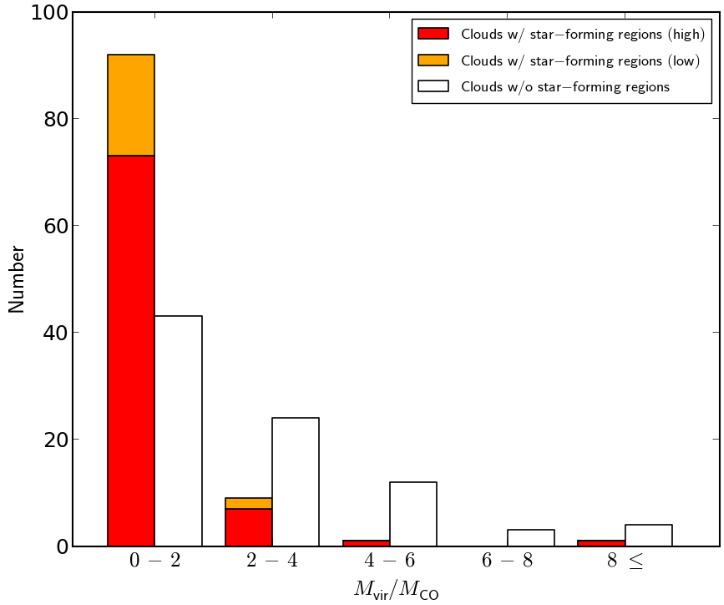

Figure 5.5: Number distribution of $M_{\rm vir}/M_{\rm CO}$ ratio. The red and orange bars show the number of clouds w/ star-forming regions with contamination rate of $<$ and $\geq$ 30 %, respectively. The white bars show the number of clouds w/o star-forming regions

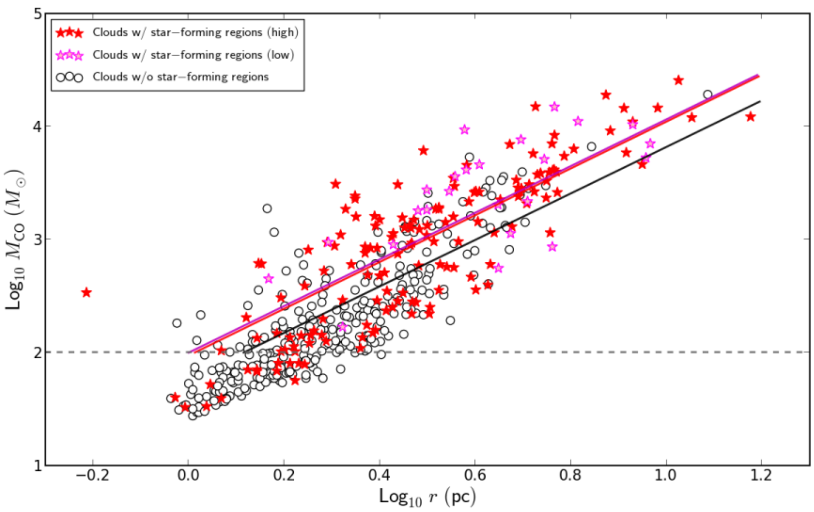

Figure 5.6: Relation between cloud mass ($M_{\rm CO}$) and cloud size (r) of whole BKP clouds at $R_{\rm G} \geq 13.5$ kpc. Red and magenta star marks show clouds w/ star-forming regions with contamination rate $<$ and $\geq$ 30 %, respectively. Black open circles show clouds w/o star-forming regions. The gray dotted line shows the completeness limit of cloud detection ($M_{\rm CO}$ = 10^2 $M_\odot$). The purple, red and black lines show the result of least-square fitting for all clouds w/ star-forming regions, only for clouds w/ star-forming regions with contamination rate $<$ 30 %, and for clouds w/o star-forming regions, respectively, for clouds with $M \geq 10^2$ $M_\odot$. See the detail in the main text.

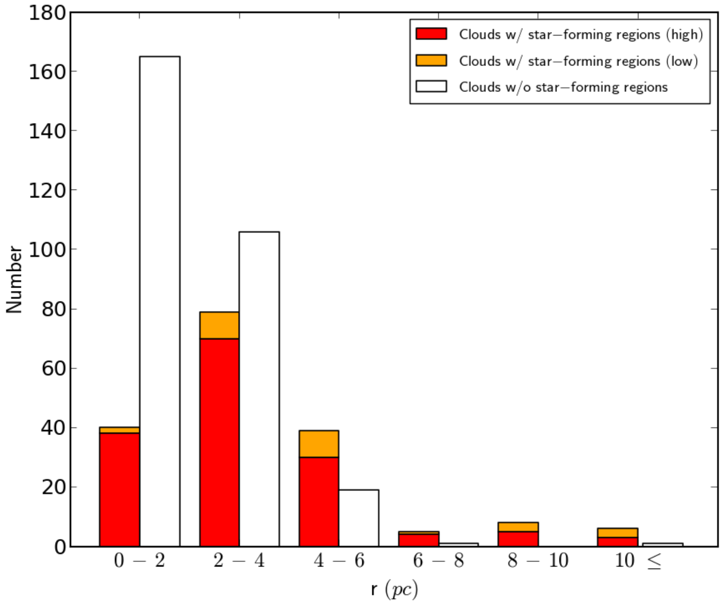

Figure 5.7: Number distribution of cloud size. The red and orange bars show the number of clouds w/ star-forming regions with contamination rate of $<$ and $\geq$ 30 %, respectively. The white bars show the number of clouds w/o star-forming regions

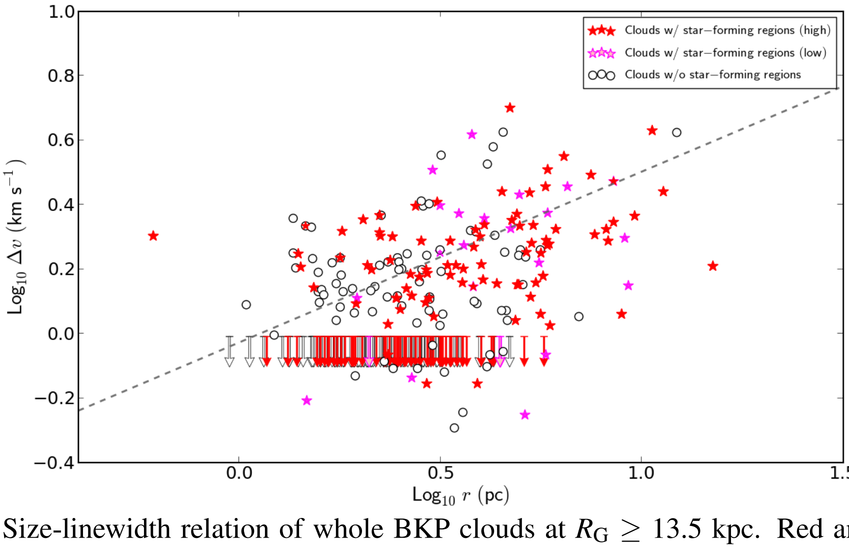

Figure 5.8: Size-linewidth relation of whole BKP clouds at $R_{\mathrm{G}} \geq 13.5$ kpc. Red and magenta star marks show clouds w/ star-forming regions with contamination rate $<$ and $\geq$ 30 %, respectively. Black open circles show clouds w/o star-forming regions. The arrows indicate the upper limit (Δv = 0.98 km s^{-1}) for 277 clouds for which linewidth is not derived in BKP2003. The gray dotted line show least-square fit through the outer Galaxy from Brand & Wouterloot (1995).

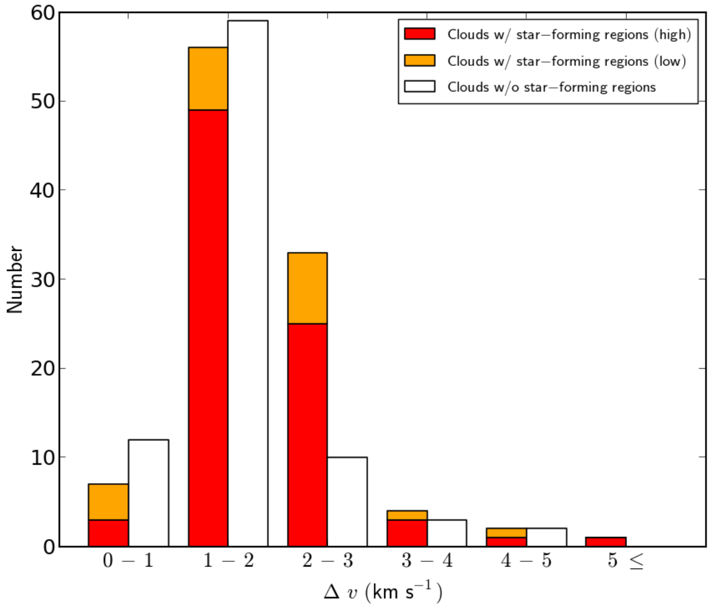

Figure 5.9: Number distribution of cloud linewidth. The red and orange bars show the number of clouds w/ star-forming regions with contamination rate of $<$ and $\geq$ 30 %, respectively. The white bars show the number of clouds w/o star-forming regions

5.2 Star-forming regions

5.2.1 Color vs cloud mass

Figure 5.10 shows the relation between *WISE* colors of newly identified star-forming regions: [3.4] - [4.6], [4.6] - [12], [4.6] - [12], and mass of their parental clouds. The star-forming regions are broadly distributed at 0.5 $\leq$ [3.4] - [4.6] $\leq$ 3, 2$\leq$ [4.6] - [12] $\leq$ 6, and 3 $\leq$ [4.6] - [22] $\leq$ 10. No clear trend of colors with increasing mass of their parental cloud is found in those plot, although some of the individual star-forming regions in massive clouds ($M \geq 10^3 M_\odot$) appear to show very red colors ([4.6] - [12] $>$ 4, [4.6] - [22] $>$ 7) while only few individual star-forming regions in lower mass clouds show such red colors. For massive clouds, reddening of [4.6] - [12] and slight blueing of [3.4] - [4.6] were expected due to PAH emission, which is known to be strong at [12] and [3.4] for massive star-forming regions with OB stars. However, the plot does not show any clear difference between low mass and high mass clouds. Therefore, as a first approximation, the spectral energy distribution (SED) at λ = 3.4 – 22 μm of those star-forming regions appear to be roughly the same within a factor of 10.

5.2.2 Luminosity vs cloud mass

Figure 5.11 shows the relation between monochromatic luminosities of newly identified star-forming regions and mass of their parental clouds. The right panel of Figure 5.11 shows the monochromatic luminosities of individual star-forming regions while the left panel of Figure 5.11 shows the integrated (total) monochromatic luminosities in each cloud. The monochromatic luminosities were calculated from *WISE* magnitudes in the AllWISE catalogue using the conversion with flux zeropoints: $F_{3.4\mu\mathrm{m}}$ = 8.1787 $\times$ 10^{-15}, $F_{4.6\mu\mathrm{m}}$ = 2.4150 $\times$ 10^{-15}, $F_{12\mu\mathrm{m}}$ = 6.5151 $\times$ 10^{-17}, $F_{22\mu\mathrm{m}}$ = 5.0901 $\times$ 10^{-18} W cm^{-2} μm^{-1} (Jarrett et al., 2011), and kinematic distance D of their parental clouds. The right panel of Figure 5.11 indicates the general trend that brighter star-forming regions are associated with more massive clouds. A similar trend is seen also for the integrated luminosities (left panel of Figure 5.11), suggesting those MIR luminosities are good indicator of star-formation activities per individual clouds $for\ all\ four\ bands$.

Figure 5.12 shows monochromatic luminosities of star-forming regions per their parental cloud mass versus mass of their parental clouds. The integrated (total) luminosity per cloud mass decrease with increasing cloud mass. The slope of the relation for [12] and [22] bands appear to be very slightly steeper than those for [3.4] and [4.6] bands. This may suggest that luminosities at [3.4] and [4.6] bands directly reflected flux from stellar clusters/aggregates while those at [12] and [22] bands mainly come from dust emission in star-forming region that may be enhanced by absorbing UV flux from stars in a large solid angle. In the plot of Figure 5.12, the star-forming regions with larger contamination rate ($>$ 30 %) appear to be concentrated at lower-luminosity and higher-cloud mass sides. This is consistent with the fact that some of those *WISE* sources are, in fact, contaminated sources, such as PNe, AGN, and foreground faint YSOs (as discussed in Chapter 3.5.2).

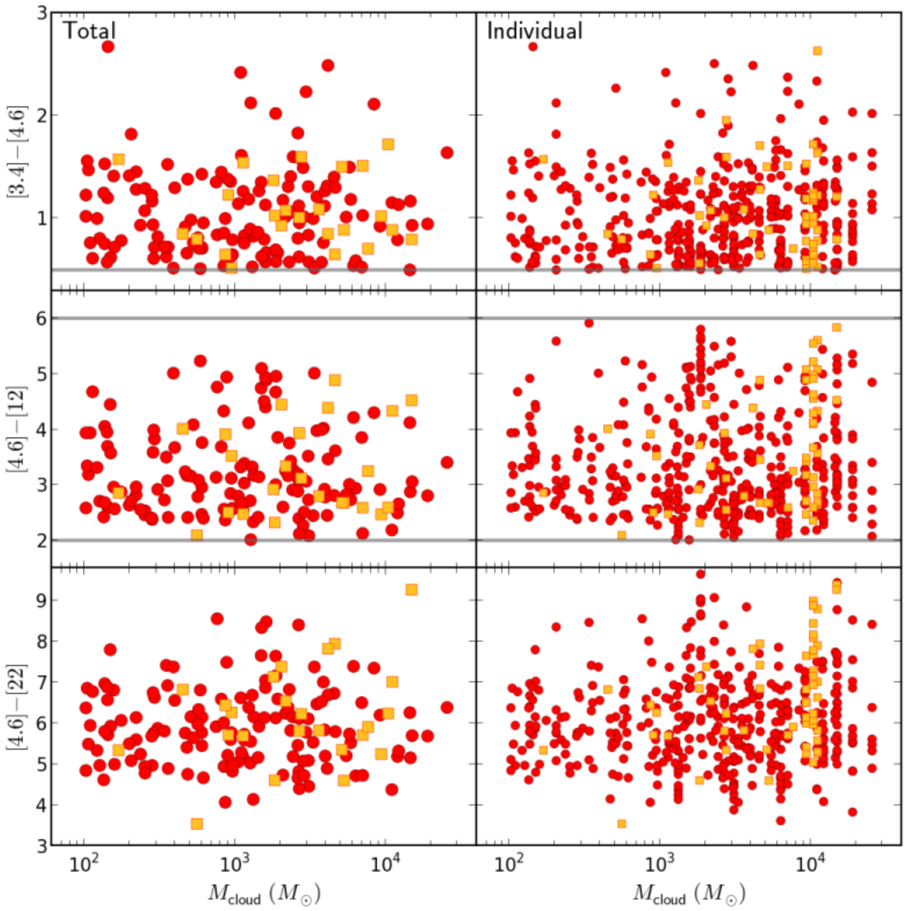

Figure 5.10: *Left*: Integrated (total) colors of newly identified star-forming regions in each cloud (top: [3.4] - [4.6], middle: [4.6] - [12], bottom: [4.6] - [22]) plotted against cloud mass. Red circles and yellow squares show the star-forming regions with contamination rate $<$ and $\geq$ 30 %, respectively. The gray lines show our defined lower limit for selecting distant star-forming regions (see Chapter 3.5.1) division for distant star-forming regions. *Right*: Individual colors of newly identified star-forming regions plotted against cloud mass. Notations are the same as in the left panel.

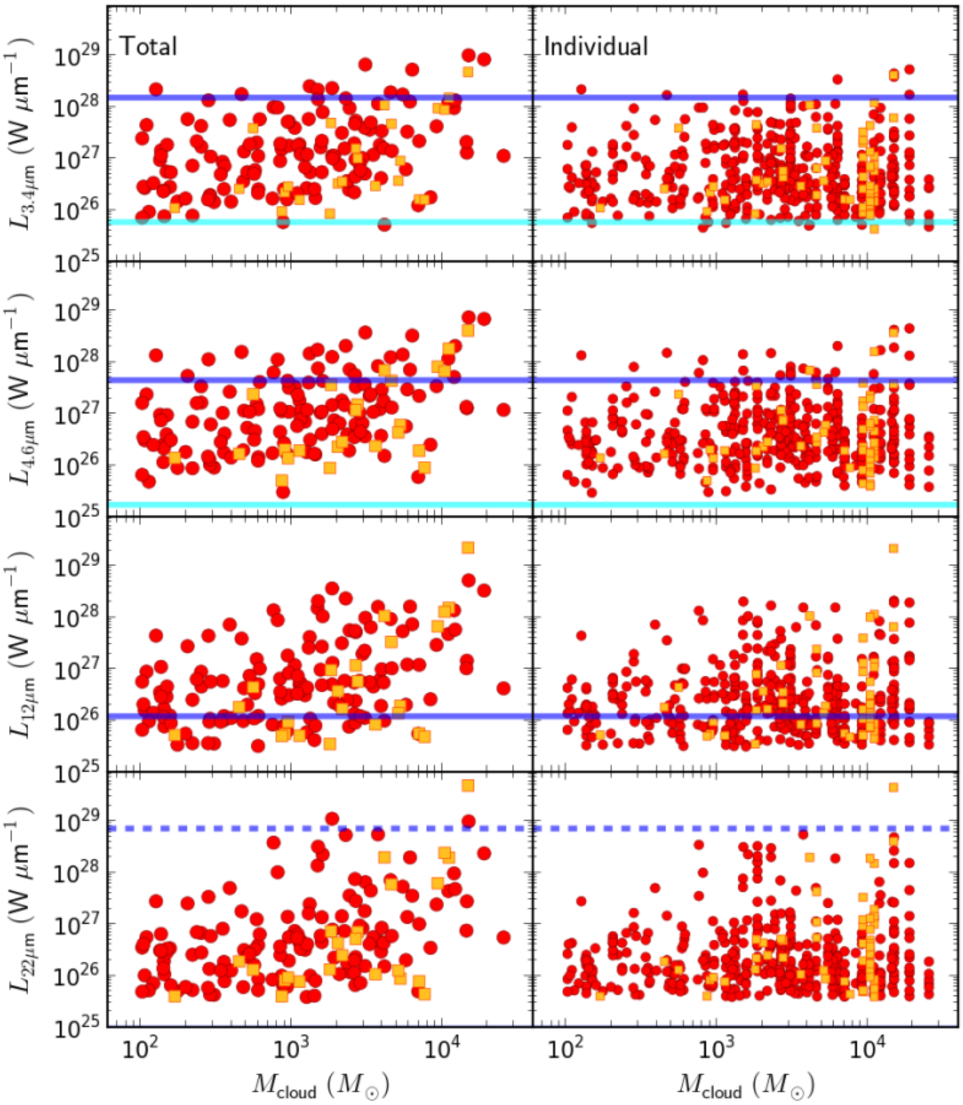

Figure 5.11: *Left*: Integrated (total) monochromatic luminosities of newly identified star-forming regions in each cloud plotted against cloud mass. Red circles and yellow squares show the star-forming regions with contamination rate $<$ and $\geq$ 30 %, respectively. The cyan and blue lines show the flux densities for A0 and B0 stars in the main sequence (see Figure 3.25). The blue dotted lines show the 22 μm flux density for an HII regions ionized by B0 star (see Figure 3.25). *Right*: Individual monochromatic luminosities of newly identified star-forming regions plotted against cloud mass. Notations are the same as in the left panel

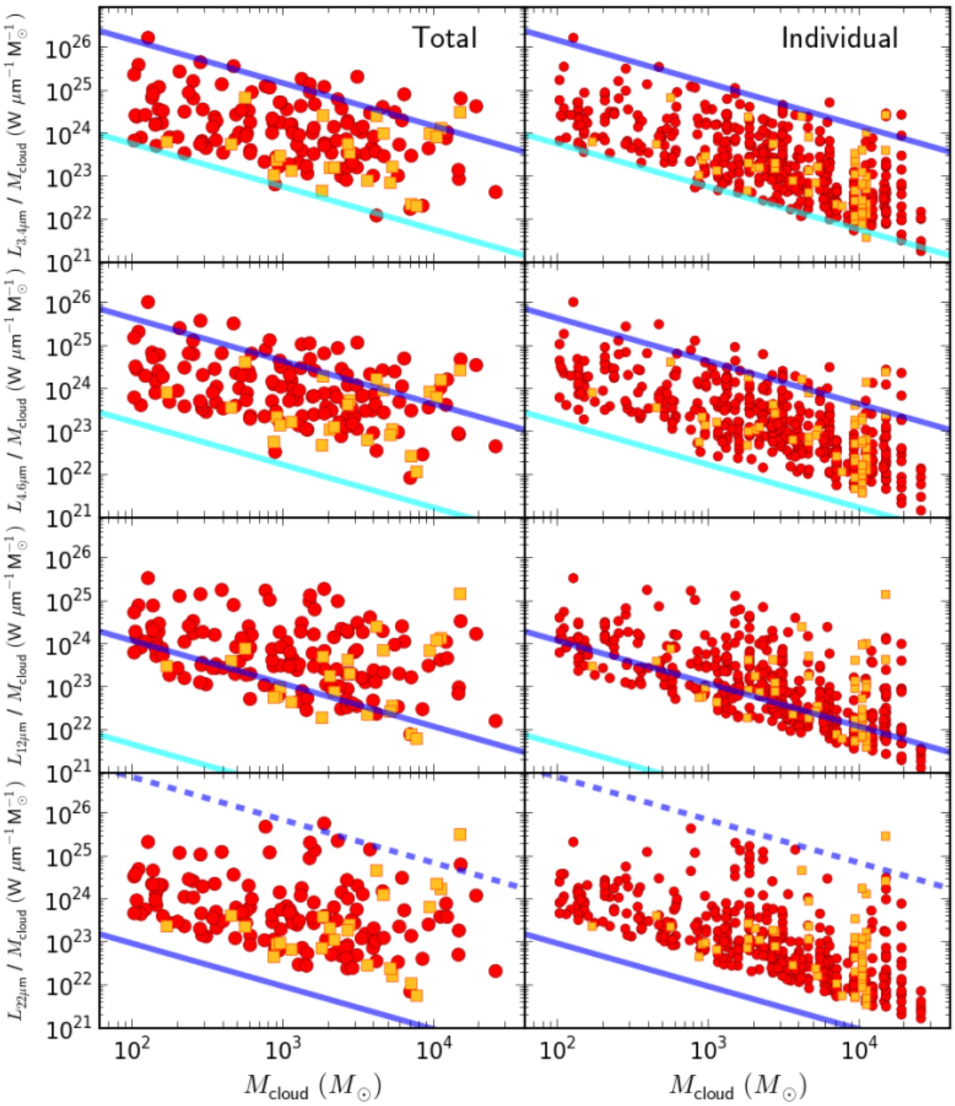

Figure 5.12: *Left*: Integrated (total) monochromatic luminosities of newly identified star-forming regions in each cloud per each cloud mass plotted against cloud mass. Red circles and yellow squares show the star-forming regions with contamination rate $<$ and $\geq$ 30 %, respectively. The cyan and blue lines show the flux densities for A0 and B0 stars in the main sequence (see Figure 3.25). The blue dotted lines show the 22 μm flux density for an HII regions ionized by B0 star (see Figure 3.25). *Right*: Individual monochromatic luminosities of newly identified star-forming regions per each cloud mass plotted against cloud mass. Notations are the same as in the left panel

Chapter 6

Star-formation activity in the outer Galaxy

In Chapter 5, I discuss the properties of molecular clouds and star-forming regions in the outer Galaxy at $R_G \geq 13.5$ kpc using the CO data and the *WISE* MIR data. In this Chapter, I discuss the variation of star-formation activities across Galactocentric radius. At R_G = 20 kpc, HI gas density and metallicity go down to less than half of those at R_G = 13.5 kpc. Thus, using *only newly identified star-forming regions*, the environmental dependance of star-forming activities could be investigated. While star formation consists of two basic processes, converting HI gas to H_2 gas, then converting H_2 gas to stars, my study focuses on the latter processes, as a first step.

6.1 WISE colors vs Galactocentric radius

Figure 6.1 shows *WISE* colors of newly identified star-forming regions: [3.4] - [4.6], [4.6] - [12], [4.6] - [22], versus Galactocentric radius. Star-forming regions are distributed in the color range of 0.5 $\leq$ [3.4] - [4.6] $\leq$ 3, 2$\leq$ [4.6] - [12] $\leq$ 6, and 3 $\leq$ [4.6] - [22] $\leq$ 10. In the right plot for individual star-forming regions, it is found that the very red sources with [3.4] - [4.6] $\geq$ 1.5, [4.6] - [22] $\geq$ 5.0, or [4.6] - [22] $\geq$ 8.0 are mostly present at $R_G < 18$ kpc, and almost all sources in the EOG ($R_G \geq 18$ kpc) are bluer than those colors. Note that this "blueing" toward larger R_G could be due to stochastic effect with the small number of sources at $R_G \geq 18$ kpc, and further study with more surveys is desirable. However, if the blueing trend is a real future, it could be interpreted as a result of no presence of massive star-forming reginos in the EOG. This is consistent with other results in the previous Chapters (see Chapter 5.2.1). Top panel of Figure 4.3 clearly shows that massive clouds are present only in the two arms at $R_{\mathrm{G}} < 18$ kpc (outer Arm, our newly found arm), and the other panels of Figure 4.3 suggest that luminous star-forming regions are not present in the EOG, though statistical argument is necessary. As such, EOG appears to be devoid of massive star-formation, which is consistent with no presence of Hα emission, which traces massive star-forming regions, in extra-galactic XUV disk (e.g. Thilker et al., 2005, see Figure 1.6).

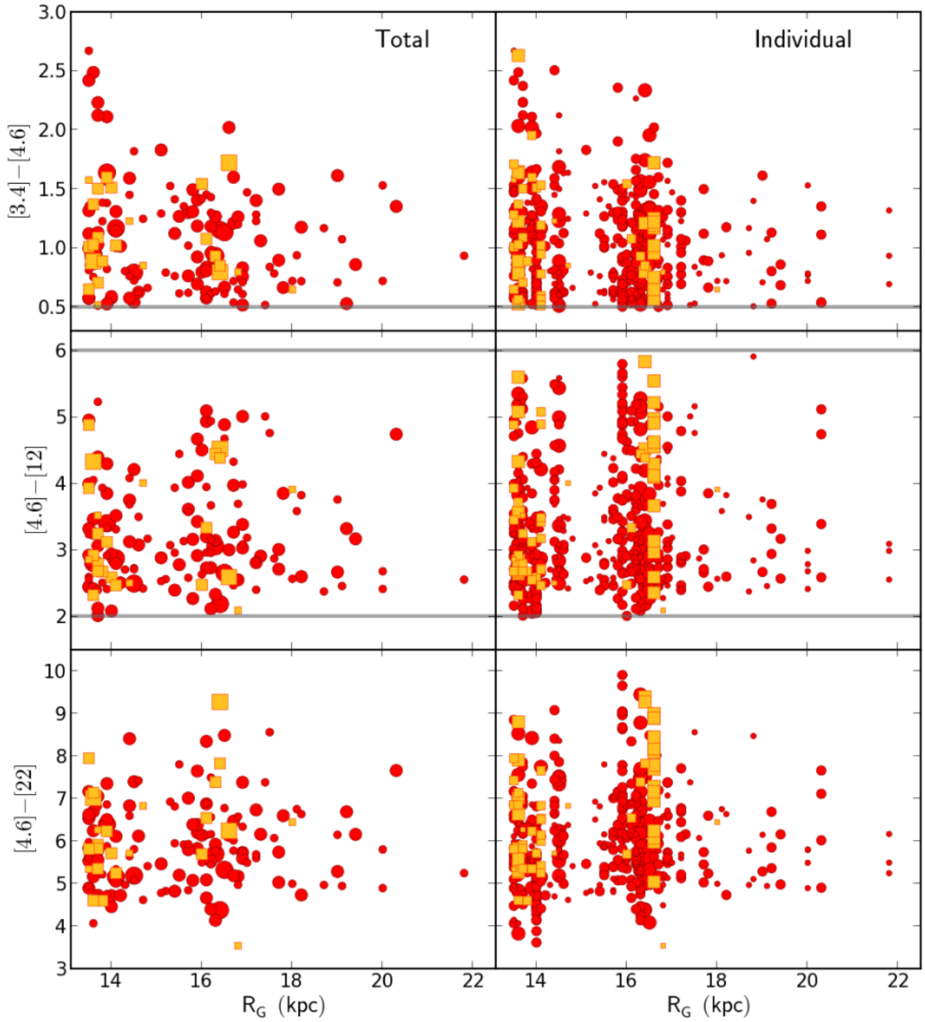

Figure 6.1: *Left*: Integrated (total) colors of newly identified star-forming regions in each cloud (top: [3.4] - [4.6], middle: [4.6] - [12], bottom: [4.6] - [22]) plotted against Galactocentric radius. Red circles and yellow squares show the star-forming regions with contamination rate $<$ and $\geq$ 30 %, respectively. The size of these markers indicate the mass of their parental molecular clouds (small: $10^2\ M_\odot \leq M_{\rm cloud} < 10^3\ M_\odot$, middle: $10^3\ M_\odot \leq M_{\rm cloud} < 10^4\ M_\odot$, large: $10^4\ M_\odot \leq M_{\rm cloud}$). The gray lines show our defined lower limit for selecting distant star-forming regions (see Chapter 3.5.1). *Right*: Colors of newly identified identified star-forming regions plotted against Galactocentric radius. Notations are the same as in the left panel.

6.2 Star formation efficiency

Next, I discuss the SFE per molecular clouds using two indices constructed only from the *WISE* data: (1) number ratio of star-forming molecular clouds to all molecular clouds, (2) monochromatic luminosities of star-forming regions per their parental cloud mass. Although these indices do not any conclusive ones, they could provide a useful measure of SFE per molecular clouds.

6.2.1 Index 1. Number ratio of star-forming molecular clouds

First index is the number ratio of star-forming molecular clouds to all molecular clouds. It is the simplest index of SFE averaged over all kinds of parameters (mass, age, etc), and the statistical number of star-forming regions in our data set enables this study for the first time. Lower plot of Figure 6.2 shows the number of clouds w/ and w/o star-forming regions versus Galactocentric radius, while upper plot shows the R_G variation of the number ratio of clouds w/ star-forming regions to all clouds for clouds with $M_{\rm cloud} \geq 10^2\ M_\odot$. The ratio is found to be roughly constant at 40 – 50 % through R_G = 13.5 – 22 kpc. Although the ratio may appear to increase slightly with increasing R_G, I could only safely say that the ratio dose not decrease in view of the statistics at larger R_G.

Figure 6.3 shows the same plot as Figure 6.2 but in three cloud mass ranges: $10^2\ M_\odot \leq M_{\rm cloud} < 10^3\ M_\odot$ (left), $10^3\ M_\odot \leq M_{\rm cloud} < 10^4\ M_\odot$ (middle), and $10^4\ M_\odot \leq M_{\rm cloud}$ (right). The ratios are found to be roughly constant within the uncertainty through R_G = 13.5 – 22 kpc, for all three cases, but the ratio itself increases with cloud mass from 20 – 40 % ($M_{\rm cloud} < 10^3\ M_\odot$) to 60 – 100 % ($M_{\rm cloud} \geq 10^3\ M_\odot$). This result indicates that almost all massive clouds with $\geq 10^3\ M_\odot$ have star-forming regions (see Chapter 5.1). It is also found that the ratio does not show any clear difference between arm (R_G = 14, 16 – 17 kpc) and inter arm ($R_G \sim 15$ and $R_G \geq 18$ kpc) regions.

In order to check the effect of detection limit on the SFE index, I examine the number ratios a number of completeness-limit values of *WISE* sources and clouds. First, I compared the ratios considering both completeness limits (*WISE* sources and clouds) with those considering only the completeness limit of clouds (Upper plot of Figure 6.4). For the latter case, the ratio at $R_G \leq 16$ kpc increases and appears to be more constant through R_G = 13.5 – 22 kpc. This result may have been caused by detection of low-brightness sources at $R_G \leq 16$ kpc (lower than A0 stars; see Figure 3.24 and 3.25). Next, I compared the ratios for two completeness limits of cloud mass: 100 $M_\odot$ and 200

$M\odot$ (Lower plot of Figure 6.4). The ratio through R_G = 13.5 – 22 kpc increases with increasing the completeness limit of cloud mass, simply indicating that the ratio becomes larger with increasing the cloud mass. Those results are also clearly shown in Figures 6.5 and 6.6, which show the number ratios and number of the clouds, respectively, in four cases: a) considering both completeness limits of *WISE* sources and clouds with 100 $M_\odot$, b) considering both completeness limits of *WISE* sources and clouds with 200 $M_\odot$, c) only considering the completeness limit of clouds with 100 $M_\odot$, and d) only considering the completeness limit of clouds with 200 $M_\odot$. Thus, I confirmed that the decreasing trend of ratio with increasing R_G is not present in any cases.

6.2.2 Index 2. Luminosity per cloud mass

Another index is "specific luminosity", which is defined as IR luminosity per cloud mass. In past studies, star-formation activities are measured by the ratio of MIR – FIR luminosity (λ = 12 – 100 μm from *IRAS* data) to molecular cloud mass (e.g. Snell et al., 2002). In this thesis, I measured the star-formation activities with the ratio of MIR luminosity to molecular cloud mass by making use of the *WISE* data. Although bolometric luminosity should be ultimately used for estimating integrated luminosity per cloud, I use monochromatic luminosities because 1) SED at λ = 3.4 – 22 μm of star-forming regions appear to be almost same (see Chapter 5.2.1 and 6.1), 2) monochromatic luminosity, in particular, at 3 – 5 μm could be best index of luminosity of star clusters/stellar aggregates since this wavelength range is not contaminated by dust emission as MIR ($\lambda \geq 10$ μm), yet the extinction is much less effective compared to shorter NIR.

The left plot of Figure 6.7 shows the variation of the monochromatic integrated (total) luminosities of star-forming regions per their parental cloud mass against Galactocentric radius. The values of specific luminosities spread widely in 4 to 5 orders: $10^{22} \leq L_{3.4\mu\mathrm{m}}/M_{\mathrm{cloud}} \leq 10^{26}$ W μm^{-1} $M_\odot^{-1}$, $10^{22} \leq L_{4.6\mu\mathrm{m}}/M_{\mathrm{cloud}} \leq 10^{26}$ W μm^{-1} $M_\odot^{-1}$, $10^{21} \leq L_{12\mu\mathrm{m}}/M_{\mathrm{cloud}} \leq 10^{26}$ W μm^{-1} $M_\odot^{-1}$, $10^{21} \leq L_{22\mu\mathrm{m}}/M_{\mathrm{cloud}} \leq 10^{26}$ W μm^{-1} $M_\odot^{-1}$. However, the luminosity distribution appears to be similar at any R_G, which is partly represented by the constancy of maximum value of L/M.

6.2.3 Environmental dependance of star formation efficiency

In previous sub-sections, I found that two kinds of SFE-indices do not significantly change through R_{G} = 13.5 – 22 kpc, in which a large variation of environment is anticipated. Interestingly no variation is found between arm and interarm regions. It looks like as if star formation property smoothly continues through all the spiral arms. The slightly increasing trend at larger R_{G} found only for the SFE-index 1 could be interpreted as the result of the presence of dark H_2 clouds, which cannot be detected by CO (e.g. Wolfire et al., 2010): they are known to increase with decreasing metallicity, in other words, increasing R_{G}. These results suggest that the star-formation activity per molecular cloud does not change significantly with environments, such as metallicity and arm/inter-arm density, and rather appears to be universal in terms of SFE.

The above results also suggest that the low SFE, converting HI to stars, found in the outer regions of disk galaxies (e.g. Bigiel et al., 2010), simply reflects the smaller number of molecular clouds in such regions. In the inner region of disk galaxies, where the ISM is dominant by H_2 molecular gas, SFE is suggested to depend on only the amount of H_2 gas, but not of HI gas (see Chapter 1.2). Our results imply that the SFE in the outer region of galaxies, where the ISM is dominant by HI gas, also simply depends only on the amount of H_2 gas as in the inner region of the galaxies.

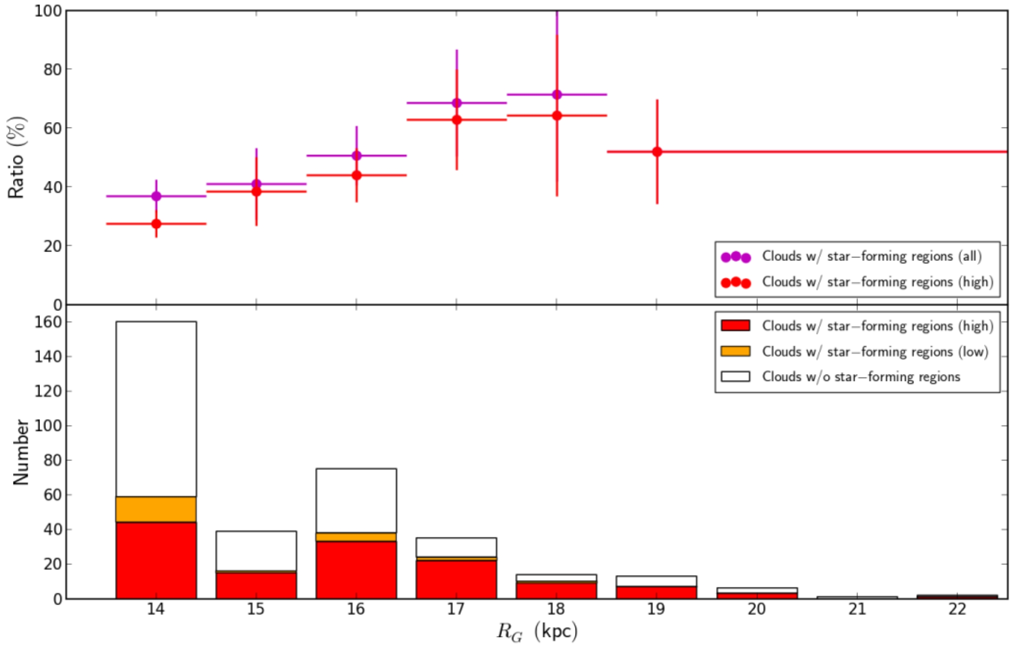

Figure 6.2: *Top*: Galactocentric variation of the ratio of clouds w/ star-forming regions to the total number of molecular clouds for clouds with $M_{\rm cloud} \geq 10^2\ M_\odot$. The red and purple marks show the ratio for clouds w/ star-forming regions with contamination rate less than 30 % and all clouds w/ star-forming regions, respectively. The error bars represent Poisson errors (1 σ), and the error bars of $R_{\rm G}$ indicate the range of $R_{\rm G}$. *Bottom*: Galactocentric variation of the number of clouds w/ star-forming regions for clouds with $M_{\rm cloud} \geq 10^2\ M_\odot$. The red and orange bars show the number of clouds w/ star-forming regions with contamination rate of $<$ and $\geq$ 30 %, respectively. The white bars show the number of clouds w/o star-forming regions.

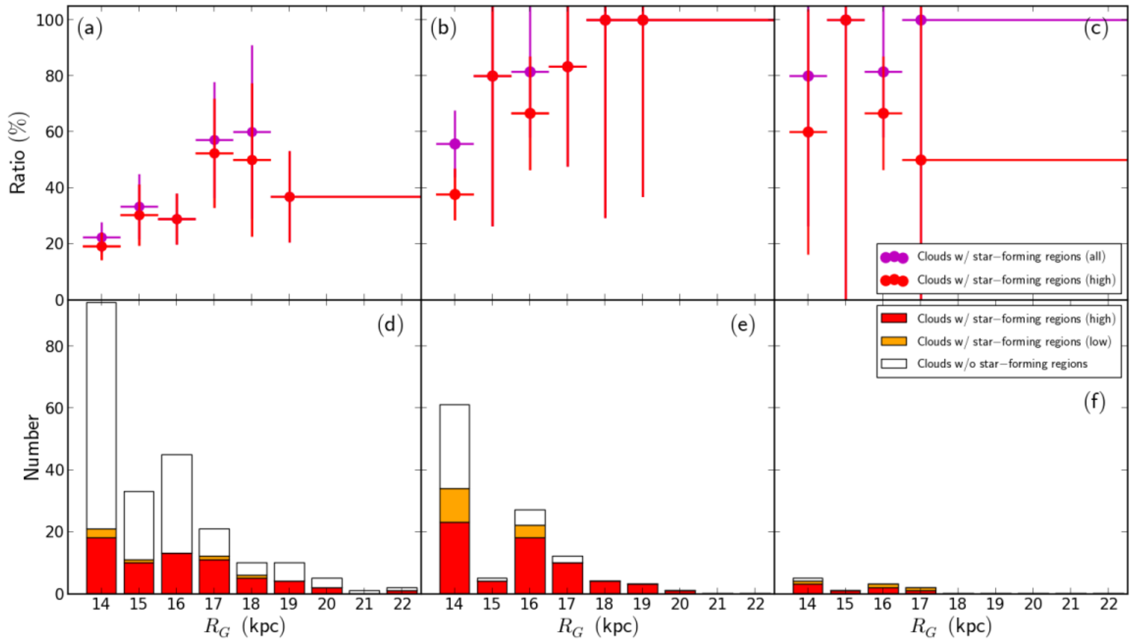

Figure 6.3: (a) Galactocentric variation of the ratio of clouds w/ star-forming regions to the total number of molecular clouds with $10^2\ M_\odot \leq M_{\rm cloud} < 10^3\ M_\odot$. The red and purple marks show the ratio for clouds w/ star-forming regions with contamination rate less than 30 % and all clouds w/ star-forming regions, respectively. The error bars represent Poisson errors (1 σ), and the error bars of $R_{\rm G}$ indicate the range of $R_{\rm G}$. (b) Same as (a), but for clouds with $10^3\ M_\odot \leq M_{\rm cloud} < 10^4\ M_\odot$. (c) Same as (a), but for clouds with $10^4\ M_\odot \leq M_{\rm cloud}$. (d) Galactocentric variation of the number of clouds w/ star-forming regions for clouds with $10^2\ M_\odot \leq M_{\rm cloud} < 10^3\ M_\odot$. The red and orange bars show the number of clouds w/ star-forming regions with contamination rate of $<$ and $\geq$ 30 %, respectively. The white bars show the number of clouds w/o star-forming regions. (e) Same as (d), but for clouds with $10^3\ M_\odot \leq M_{\rm cloud} < 10^4\ M_\odot$. (f) Same as (d), but for clouds with $10^4\ M_\odot \leq M_{\rm cloud}$.

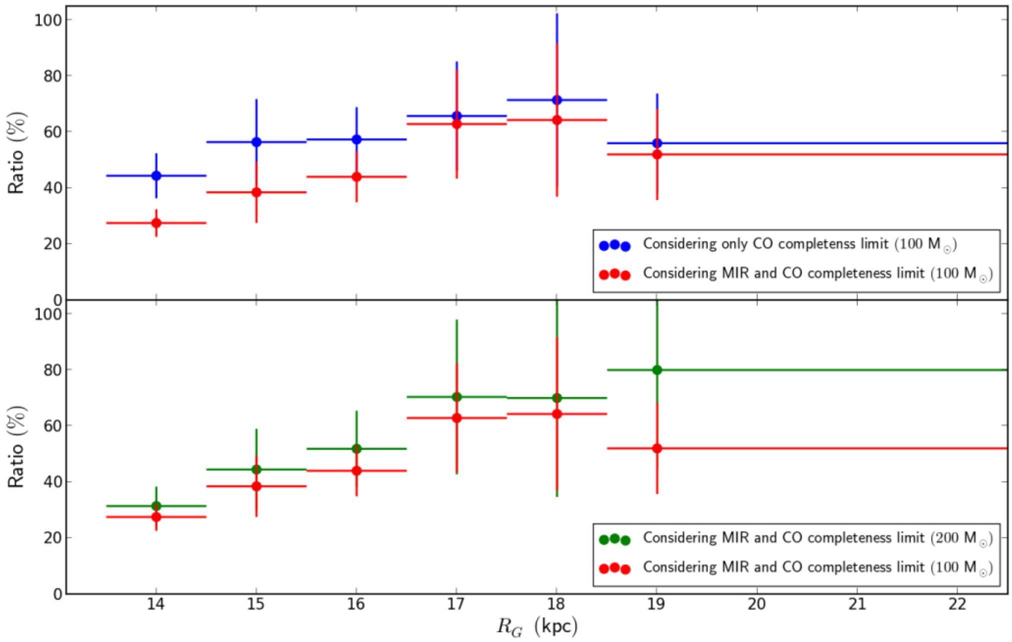

Figure 6.4: Galactocentric variation of ratio of the number of clouds w/ star-forming regions to the total number of clouds with contamination rate less than 30 %. *Top* The red and blue marks show the ratio considering both completeness limit (*WISE* MIR sources and clouds) and only the completeness limit of clouds (100 $M_\odot$), respectively. *Bottom* The red and green marks show the ratio considering both completeness limit of *WISE* MIR sources and clouds (100 $M_\odot$) and both completeness limit of *WISE* MIR sources and clouds (200 $M_\odot$), respectively.

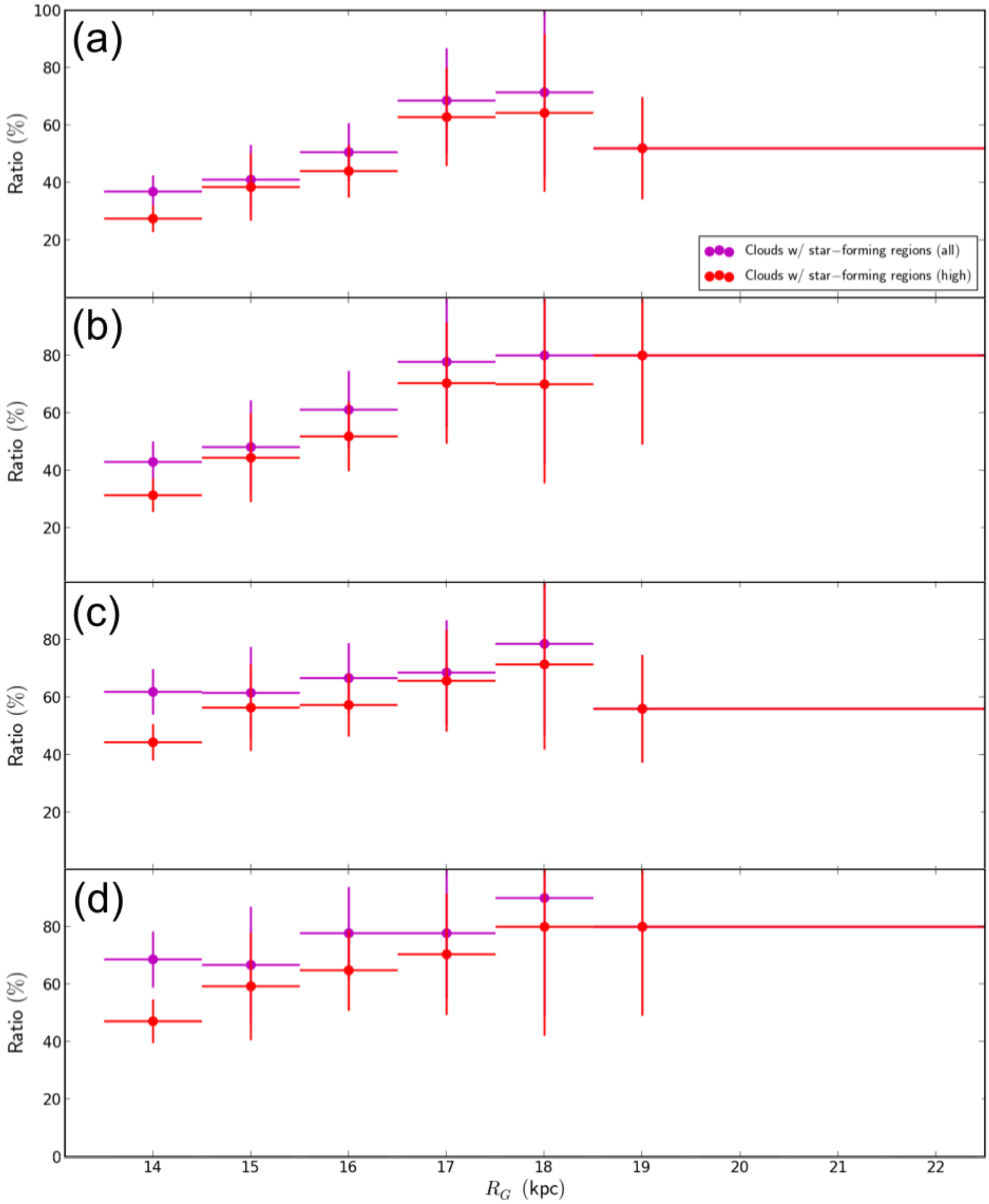

Figure 6.5: Galactocentric variation of ratios of the number of clouds w/ star-forming regions to the total number of clouds in four cases: (a) considering both completeness limit of *WISE* MIR sources and clouds with 100 $M_{\odot}$, (b) considering both completeness limit of *WISE* MIR sources and clouds with 200 $M_{\odot}$, (c) only considering the completeness limit of clouds with 100 $M_{\odot}$, and (b) only considering the completeness limit of clouds with 200 $M_{\odot}$.

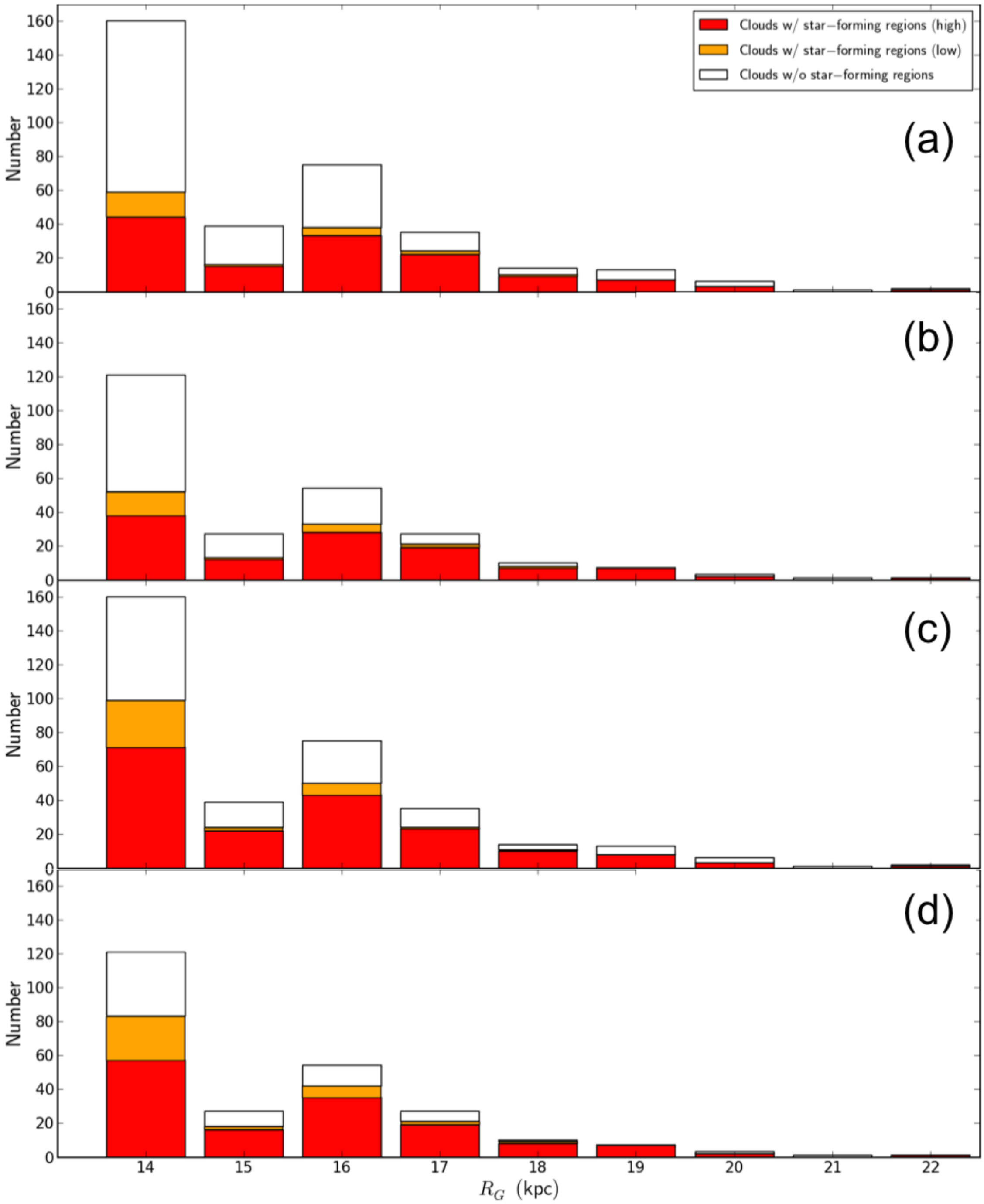

Figure 6.6: Galactocentric variation of number of clouds w/ star-forming regions to the total number of clouds in four cases: (a) considering both completeness limit of *WISE* MIR sources and clouds with 100 $M_{\odot}$, (b) considering both completeness limit of *WISE* MIR sources and clouds with 200 $M_{\odot}$, (c) only considering the completeness limit of clouds with 100 $M_{\odot}$, and (b) only considering the completeness limit of clouds with 200 $M_{\odot}$.

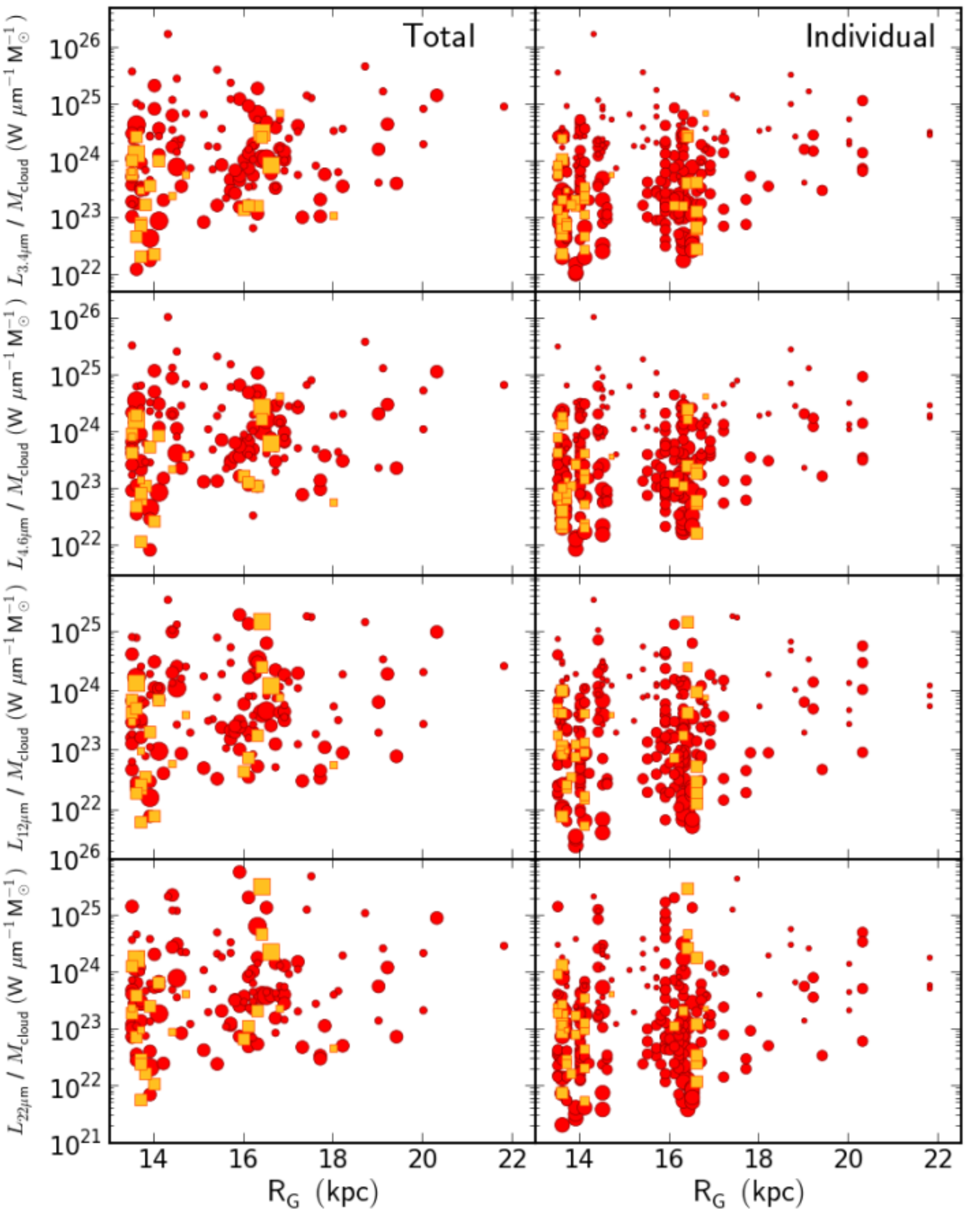

Figure 6.7: *Left*: The integrated (total) monochromatic luminosities of star-forming regions per cloud mass plotted against Galactocentric radius. Red circles and yellow square show the star-forming regions with contamination rate $<$ and $\geq$ 30 %, respectively. *Right*: The monochromatic luminosities of individual star-forming regions per their parental cloud mass plotted against Galactocentric radius. Notations are the same as in the left panel.

Chapter 7

Summary

In this thesis, I presented a study of global properties of star formation in the outer Galaxy ($R_G \geq$ 13.5 kpc). The outer Galaxy has a very different environment from the solar neighborhood with a much lower gas density (e.g. Wolfire et al., 2003) and lower metallicity (e.g. Smartt & Rolleston, 1997). Such an extreme environment is considered to have similar characteristics as that in the early phase of the formation of the Galaxy, in particular, in the Thick disk formation (Ferguson et al., 1998; Kobayashi et al., 2008). The outer Galaxy serves as an excellent laboratory for studying star-forming processes in low-gas density and low-metallicity environments also because there is no complex star formation history and not much large number of field stars as in the inner Galaxy.

As a pilot study of star-formation in the outer Galaxy, I studied the very distant molecular cloud Digel Cloud 1 (R_G = 22 kpc; Digel et al., 1994) with ^{12}CO(1-0) lines using the Nobeyama 45 m radio telescope as well as with NIR wavelength using the Subaru 8.2 m telescope. The main results are as follows:

1. With NIR imaging and ^{12}CO mapping that covers the entire Cloud 1, I detected two young embedded clusters located in two dense cores.

2. Using properties of the K-band (2.2 μm) luminosity function (KLF) and disk fraction, I have estimated the age of the clusters to be < 1 Myr.

3. Using properties of the KLF and the above age, I have estimated the photometric distance of the clusters to be $D \geq 12$ kpc ($R_G \geq 19$ kpc), which is consistent with the kinematic distance.

4. Based on previous research on Complex H and the latest HI survey data I suggest that the impact of HVC onto the outer part of the Galactic disk could be major trigger of Cloud 1 formation as well as star formation in Cloud 1.

Through this study, I confirmed that we can investigate star-formation process at molecular-cloud scale ($\sim$ pc scale), same as in the solar neighborhood, even in such very distant star-forming regions using large telescopes and large-scale survey data.

To clarify the global nature of star-formation activity in the outer Galaxy, I developed an identification criteria of star-forming regions with MIR all-sky survey data by *WISE*, which can effectively pick up star-forming regions by combining with CO survey data in the outer Galaxy. Using the criteria, I searched for star-forming regions within the area of 320 deg^2 to identify about 711 new star-forming regions, which enable statistical studies of star-formation activity in the outer Galaxy for the first time. Using these newly identified star-forming regions, I studied distribution and properties of star-formation in the outer Galaxy. The main results are as follows:

1. From the distribution of newly discovered star-forming regions, I confirmed perhaps a new arm structure beyond the outer arm.

2. Using the properties of molecular clouds w/ and w/o star-forming regions, I found clear difference between them, such as mass distribution, size, and velocity width.

Using newly identified star-forming regions, I study the variation of star-formation activities across the Galactocentric radius. At R_G = 20 kpc, HI gas density and metallicity go down to less than half of those at R_G = 13.5 kpc. Thus, using only newly identified starforming regions, the environmental dependence of star-forming activities can be investigated. While star formation consists of two basic processes, converting HI gas to H_2 gas, then converting H_2 gas to stars, this study focuses on the latter processes, as a first step to explore this unexploited region. The main result as follows:

1. Using the variation of *WISE* color and magnitude as well as cloud mass spectrum with the Galactocentric radius, I found that massive star-forming regions are present only at $R_G < 18$ kpc.

2. Using two constructed SFE-indices, 1) the number ratio of clouds with star-forming region to all

clouds, 2) MIR specific luminosity per cloud mass, I found that these indices do not significantly change at R_{G} = 13.5 – 20 kpc.

These results suggest that the star formation processes inside molecular cloud do not heavily depend on the environmental parameters, such as metallicity, thus the low SFE found in the outer regions of disk galaxies (e.g. Bigiel et al., 2010) simply reflect the lower number of molecular clouds in such region. SFE in the inner galaxy, where the ISM is dominated by H_2 molecular gas, is suggested to depend only on the amount of H_2 gas, but not of HI gas (e.g. Schruba et al., 2011). In this thesis, I found SFE in the outer Galaxy, where the ISM is dominated by HI gas, may also simply depend on the amount of H_2 gas as in the inner Galaxy.

ACKNOWLWDGEMENT

First of all, I would like to express my best gratitude to my supervisor, Dr. Naoto Kobayashi (University of Tokyo) for encouraging me through my graduate course. He introduced me to infrared astronomy. I would like to thank him for giving me a lot of opportunities and advices to make researches of many interesting topics. Without his supervision and constant help, I could not finish my research.

I would like to thank Dr. Masao Saito (NAOJ) for his tremendous support of my research, especially in terms of radio astronomy. In spite of his tight schedule, he taught me a lot of important things. I also thank him for giving me great opportunities to see foreign researches. I am also very grateful to Dr. Chikako Yasui (University of Tokyo) for giving me valuable advice on my research. She taught me a lot about analyzing method of near-infrared data. I am grateful to Satoshi Hamano (Kyoto Sangyo University), who always help when I have trouble in my research. His advises accurately point out my problems, and let my works proceed. I also would like to thank Dr. Alan T. Tokunaga (University of Hawaii) for his warm encouragement throughout my study. He gave many insightful comments on my thesis work. I am greatly benefited from wide-ranging discussion with Dr. Noriyuki Matsunaga (University of Tokyo) and Dr. Takuji Tsujimoto (NAOJ). I am also grateful to my colleagues, Mr. Kei Fukue and Ms. Haruka Takahashi (University of Tokyo).

During my graduate course, I visited Kiso Observatory many times for study and observations. I am really grateful to all staff of Kiso Observatory for their kind help and encouragement. I also visited many times at NAOJ Nobeyama Radio Observatory for study and observations. I would like to thank all of the student and staff for their valuable comments on my research and kindly support of my observations. I also stayed Chile at three months for study, and thank all staff of Joint ALMA Observatory and NAOJ Chile Observatory for their kind hospitality during my stay.

Finally, I would like to express my gratitude to my parents, who allow me to go on the graduate school and continuously support me both mentally and financially. I also thanks my sisters for their support and encouragement throughout my study.

This thesis has been reviewed by Dr. Kotaro Kohno, Dr. Motohide Tamura, Dr. Hirokazu Kataza (University of Tokyo), Dr. Sachiko Onodera (Meisei University), and Dr. Katsuya Okoshi (Tokyo University of Science) and has their endorsement.

Bibliography

Adams, E. A. K., Giovanelli, R., & Haynes, M. P. 2013, ApJ, 768, 77

Anderson, L. D., Bania, T. M., Balser, D. S., et al. 2014, ApJS, 212, 1

Anderson, L. D., Armentrout, W. P., Johnstone, B. M., et al. 2015, ApJS, 221, 26

Amôres, E. B., & Lépine, J. R. D. 2005, AJ, 130, 659

Ballesteros-Paredes, J., Klessen, R. S., Mac Low, M.-M., & Vazquez-Semadeni, E. 2007, in Protostars and Planets V, ed. B. Reipurth D. Jewitt, & K. Keil (Tucson, AZ: Univ. Arizona Press), 63

Beichman, C. A., Neugebauer, G., Habing, H. J., Clegg, P. E., & Chester, T. J. 1988, Infrared astronomical satellite (IRAS) catalogs and atlases. Volume 1: Explanatory supplement, 1,

Benjamin, R. A., Churchwell, E., Babler, B. L., et al. 2003, PASP, 115, 953

Bessell, M. S., & Brett, J. M. 1988, PASP, 100, 1134

Bigiel, F., Leroy, A., Walter, F., et al. 2008, AJ, 136, 2846

Bigiel, F., Leroy, A., Walter, F., et al. 2010, AJ, 140, 1194

Blitz, L., Spergel, D. N., Teuben, P. J., Hartmann, D., & Burton, W. B. 1999, ApJ, 514, 818

Bolatto, A. D., Leroy, A. K., Jameson, K., et al. 2011, ApJ, 741, 12

Bolatto, A. D., Wolfire, M., & Leroy, A. K. 2013, ARA&A, 51, 207

Brand, J., & Blitz, L. 1993, A&A, 275, 67

Brand, J., & Wouterloot, J. G. A. 1994, A&AS, 103, 503

Brand, J., & Wouterloot, J. G. A. 1995, A&A, 303, 851

Brand, J., & Wouterloot, J. G. A. 2007, A&A, 464, 909

Brunt, C. M., Ontkean, J., & Knee, L. B. G. 2000, Bulletin of the American Astronomical Society, 197, 508

Brunt, C. M., Kerton, C. R., & Pomerleau, C. 2003, ApJS, 144, 47

Buser, R. 2000, Science, 287, 69

Churchwell, E., Babler, B. L., Meade, M. R., et al. 2009, PASP, 121, 213

Comeron, F., & Torra, J. 1992, A&A, 261, 94

Cox, A. N. 2000, Allen's Astrophysical Quantities,

Crosthwaite, L. P., Turner, J. L., Buchholz, L., Ho, P. T. P., & Martin, R. N. 2002, AJ, 123, 1892

Daddi, E., Elbaz, D., Walter, F., et al. 2010, ApJ, 714, L118

Davenport, J. R. A., Ivezić, Ž., Becker, A. C., et al. 2014, MNRAS, 440, 3430

da Cunha, E., Charlot, S., & Elbaz, D. 2008, MNRAS, 388, 1595

de Geus, E. J., Vogel, S. N., Digel, S. W., & Gruendl, R. A. 1993, ApJL, 413, L97

Dekel, A., Birnboim, Y., Engel, G., et al. 2009, Nature, 457, 451

Dickman, R. L. 1978, ApJS, 37, 407

Digel, S., de Geus, E., & Thaddeus, P. 1994, ApJ, 422, 92

Drew, J. E., Greimel, R., Irwin, M. J., et al. 2005, MNRAS, 362, 753

Elmegreen, B. G. 1998, in ASP Conf. Ser. 148, Origins, ed. C. E. Woodward, J. Michael Shull, & H. A. Thronson, Jr. (San Francisco, CA: ASP), 150

Elmegreen, B. G. 2011, EAS Publications Series, Vol. 51, 45

Elmegreen, B. G. 2012, in IAU Symp. 284, The Spectral Energy Distribution of Galatxies, ed. R. J. Tuffs & C. C. Popescu (Cambridge: Cambridge Univ. Press), 317

Emerson, D. T., & Graeve, R. 1988, A&A, 190, 353

Fabinsky, B. 2006, Proc. SPIE, 6271, 627111

Ferguson, A. M. N., Gallagher, J. S., & Wyse, R. F. G. 1998, AJ, 116, 673

Fich, M., Dahl, G. P., & Treffers, R. R. 1990, AJ, 99, 622

Fox, A. J., Wakker, B. P., Barger, K. A., et al. 2014, ApJ, 787, 147

Freeman, K., & Bland-Hawthorn, J. 2002, ARA&A, 40, 487

Frerking, M. A., Langer, W. D., & Wilson, R. W. 1982, ApJ, 262, 590

Gil de Paz, A., Madore, B. F., Boissier, S., et al. 2005, ApJ, 627, L29

Gratier, P., Braine, J., Rodriguez-Fernandez, N. J., et al. 2012, A&A, 542, A108

Georgelin, Y. M., & Georgelin, Y. P. 1976, A&A, 49, 57

Hachisuka, K., Choi, Y. K., Reid, M. J., et al. 2015, ApJ, 800, 2

Haisch, K. E., Jr., Lada, E. A., & Lada, C. J. 2001, ApJL, 553, L153

Heiles, C. 1979, ApJ, 229, 533

Hernández, J., Hartmann, L., Megeath, T., et al. 2007, ApJ, 662, 1067

Heyer, M. H., Brunt, C., Snell, R. L., et al. 1998, ApJS, 115, 241

Heyer, M. H., Carpenter, J. M., & Snell, R. L. 2001, ApJ, 551, 852

Hou, L. G., & Han, J. L. 2014, A&A, 569, A125

Hughes, V. A., & MacLeod, G. C. 1989, AJ, 97, 786

Ichikawa, T., Suzuki, R., Tokoku, C., et al. 2006, Proc. SPIE, 6269, Izumi, N., Kobayashi, N., Yasui, C., et al. 2014, ApJ, 795, 66

Jarrett, T. H., Cohen, M., Masci, F., et al. 2011, ApJ, 735, 112

Kalberla, P. M. W., Burton, W. B., Hartmann, D., et al. 2005, A&A, 440, 775

Kalberla, P. M. W., & Dedes, L. 2008, A&A, 487, 951

Kennicutt, R. C., & Evans, N. J. 2012, ARA&A, 50, 531

Kerton, C. R., & Brunt, C. M. 2003, A&A, 399, 1083

Kobayashi, N., & Tokunaga, A. T. 2000, ApJ, 532, 423

Kobayashi, N., Yasui, C., Tokunaga, A. T., & Saito, M. 2008, ApJ, 683, 178

Koenig, X. P., Leisawitz, D. T., Benford, D. J., et al. 2012, ApJ, 744, 130

Koenig, X. P., & Leisawitz, D. T. 2014, ApJ, 791, 131

Krumholz, M. R., McKee, C. F., & Tumlinson, J. 2008, ApJ, 689, 865

Krumholz, M. R., McKee, C. F., & Tumlinson, J. 2009a, ApJ, 693, 216

Krumholz, M. R., McKee, C. F., & Tumlinson, J. 2009b, ApJ, 699, 850

Krumholz, M. R. 2012, ApJ, 759, 9

Krumholz, M. R. 2013, MNRAS, 436, 2747

Krumholz, M. R. 2014, Phys. Rep., 539, 49

Lada, E. A. 1999, NATO ASIC Proc. 540: The Origin of Stars and Planetary Systems, 441

Lada, C. J., & Lada, E. A. 2003, ARA&A, 41, 57

Lee, H.-T., & Chen, W. P. 2009, ApJ, 694, 1423

Lee, H.-T., & Lim, J. 2008, ApJ, 679, 1352

Leggett, S. K., Currie, M. J., Varricatt, W. P., et al. 2006, MNRAS, 373, 781

Lehner, N., & Howk, J. C. 2011, Science, 334, 955

Leroy, A. K., Bolatto, A., Gordon, K., et al. 2011, ApJ, 737, 12

Lepine, J. R. D., & Duvert, G. 1994, A&A, 286, 60

Lockman, F. J. 2003, ApJL, 591, L33

Lockman, F. J., Benjamin, R. A., Heroux, A. J., & Langston, G. I. 2008, ApJ, 679, L21

McKee, C. F., & Krumholz, M. R. 2010, ApJ, 709, 308

MacLaren, I., Richardson, K. M., & Wolfendale, A. W. 1988, ApJ, 333, 821

Marasco, A., Marinacci, F., & Fraternali, F. 2013, MNRAS, 433, 1634

May, J., Alvarez, H., & Bronfman, L. 1997, A&A, 327, 325

McClure-Griffiths, N. M., Staveley-Smith, L., Lockman, F. J., et al. 2008, ApJ, 673, L143

Meisner, A. M., & Finkbeiner, D. P. 2014, ApJ, 781, 5

Miller, E. D., Bregman, J. N., & Wakker, B. P. 2009, ApJ, 692, 470

Mirabel, I. F., & Morras, R. 1990, ApJ, 356, 130

Morras, R., Bajaja, E., & Arnal, E. M. 1998, A&A, 334, 659

Mouschovias, T. C., Tassis, K., & Kunz, M. W. 2006, ApJ, 646, 1043

Muench, A. A., Lada, E. A., & Lada, C. J. 2000, ApJ, 533, 358

Muench, A. A., Lada, E. A., Lada, C. J., & Alves, J. 2002, ApJ, 573, 366

Nakagawa, M., Onishi, T., Mizuno, A., & Fukui, Y. 2005, PASJ, 57, 917

Nakanishi, H., & Sofue, Y. 2003, PASJ, 55, 191

Nakanishi, H., & Sofue, Y. 2006, PASJ, 58, 847

Neugebauer, G., Habing, H. J., van Duinen, R., et al. 1984, ApJ, 278, L1

Norman, C. A., & Ikeuchi, S. 1989, ApJ, 345, 372

Ostriker, E. C., McKee, C. F., & Leroy, A. K. 2010, ApJ, 721, 975

Pflamm-Altenburg, J., & Kroupa, P. 2008, Nature, 455, 641

Putman, M. E. 2006, ApJ, 645, 1164

Putman, M. E., Saul, D. R., & Mets, E. 2011, MNRAS, 418, 1575

Putman, M. E., Peek, J. E. G., & Joung, M. R. 2012, ARA&A, 50, 491

Reid, M. J., Menten, K. M., Brunthaler, A., et al. 2014, ApJ, 783, 130

Rieke, G. H., & Lebofsky, M. J. 1985, ApJ, 288, 618

Rubio, M., Elmegreen, B. G., Hunter, D. A., et al. 2015, Nature, 525, 218

Rudolph, A. L., Brand, J., de Geus, E. J., & Wouterloot, J. G. A. 1996, ApJ, 458, 653

Rudolph, A. L., Fich, M., Bell, G. R., et al. 2006, ApJS, 162, 346

Ruffle, P. 2006, PhD thesis

Sakai, N., Sato, M., Motogi, K., et al. 2014, PASJ, 66, 3

Sawada, T., Ikeda, N., Sunada, K., et al. 2008, PASJ, 60, 445

Schruba, A., Leroy, A. K., Walter, F., et al. 2011, AJ, 142, 37

Shi, Y., Armus, L., Helou, G., et al. 2014, Nature, 514, 335

Siess, L., Dufour, E., & Forestini, M. 2000, A&A, 358, 593

Simon, J. D., Blitz, L., Cole, A. A., Weinberg, M. D., & Cohen, M. 2006, ApJ, 640, 270

Smartt, S. J., Dufton, P. L., & Rolleston, W. R. J. 1996, A&A, 305, 164

Smartt, S. J., & Rolleston, W. R. J. 1997, ApJ, 481, L47

Smith, G. P. 1963, Bull. Astron. Inst. Netherlands, 17, 203

Snell, R. L., Carpenter, J. M., & Heyer, M. H. 2002, ApJ, 578, 229 b

Stil, J. M., & Irwin, J. A. 2001, ApJ, 563, 816

Strasser, S. T., Dickey, J. M., Taylor, A. R., et al. 2007, AJ, 134, 2252

Sun, Y., Xu, Y., Yang, J., et al. 2015, ApJ, 798, L27

Sunada, K., Yamaguchi, C., Nakai, N., et al. 2000, Proc. SPIE, 4015, 237

Taylor, A. R., Gibson, S. J., Peracaula, M., et al. 2003, AJ, 125, 3145

Tenorio-Tagle, G. 1981, A&A, 94, 338

Testi, L., Palla, F., & Natta, A. 1999, A&A, 342, 515

Thilker, D. A., Bianchi, L., Boissier, S., et al. 2005, ApJ, 619, L79

Thilker, D. A., Bianchi, L., Meurer, G., et al. 2007, ApJS, 173, 538

Tilanus, R. P. J., & Allen, R. J. 1993, A&A, 274, 707

Tokunaga, A. T., Simons, D. A., & Vacca, W. D. 2002, PASP, 114, 180

Vallée, J. P. 2008, AJ, 135, 1301

Wakker, B. P., & van Woerden, H. 1991, A&A, 250, 509

Wakker, B. P., & van Woerden, H. 1997, ARA&A, 35, 217

Weidner, C., & Kroupa, P. 2006, MNRAS, 365, 1333

Werner, M. W., Roellig, T. L., Low, F. J., et al. 2004, ApJS, 154, 1

Westerhout, G., & Wendlandt, H.-U. 1982, A&AS, 49, 143

Westmeier, T., Brüns, C., & Kerp, J. 2008, MNRAS, 390, 1691

Wolfire, M. G., McKee, C. F., Hollenbach, D., & Tielens, A. G. G. M. 2003, ApJ, 587, 278

Wolfire, M. G., Hollenbach, D., & McKee, C. F. 2010, ApJ, 716, 1191

Wouterloot, J. G. A., Brand, J., Burton, W. B., & Kwee, K. K. 1990, A&A, 230, 21

Wright, E. L., Eisenhardt, P. R. M., Mainzer, A. K., et al. 2010, AJ, 140, 1868

Yadav, R. K., Pandey, A. K., Sharma, S., et al. 2015, New A, 34, 27

Yamaguchi, C., Sunada, K., Iizuka, Y., Iwashita, H., & Noguchi, T. 2000, Proc. SPIE, 4015, 614

Yasui, C., Kobayashi, N., Tokunaga, A. T., Terada, H., & Saito, M. 2006, ApJ, 649, 753

Yasui, C., Kobayashi, N., Tokunaga, A. T., Terada, H., & Saito, M. 2008, ApJ, 675, 443

Yasui, C., Kobayashi, N.,Tokunaga, A. T., Saito, M., & Tokoku, C. 2009, ApJ, 705, 54

Yasui, C., Kobayashi, N., Tokunaga, A. T., Saito, M., & Tokoku, C. 2010, ApJ, 723, L113

Yasui, C., Kobayashi, N., Hamano, S., et al. 2016, ApJ, 817, 181

Yun, J. L., Elia, D., Djupvik, A. A., Torrelles, J. M., & Molinari, S. 2015, MNRAS, 452, 1523

Appendix A

List of newly identified star-forming regions and their parental clouds

The detailed information of newly identified star-forming regions and their parental molecular clouds are summarized in this appendix. Table A.1 is for the star-forming molecular clouds, and Table A.2 is for the star-forming regions.

Table A.1: New candidates of star-forming molecular clouds

Star-forming molecular cloud	Galactic coordinate l	b	V_{LSR} [km s^{-1}]	D [kpc]	R_G [kpc]	Number of candidates in the cloud	Contamination rate [%]	Note
[BKP2003]8672	139.344	2.891	-52.87	5.85	13.5	4	37.1	
[BKP2003]8674	139.397	2.768	-53.34	5.93	13.6	4	12.8	
[BKP2003]8713	136.314	0.165	-57.64	6.23	13.7	15	16.7	
[BKP2003]8715	136.269	0.260	-56.09	5.98	13.5	1	200.0	
[BKP2003]8911	139.096	3.518	-54.32	6.06	13.7	5	6.3	
[BKP2003]8918	141.464	4.484	-50.66	5.8	13.5	2	17.3	
[BKP2003]9254	136.789	0.445	-59.82	6.65	14.1	11	32.8	
[BKP2003]9255	136.866	0.257	-56.94	6.18	13.7	3	99.1	
[BKP2003]9256	136.826	0.350	-56.66	6.13	13.6	3	49.4	
[BKP2003]9257	136.956	0.192	-57.17	6.23	13.7	4	45.6	
[BKP2003]9258	136.901	0.097	-56.26	6.07	13.6	5	33.2	
[BKP2003]9303	140.204	2.618	-53.40	6.05	13.7	1	12.0	
[BKP2003]9377	141.145	1.480	-56.73	6.8	14.4	3	17.3	
[BKP2003]9429	136.648	0.313	-56.45	6.07	13.6	4	63.2	
[BKP2003]9430	136.652	0.371	-56.76	6.12	13.6	5	59.5	
[BKP2003]9486	138.662	3.442	-55.95	6.28	13.8	1	55.6	
[BKP2003]9518	136.712	0.662	-56.60	6.11	13.6	1	131.0	
[BKP2003]9526	137.244	1.116	-56.66	6.18	13.7	2	148.0	
[BKP2003]9540	135.696	1.777	-56.86	6.04	13.5	2	43.5	
[BKP2003]9567	138.383	3.402	-55.88	6.23	13.8	1	11.9	
[BKP2003]9571	138.793	3.575	-56.40	6.38	13.9	1	26.9	
[BKP2003]9572	138.940	3.614	-56.25	6.37	13.9	3	13.5	
[BKP2003]9583	137.788	-0.307	-56.83	6.28	13.8	1	29.5	
[BKP2003]9593	135.800	0.090	-56.70	6.02	13.5	2	3.11	
[BKP2003]9596	137.069	0.146	-56.70	6.16	13.7	1	12.9	
[BKP2003]9600	135.612	0.349	-58.09	6.22	13.7	2	16.9	
[BKP2003]9607	141.054	0.640	-57.56	6.94	14.6	1	67.2	
[BKP2003]9608	135.977	0.627	-57.23	6.12	13.6	2	5.14	
[BKP2003]9756	139.135	0.192	-59.07	6.87	14.4	2	4.72	
[BKP2003]9760	137.315	0.350	-60.17	6.78	14.2	2	14.0	
[BKP2003]9761	134.750	0.385	-58.89	6.25	13.6	1	6.83	
[BKP2003]9764	137.140	0.467	-58.35	6.45	13.9	1	17.6	
[BKP2003]9779	137.308	1.099	-58.66	6.52	14.0	1	128.0	
[BKP2003]9791	138.613	1.557	-59.74	6.91	14.4	2	15.8	02587+6008
[BKP2003]9792	138.548	1.522	-59.68	6.89	14.4	2	14.8	02587+6008
[BKP2003]9833	137.380	0.457	-59.55	6.68	14.2	1	25.4	
[BKP2003]9836	132.831	0.605	-59.62	6.18	13.5	1	49.2	
[BKP2003]9838	136.344	0.818	-59.56	6.55	14.0	2	9.34	
[BKP2003]9910	133.395	0.140	-60.00	6.28	13.6	3	6.32	
[BKP2003]9911	137.064	0.190	-60.00	6.72	14.2	2	22.5	
[BKP2003]9914	131.151	0.344	-61.32	6.29	13.5	4	5.82	01587+6148
[BKP2003]9922	136.356	0.976	-62.04	6.97	14.4	7	21.7	02413+6037
[BKP2003]9949	134.096	2.672	-60.20	6.4	13.7	1	5.84	
[BKP2003]9993	132.615	1.465	-61.28	6.41	13.7	2	5.57	
[BKP2003]9994	135.432	1.540	-61.95	6.83	14.2	1	23.8	

Table A.1 (Continued.)

Star-forming molecular cloud	Galactic coordinate l	b	V_{LSR} [km s^{-1}]	D [kpc]	R_{G} [kpc]	Number of candidates in the cloud	Contamination rate [%]	Note
[BKP2003]10096	139.399	-2.044	-62.47	7.59	15.1	1	4.13	
[BKP2003]10105	136.501	0.488	-62.95	7.15	14.5	6	3.02	
[BKP2003]10106	131.263	0.522	-63.08	6.56	13.7	2	0.905	
[BKP2003]10115	131.928	1.305	-64.77	6.89	14.1	7	10.8	
[BKP2003]10120	135.724	1.524	-63.31	7.11	14.5	2	6.07	
[BKP2003]10123	125.614	1.619	-66.04	6.63	13.5	4	32.4	
[BKP2003]10164	136.138	1.085	-64.30	7.34	14.7	1	45.4	
[BKP2003]10171	130.493	1.481	-64.37	6.7	13.8	3	13.5	
[BKP2003]10172	132.484	1.694	-64.78	6.95	14.2	9	16.0	
[BKP2003]10174	132.613	1.727	-64.06	6.85	14.1	2	11.2	
[BKP2003]10208	120.433	3.623	-71.85	7.28	13.7	2	117.0	
[BKP2003]10209	120.203	3.659	-70.06	7.04	13.5	2	75.5	
[BKP2003]10227	125.349	0.366	-67.78	6.85	13.7	5	23.4	
[BKP2003]10282	128.898	1.231	-65.72	6.77	13.8	1	12.3	
[BKP2003]10295	131.104	2.158	-65.64	6.95	14.1	1	8.59	
[BKP2003]10332	125.082	0.765	-67.74	6.83	13.6	8	34.2	
[BKP2003]10333	125.077	0.879	-68.00	6.87	13.7	8	4.85	
[BKP2003]10340	130.876	2.294	-65.83	6.96	14.1	1	9.13	
[BKP2003]10369	122.321	4.084	-69.09	6.96	13.5	4	21.9	
[BKP2003]10376	123.375	1.599	-68.67	6.9	13.6	3	16.0	
[BKP2003]10406	127.792	0.425	-67.90	7.01	13.9	1	3.99	
[BKP2003]10412	123.171	1.462	-67.96	6.79	13.5	1	14.3	
[BKP2003]10423	122.007	2.770	-69.33	6.96	13.5	7	23.2	
[BKP2003]10424	121.855	2.907	-68.98	6.91	13.5	11	14.4	
[BKP2003]10449	138.437	2.154	-68.48	8.64	16.0	1	14.6	
[BKP2003]10450	123.565	2.365	-68.43	6.88	13.6	3	2.43	
[BKP2003]10472	120.727	4.068	-69.90	7.03	13.5	4	26.0	
[BKP2003]10473	120.915	4.222	-70.45	7.11	13.6	4	27.0	
[BKP2003]10477	120.915	4.984	-69.65	7.02	13.5	2	16.6	
[BKP2003]10485	135.824	2.374	-69.51	8.3	15.6	1	4.67	
[BKP2003]10487	122.156	2.684	-69.07	6.93	13.5	2	3.58	
[BKP2003]10505	123.138	4.054	-69.81	7.09	13.7	4	2.9	
[BKP2003]10508	121.277	4.271	-69.07	6.93	13.5	1	5.64	
[BKP2003]10510	120.810	4.916	-69.44	6.99	13.5	2	19.9	
[BKP2003]10514	131.651	1.791	-71.67	8.03	15.1	1	29.7	
[BKP2003]10515	124.382	1.981	-71.95	7.42	14.1	9	25.9	
[BKP2003]10516	124.509	1.867	-72.23	7.47	14.1	1	27.1	
[BKP2003]10520	119.728	2.270	-70.42	7.06	13.5	2	4.68	
[BKP2003]10526	121.777	2.630	-70.37	7.1	13.6	5	2.43	
[BKP2003]10528	135.208	2.725	-72.23	8.74	15.9	12	2.74	02383+6241
[BKP2003]10532	120.534	2.939	-70.20	7.05	13.5	1	33.7	
[BKP2003]10534	136.750	3.033	-70.60	8.73	16.0	1	20.5	
[BKP2003]10550	125.198	1.346	-70.72	7.27	14.0	1	5.14	
[BKP2003]10554	120.014	2.196	-71.04	7.14	13.6	1	19.5	
[BKP2003]10555	134.926	2.365	-71.76	8.58	15.8	4	20.5	
[BKP2003]10556	135.659	2.488	-70.86	8.55	15.8	1	6.38	

Table A.1 (Continued.)

Star-forming molecular cloud	Galactic coordinate l	b	V_{LSR} [km s^{-1}]	D [kpc]	R_{G} [kpc]	Number of candidates in the cloud	Contamination rate [%]	Note
[BKP2003]10570	123.376	1.574	-72.63	7.46	14.1	2	8.43	
[BKP2003]10571	122.731	1.638	-71.77	7.31	13.9	1	7.79	
[BKP2003]10572	118.319	1.971	-72.29	7.29	13.6	1	9.31	
[BKP2003]10573	118.359	2.050	-71.54	7.19	13.5	2	2.18	
[BKP2003]10578	135.623	2.754	-72.67	8.92	16.1	2	14.8	02421+6233
[BKP2003]10579	136.670	2.861	-71.64	8.94	16.2	3	5.93	
[BKP2003]10580	135.639	2.990	-72.28	8.85	16.1	1	9.4	
[BKP2003]10585	117.202	5.059	-73.49	7.5	13.6	8	38.9	
[BKP2003]10586	117.422	5.099	-72.83	7.42	13.6	6	8.94	
[BKP2003]10587	138.264	0.605	-72.88	9.6	16.9	4	6.8	
[BKP2003]10588	138.408	0.644	-72.60	9.58	16.9	6	9.41	
[BKP2003]10589	136.366	0.848	-74.29	9.43	16.6	19	36.4	02407+6029b
[BKP2003]10591	125.331	1.733	-73.42	7.7	14.4	1	53.0	
[BKP2003]10592	133.788	2.196	-72.65	8.55	15.7	1	16.4	
[BKP2003]10596	120.089	2.354	-72.37	7.33	13.7	2	25.2	
[BKP2003]10614	138.524	0.777	-73.56	9.85	17.2	2	6.87	
[BKP2003]10624	133.401	2.041	-74.37	8.82	15.9	3	9.37	
[BKP2003]10627	135.371	2.712	-73.73	9.1	16.3	4	5.34	
[BKP2003]10635	121.204	4.034	-73.64	7.56	14.0	5	13.7	
[BKP2003]10636	133.884	0.365	-74.61	8.95	16.1	1	52.9	
[BKP2003]10643	135.962	0.800	-75.97	9.72	16.9	7	26.7	02376+6030
[BKP2003]10644	113.727	0.903	-75.75	7.77	13.6	1	16.0	
[BKP2003]10645	113.620	0.924	-75.53	7.74	13.6	1	20.8	
[BKP2003]10649	136.192	2.261	-74.84	9.53	16.7	1	18.0	
[BKP2003]10650	112.135	2.398	-79.21	8.27	13.9	3	26.7	
[BKP2003]10651	112.325	2.505	-78.46	8.17	13.8	1	134.0	
[BKP2003]10652	133.778	2.456	-75.38	9.11	16.2	1	9.36	
[BKP2003]10653	111.884	2.769	-79.26	8.29	13.9	13	19.6	
[BKP2003]10656	132.138	1.768	-75.67	8.86	15.9	1	6.3	
[BKP2003]10658	109.746	3.417	-77.13	8.09	13.6	1	14.4	
[BKP2003]10661	109.174	4.935	-76.34	8.05	13.5	4	6.43	
[BKP2003]10664	138.571	0.774	-76.97	10.8	18.0	2	3.62	
[BKP2003]10666	134.196	1.395	-76.49	9.42	16.5	1	21.1	
[BKP2003]10667	124.152	1.931	-76.96	8.17	14.7	3	1.87	
[BKP2003]10670	112.331	2.243	-78.84	8.22	13.9	2	25.1	
[BKP2003]10674	121.757	3.292	-77.86	8.2	14.6	5	27.3	
[BKP2003]10681	131.212	1.142	-77.86	9.13	16.1	3	10.3	
[BKP2003]10683	131.447	1.164	-77.31	9.06	16.0	1	3.81	
[BKP2003]10684	131.855	1.323	-78.80	9.44	16.4	1	49.9	02071+6235
[BKP2003]10685	123.596	1.956	-77.63	8.25	14.8	1	9.35	
[BKP2003]10686	124.519	2.059	-77.96	8.36	14.9	1	13.5	
[BKP2003]10687	124.485	2.190	-77.31	8.26	14.8	2	7.96	
[BKP2003]10688	132.783	2.213	-77.72	9.4	16.4	1	4.28	
[BKP2003]10692	104.394	2.822	-80.20	8.77	13.6	13	17.2	
[BKP2003]10696	135.984	0.675	-78.40	10.3	17.4	1	13.9	
[BKP2003]10700	130.681	1.447	-78.91	9.25	16.1	2	41.5	

Table A.1 (Continued.)

Star-forming molecular cloud	Galactic coordinate l	b	V_{LSR} [km s^{-1}]	D [kpc]	R_{G} [kpc]	Number of candidates in the cloud	Contamination rate [%]	Note
[BKP2003]10701	132.164	1.545	-78.24	9.38	16.3	1	55.8	
[BKP2003]10703	126.337	2.250	-79.28	8.75	15.4	5	5.43	
[BKP2003]10705	124.597	2.262	-78.92	8.53	15.1	1	21.9	
[BKP2003]10707	135.385	2.685	-78.75	10.3	17.4	1	4.44	
[BKP2003]10708	109.857	2.718	-81.42	8.65	14.0	18	9.74	
[BKP2003]10709	109.934	2.790	-80.74	8.55	14.0	22	17.9	
[BKP2003]10710	109.889	2.918	-80.57	8.53	13.9	2	55.7	
[BKP2003]10711	104.164	2.705	-80.47	8.82	13.7	1	124.0	
[BKP2003]10713	104.279	2.901	-79.44	8.68	13.6	7	8.3	
[BKP2003]10715	114.559	4.551	-78.74	8.22	14.0	1	24.9	
[BKP2003]10717	131.448	0.848	-79.42	9.49	16.4	3	10.9	
[BKP2003]10719	127.251	1.470	-80.83	9.13	15.8	4	10.2	
[BKP2003]10720	130.553	1.560	-78.96	9.24	16.1	2	9.66	
[BKP2003]10724	104.462	3.119	-81.11	8.89	13.7	2	33.9	
[BKP2003]10725	104.424	3.052	-80.36	8.79	13.7	1	24.9	
[BKP2003]10728	136.020	0.364	-80.50	10.9	18.0	1	77.5	
[BKP2003]10730	129.180	1.427	-80.01	9.23	16.0	2	8.5	
[BKP2003]10731	129.564	1.689	-80.25	9.34	16.1	2	11.0	
[BKP2003]10732	127.535	1.867	-80.97	9.19	15.9	14	8.75	
[BKP2003]10733	128.857	1.862	-80.43	9.27	16.0	3	1.71	
[BKP2003]10734	129.117	1.966	-81.30	9.48	16.2	7	7.07	
[BKP2003]10735	128.771	1.994	-82.03	9.58	16.3	24	11.0	
[BKP2003]10736	128.924	2.138	-80.36	9.27	16.0	6	3.98	
[BKP2003]10737	123.843	2.231	-80.02	8.66	15.1	1	6.42	
[BKP2003]10739	128.102	2.485	-80.92	9.27	16.0	1	32.9	
[BKP2003]10740	103.866	2.822	-83.32	9.22	13.9	4	25.1	
[BKP2003]10743	116.482	3.997	-79.79	8.35	14.3	1	4.77	
[BKP2003]10744	114.187	4.297	-80.02	8.39	14.2	1	8.39	
[BKP2003]10750	129.515	1.525	-80.61	9.4	16.2	1	18.5	
[BKP2003]10752	129.059	1.602	-81.28	9.46	16.2	1	16.9	
[BKP2003]10753	125.109	1.609	-81.43	9.0	15.5	3	2.08	
[BKP2003]10755	126.220	2.024	-81.16	9.07	15.7	5	13.9	
[BKP2003]10756	128.889	1.998	-81.50	9.49	16.2	1	13.4	
[BKP2003]10758	123.929	2.239	-80.61	8.76	15.2	1	5.06	
[BKP2003]10760	103.481	2.798	-81.65	9.03	13.8	1	11.7	
[BKP2003]10761	103.568	2.838	-81.20	8.96	13.7	1	11.4	
[BKP2003]10762	104.323	4.287	-85.56	9.52	14.2	2	109.0	
[BKP2003]10765	125.082	1.416	-82.37	9.16	15.7	1	24.6	
[BKP2003]10766	128.836	1.518	-82.20	9.61	16.3	2	19.3	
[BKP2003]10770	105.277	4.470	-82.60	9.07	13.9	4	4.39	
[BKP2003]10771	107.240	4.760	-81.95	8.88	14.0	1	23.8	
[BKP2003]10774	128.814	1.324	-83.15	9.8	16.5	13	17.6	
[BKP2003]10775	125.160	1.550	-82.26	9.15	15.7	3	4.73	
[BKP2003]10776	128.881	1.568	-82.26	9.63	16.4	4	1.79	
[BKP2003]10777	121.022	1.914	-82.98	8.95	15.2	2	10.6	
[BKP2003]10780	102.884	2.883	-84.44	9.44	14.0	2	61.3	

Table A.1 (Continued.)

Star-forming molecular cloud	Galactic coordinate l	b	V_{LSR} [km s^{-1}]	D [kpc]	R_{G} [kpc]	Number of candidates in the cloud	Contamination rate [%]	Note
[BKP2003]10783	105.191	4.616	-82.26	9.03	13.9	1	4.38	
[BKP2003]10784	125.012	1.597	-83.91	9.44	15.9	3	17.0	
[BKP2003]10785	130.442	1.576	-83.33	10.1	16.9	1	14.7	
[BKP2003]10787	119.651	2.036	-83.08	8.9	15.0	1	9.66	
[BKP2003]10789	103.265	2.744	-83.29	9.26	13.9	1	3.21	
[BKP2003]10792	125.054	2.146	-84.95	9.64	16.1	3	15.9	
[BKP2003]10793	122.626	2.196	-84.42	9.31	15.6	2	12.7	
[BKP2003]10794	124.651	2.515	-87.30	10.1	16.4	2	76.5	
[BKP2003]10795	124.559	2.527	-88.75	10.3	16.7	4	4.71	
[BKP2003]10796	124.485	2.526	-87.13	10.0	16.4	13	18.2	
[BKP2003]10797	102.632	3.697	-88.25	10.0	14.5	9	19.9	
[BKP2003]10798	132.306	1.971	-84.85	10.9	17.8	2	5.36	
[BKP2003]10803	103.393	2.871	-85.03	9.48	14.1	1	26.1	
[BKP2003]10804	119.150	1.718	-86.50	9.43	15.5	7	7.77	
[BKP2003]10805	119.011	1.715	-86.03	9.35	15.4	2	9.7	
[BKP2003]10807	132.371	1.979	-86.18	11.3	18.1	1	10.1	
[BKP2003]10811	125.805	3.038	-86.41	10.0	16.5	1	9.84	
[BKP2003]10812	125.219	3.187	-85.70	9.83	16.3	1	8.39	
[BKP2003]10816	104.008	4.202	-87.90	9.87	14.5	3	28.1	
[BKP2003]10819	132.162	2.524	-86.96	11.4	18.2	1	12.0	
[BKP2003]10820	123.423	2.534	-87.24	9.9	16.2	1	39.0	
[BKP2003]10824	104.057	4.063	-86.75	9.7	14.3	1	6.31	
[BKP2003]10827	112.925	4.244	-87.32	9.47	15.0	1	13.3	
[BKP2003]10828	125.167	1.959	-88.64	10.4	16.8	2	13.2	
[BKP2003]10829	125.539	2.266	-88.13	10.3	16.8	1	36.9	
[BKP2003]10830	102.823	3.712	-89.11	10.1	14.6	2	5.62	
[BKP2003]10831	123.982	2.493	-89.22	10.3	16.7	3	5.53	
[BKP2003]10832	125.573	2.750	-89.33	10.6	17.0	1	1.87	
[BKP2003]10834	117.574	1.771	-89.68	9.89	15.7	1	5.16	
[BKP2003]10835	123.066	1.350	-91.31	10.6	16.8	1	3.27	
[BKP2003]10836	112.093	2.334	-90.69	9.95	15.3	2	7.92	
[BKP2003]10841	118.123	1.580	-92.42	10.4	16.2	9	5.78	
[BKP2003]10844	111.802	2.360	-91.33	10.1	15.4	1	9.46	
[BKP2003]10845	118.042	1.555	-92.15	10.3	16.2	3	1.38	
[BKP2003]10848	111.891	2.094	-93.47	10.4	15.7	4	16.8	
[BKP2003]10849	110.544	2.413	-92.15	10.2	15.4	2	7.35	
[BKP2003]10850	111.763	2.248	-93.47	10.4	15.7	2	2.25	
[BKP2003]10851	124.288	1.564	-95.11	11.6	17.8	3	5.64	
[BKP2003]10852	124.211	2.121	-94.41	11.5	17.7	1	27.9	
[BKP2003]10853	107.690	2.133	-93.80	10.5	15.4	1	2.92	
[BKP2003]10855	109.311	2.585	-94.17	10.5	15.6	1	14.7	
[BKP2003]10857	117.765	1.117	-95.57	11.0	16.7	4	8.13	
[BKP2003]10858	123.138	1.493	-95.10	11.4	17.6	1	5.26	
[BKP2003]10859	122.602	1.648	-95.51	11.4	17.5	2	3.74	
[BKP2003]10861	122.554	1.738	-96.22	11.6	17.7	2	16.8	
[BKP2003]10862	128.017	1.972	-95.70	12.5	19.0	1	10.2	

Table A.1 (Continued.)

Star-forming molecular cloud	Galactic coordinate l	b	V_{LSR} [km s^{-1}]	D [kpc]	R_{G} [kpc]	Number of candidates in the cloud	Contamination rate [%]	Note
[BKP2003]10863	114.273	2.018	-95.10	10.7	16.2	1	10.3	
[BKP2003]10864	118.022	1.540	-96.26	11.1	16.9	5	3.98	
[BKP2003]10866	117.800	1.590	-96.39	11.1	16.8	1	13.8	
[BKP2003]10867	125.255	2.043	-95.78	11.9	18.2	1	13.8	
[BKP2003]10870	109.648	2.704	-99.04	11.4	16.3	1	84.0	
[BKP2003]10871	109.787	2.714	-99.22	11.4	16.3	9	5.86	
[BKP2003]10872	114.341	0.787	-101.21	11.8	17.2	8	4.58	
[BKP2003]10873	114.213	0.847	-101.94	12.0	17.3	1	22.8	
[BKP2003]10874	127.876	2.190	-99.73	13.6	20.0	1	15.4	
[BKP2003]10875	127.981	2.406	-99.57	13.6	20.0	3	1.66	
[BKP2003]10876	116.320	2.410	-99.66	11.7	17.2	1	7.95	
[BKP2003]10877	131.156	1.389	-101.06	15.3	21.8	3	1.27	Cloud 1b
[BKP2003]10878	109.284	2.076	-101.29	11.7	16.6	3	4.23	
[BKP2003]10883	123.483	1.489	-101.94	13.1	19.1	2	2.86	
[BKP2003]10885	137.757	-0.971	-103.54	21.5	28.3	4	8.51	Cloud 2-N
[BKP2003]10886	137.770	-1.067	-102.68	20.9	27.8	7	2.46	Cloud 2-S
[BKP2003]10888	122.386	1.769	-102.51	13.0	19.0	1	13.7	
[BKP2003]10890	123.363	1.653	-103.28	13.4	19.4	2	12.6	
[BKP2003]10892	121.806	3.058	-103.97	13.3	19.2	4	16.1	
[BKP2003]10895	122.771	2.526	-107.35	14.4	20.3	4	3.78	
[BKP2003]10896	117.585	3.962	-106.26	13.2	18.7	2	6.0	
[BKP2003]10897	118.153	3.424	-106.99	13.5	19.0	1	6.93	
[BKP2003]10898	116.727	3.542	-107.28	13.4	18.8	2	3.91	

Table A.2: New candidates of star-forming regions

Star-forming molecular cloud	AllWISE source	Coordinate l	b	3.4 μm [mag]	$\sigma_{3.4}$ [mag]	4.6 μm [mag]	$\sigma_{4.6}$ [mag]	12 μm [mag]	σ_{12} [mag]	22 μm [mag]	σ_{22} [mag]
[BKP2003]8672	J031418.89+610923.1	139.312	2.914	14.247	0.028	12.973	0.029	10.343	0.082	7.576	0.161
	J031423.41+610435.3	139.361	2.850	13.967	0.030	13.165	0.029	10.388	0.076	7.811	0.166
	J031428.58+610937.6	139.327	2.927	15.809	0.054	15.303	0.091	11.113	0.149	8.391	null
	J031511.68+610614.5	139.430	2.925	16.654	0.088	14.935	0.068	11.607	0.194	8.579	null
[BKP2003]8674	J031351.58+610238.0	139.324	2.789	12.832	0.024	11.965	0.023	9.549	0.058	6.803	0.083
	J031407.57+605939.0	139.377	2.763	14.185	0.028	12.837	0.026	10.373	0.080	8.443	0.288
	J031415.70+605652.0	139.415	2.732	14.321	0.030	13.754	0.037	10.811	0.093	8.128	0.237
	J031416.94+605737.4	139.411	2.744	14.737	0.039	13.455	0.034	10.667	0.087	7.642	0.154
[BKP2003]8713	J024148.88+600531.8	136.285	0.114	13.783	0.028	12.471	0.025	9.423	0.042	6.285	0.050
	J024149.86+600520.1	136.289	0.112	13.269	0.026	12.697	0.028	8.635	0.027	6.373	0.052
	J024151.87+600458.0	136.295	0.108	12.460	0.024	11.437	0.021	9.097	0.031	6.929	0.080
	J024206.60+600741.8	136.304	0.162	13.787	0.035	13.120	0.032	10.883	0.106	8.180	0.252
	J024214.69+600618.9	136.329	0.148	14.201	0.030	13.618	0.039	9.831	0.050	6.692	0.086
	J024215.38+600726.3	136.322	0.165	14.474	0.034	13.279	0.031	11.164	0.185	8.464	0.374
	J024224.76+600719.8	136.341	0.172	12.763	0.024	12.211	0.024	7.096	0.016	5.898	0.054
	J024233.95+600644.4	136.362	0.171	13.362	0.027	10.989	0.021	8.482	0.029	5.368	0.035
	J024244.50+600334.7	136.404	0.132	13.809	0.033	11.573	0.022	9.335	0.055	5.814	0.059
	J024245.41+600617.4	136.387	0.174	14.094	0.027	13.374	0.032	10.767	0.101	8.487	0.375
	J024248.56+600602.9	136.395	0.173	15.617	0.049	13.705	0.037	10.612	0.116	8.096	0.234
	J024257.66+600352.9	136.427	0.148	12.696	0.023	11.065	0.021	7.904	0.022	4.759	0.027
	J024356.74+595303.8	136.614	0.036	16.119	0.072	13.984	0.038	11.053	0.115	8.498	0.280
	J024406.56+595224.4	136.637	0.034	13.366	0.026	12.274	0.024	9.266	0.035	6.625	0.066
	J024424.24+594831.8	136.698	-0.009	12.707	0.024	11.677	0.022	9.552	0.045	6.953	0.122
[BKP2003]8715	J024154.89+601947.9	136.199	0.335	16.316	0.122	15.134	0.085	10.967	0.197	8.345	0.300
[BKP2003]8911	J031525.27+614509.2	139.113	3.491	11.611	0.022	11.057	0.021	7.462	0.016	5.564	0.037
	J031537.05+614824.8	139.104	3.550	14.751	0.033	13.737	0.035	10.727	0.094	8.337	0.258
	J031606.42+614821.1	139.154	3.579	12.461	0.024	10.337	0.020	8.324	0.022	4.782	0.029
	J031607.35+614813.4	139.157	3.578	13.700	0.037	12.732	0.045	10.271	0.087	7.977	0.314
	J031619.81+614806.1	139.179	3.590	13.940	0.026	12.719	0.025	10.153	0.064	7.419	0.118
[BKP2003]8918	J033619.70+611402.6	141.479	4.449	16.035	0.055	15.248	0.069	11.374	0.125	8.717	null
	J033622.69+611745.7	141.447	4.503	12.052	0.024	11.239	0.021	8.453	0.023	5.264	0.031
[BKP2003]9254	J024618.86+601406.1	136.733	0.478	12.486	0.025	11.889	0.026	8.469	0.056	5.360	0.058
	J024619.44+601304.2	136.742	0.463	10.711	0.033	9.930	0.025	4.850	0.014	2.276	0.021
	J024620.08+601322.3	136.741	0.468	10.861	0.021	9.668	0.018	6.491	0.015	3.670	0.018
	J024625.68+601325.6	136.751	0.474	10.313	0.024	8.781	0.020	6.061	0.022	3.362	0.030
	J024630.16+601320.3	136.760	0.477	14.229	0.052	13.661	0.048	8.769	0.109	6.829	0.150
	J024633.65+600859.0	136.798	0.414	11.537	0.020	11.024	0.023	8.321	0.044	4.521	0.042
	J024641.41+600832.1	136.815	0.415	13.073	0.033	12.051	0.026	9.582	0.064	6.803	0.121
	J024643.05+601021.4	136.805	0.443	13.958	0.054	13.011	0.042	9.525	0.100	6.867	0.196
	J024647.57+601001.5	136.816	0.442	14.003	0.039	12.995	0.034	10.447	0.125	5.606	0.060
	J024701.43+600841.3	136.852	0.435	15.964	0.105	15.304	0.104	9.557	0.052	7.175	0.101
	J024705.85+601011.1	136.849	0.461	13.846	0.050	12.564	0.033	9.387	0.049	7.216	0.111
[BKP2003]9255	J024628.87+595938.8	136.855	0.270	15.140	0.053	14.514	0.076	11.040	0.166	8.502	null
	J024629.55+595942.0	136.856	0.271	14.325	0.034	13.662	0.043	10.762	0.131	8.179	0.376
	J024634.58+595919.6	136.868	0.270	14.563	0.035	13.845	0.041	11.339	0.183	8.934	null
[BKP2003]9256	J024623.83+600553.1	136.801	0.359	9.777	0.022	8.748	0.019	6.426	0.015	4.145	0.021
	J024624.05+600606.5	136.800	0.363	12.469	0.035	11.904	0.027	8.186	0.030	5.052	0.041
	J024635.49+600422.1	136.834	0.347	14.135	0.029	12.901	0.027	10.160	0.088	7.460	0.170
[BKP2003]9257	J024642.84+595312.1	136.928	0.185	14.384	0.051	13.178	0.032	10.073	0.062	7.243	0.110
	J024644.63+595246.9	136.934	0.180	15.985	0.073	15.214	0.081	10.701	0.088	7.647	0.154
	J024645.28+595339.4	136.929	0.194	12.919	0.024	12.156	0.023	9.538	0.040	7.204	0.126
	J024709.02+595336.3	136.974	0.215	13.203	0.023	12.127	0.022	9.617	0.049	7.327	0.103

Table A.2 (Continued.)

Star-forming molecular cloud	AllWISE source	Coordinate l	b	3.4 μm [mag]	$\sigma_{3.4}$ [mag]	4.6 μm [mag]	$\sigma_{4.6}$ [mag]	12 μm [mag]	σ_{12} [mag]	22 μm [mag]	σ_{22} [mag]
[BKP2003]9258	J024602.76+594955.3	136.875	0.100	14.764	0.037	14.044	0.046	11.243	0.191	8.758	null
	J024607.52+594933.0	136.887	0.098	14.722	0.035	13.747	0.037	11.257	0.157	8.125	null
	J024610.47+595014.5	136.888	0.111	14.083	0.095	12.712	0.030	9.791	0.060	5.576	0.037
	J024616.84+595111.1	136.893	0.131	14.773	0.034	13.582	0.032	10.975	0.119	8.791	0.456
	J024620.83+594156.4	136.966	-0.004	15.329	0.045	14.534	0.053	10.074	0.059	7.812	0.177
[BKP2003]9303	J031914.50+602451.1	140.215	2.601	15.913	0.060	15.218	0.083	9.300	0.044	6.914	0.073
[BKP2003]9377	J032043.35+585933.4	141.138	1.503	9.984	0.025	8.453	0.021	4.552	0.013	1.507	0.011
	J032046.47+585945.6	141.142	1.509	14.528	0.034	12.936	0.028	9.811	0.048	4.528	0.033
	J032050.06+585554.5	141.183	1.459	13.769	0.026	13.055	0.027	10.485	0.078	7.449	0.149
[BKP2003]9429	J024514.57+600557.7	136.671	0.299	14.400	0.032	13.154	0.030	10.574	0.098	7.798	0.154
	J024516.54+600614.2	136.672	0.305	14.440	0.040	13.507	0.036	10.890	0.134	8.614	0.333
	J024517.15+600712.4	136.667	0.320	14.291	0.031	13.328	0.032	9.952	0.059	7.402	0.121
	J024517.78+600619.1	136.674	0.307	13.395	0.028	12.668	0.026	10.160	0.073	7.243	0.103
[BKP2003]9430	J024524.83+601026.8	136.658	0.376	14.662	0.031	13.004	0.027	10.416	0.075	8.832	0.505
	J024527.29+601149.6	136.653	0.399	16.510	0.089	15.989	0.154	10.838	0.114	8.040	0.213
	J024531.87+600947.8	136.676	0.372	15.576	0.057	14.449	0.059	11.596	0.196	5.875	0.046
	J024537.25+600837.4	136.694	0.359	16.773	0.122	15.866	0.153	11.462	0.212	8.692	0.423
	J024548.14+600824.0	136.716	0.365	15.321	0.054	14.360	0.051	10.676	0.102	8.171	0.193
[BKP2003]9486	J031216.83+615617.8	138.699	3.458	14.944	0.037	14.057	0.038	11.483	0.165	8.179	null
[BKP2003]9518	J024643.53+602348.2	136.710	0.646	16.377	0.158	15.391	0.106	10.071	0.068	7.517	0.145
[BKP2003]9526	J025217.13+603753.5	137.222	1.157	13.379	0.033	12.848	0.036	10.655	0.140	8.665	null
	J025218.31+603355.6	137.254	1.099	12.794	0.025	12.276	0.026	8.755	0.032	6.011	0.048
[BKP2003]9540	J024303.53+614907.2	135.707	1.748	10.910	0.023	9.900	0.019	5.969	0.014	4.087	0.020
	J024315.87+615005.2	135.723	1.772	14.567	0.031	13.652	0.032	10.439	0.078	8.534	0.298
[BKP2003]9567	J030927.42+620316.8	138.354	3.389	14.325	0.030	13.097	0.028	9.161	0.036	6.719	0.063
[BKP2003]9571	J031311.01+615852.4	138.768	3.549	14.050	0.028	13.233	0.029	10.567	0.074	7.914	0.204
[BKP2003]9572	J031433.22+615816.6	138.911	3.624	16.308	0.073	15.588	0.105	11.311	0.135	8.884	null
	J031502.42+615408.5	138.996	3.595	14.813	0.033	14.055	0.037	10.935	0.099	8.242	0.257
	J031527.99+615211.6	139.056	3.594	14.219	0.028	13.462	0.033	10.869	0.111	7.423	0.125
[BKP2003]9583	J025122.95+590629.7	137.801	-0.256	13.994	0.030	13.120	0.030	10.480	0.079	8.835	0.457
[BKP2003]9593	J023806.81+601514.5	135.799	0.075	16.214	0.067	15.604	0.112	10.795	0.119	8.154	null
	J023817.04+601640.0	135.809	0.105	15.180	0.047	14.665	0.063	10.917	0.161	8.313	null
[BKP2003]9596	J024735.40+594927.3	137.054	0.176	13.252	0.025	12.472	0.024	9.618	0.051	8.018	0.244
[BKP2003]9600	J023736.17+603506.2	135.609	0.353	15.224	0.044	14.681	0.058	10.904	0.213	7.364	0.122
	J023739.51+603450.0	135.617	0.352	9.545	0.023	8.588	0.020	6.190	0.016	3.923	0.026
[BKP2003]9607	J031638.41+581849.1	141.051	0.645	14.907	0.036	13.770	0.037	10.988	0.157	8.760	null
[BKP2003]9608	J024114.28+604125.6	135.974	0.630	13.478	0.025	12.937	0.028	10.229	0.097	8.434	0.251
	J024117.76+604053.3	135.985	0.624	16.174	0.081	15.644	0.124	10.748	0.133	8.528	null
[BKP2003]9756	J030210.17+585433.5	139.123	0.210	13.414	0.025	12.718	0.025	10.243	0.062	8.583	0.322
	J030219.48+585204.4	139.161	0.183	14.187	0.030	13.578	0.031	10.570	0.100	7.612	0.175
[BKP2003]9760	J025016.37+595139.0	137.341	0.356	15.553	0.133	14.866	0.093	9.400	0.178	7.414	0.251
	J025018.01+595134.3	137.345	0.356	15.120	0.134	14.560	0.082	9.497	0.154	7.735	0.246
[BKP2003]9761	J023120.85+605715.2	134.762	0.398	13.514	0.025	11.398	0.022	8.423	0.027	5.704	0.036
[BKP2003]9764	J024924.05+600341.6	137.155	0.488	8.961	0.022	8.236	0.020	4.993	0.015	3.183	0.022
[BKP2003]9779	J025243.81+603302.5	137.307	1.110	15.203	0.055	14.465	0.059	10.345	0.116	7.138	0.147
[BKP2003]9791	J030336.77+602055.1	138.588	1.558	15.035	0.050	11.792	0.023	9.228	0.117	5.419	0.078
	J030350.14+602013.2	138.618	1.562	9.211	0.023	7.760	0.020	4.075	0.014	1.167	0.011
[BKP2003]9792	J030258.27+601920.8	138.531	1.497	11.484	0.024	10.787	0.021	7.898	0.061	6.088	0.113
	J030311.26+602007.6	138.548	1.521	12.065	0.024	11.302	0.024	7.219	0.023	5.658	0.041
[BKP2003]9833	J025038.03+595516.5	137.355	0.430	14.859	0.034	14.309	0.044	8.998	0.035	6.030	0.061
[BKP2003]9836	J021653.60+614918.2	132.838	0.605	15.025	0.119	14.184	0.054	9.940	0.115	6.980	0.139
[BKP2003]9838	J024427.51+604136.2	136.332	0.796	14.218	0.088	12.995	0.070	8.704	0.060	5.711	0.099
	J024440.19+604230.6	136.349	0.821	10.755	0.025	10.139	0.021	4.591	0.016	1.142	0.017

Table A.2 (Continued.)

Star-forming molecular cloud	AllWISE source	Coordinate l	b	3.4 μm [mag]	$\sigma_{3.4}$ [mag]	4.6 μm [mag]	$\sigma_{4.6}$ [mag]	12 μm [mag]	σ_{12} [mag]	22 μm [mag]	σ_{22} [mag]
[BKP2003]9910	J022006.20+611258.1	133.399	0.159	14.064	0.045	13.052	0.042	9.630	0.094	6.799	0.127
	J022011.50+611114.9	133.419	0.136	14.728	0.213	14.214	0.118	8.573	0.187	5.817	0.269
	J022016.80+611320.6	133.417	0.172	15.734	0.081	15.075	0.115	9.377	0.064	6.910	0.099
[BKP2003]9911	J024735.40+594927.3	137.054	0.176	13.252	0.025	12.472	0.024	9.618	0.051	8.018	0.244
	J024754.33+595033.4	137.082	0.210	15.416	0.041	13.920	0.039	10.672	0.093	8.827	0.388
[BKP2003]9914	J020223.40+620245.3	131.143	0.311	11.472	0.023	10.891	0.021	5.935	0.014	3.726	0.020
	J020236.09+620513.8	131.156	0.357	17.110	0.118	15.782	0.115	11.072	0.142	7.114	0.103
	J020238.68+620543.8	131.158	0.367	15.452	0.070	14.775	0.071	11.362	0.184	8.130	0.233
	J020239.51+620525.3	131.161	0.362	14.789	0.033	13.923	0.038	11.324	0.173	8.290	0.282
[BKP2003]9922	J024510.24+604956.4	136.352	0.959	10.572	0.023	9.502	0.021	5.327	0.017	0.425	0.008
	J024510.79+604937.1	136.355	0.955	9.941	0.024	7.435	0.020	3.379	0.014	-0.009	0.015
	J024512.35+604951.0	136.356	0.959	9.945	0.163	9.368	0.099	5.615	0.082	2.540	0.030
	J024514.20+605059.1	136.352	0.978	11.808	0.025	10.998	0.022	7.252	0.033	4.747	0.035
	J024514.44+605050.7	136.353	0.976	11.918	0.027	11.315	0.026	6.741	0.027	4.667	0.039
	J024527.40+605513.5	136.346	1.054	14.674	0.136	14.052	0.129	8.558	0.212	6.046	0.172
	J024545.93+605141.7	136.405	1.016	14.924	0.075	13.897	0.052	10.519	0.178	7.722	0.314
[BKP2003]9949	J023319.27+631717.7	134.090	2.645	15.614	0.078	15.083	0.081	10.172	0.073	7.816	0.154
[BKP2003]9993	J021739.16+624454.3	132.620	1.510	17.537	0.187	15.598	0.113	11.172	0.118	9.030	0.473
	J021739.97+624427.5	132.624	1.503	16.120	0.069	15.558	0.120	11.190	0.141	8.413	null
[BKP2003]9994	J024021.06+614425.0	135.448	1.544	13.853	0.029	12.550	0.025	10.294	0.115	8.081	0.296
[BKP2003]10096	J025556.84+564804.2	139.385	-2.040	15.667	0.048	14.460	0.050	10.898	0.129	8.624	0.328
[BKP2003]10105	J024425.41+602138.4	136.468	0.493	12.515	0.026	11.014	0.021	7.932	0.026	5.252	0.035
	J024438.91+602011.2	136.503	0.483	13.859	0.050	13.359	0.041	7.771	0.024	5.001	0.029
	J024439.11+602031.9	136.501	0.488	11.202	0.020	10.599	0.021	7.687	0.023	4.655	0.030
	J024439.23+602024.9	136.502	0.486	12.777	0.037	10.653	0.023	7.188	0.020	4.325	0.028
	J024441.98+602023.6	136.508	0.488	11.061	0.029	10.270	0.022	6.943	0.026	4.475	0.033
	J024444.28+602037.6	136.510	0.494	11.532	0.024	9.712	0.020	7.000	0.030	4.627	0.039
[BKP2003]10106	J020350.40+621316.1	131.258	0.526	14.592	0.046	13.692	0.040	9.870	0.073	6.377	0.060
	J020352.71+621311.2	131.263	0.526	13.261	0.028	12.140	0.023	9.336	0.037	6.716	0.083
[BKP2003]10115	J021112.47+624639.0	131.911	1.305	13.612	0.026	12.846	0.028	10.666	0.130	7.791	0.165
	J021117.02+624715.0	131.916	1.317	14.008	0.027	12.826	0.027	10.352	0.096	7.773	0.179
	J021117.48+624108.3	131.948	1.220	16.046	0.055	14.915	0.063	11.589	0.180	8.759	0.410
	J021131.17+624646.9	131.944	1.318	14.861	0.035	13.974	0.038	11.617	0.211	8.975	0.435
	J021141.40+624052.3	131.992	1.230	11.664	0.023	10.560	0.020	7.901	0.021	6.147	0.046
	J021148.38+624101.5	132.004	1.236	13.253	0.028	12.729	0.027	9.632	0.054	7.246	0.103
	J021150.14+623936.3	132.015	1.215	10.504	0.023	9.194	0.019	5.676	0.014	3.084	0.021
[BKP2003]10120	J024217.44+613754.8	135.702	1.540	15.167	0.035	14.402	0.041	10.496	0.127	7.653	0.149
	J024226.28+613638.7	135.727	1.528	12.514	0.030	11.789	0.024	9.062	0.050	5.980	0.054
[BKP2003]10123	J011546.02+642145.7	125.561	1.615	14.416	0.029	13.288	0.028	10.638	0.081	8.128	0.224
	J011617.50+642156.9	125.617	1.624	13.370	0.025	11.660	0.022	8.980	0.033	4.234	0.024
	J011618.03+642136.4	125.618	1.618	10.121	0.019	8.838	0.018	5.387	0.015	1.990	0.015
	J011619.96+642135.5	125.622	1.618	12.062	0.028	11.411	0.030	6.526	0.020	3.464	0.019
[BKP2003]10164	J024354.55+610203.7	136.128	1.078	13.283	0.025	12.431	0.023	8.422	0.038	5.605	0.046
[BKP2003]10171	J015919.64+632032.7	130.460	1.467	12.451	0.149	11.728	0.022	9.682	0.048	7.235	0.132
	J020002.11+632033.1	130.537	1.488	15.668	0.053	14.427	0.050	11.523	0.191	7.474	0.129
	J020003.28+632045.9	130.538	1.492	13.102	0.026	11.717	0.021	9.210	0.036	6.500	0.063
[BKP2003]10172	J021646.76+630233.3	132.430	1.755	14.410	0.033	12.806	0.026	10.255	0.066	7.884	0.223
	J021706.37+625910.3	132.483	1.714	14.908	0.041	12.977	0.029	10.111	0.062	7.248	0.124
	J021706.75+630031.9	132.476	1.736	14.388	0.041	13.188	0.032	10.756	0.096	7.851	0.180
	J021709.27+625744.8	132.496	1.693	15.917	0.055	14.815	0.066	11.455	0.184	8.934	null
	J021710.56+625845.6	132.493	1.710	14.701	0.035	13.698	0.039	11.037	0.134	8.663	null
	J021711.18+625734.4	132.500	1.692	15.280	0.056	14.282	0.054	11.238	0.167	8.604	0.383
	J021720.75+625647.9	132.522	1.686	12.262	0.023	11.246	0.021	8.739	0.026	6.525	0.059

Table A.2 (Continued.)

Star-forming molecular cloud	AllWISE source	Coordinate l	b	3.4 μm [mag]	$\sigma_{3.4}$ [mag]	4.6 μm [mag]	$\sigma_{4.6}$ [mag]	12 μm [mag]	σ_{12} [mag]	22 μm [mag]	σ_{22} [mag]
	J021733.90+625530.6	132.552	1.673	16.733	0.114	15.886	0.163	10.269	0.064	8.153	0.198
	J021747.06+625052.0	132.601	1.608	15.673	0.063	14.907	0.072	10.484	0.082	8.452	0.322
[BKP2003]10174	J021817.28+625803.1	132.616	1.740	12.851	0.024	11.851	0.021	8.539	0.027	6.515	0.069
	J021817.66+625656.1	132.623	1.723	14.138	0.030	12.789	0.026	9.974	0.080	7.592	0.159
[BKP2003]10208	J002628.82+662216.7	120.430	3.621	15.189	0.039	13.918	0.036	11.498	0.196	6.889	0.088
	J002640.54+662230.5	120.450	3.623	12.878	0.025	11.375	0.021	8.695	0.027	6.025	0.054
[BKP2003]10209	J002357.49+661840.3	120.172	3.587	16.329	0.061	14.529	0.046	9.788	0.049	5.848	0.039
	J002506.96+663038.5	120.308	3.773	15.567	0.046	13.597	0.032	9.228	0.035	7.806	0.207
[BKP2003]10227	J011234.42+631141.2	125.312	0.421	14.959	0.043	13.492	0.035	10.843	0.104	8.239	0.351
	J011240.69+630919.1	125.327	0.382	14.802	0.043	14.022	0.047	10.763	0.124	8.319	0.290
	J011245.56+630810.2	125.338	0.364	13.111	0.030	12.490	0.034	6.906	0.019	4.737	0.029
	J011246.19+630810.8	125.339	0.364	12.087	0.024	11.490	0.022	6.185	0.015	4.642	0.030
	J011250.40+630646.6	125.349	0.342	14.496	0.034	12.264	0.026	9.200	0.039	6.484	0.067
[BKP2003]10282	J014512.40+632718.8	128.896	1.208	13.891	0.029	13.169	0.028	10.963	0.126	8.852	0.444
[BKP2003]10295	J020634.42+634904.9	131.106	2.145	14.338	0.168	13.560	0.032	10.446	0.072	7.883	0.186
[BKP2003]10332	J011028.37+632913.4	125.054	0.694	13.734	0.028	12.087	0.023	9.401	0.040	6.781	0.083
	J011028.52+632932.1	125.054	0.699	15.075	0.041	12.444	0.024	9.774	0.058	6.620	0.087
	J011030.58+633215.8	125.055	0.745	13.317	0.029	12.423	0.025	9.780	0.084	7.155	0.158
	J011031.20+632919.0	125.060	0.696	13.123	0.026	11.897	0.023	9.055	0.033	6.321	0.055
	J011048.26+633414.0	125.085	0.780	8.961	0.023	7.325	0.019	3.756	0.015	0.692	0.021
	J011049.20+633341.9	125.087	0.771	12.261	0.026	11.734	0.026	6.131	0.013	2.933	0.026
	J011051.97+633340.1	125.093	0.771	11.961	0.031	11.177	0.025	6.098	0.019	3.272	0.029
	J011053.09+633327.3	125.095	0.768	11.542	0.027	10.654	0.021	6.323	0.019	3.638	0.027
[BKP2003]10333	J011040.55+633827.4	125.066	0.849	15.740	0.098	14.066	0.044	10.197	0.111	7.148	0.139
	J011040.76+634125.4	125.062	0.898	14.018	0.030	13.390	0.034	8.259	0.027	5.542	0.053
	J011044.05+634042.7	125.069	0.887	12.855	0.027	11.769	0.025	8.267	0.026	5.599	0.039
	J011044.88+633857.1	125.073	0.858	13.523	0.033	12.785	0.030	9.709	0.064	7.818	0.244
	J011046.44+634027.0	125.074	0.883	14.257	0.036	13.125	0.033	8.724	0.033	6.074	0.051
	J011054.17+633704.5	125.092	0.828	15.129	0.052	14.261	0.052	10.700	0.155	7.531	0.160
	J011056.71+633718.7	125.097	0.832	15.455	0.058	13.242	0.033	10.285	0.102	7.035	0.094
	J011059.31+633759.3	125.101	0.844	13.880	0.030	12.852	0.027	10.171	0.081	7.746	0.194
[BKP2003]10340	J020437.89+640149.3	130.841	2.288	14.819	0.037	14.017	0.041	10.957	0.119	8.601	0.372
[BKP2003]10369	J004415.62+665442.0	122.227	4.050	9.163	0.022	8.180	0.019	3.465	0.013	-0.669	0.014
	J004446.81+665706.3	122.279	4.089	12.169	0.025	11.008	0.022	8.109	0.022	5.634	0.044
	J004451.85+665753.3	122.287	4.101	12.780	0.024	12.015	0.023	9.002	0.030	6.321	0.056
	J004504.14+665820.4	122.308	4.108	13.451	0.040	12.877	0.029	8.883	0.030	6.348	0.053
[BKP2003]10376	J005521.72+642642.8	123.355	1.577	14.167	0.028	13.636	0.032	11.520	0.197	9.114	0.542
	J005538.36+642725.9	123.385	1.589	15.667	0.050	14.685	0.055	11.191	0.139	8.352	null
	J005548.32+642936.7	123.402	1.626	14.929	0.051	13.605	0.035	10.967	0.122	7.840	null
[BKP2003]10406	J013419.78+625339.7	127.795	0.428	13.084	0.027	11.524	0.022	8.182	0.019	4.665	0.026
[BKP2003]10412	J005334.06+642034.8	123.163	1.472	10.924	0.023	10.065	0.020	7.503	0.017	5.123	0.033
[BKP2003]10423	J004220.14+653654.5	121.992	2.760	14.959	0.032	13.469	0.029	10.062	0.052	6.296	0.056
	J004237.30+653902.4	122.022	2.795	14.095	0.027	12.624	0.024	9.079	0.034	6.022	0.044
	J004243.33+653609.1	122.031	2.746	15.820	0.047	15.306	0.082	11.469	0.211	8.642	null
	J004325.61+653843.5	122.105	2.787	14.940	0.039	13.937	0.039	10.494	0.093	7.937	0.213
	J004326.88+653811.7	122.107	2.778	11.594	0.023	10.109	0.020	7.626	0.018	5.631	0.042
	J004329.40+653718.0	122.111	2.763	14.499	0.031	13.782	0.032	11.516	0.189	9.083	0.485
	J004331.00+653742.1	122.114	2.769	12.931	0.023	11.614	0.021	9.164	0.031	6.721	0.067
[BKP2003]10424	J004015.54+654706.1	121.785	2.938	15.591	0.042	14.647	0.057	10.464	0.080	6.327	0.054
	J004017.77+654648.0	121.788	2.933	12.996	0.044	11.989	0.035	9.486	0.056	6.888	0.135
	J004039.56+654405.6	121.823	2.886	15.542	0.040	14.918	0.063	11.740	0.219	8.283	null
	J004110.03+654548.7	121.877	2.913	10.684	0.028	10.067	0.028	7.904	0.024	6.001	0.043
	J004116.78+654558.1	121.888	2.915	16.756	0.108	15.878	0.133	11.372	0.146	8.304	0.239

Table A.2 (Continued.)

Star-forming molecular cloud	AllWISE source	Coordinate l	b	3.4 μm [mag]	$\sigma_{3.4}$ [mag]	4.6 μm [mag]	$\sigma_{4.6}$ [mag]	12 μm [mag]	σ_{12} [mag]	22 μm [mag]	σ_{22} [mag]
	J004119.56+654516.6	121.893	2.903	13.767	0.026	12.648	0.025	9.397	0.035	7.013	0.104
	J004126.66+654257.3	121.903	2.864	13.423	0.026	11.891	0.023	9.176	0.032	6.429	0.059
	J004130.51+654601.8	121.912	2.915	14.616	0.030	13.360	0.026	10.239	0.064	7.123	0.096
	J004133.58+654604.5	121.917	2.916	15.353	0.035	14.451	0.039	10.787	0.109	7.595	0.135
	J004135.64+654828.3	121.922	2.955	13.958	0.029	13.129	0.029	10.684	0.094	6.770	0.080
	J004135.99+654819.5	121.923	2.953	12.499	0.023	11.501	0.021	9.056	0.036	5.967	0.047
[BKP2003]10449	J030446.91+605645.3	138.422	2.150	14.108	0.030	12.692	0.025	10.058	0.081	7.193	0.109
[BKP2003]10450	J005724.58+651356.3	123.558	2.368	14.245	0.029	13.522	0.032	10.136	0.081	7.485	0.150
	J005728.54+651253.5	123.565	2.351	15.560	0.038	13.907	0.036	11.117	0.162	8.205	0.282
	J005729.16+651221.4	123.566	2.342	15.704	0.047	15.129	0.083	11.435	0.211	8.298	null
[BKP2003]10472	J002840.08+665034.3	120.691	4.070	13.606	0.026	12.292	0.023	8.846	0.029	5.431	0.037
	J002846.26+665205.6	120.703	4.095	13.323	0.024	12.550	0.023	10.141	0.066	7.995	0.181
	J002851.15+664958.5	120.708	4.059	14.811	0.034	14.120	0.036	11.268	0.196	7.873	0.190
	J002851.93+664943.6	120.709	4.055	13.271	0.024	12.149	0.022	9.228	0.039	6.311	0.059
[BKP2003]10473	J002918.13+665814.4	120.764	4.192	14.275	0.040	13.522	0.036	11.088	0.139	8.229	0.269
	J002950.91+665816.0	120.818	4.188	14.374	0.030	13.677	0.031	11.249	0.127	8.675	null
	J003058.01+670414.6	120.935	4.278	14.956	0.094	12.468	0.026	9.004	0.029	5.775	0.041
	J003125.67+670325.4	120.979	4.261	15.109	0.035	13.592	0.033	10.047	0.075	7.441	0.115
[BKP2003]10477	J003002.85+674529.3	120.903	4.971	13.841	0.025	13.239	0.029	10.861	0.100	8.355	0.258
	J003019.35+674539.3	120.929	4.971	13.697	0.032	12.338	0.026	9.494	0.039	6.735	0.076
[BKP2003]10485	J024614.53+622000.4	135.828	2.372	13.440	0.029	12.480	0.026	9.954	0.053	7.625	0.145
[BKP2003]10487	J004355.64+653238.8	122.154	2.684	12.694	0.025	12.036	0.023	9.392	0.038	7.023	0.086
	J004355.93+653249.2	122.154	2.687	12.340	0.025	11.464	0.023	9.144	0.033	7.492	0.126
[BKP2003]10505	J005315.66+665452.1	123.111	4.043	14.824	0.037	14.010	0.040	10.996	0.125	6.782	0.082
	J005315.82+665525.1	123.111	4.053	15.231	0.036	14.647	0.052	11.474	0.186	8.004	0.222
	J005316.01+665507.9	123.112	4.048	15.688	0.052	14.797	0.063	11.141	0.145	7.712	0.175
	J005318.19+665509.9	123.115	4.048	15.302	0.044	14.703	0.062	10.950	0.125	7.721	0.172
[BKP2003]10508	J003431.15+670554.3	121.283	4.281	14.354	0.032	13.603	0.032	11.168	0.121	8.701	0.344
[BKP2003]10510	J002911.39+674047.4	120.815	4.900	13.395	0.025	10.975	0.019	7.654	0.016	4.352	0.020
	J002919.85+674309.1	120.831	4.938	14.769	0.031	14.194	0.042	10.862	0.119	8.352	0.249
[BKP2003]10514	J021032.38+632117.7	131.664	1.832	13.650	0.028	11.819	0.023	8.936	0.030	6.356	0.059
[BKP2003]10515	J010427.65+645852.2	124.309	2.144	14.571	0.058	13.341	0.043	10.469	0.086	7.794	0.214
	J010430.87+645658.7	124.316	2.113	14.700	0.086	13.679	0.085	11.190	0.211	7.904	null
	J010503.04+644215.6	124.386	1.871	13.657	0.027	12.732	0.027	10.262	0.070	7.730	0.161
	J010527.29+644637.8	124.425	1.946	12.915	0.025	12.097	0.024	9.594	0.038	7.490	0.120
	J010531.38+644303.0	124.436	1.887	11.833	0.024	10.478	0.021	6.263	0.015	2.734	0.019
	J010536.06+644548.7	124.442	1.933	13.164	0.026	11.995	0.023	9.121	0.032	6.841	0.079
	J010536.83+644521.7	124.443	1.926	13.801	0.029	13.021	0.029	10.682	0.085	7.807	0.168
	J010539.41+644112.9	124.452	1.857	16.911	0.127	14.726	0.071	10.937	0.132	8.160	0.230
	J010540.93+644028.6	124.455	1.845	14.838	0.035	14.081	0.043	10.435	0.073	7.724	0.144
[BKP2003]10516	J010617.32+644115.2	124.519	1.862	10.362	0.023	9.219	0.019	6.422	0.015	4.165	0.024
[BKP2003]10520	J002109.86+645651.3	119.732	2.264	14.531	0.036	11.860	0.023	9.266	0.040	6.142	0.050
	J002113.80+645608.6	119.738	2.252	14.556	0.056	13.457	0.042	10.316	0.091	7.498	0.239
[BKP2003]10526	J004004.31+652908.0	121.752	2.640	12.927	0.032	12.402	0.031	7.485	0.019	5.727	0.039
	J004005.54+652858.6	121.754	2.637	12.507	0.026	11.618	0.024	7.381	0.019	5.210	0.040
	J004006.77+652852.9	121.756	2.636	12.433	0.029	11.567	0.023	8.218	0.025	5.613	0.037
	J004009.97+652900.5	121.762	2.637	14.537	0.043	13.782	0.036	9.729	0.068	6.812	0.092
	J004026.13+653010.6	121.791	2.656	15.898	0.055	15.329	0.079	11.404	0.168	9.032	null
[BKP2003]10528	J024216.31+625322.9	135.179	2.684	13.519	0.016	12.852	0.014	7.245	0.005	4.223	0.018
	J024217.33+625324.8	135.180	2.685	13.283	0.026	12.582	0.025	6.782	0.014	3.904	0.021
	J024218.97+625405.0	135.178	2.697	10.779	0.027	10.148	0.024	4.700	0.015	1.179	0.034
	J024219.76+625430.3	135.177	2.704	11.636	0.016	11.042	0.014	5.957	0.006	1.138	0.004
	J024219.87+625404.0	135.180	2.697	10.650	0.029	9.917	0.027	4.705	0.019	0.871	0.029

Table A.2 (Continued.)

Star-forming molecular cloud	AllWISE source	Coordinate l	b	3.4 μm [mag]	$\sigma_{3.4}$ [mag]	4.6 μm [mag]	$\sigma_{4.6}$ [mag]	12 μm [mag]	σ_{12} [mag]	22 μm [mag]	σ_{22} [mag]
	J024220.30+625447.2	135.176	2.708	13.346	0.026	12.741	0.025	7.580	0.018	3.090	0.008
	J024221.73+625403.6	135.183	2.698	9.942	0.025	9.344	0.021	4.601	0.016	0.384	0.018
	J024222.00+625438.4	135.180	2.707	13.455	0.019	12.914	0.026	7.249	0.015	1.960	0.006
	J024224.73+625407.2	135.188	2.702	11.196	0.021	10.637	0.021	5.297	0.012	1.596	0.020
	J024238.04+625430.8	135.208	2.718	12.918	0.034	12.414	0.037	7.502	0.026	4.628	0.032
	J024239.14+625425.3	135.211	2.718	12.029	0.028	10.790	0.022	7.045	0.022	4.247	0.037
	J024241.28+625436.3	135.213	2.722	13.539	0.027	12.843	0.030	8.172	0.040	5.197	0.042
[BKP2003]10532	J002806.28+654134.4	120.531	2.930	14.120	0.037	12.544	0.027	9.687	0.052	7.204	0.114
[BKP2003]10534	J025551.00+623133.9	136.739	3.038	13.730	0.027	12.657	0.026	9.588	0.038	9.046	0.523
[BKP2003]10550	J011215.77+640638.1	125.203	1.331	14.490	0.029	13.508	0.027	10.503	0.107	8.206	0.233
[BKP2003]10554	J002348.40+645453.7	120.007	2.200	15.909	0.061	14.077	0.039	11.622	0.209	7.961	0.175
[BKP2003]10555	J023847.73+623907.0	134.913	2.304	12.128	0.024	10.889	0.022	8.121	0.022	5.333	0.036
	J023848.68+623916.7	134.913	2.308	12.815	0.025	11.506	0.022	8.344	0.023	5.119	0.033
	J023848.95+623904.3	134.915	2.305	13.853	0.043	13.182	0.054	10.253	0.094	8.082	0.308
	J024013.49+624827.2	134.999	2.513	15.799	0.051	14.416	0.050	11.580	0.207	8.326	null
[BKP2003]10556	J024524.99+623107.4	135.662	2.498	16.016	0.055	14.490	0.050	11.270	0.157	9.078	null
[BKP2003]10570	J005521.72+642642.8	123.355	1.577	14.167	0.028	13.636	0.032	11.520	0.197	9.114	0.542
	J005538.36+642725.9	123.385	1.589	15.667	0.050	14.685	0.055	11.191	0.139	8.352	null
[BKP2003]10571	J004938.22+643041.7	122.738	1.641	13.916	0.030	13.093	0.027	10.176	0.079	7.216	0.108
[BKP2003]10572	J000822.81+642619.4	118.307	1.954	15.247	0.038	14.729	0.053	11.984	0.195	9.424	0.444
[BKP2003]10573	J000838.28+643414.0	118.356	2.080	15.598	0.038	14.763	0.048	11.991	0.198	9.136	0.375
	J000847.62+643130.9	118.365	2.032	16.927	0.090	15.412	0.074	12.184	0.207	9.033	0.298
[BKP2003]10578	J024558.90+624708.0	135.607	2.767	12.086	0.023	11.316	0.021	7.805	0.021	5.131	0.036
	J024607.12+624630.3	135.626	2.765	9.447	0.022	8.817	0.020	3.721	0.014	0.474	0.016
[BKP2003]10579	J025433.63+622522.9	136.654	2.878	14.648	0.034	12.381	0.023	9.650	0.045	6.623	0.074
	J025441.86+622337.0	136.681	2.859	14.241	0.034	13.255	0.032	10.098	0.050	7.096	0.110
	J025442.10+622350.0	136.680	2.862	13.644	0.026	12.906	0.027	10.089	0.049	7.404	0.145
[BKP2003]10580	J024714.65+625929.4	135.649	3.015	13.814	0.037	13.238	0.033	9.289	0.053	6.349	0.066
[BKP2003]10585	J235052.48+671316.9	117.105	5.037	14.584	0.038	13.422	0.030	10.225	0.058	8.289	0.186
	J235121.84+671707.9	117.166	5.089	15.618	0.042	14.959	0.056	11.029	0.108	8.824	0.276
	J235122.74+671447.0	117.159	5.050	16.106	0.047	14.765	0.050	10.913	0.077	8.951	0.349
	J235125.05+671706.4	117.171	5.087	15.784	0.052	15.108	0.064	10.896	0.099	8.882	0.297
	J235127.13+671415.4	117.164	5.040	12.968	0.025	12.017	0.022	9.590	0.038	7.531	0.119
	J235127.51+672023.7	117.188	5.140	15.286	0.034	14.406	0.040	10.608	0.062	7.963	0.149
	J235134.60+671400.3	117.174	5.033	15.095	0.044	13.902	0.038	10.619	0.061	7.803	0.129
	J235145.71+671541.3	117.198	5.056	13.702	0.023	12.855	0.023	10.340	0.074	7.760	0.140
[BKP2003]10586	J235340.86+671942.0	117.395	5.080	16.358	0.090	15.223	0.081	10.577	0.182	7.928	0.206
	J235350.49+672128.0	117.416	5.105	15.198	0.044	13.914	0.043	10.420	0.112	7.199	0.128
	J235351.56+671924.1	117.410	5.071	15.971	0.080	15.471	0.095	9.861	0.071	8.589	0.388
	J235358.19+672143.9	117.430	5.107	14.271	0.038	12.964	0.030	9.030	0.064	6.074	0.068
	J235359.54+672125.1	117.430	5.101	14.532	0.039	13.905	0.040	9.195	0.069	7.584	0.208
	J235402.47+672037.6	117.432	5.087	15.881	0.109	15.363	0.118	9.438	0.048	7.009	0.102
[BKP2003]10587	J025746.12+594000.3	138.270	0.611	14.346	0.033	12.777	0.027	10.311	0.072	7.647	0.218
	J025750.79+593951.4	138.280	0.614	14.566	0.044	13.991	0.040	9.911	0.134	7.274	0.154
	J025754.44+594003.0	138.285	0.620	14.624	0.032	13.595	0.034	9.107	0.051	6.526	0.075
	J025759.32+593959.7	138.295	0.624	14.369	0.055	13.657	0.048	10.572	0.144	7.320	0.205
[BKP2003]10588	J025816.30+593650.1	138.351	0.594	15.393	0.042	14.845	0.062	10.690	0.135	8.189	0.303
	J025844.37+593907.3	138.385	0.655	14.295	0.031	12.972	0.028	10.111	0.079	7.382	0.148
	J025848.86+593839.1	138.397	0.653	15.521	0.051	14.828	0.062	10.274	0.091	7.454	0.112
	J025855.70+593645.1	138.425	0.632	16.981	0.157	16.052	0.184	10.438	0.085	7.820	0.165
	J025946.14+593603.9	138.524	0.672	12.413	0.025	11.654	0.022	8.623	0.028	6.063	0.046
	J025949.61+593542.5	138.533	0.670	15.635	0.048	14.855	0.067	10.299	0.065	7.912	0.164
[BKP2003]10589	J024253.79+604703.0	136.120	0.799	15.143	0.058	14.534	0.061	9.316	0.047	5.646	0.044

Table A.2 (Continued.)

Star-forming molecular cloud	AllWISE source	Coordinate l	b	3.4 μm [mag]	$\sigma_{3.4}$ [mag]	4.6 μm [mag]	$\sigma_{4.6}$ [mag]	12 μm [mag]	σ_{12} [mag]	22 μm [mag]	σ_{22} [mag]
	J024256.29+604704.5	136.125	0.801	14.615	0.038	13.912	0.040	8.934	0.038	5.817	0.064
	J024259.82+604713.3	136.130	0.807	15.010	0.038	14.414	0.051	9.834	0.061	6.244	0.065
	J024300.53+604720.4	136.131	0.809	15.095	0.063	14.530	0.055	9.977	0.063	6.843	0.082
	J024332.92+604537.3	136.203	0.810	16.483	0.162	15.535	0.130	9.988	0.103	8.747	0.372
	J024336.65+604551.4	136.208	0.817	16.550	0.172	15.844	0.153	10.065	0.149	8.579	null
	J024339.81+604601.4	136.213	0.822	16.615	0.168	15.492	0.123	10.071	0.113	8.329	null
	J024346.10+604637.8	136.220	0.837	15.895	0.067	15.227	0.091	10.130	0.188	8.802	0.526
	J024421.32+604127.5	136.321	0.789	14.220	0.047	13.569	0.048	8.659	0.077	5.123	0.045
	J024422.18+604114.4	136.324	0.786	14.434	0.089	13.479	0.139	8.852	0.093	4.591	0.036
	J024422.36+604133.8	136.322	0.791	14.265	0.033	13.072	0.035	8.978	0.078	5.286	0.032
	J024425.77+604143.5	136.328	0.797	14.457	0.160	13.205	0.139	9.536	0.202	6.264	0.155
	J024427.51+604136.2	136.332	0.796	14.218	0.088	12.995	0.070	8.704	0.060	5.711	0.099
	J024438.68+604603.1	136.321	0.873	12.806	0.034	11.636	0.026	9.280	0.068	6.596	0.100
	J024440.19+604230.6	136.349	0.821	10.755	0.025	10.139	0.021	4.591	0.016	1.142	0.017
	J024457.48+604225.6	136.381	0.835	12.032	0.025	10.310	0.022	7.717	0.026	4.069	0.031
	J024458.20+604259.7	136.379	0.844	13.688	0.037	12.936	0.049	8.816	0.033	5.776	0.052
	J024458.97+604250.7	136.381	0.842	12.726	0.026	11.505	0.026	8.368	0.029	5.431	0.049
	J024459.59+604345.7	136.376	0.857	13.900	0.035	12.879	0.032	9.912	0.083	6.904	0.090
[BKP2003]10591	J011347.06+643050.2	125.334	1.747	13.560	0.026	12.331	0.024	9.828	0.048	6.618	0.065
[BKP2003]10592	J022954.28+630148.1	133.830	2.261	14.300	0.029	13.652	0.033	10.619	0.097	8.232	0.239
[BKP2003]10596	J002425.88+650454.7	120.090	2.359	11.447	0.022	10.249	0.021	7.243	0.018	3.898	0.021
	J002432.57+650448.8	120.102	2.356	12.288	0.036	11.776	0.025	6.545	0.015	4.962	0.031
[BKP2003]10614	J030004.32+594238.8	138.506	0.787	14.424	0.034	13.734	0.038	10.485	0.099	8.255	0.323
	J030014.44+594042.8	138.540	0.768	14.436	0.035	13.207	0.030	10.805	0.118	7.522	0.160
[BKP2003]10624	J022540.00+625921.8	133.396	2.048	14.911	0.046	13.635	0.037	9.566	0.060	6.695	0.113
	J022546.04+625748.5	133.416	2.028	14.925	0.038	13.738	0.037	9.623	0.056	7.349	0.102
	J022547.44+625910.2	133.411	2.050	12.937	0.027	11.537	0.021	9.162	0.060	6.157	0.049
[BKP2003]10627	J024401.92+624822.3	135.396	2.692	10.647	0.020	9.453	0.020	6.559	0.015	4.114	0.022
	J024413.83+624819.4	135.417	2.701	14.631	0.030	13.561	0.033	9.915	0.052	7.187	0.091
	J024416.20+624823.9	135.421	2.704	14.492	0.034	13.698	0.038	9.514	0.045	6.928	0.086
	J024418.17+624815.2	135.425	2.703	13.276	0.024	12.643	0.025	9.523	0.047	6.871	0.074
[BKP2003]10635	J003402.22+665059.7	121.219	4.036	13.233	0.025	12.481	0.023	10.036	0.092	8.259	0.278
	J003403.83+665029.6	121.221	4.028	14.124	0.028	13.267	0.027	10.905	0.155	7.930	0.246
	J003410.17+665057.2	121.232	4.035	14.147	0.030	13.588	0.033	10.800	0.143	7.935	0.175
	J003411.55+664939.3	121.233	4.013	13.284	0.026	12.737	0.026	9.737	0.059	7.827	0.187
	J003415.36+665120.7	121.241	4.041	15.285	0.038	13.685	0.033	10.853	0.116	7.626	0.134
[BKP2003]10636	J022430.40+611353.6	133.891	0.356	13.917	0.029	13.265	0.034	10.918	0.126	8.160	0.298
[BKP2003]10643	J024129.21+604327.8	135.988	0.673	10.677	0.022	10.159	0.020	5.148	0.015	2.779	0.018
	J024148.47+604853.0	135.987	0.772	15.820	0.052	14.573	0.054	11.229	0.162	8.374	null
	J024156.78+605113.4	135.986	0.814	15.289	0.051	14.023	0.044	10.714	0.134	8.412	0.336
	J024202.34+605240.4	135.986	0.841	15.990	0.094	15.428	0.107	10.233	0.116	8.264	0.279
	J024202.89+605232.2	135.988	0.839	16.101	0.105	15.390	0.110	10.490	0.143	8.193	0.263
	J024204.42+605202.2	135.995	0.833	16.339	0.191	15.470	0.115	9.944	0.117	8.167	0.250
	J024209.73+605240.4	136.000	0.847	16.587	0.111	16.026	0.159	10.082	0.079	7.813	0.232
[BKP2003]10644	J233046.29+621944.5	113.718	0.909	11.491	0.022	10.491	0.019	8.125	0.022	6.426	0.044
[BKP2003]10645	J233009.24+621831.9	113.644	0.912	13.603	0.027	12.741	0.026	10.301	0.068	8.094	0.143
[BKP2003]10649	J024836.92+620541.7	136.180	2.276	14.056	0.029	13.335	0.032	10.867	0.175	7.561	0.140
[BKP2003]10650	J231310.32+630839.3	112.097	2.358	14.345	0.044	13.818	0.036	9.966	0.064	7.314	0.085
	J231317.89+631031.3	112.122	2.382	15.272	0.045	13.746	0.035	10.673	0.064	6.822	0.056
	J231325.63+631225.3	112.147	2.406	16.025	0.140	14.636	0.054	9.339	0.032	5.266	0.033
[BKP2003]10651	J231447.54+633106.9	112.404	2.640	12.158	0.023	11.269	0.021	8.593	0.029	6.670	0.059
[BKP2003]10652	J023010.65+631333.4	133.786	2.454	12.162	0.021	10.731	0.020	7.774	0.017	5.279	0.031
[BKP2003]10653	J230911.95+632606.0	111.793	2.796	14.869	0.038	14.202	0.041	10.444	0.076	8.929	null

Table A.2 (Continued.)

Star-forming molecular cloud	AllWISE source	Coordinate l	b	3.4 μm [mag]	$\sigma_{3.4}$ [mag]	4.6 μm [mag]	$\sigma_{4.6}$ [mag]	12 μm [mag]	σ_{12} [mag]	22 μm [mag]	σ_{22} [mag]
	J230939.51+632622.5	111.843	2.781	13.872	0.028	13.279	0.029	10.804	0.125	8.313	0.185
	J230943.12+633505.5	111.905	2.912	15.499	0.043	14.900	0.058	10.995	0.141	9.202	0.410
	J230950.90+632622.5	111.862	2.773	13.095	0.027	11.856	0.021	9.784	0.055	6.958	0.063
	J231004.96+633137.3	111.920	2.843	13.516	0.027	12.371	0.025	9.476	0.038	6.761	0.075
	J231004.97+633129.2	111.919	2.841	15.128	0.051	14.069	0.054	10.694	0.091	7.788	0.170
	J231005.78+633115.7	111.919	2.837	14.584	0.052	13.926	0.052	10.883	0.118	7.703	0.169
	J231005.79+632941.0	111.909	2.813	13.575	0.030	12.890	0.030	10.816	0.090	9.001	0.481
	J231026.19+633339.2	111.969	2.860	13.461	0.024	11.952	0.022	9.392	0.038	6.474	0.046
	J231029.83+633357.8	111.978	2.862	15.387	0.131	14.302	0.050	9.456	0.035	5.879	0.038
	J231032.29+633346.7	111.981	2.857	14.813	0.066	12.792	0.027	10.500	0.066	7.465	0.090
	J231040.27+633408.6	111.997	2.857	15.153	0.035	13.513	0.031	10.110	0.053	7.126	0.093
	J231040.77+633410.8	111.998	2.858	15.250	0.038	14.334	0.039	10.866	0.095	7.329	0.093
[BKP2003]10656	J021408.57+630916.9	132.111	1.767	16.360	0.066	14.953	0.065	11.452	0.156	8.306	0.266
[BKP2003]10658	J225005.10+630959.5	109.728	3.449	15.069	0.034	14.118	0.034	11.659	0.139	9.166	0.383
[BKP2003]10661	J223912.07+641532.0	109.174	4.979	8.937	0.023	7.732	0.021	5.379	0.014	3.585	0.018
	J223925.93+641230.8	109.172	4.922	13.344	0.027	11.847	0.021	8.891	0.019	5.736	0.028
	J223936.08+641504.2	109.209	4.951	12.977	0.032	12.057	0.022	8.820	0.021	6.295	0.034
	J223937.52+641205.6	109.187	4.906	16.297	0.107	15.495	0.075	10.076	0.033	7.877	0.088
[BKP2003]10664	J030026.65+594102.2	138.560	0.785	13.318	0.026	12.596	0.025	10.029	0.062	7.601	0.132
	J030028.59+594105.4	138.563	0.788	15.535	0.071	14.641	0.064	11.525	0.208	8.403	0.282
[BKP2003]10666	J023000.73+620519.1	134.191	1.391	14.940	0.064	14.327	0.062	9.651	0.074	7.552	0.170
[BKP2003]10667	J010250.59+644641.9	124.147	1.934	13.750	0.035	12.112	0.030	8.640	0.033	5.735	0.054
	J010250.74+644647.0	124.147	1.935	14.598	0.058	13.563	0.076	10.527	0.144	8.116	0.428
	J010257.02+644659.5	124.158	1.939	12.391	0.024	11.143	0.021	8.722	0.028	6.528	0.057
[BKP2003]10670	J231513.49+630240.4	112.277	2.181	15.304	0.047	14.588	0.055	10.638	0.088	7.979	0.197
	J231515.34+630504.7	112.295	2.217	14.519	0.038	13.867	0.038	9.939	0.101	8.631	0.330
[BKP2003]10674	J003926.45+660905.0	121.718	3.308	16.506	0.081	14.110	0.044	10.991	0.102	7.422	0.133
	J003927.19+660857.3	121.719	3.306	15.480	0.044	13.410	0.032	11.153	0.116	6.683	0.073
	J003944.68+660837.3	121.748	3.299	13.546	0.026	12.419	0.024	9.409	0.036	6.745	0.079
	J003947.29+660847.8	121.753	3.302	13.038	0.023	12.226	0.021	9.589	0.042	7.233	0.109
	J003949.47+660917.4	121.757	3.310	13.343	0.024	12.716	0.024	9.639	0.044	6.598	0.065
[BKP2003]10681	J020433.24+624716.4	131.180	1.093	12.877	0.030	12.145	0.023	9.470	0.045	7.213	0.104
	J020449.13+625035.5	131.193	1.154	14.496	0.039	13.672	0.038	9.860	0.052	7.927	0.194
	J020506.52+624935.9	131.230	1.148	11.943	0.023	11.135	0.021	7.936	0.019	6.472	0.069
[BKP2003]10683	J020703.03+624612.0	131.458	1.157	15.655	0.046	14.124	0.041	10.556	0.080	7.617	0.135
[BKP2003]10684	J021049.90+624910.4	131.857	1.332	9.774	0.020	8.923	0.015	4.537	0.014	1.098	0.013
[BKP2003]10685	J005756.19+644822.7	123.624	1.943	13.469	0.036	12.881	0.035	9.083	0.041	7.633	0.173
[BKP2003]10686	J010637.34+645441.8	124.542	2.087	14.426	0.033	13.307	0.032	10.559	0.200	7.638	0.149
[BKP2003]10687	J010610.87+650044.9	124.489	2.185	13.178	0.025	12.515	0.025	9.345	0.036	7.105	0.091
	J010611.18+650009.2	124.490	2.176	15.495	0.057	14.916	0.075	11.604	0.207	8.291	null
[BKP2003]10688	J022107.24+632112.4	132.788	2.211	14.111	0.031	13.330	0.031	10.844	0.116	8.086	0.268
[BKP2003]10692	J221349.85+595429.4	104.351	2.850	12.090	0.026	11.509	0.023	8.919	0.049	7.684	0.293
	J221354.93+595300.1	104.345	2.824	9.104	0.021	8.057	0.019	4.708	0.013	2.533	0.018
	J221355.31+595445.6	104.362	2.847	14.870	0.077	14.042	0.048	8.857	0.042	6.485	0.078
	J221358.29+595723.3	104.392	2.880	12.526	0.025	11.878	0.024	6.524	0.016	4.852	0.034
	J221401.25+595205.6	104.348	2.804	10.271	0.023	9.415	0.020	6.327	0.017	4.583	0.026
	J221401.91+595650.0	104.393	2.868	13.730	0.041	12.802	0.033	9.528	0.049	6.932	0.108
	J221402.80+595333.0	104.364	2.822	15.215	0.054	14.335	0.057	10.504	0.200	5.806	0.049
	J221402.85+595142.2	104.347	2.796	14.036	0.043	13.422	0.042	9.519	0.053	6.555	0.096
	J221403.92+595341.7	104.367	2.823	13.230	0.062	11.196	0.049	8.602	0.079	5.634	0.106
	J221403.94+595348.3	104.368	2.824	11.084	0.023	9.485	0.020	6.409	0.018	3.792	0.026
	J221410.52+594911.7	104.336	2.753	7.879	0.024	6.733	0.020	3.730	0.015	1.217	0.015
	J221412.04+600319.0	104.472	2.945	14.038	0.041	13.091	0.033	10.287	0.068	7.404	0.114

Table A.2 (Continued.)

Star-forming molecular cloud	AllWISE source	Coordinate l	b	3.4 μm [mag]	$\sigma_{3.4}$ [mag]	4.6 μm [mag]	$\sigma_{4.6}$ [mag]	12 μm [mag]	σ_{12} [mag]	22 μm [mag]	σ_{22} [mag]
	J221415.49+595334.4	104.386	2.807	11.903	0.024	11.127	0.019	8.717	0.033	6.301	0.053
[BKP2003]10696	J024129.21+604327.8	135.988	0.673	10.677	0.022	10.159	0.020	5.148	0.015	2.779	0.018
[BKP2003]10700	J020057.89+631539.8	130.659	1.437	13.433	0.030	12.354	0.027	9.018	0.032	5.812	0.052
	J020133.26+631420.4	130.729	1.434	14.986	0.174	14.277	0.044	11.162	0.141	8.735	0.380
[BKP2003]10701	J021347.71+625426.9	132.151	1.519	14.447	0.033	13.899	0.039	10.878	0.111	8.553	0.423
[BKP2003]10703	J012338.00+645249.8	126.342	2.222	13.076	0.026	11.952	0.022	9.556	0.041	7.132	0.128
	J012347.52+645748.9	126.348	2.307	14.727	0.033	13.674	0.033	11.463	0.176	7.284	0.107
	J012352.23+645459.2	126.363	2.261	14.158	0.029	13.580	0.035	10.509	0.104	8.358	0.325
	J012356.46+645157.4	126.376	2.212	14.678	0.036	13.368	0.033	10.668	0.092	8.471	0.411
	J012359.17+645635.5	126.371	2.289	13.909	0.028	13.347	0.033	10.611	0.107	8.142	0.253
[BKP2003]10705	J010721.57+650410.5	124.610	2.250	11.570	0.023	10.277	0.021	7.745	0.019	5.497	0.040
[BKP2003]10707	J024401.92+624822.3	135.396	2.692	10.647	0.020	9.453	0.020	6.559	0.015	4.114	0.022
[BKP2003]10708	J225340.98+623331.4	109.826	2.722	11.295	0.023	10.469	0.020	8.137	0.024	6.333	0.053
	J225342.66+623641.2	109.852	2.768	12.184	0.023	11.109	0.021	8.298	0.029	6.033	0.059
	J225345.45+623604.7	109.852	2.757	11.608	0.023	10.778	0.020	8.684	0.026	6.315	0.073
	J225347.49+623220.5	109.828	2.699	12.509	0.024	11.801	0.020	9.464	0.074	7.257	0.095
	J225348.73+623602.1	109.858	2.753	9.464	0.028	8.816	0.020	6.763	0.015	4.936	0.030
	J225349.09+623344.4	109.841	2.719	12.275	0.024	11.472	0.021	9.112	0.031	7.000	0.083
	J225349.72+623519.5	109.854	2.742	9.259	0.017	8.560	0.014	5.961	0.012	3.782	0.027
	J225350.10+623502.3	109.853	2.737	10.466	0.026	9.866	0.021	7.359	0.018	4.266	0.027
	J225351.06+623518.3	109.856	2.741	9.748	0.026	8.999	0.021	6.348	0.014	3.858	0.026
	J225352.49+623531.7	109.860	2.743	10.862	0.023	10.242	0.020	8.070	0.022	5.173	0.035
	J225355.45+623714.1	109.878	2.766	11.781	0.024	11.188	0.022	9.139	0.038	7.939	0.168
	J225356.41+623441.9	109.861	2.727	11.040	0.023	10.074	0.019	7.483	0.024	4.897	0.037
	J225358.39+623348.4	109.858	2.712	12.874	0.038	12.336	0.022	7.887	0.026	5.943	0.052
	J225359.28+623320.5	109.856	2.704	13.352	0.031	12.852	0.031	10.291	0.088	8.056	null
	J225403.41+623254.8	109.860	2.694	12.863	0.025	12.329	0.025	9.709	0.049	7.199	0.087
	J225405.54+623534.3	109.883	2.732	9.602	0.020	8.928	0.019	6.634	0.015	4.655	0.028
	J225407.89+623558.4	109.890	2.736	11.887	0.024	11.309	0.022	9.226	0.034	6.852	0.071
	J225415.94+623343.6	109.888	2.696	12.720	0.023	12.011	0.021	9.654	0.036	8.363	0.212
[BKP2003]10709	J225251.20+624105.0	109.795	2.877	11.764	0.023	11.017	0.020	8.473	0.021	6.631	0.046
	J225301.41+623951.5	109.804	2.850	14.567	0.031	13.675	0.030	10.846	0.074	8.467	0.171
	J225313.15+623855.7	109.817	2.827	13.838	0.036	11.867	0.023	8.754	0.027	6.146	0.039
	J225327.71+623805.9	109.836	2.802	13.256	0.026	12.288	0.024	10.172	0.059	8.990	0.310
	J225336.56+623649.0	109.842	2.775	8.309	0.029	7.533	0.022	5.432	0.016	3.919	0.028
	J225337.59+623803.0	109.853	2.793	11.867	0.026	11.076	0.022	8.731	0.032	6.439	0.095
	J225340.12+623910.1	109.866	2.808	11.217	0.023	10.322	0.020	7.705	0.019	5.642	0.037
	J225352.17+623746.3	109.876	2.777	11.406	0.022	10.693	0.019	8.013	0.024	5.764	0.082
	J225409.06+624117.4	109.931	2.815	11.809	0.023	11.218	0.021	9.144	0.030	6.854	0.077
	J225422.60+623845.6	109.936	2.766	13.808	0.029	12.793	0.026	10.274	0.065	7.776	0.139
	J225425.29+623931.0	109.946	2.775	11.863	0.022	10.194	0.020	7.379	0.021	4.833	0.026
	J225426.08+623805.6	109.937	2.753	15.291	0.036	14.673	0.049	10.676	0.099	8.170	0.311
	J225429.33+624427.9	109.989	2.846	16.173	0.076	15.108	0.067	10.817	0.083	7.957	0.131
	J225433.48+624324.4	109.988	2.827	13.582	0.026	12.535	0.025	9.820	0.052	6.487	0.050
	J225434.09+624053.6	109.971	2.788	13.769	0.028	12.936	0.026	10.889	0.141	8.249	0.351
	J225435.64+624324.6	109.992	2.825	13.590	0.026	12.548	0.025	9.964	0.044	6.868	0.062
	J225436.12+624304.6	109.990	2.819	10.559	0.022	9.863	0.019	7.731	0.018	5.716	0.036
	J225446.12+623840.8	109.976	2.745	14.170	0.027	13.650	0.032	9.332	0.062	7.398	0.168
	J225447.28+623843.6	109.978	2.745	15.125	0.038	13.707	0.033	10.380	0.148	7.254	0.152
	J225448.00+623855.2	109.981	2.747	14.669	0.037	13.640	0.035	10.137	0.117	6.825	0.083
	J225450.35+623821.1	109.981	2.737	11.032	0.022	10.383	0.020	8.113	0.021	5.863	0.043
	J225506.58+623534.7	109.989	2.682	12.119	0.025	11.529	0.023	8.592	0.045	6.814	0.159
[BKP2003]10710	J225319.75+624534.1	109.877	2.921	13.050	0.032	11.094	0.022	8.544	0.026	5.745	0.034

Table A.2 (Continued.)

Star-forming molecular cloud	AllWISE source	Coordinate l	b	3.4 μm [mag]	$\sigma_{3.4}$ [mag]	4.6 μm [mag]	$\sigma_{4.6}$ [mag]	12 μm [mag]	σ_{12} [mag]	22 μm [mag]	σ_{22} [mag]
	J225326.13+624547.3	109.890	2.918	12.739	0.051	11.141	0.024	8.021	0.023	4.910	0.024
[BKP2003]10711	J221247.34+594407.0	104.144	2.782	14.209	0.058	13.502	0.049	10.254	0.071	7.590	0.131
[BKP2003]10713	J221252.26+595423.0	104.250	2.917	14.177	0.036	13.078	0.027	10.406	0.082	7.395	0.101
	J221259.09+595226.4	104.244	2.882	15.933	0.072	14.724	0.058	10.393	0.066	7.239	0.091
	J221259.74+595247.8	104.248	2.886	15.232	0.038	14.350	0.043	10.904	0.089	7.197	0.093
	J221301.10+595223.7	104.247	2.879	13.156	0.040	12.593	0.028	7.541	0.015	5.892	0.042
	J221314.94+595439.0	104.292	2.894	11.460	0.025	10.811	0.021	6.054	0.013	4.365	0.025
	J221316.60+595428.2	104.293	2.889	13.075	0.034	12.056	0.025	8.802	0.030	5.813	0.047
	J221322.22+595300.2	104.289	2.862	13.894	0.050	13.254	0.030	9.096	0.054	6.377	0.063
[BKP2003]10715	J232749.66+660423.3	114.585	4.566	15.625	0.041	14.704	0.050	11.317	0.093	8.909	0.251
[BKP2003]10717	J020608.00+622644.7	131.450	0.816	14.412	0.030	13.795	0.038	11.428	0.189	8.234	0.233
	J020626.53+622822.6	131.477	0.852	16.993	0.123	16.202	0.195	11.472	0.204	8.051	0.233
	J020648.22+622935.2	131.511	0.883	15.070	0.046	14.308	0.054	10.794	0.100	8.764	0.488
[BKP2003]10719	J013045.12+640110.2	127.222	1.476	14.750	0.045	12.392	0.034	8.613	0.032	5.232	0.045
	J013045.62+640058.5	127.223	1.473	13.843	0.027	12.761	0.029	9.591	0.046	5.636	0.038
	J013046.00+640106.0	127.224	1.475	14.224	0.035	12.321	0.033	8.824	0.039	6.119	0.091
	J013059.41+640131.4	127.247	1.486	13.739	0.026	12.245	0.024	9.975	0.053	7.170	0.100
[BKP2003]10720	J020002.15+632424.8	130.520	1.550	15.085	0.050	13.631	0.037	10.669	0.102	7.489	0.170
	J020004.46+632313.2	130.529	1.532	15.471	0.050	14.384	0.049	11.302	0.164	8.597	0.308
[BKP2003]10724	J221300.67+601248.1	104.439	3.159	13.559	0.028	12.470	0.024	9.672	0.038	6.643	0.058
	J221319.35+601129.1	104.459	3.119	14.434	0.029	13.634	0.028	10.761	0.086	8.121	0.197
[BKP2003]10725	J221336.25+600713.0	104.447	3.041	15.117	0.038	14.284	0.042	11.319	0.128	8.710	null
[BKP2003]10728	J024108.19+602427.5	136.079	0.367	15.243	0.045	14.594	0.055	10.682	0.109	8.149	null
[BKP2003]10730	J014754.00+633617.6	129.158	1.418	15.023	0.146	14.405	0.047	11.534	0.194	9.081	null
	J014812.13+633604.8	129.192	1.422	15.049	0.038	14.469	0.048	10.386	0.073	8.198	0.232
[BKP2003]10731	J015206.74+634727.7	129.571	1.704	14.083	0.029	13.548	0.032	9.051	0.029	6.198	0.055
	J015208.78+634714.0	129.575	1.701	11.585	0.022	11.008	0.021	6.073	0.014	4.134	0.026
[BKP2003]10732	J013313.23+641759.0	127.444	1.795	12.649	0.024	11.186	0.021	7.903	0.018	5.025	0.032
	J013313.28+641743.8	127.444	1.791	12.119	0.035	11.446	0.028	6.570	0.013	4.721	0.027
	J013343.84+642047.3	127.491	1.850	14.211	0.028	13.325	0.031	10.464	0.079	6.814	0.082
	J013345.83+642059.8	127.494	1.854	13.356	0.025	12.048	0.023	8.910	0.031	5.246	0.034
	J013348.35+642052.9	127.498	1.853	15.039	0.035	13.994	0.036	10.724	0.109	6.891	0.086
	J013405.13+642234.8	127.524	1.886	15.390	0.049	14.651	0.058	11.714	0.215	8.910	null
	J013415.73+642203.5	127.544	1.880	13.909	0.031	12.405	0.026	10.231	0.075	7.325	0.132
	J013416.87+642157.9	127.546	1.879	13.634	0.026	12.716	0.027	10.045	0.059	6.677	0.067
	J013420.93+642218.0	127.552	1.886	14.677	0.040	14.056	0.051	9.105	0.037	7.022	0.090
	J013421.26+642214.6	127.553	1.885	15.522	0.051	14.302	0.052	9.607	0.055	7.036	0.113
	J013422.74+642142.7	127.557	1.877	13.968	0.029	12.780	0.026	9.792	0.057	7.340	0.143
	J013430.41+642249.9	127.568	1.897	14.899	0.032	14.021	0.037	11.177	0.147	8.102	0.219
	J013432.78+642259.5	127.572	1.901	13.995	0.027	13.070	0.027	10.154	0.063	6.870	0.077
	J013432.80+642316.2	127.571	1.905	12.914	0.024	11.733	0.021	9.086	0.032	6.317	0.051
[BKP2003]10733	J014554.78+640518.7	128.841	1.844	14.506	0.036	13.560	0.037	10.487	0.082	8.032	0.218
	J014556.06+640509.5	128.844	1.842	14.050	0.031	12.728	0.026	9.880	0.051	7.580	0.145
	J014610.75+640701.4	128.863	1.878	14.038	0.027	12.644	0.024	9.320	0.035	7.149	0.113
[BKP2003]10734	J014825.23+640920.8	129.094	1.968	13.476	0.030	12.546	0.027	8.828	0.031	6.042	0.047
	J014828.77+640900.7	129.101	1.964	11.439	0.023	10.841	0.020	5.650	0.014	3.834	0.024
	J014830.18+640921.6	129.102	1.970	12.706	0.023	12.090	0.023	7.866	0.024	5.480	0.035
	J014833.94+640903.8	129.110	1.967	13.591	0.030	12.226	0.024	8.619	0.032	5.771	0.049
	J014835.61+640908.2	129.113	1.969	13.912	0.031	13.043	0.029	9.224	0.039	5.969	0.048
	J014839.77+640946.8	129.118	1.981	12.686	0.025	11.725	0.021	9.444	0.041	6.709	0.085
	J014842.28+641031.7	129.120	1.994	12.850	0.030	11.892	0.023	9.776	0.049	7.494	0.165
[BKP2003]10735	J014438.30+640228.5	128.714	1.768	14.700	0.047	13.196	0.035	9.774	0.057	6.040	0.076
	J014438.81+640241.6	128.714	1.772	14.652	0.031	13.376	0.029	10.592	0.088	6.865	0.083

Table A.2 (Continued.)

Star-forming molecular cloud	AllWISE source	Coordinate l	b	3.4 μm [mag]	$\sigma_{3.4}$ [mag]	4.6 μm [mag]	$\sigma_{4.6}$ [mag]	12 μm [mag]	σ_{12} [mag]	22 μm [mag]	σ_{22} [mag]
	J014439.56+640213.7	128.717	1.765	13.824	0.027	12.531	0.024	9.583	0.040	6.036	0.049
	J014440.59+640455.3	128.710	1.809	14.868	0.040	14.201	0.045	11.205	0.160	8.659	null
	J014441.61+640316.4	128.717	1.783	13.823	0.031	12.888	0.027	10.141	0.065	8.490	0.323
	J014451.13+641236.5	128.702	1.939	12.675	0.037	11.706	0.034	8.603	0.033	5.752	0.049
	J014456.01+635311.1	128.778	1.624	15.057	0.042	14.297	0.044	10.626	0.131	8.506	0.342
	J014501.50+641216.7	128.722	1.937	13.282	0.027	12.359	0.023	9.359	0.039	7.070	0.115
	J014516.42+640946.1	128.757	1.902	14.643	0.032	13.941	0.037	9.478	0.041	7.043	0.108
	J014527.24+641434.3	128.760	1.984	11.904	0.025	10.940	0.021	7.079	0.016	4.592	0.032
	J014531.61+641503.1	128.766	1.994	13.975	0.030	13.407	0.032	8.125	0.031	5.767	0.060
	J014531.62+641451.8	128.766	1.991	13.994	0.030	13.041	0.027	8.223	0.033	5.586	0.049
	J014532.98+641515.0	128.767	1.997	12.881	0.027	12.341	0.025	7.272	0.026	4.831	0.043
	J014536.86+641555.3	128.772	2.010	11.384	0.024	10.862	0.022	5.694	0.022	1.416	0.017
	J014538.85+641908.2	128.764	2.063	14.127	0.045	13.431	0.037	9.620	0.061	6.707	0.084
	J014539.89+641601.1	128.777	2.012	8.428	0.014	7.856	0.017	3.925	0.012	0.159	0.014
	J014540.14+641608.5	128.777	2.015	8.266	0.024	6.995	0.021	3.830	0.016	0.806	0.021
	J014541.17+641632.1	128.777	2.021	12.950	0.029	12.105	0.027	6.946	0.022	3.323	0.018
	J014542.55+641906.4	128.771	2.064	11.077	0.024	10.518	0.021	7.903	0.022	5.518	0.039
	J014551.23+641605.7	128.797	2.018	11.299	0.024	9.811	0.021	6.755	0.016	4.230	0.023
	J014552.52+641608.6	128.799	2.019	11.269	0.022	10.302	0.020	7.104	0.016	4.754	0.027
	J014607.43+641457.6	128.829	2.006	12.860	0.026	11.926	0.022	8.870	0.032	6.229	0.068
	J014608.79+641829.0	128.819	2.064	14.580	0.033	13.012	0.029	9.845	0.053	7.672	0.186
	J014615.41+641914.4	128.828	2.078	15.026	0.041	14.347	0.049	11.010	0.124	8.129	0.282
[BKP2003]10736	J014646.00+642308.8	128.869	2.154	15.246	0.043	14.532	0.060	10.743	0.097	7.673	0.208
	J014712.97+642045.7	128.925	2.125	13.448	0.027	12.503	0.028	9.592	0.039	7.154	0.110
	J014715.07+642129.5	128.926	2.138	13.988	0.033	13.206	0.038	8.579	0.023	6.340	0.060
	J014716.10+642136.5	128.927	2.140	13.596	0.030	12.842	0.032	10.833	0.139	7.219	0.150
	J014716.33+642132.2	128.928	2.139	13.284	0.028	12.413	0.027	8.575	0.025	6.334	0.065
	J014716.60+642129.3	128.928	2.139	13.672	0.030	12.875	0.033	8.370	0.024	6.738	0.097
[BKP2003]10737	J005956.61+650546.4	123.828	2.239	13.831	0.026	13.275	0.029	10.919	0.132	8.464	0.324
[BKP2003]10739	J014055.46+645428.0	128.150	2.539	14.326	0.030	12.782	0.027	10.307	0.086	7.090	0.100
[BKP2003]10740	J221041.20+593618.2	103.852	2.827	15.812	0.066	14.648	0.056	11.168	0.158	8.546	0.270
	J221051.71+593659.3	103.877	2.823	14.766	0.050	13.487	0.042	10.441	0.074	7.162	0.126
	J221051.98+593705.5	103.878	2.825	14.284	0.036	13.664	0.042	11.272	0.150	7.117	0.123
	J221117.84+593836.2	103.937	2.814	15.151	0.068	13.039	0.028	8.740	0.027	5.688	0.043
[BKP2003]10743	J234723.21+660408.2	116.492	4.001	13.134	0.025	11.832	0.023	9.174	0.027	6.410	0.046
[BKP2003]10744	J232503.18+654329.0	114.203	4.328	14.811	0.028	13.739	0.029	11.092	0.079	8.567	0.203
[BKP2003]10750	J015109.02+633544.2	129.512	1.489	14.451	0.092	13.152	0.035	9.480	0.050	6.591	0.076
[BKP2003]10752	J014722.46+634923.5	129.054	1.618	14.775	0.048	13.716	0.039	11.250	0.158	8.750	0.442
[BKP2003]10753	J011140.19+642332.0	125.117	1.606	13.393	0.028	12.756	0.029	9.262	0.042	6.889	0.100
	J011141.78+642441.8	125.118	1.626	14.337	0.058	12.779	0.029	9.334	0.041	6.622	0.078
	J011141.89+642448.9	125.118	1.628	15.382	0.056	14.765	0.076	10.318	0.094	6.963	0.104
[BKP2003]10755	J012149.14+644213.3	126.172	2.023	14.623	0.030	13.979	0.034	9.746	0.054	7.765	0.173
	J012153.46+644001.7	126.184	1.988	14.934	0.032	13.958	0.035	11.197	0.164	8.349	0.248
	J012209.47+644326.2	126.205	2.048	11.996	0.023	10.695	0.020	7.081	0.016	4.899	0.026
	J012241.18+644223.9	126.263	2.037	16.818	0.127	15.044	0.072	11.211	0.171	8.741	0.414
	J012249.63+644509.9	126.273	2.085	16.010	0.062	14.202	0.042	10.821	0.106	7.584	0.132
[BKP2003]10756	J014641.40+641422.8	128.892	2.009	11.326	0.023	10.518	0.020	7.140	0.016	5.074	0.032
[BKP2003]10758	J010055.33+650610.4	123.931	2.250	14.715	0.038	14.111	0.047	11.020	0.173	8.862	null
[BKP2003]10760	J220825.34+592404.7	103.499	2.827	14.775	0.029	13.789	0.032	11.027	0.107	8.281	0.215
[BKP2003]10761	J220837.71+592641.0	103.546	2.847	15.048	0.058	13.489	0.035	10.494	0.082	7.944	0.163
[BKP2003]10762	J220628.99+610313.9	104.272	4.308	14.835	0.031	14.076	0.038	11.752	0.205	8.673	null
	J220715.93+610454.0	104.365	4.275	15.286	0.043	14.603	0.052	10.380	0.061	8.728	0.409
[BKP2003]10765	J011107.25+641222.4	125.072	1.416	13.441	0.030	12.877	0.028	10.514	0.090	7.876	0.163

Table A.2 (Continued.)

Star-forming molecular cloud	AllWISE source	Coordinate l	b	3.4 μm [mag]	$\sigma_{3.4}$ [mag]	4.6 μm [mag]	$\sigma_{4.6}$ [mag]	12 μm [mag]	σ_{12} [mag]	22 μm [mag]	σ_{22} [mag]
[BKP2003]10766	J014510.78+634530.9	128.831	1.504	14.312	0.029	13.045	0.029	9.901	0.053	7.122	0.093
	J014523.20+634651.7	128.848	1.531	14.231	0.030	13.060	0.030	10.374	0.088	8.185	0.302
[BKP2003]10770	J221240.73+614526.0	105.287	4.452	13.270	0.025	12.056	0.022	9.352	0.029	6.515	0.048
	J221241.34+614513.5	105.286	4.448	12.907	0.023	12.084	0.022	8.779	0.023	6.575	0.049
	J221244.12+614516.9	105.291	4.446	13.834	0.026	13.109	0.027	11.008	0.083	7.898	0.128
	J221256.56+614434.8	105.304	4.422	13.235	0.026	11.853	0.022	9.440	0.030	7.101	0.074
[BKP2003]10771	J222518.59+630624.4	107.256	4.772	16.598	0.103	14.184	0.040	10.381	0.078	7.688	0.123
[BKP2003]10774	J014325.27+632903.2	128.695	1.196	14.772	0.033	13.811	0.033	11.337	0.157	8.733	null
	J014409.73+633106.4	128.769	1.246	14.592	0.032	13.287	0.028	10.384	0.071	7.897	0.193
	J014419.01+633619.0	128.768	1.334	13.557	0.027	12.623	0.026	9.926	0.072	6.996	0.080
	J014421.74+633625.8	128.773	1.337	13.172	0.025	11.613	0.022	8.488	0.026	5.133	0.028
	J014425.33+633636.8	128.779	1.342	9.984	0.023	8.028	0.019	5.546	0.015	3.015	0.020
	J014426.32+633520.5	128.785	1.321	13.400	0.025	12.055	0.021	8.811	0.028	6.766	0.084
	J014438.57+633154.6	128.819	1.270	14.526	0.033	13.192	0.031	9.348	0.036	7.360	0.123
	J014503.06+634054.5	128.833	1.426	14.882	0.038	14.324	0.050	11.525	0.204	8.342	null
	J014506.09+633541.2	128.856	1.342	14.135	0.028	13.018	0.026	10.661	0.095	7.423	0.141
	J014508.14+633411.7	128.865	1.319	14.220	0.032	13.554	0.033	11.124	0.134	8.362	0.294
	J014510.46+633428.9	128.868	1.324	12.085	0.023	10.923	0.020	8.640	0.029	6.840	0.084
	J014532.78+633541.6	128.904	1.352	13.391	0.032	12.527	0.027	10.141	0.059	7.388	0.139
	J014535.07+633555.8	128.908	1.357	13.650	0.027	12.516	0.024	9.859	0.046	7.193	0.093
[BKP2003]10775	J011157.51+642023.5	125.152	1.557	14.211	0.034	13.482	0.031	9.102	0.039	6.454	0.077
	J011201.15+642028.8	125.158	1.559	11.953	0.024	11.387	0.022	8.867	0.035	6.586	0.071
	J011202.41+642040.9	125.160	1.562	13.542	0.028	12.920	0.029	9.347	0.037	6.990	0.098
[BKP2003]10776	J014541.75+634850.3	128.875	1.570	13.441	0.028	12.325	0.024	9.694	0.054	6.525	0.077
	J014542.05+634859.3	128.875	1.573	12.832	0.025	12.130	0.024	9.519	0.048	6.935	0.093
	J014552.32+634947.1	128.891	1.590	14.412	0.037	13.882	0.041	10.329	0.086	8.566	0.472
	J014553.01+634854.7	128.895	1.576	14.806	0.038	13.588	0.033	10.555	0.079	8.466	0.332
[BKP2003]10777	J003328.40+644348.6	121.015	1.925	11.622	0.023	10.829	0.021	8.267	0.021	6.004	0.055
	J003337.51+644350.7	121.031	1.925	16.011	0.056	14.076	0.037	10.836	0.100	7.504	0.133
[BKP2003]10780	J220347.25+585927.1	102.777	2.844	15.127	0.041	14.523	0.048	12.100	0.216	9.252	0.442
	J220419.64+590754.0	102.917	2.916	14.343	0.037	12.831	0.026	10.241	0.061	7.120	0.085
[BKP2003]10783	J221055.96+615119.2	105.174	4.650	14.084	0.031	13.280	0.030	8.560	0.025	6.472	0.049
[BKP2003]10784	J010955.73+642139.6	124.931	1.561	16.462	0.082	15.722	0.118	11.477	0.206	8.684	null
	J011023.83+642235.6	124.981	1.580	13.422	0.027	12.799	0.029	10.670	0.098	8.905	0.478
	J011058.05+642708.7	125.036	1.661	13.452	0.027	12.044	0.023	8.616	0.028	6.221	0.059
[BKP2003]10785	J015924.37+632736.4	130.438	1.583	14.279	0.033	13.668	0.037	9.681	0.051	7.907	0.206
[BKP2003]10787	J002045.36+644200.1	119.660	2.023	15.061	0.040	14.546	0.049	10.447	0.073	8.522	0.278
[BKP2003]10789	J220722.77+591120.4	103.267	2.732	13.344	0.024	12.329	0.023	9.956	0.054	7.731	0.133
[BKP2003]10792	J011118.39+645554.3	125.036	2.141	14.428	0.028	13.212	0.027	10.716	0.097	6.848	0.080
	J011120.06+645717.2	125.037	2.164	13.541	0.027	12.703	0.029	9.973	0.047	7.616	0.131
[BKP2003]10792	J011121.48+645634.0	125.040	2.153	15.628	0.061	14.906	0.069	11.029	0.140	8.389	0.305
[BKP2003]10793	J004830.36+650412.8	122.623	2.200	14.270	0.036	12.916	0.028	9.781	0.053	6.999	0.082
	J004838.49+650234.5	122.637	2.173	17.208	0.136	14.741	0.051	10.873	0.137	7.077	0.095
[BKP2003]10794	J010751.15+652121.9	124.644	2.539	8.458	0.025	7.246	0.020	1.410	0.008	-2.147	0.002
	J010753.17+652108.3	124.647	2.535	10.534	0.054	9.737	0.038	5.214	0.023	0.466	0.009
[BKP2003]10795	J010653.78+652032.5	124.545	2.519	12.752	0.025	11.500	0.022	9.046	0.034	6.629	0.075
	J010658.60+652057.7	124.553	2.527	12.146	0.042	11.249	0.028	6.090	0.015	4.056	0.027
	J010701.18+652048.7	124.557	2.524	10.853	0.018	10.351	0.022	7.836	0.021	4.422	0.032
	J010704.56+652053.9	124.563	2.526	11.553	0.033	9.953	0.022	6.684	0.016	4.768	0.032
[BKP2003]10796	J010420.48+651404.5	124.284	2.397	13.211	0.024	12.271	0.023	9.767	0.051	7.880	0.183
	J010421.11+651426.4	124.285	2.403	14.788	0.033	13.728	0.033	11.168	0.123	8.981	0.495
	J010453.56+652008.0	124.336	2.501	15.281	0.035	14.340	0.042	11.125	0.168	8.505	0.312
	J010512.57+651651.8	124.372	2.448	14.977	0.031	13.786	0.033	11.295	0.148	8.736	0.448

Table A.2 (Continued.)

Star-forming molecular cloud	AllWISE source	Coordinate l	b	3.4 μm [mag]	$\sigma_{3.4}$ [mag]	4.6 μm [mag]	$\sigma_{4.6}$ [mag]	12 μm [mag]	σ_{12} [mag]	22 μm [mag]	σ_{22} [mag]
	J010545.40+651712.4	124.429	2.457	15.013	0.032	13.740	0.031	11.116	0.134	8.460	null
	J010601.25+652144.1	124.452	2.534	14.807	0.035	13.801	0.039	11.207	0.150	9.012	0.453
	J010607.71+652030.5	124.465	2.514	14.857	0.039	13.815	0.044	10.123	0.062	7.587	0.146
	J010609.38+652055.9	124.467	2.521	13.394	0.027	12.159	0.024	9.705	0.042	6.781	0.067
	J010609.85+652034.4	124.468	2.515	14.547	0.035	13.224	0.034	9.779	0.044	6.962	0.085
	J010624.58+652058.6	124.494	2.523	11.704	0.023	9.960	0.020	6.641	0.015	4.080	0.025
	J010630.79+651839.8	124.507	2.485	14.044	0.027	11.708	0.022	7.514	0.017	4.201	0.021
	J010631.37+651903.9	124.507	2.492	10.348	0.023	9.237	0.020	6.705	0.016	4.241	0.021
	J010634.81+652010.1	124.512	2.511	12.083	0.023	10.929	0.020	8.742	0.026	6.554	0.062
[BKP2003]10797	J215832.45+593809.4	102.632	3.762	11.487	0.022	10.975	0.021	5.536	0.013	3.457	0.023
	J215832.69+593400.6	102.590	3.707	15.003	0.066	13.316	0.030	10.476	0.071	7.317	0.088
	J215834.25+593800.9	102.633	3.758	10.542	0.024	9.912	0.021	4.916	0.018	2.412	0.025
	J215841.04+593715.6	102.637	3.740	14.548	0.031	13.319	0.028	8.748	0.030	5.988	0.047
	J215857.91+593709.4	102.664	3.716	15.150	0.067	13.861	0.048	10.493	0.083	7.625	0.149
	J215858.98+593235.1	102.619	3.655	13.468	0.039	12.579	0.025	9.912	0.043	7.053	0.074
	J215919.14+594010.0	102.730	3.729	13.763	0.027	12.971	0.026	10.476	0.061	7.785	0.118
	J215919.96+594125.5	102.745	3.745	14.101	0.030	13.249	0.028	11.019	0.088	9.257	null
	J215920.92+594217.7	102.755	3.755	13.357	0.026	12.756	0.025	10.086	0.051	9.188	0.485
[BKP2003]10798	J021620.61+631735.7	132.302	1.977	14.920	0.069	14.183	0.067	10.886	0.139	8.443	null
	J021621.32+631736.6	132.303	1.977	14.027	0.032	13.459	0.034	10.402	0.082	8.625	0.442
[BKP2003]10803	J220734.11+592100.9	103.381	2.849	15.379	0.039	14.454	0.043	11.664	0.164	9.185	0.488
[BKP2003]10804	J001611.34+642156.3	119.130	1.754	13.742	0.032	13.198	0.032	10.892	0.074	8.797	null
	J001611.57+642157.7	119.130	1.755	13.951	0.031	13.361	0.029	11.060	0.083	9.008	null
	J001618.54+641736.5	119.133	1.681	13.989	0.028	12.915	0.027	10.365	0.042	7.649	0.098
	J001626.91+642014.9	119.154	1.723	14.255	0.025	13.478	0.027	10.813	0.066	8.265	0.170
	J001633.14+642214.7	119.170	1.754	13.315	0.033	12.311	0.023	9.848	0.035	6.419	0.053
	J001635.56+642014.1	119.169	1.720	11.779	0.022	10.510	0.020	7.730	0.017	5.312	0.027
	J001635.86+641954.8	119.169	1.715	12.266	0.022	11.250	0.021	8.445	0.018	5.863	0.032
[BKP2003]10805	J001507.57+641812.3	119.007	1.709	15.398	0.043	14.890	0.057	11.012	0.065	9.441	0.441
	J001518.29+641822.5	119.027	1.709	14.205	0.036	13.560	0.036	10.660	0.056	8.439	0.205
[BKP2003]10807	J021707.62+631625.0	132.392	1.987	14.590	0.044	13.651	0.038	10.065	0.063	6.901	0.107
[BKP2003]10811	J011926.47+654545.5	125.804	3.047	10.235	0.022	9.566	0.020	4.679	0.014	1.081	0.016
[BKP2003]10812	J011402.67+655707.4	125.235	3.182	15.826	0.051	15.260	0.087	11.522	0.192	8.314	0.251
[BKP2003]10816	J220506.15+604857.9	103.996	4.215	13.226	0.025	12.186	0.023	9.160	0.034	6.509	0.061
	J220514.85+604840.0	104.007	4.200	9.804	0.022	9.114	0.019	4.223	0.013	1.253	0.012
	J220518.81+604843.3	104.014	4.196	12.811	0.024	12.269	0.023	8.057	0.021	4.873	0.036
[BKP2003]10819	J021638.73+635124.2	132.152	2.521	13.079	0.025	11.902	0.023	9.302	0.037	7.170	0.105
[BKP2003]10820	J005612.64+652442.8	123.429	2.545	15.780	0.104	14.802	0.066	10.445	0.207	8.131	null
[BKP2003]10824	J220609.07+604241.3	104.037	4.055	9.065	0.023	8.259	0.020	5.553	0.014	3.291	0.016
[BKP2003]10827	J231356.85+651139.1	112.934	4.232	16.117	0.049	13.425	0.028	10.831	0.085	7.987	0.136
[BKP2003]10828	J011230.93+644506.5	125.178	1.972	12.075	0.024	11.003	0.021	8.727	0.027	6.515	0.067
	J011324.04+645245.1	125.262	2.107	11.177	0.022	10.528	0.021	7.949	0.022	5.558	0.035
[BKP2003]10829	J011622.85+650014.7	125.565	2.260	11.076	0.022	10.278	0.021	8.186	0.020	6.741	0.065
[BKP2003]10830	J220000.52+594259.6	102.828	3.714	12.857	0.026	11.223	0.020	7.935	0.023	4.919	0.035
	J220001.96+594304.6	102.832	3.713	14.656	0.038	14.029	0.036	10.530	0.108	6.609	0.061
[BKP2003]10831	J010113.90+652137.6	123.953	2.508	14.584	0.033	14.068	0.043	11.422	0.214	8.612	0.396
	J010122.48+652111.4	123.969	2.502	15.410	0.046	14.559	0.053	10.173	0.066	6.544	0.072
	J010133.77+652046.0	123.989	2.495	12.763	0.025	12.224	0.023	7.895	0.019	6.211	0.055
[BKP2003]10832	J011649.95+652935.5	125.564	2.751	14.042	0.032	12.570	0.027	9.385	0.045	7.080	0.097
[BKP2003]10834	J000153.60+640836.2	117.562	1.790	14.102	0.026	13.465	0.026	11.014	0.081	8.819	0.237
[BKP2003]10835	J005242.61+641316.5	123.070	1.350	14.170	0.036	12.969	0.028	9.274	0.034	6.395	0.062
[BKP2003]10836	J231310.32+630839.3	112.097	2.358	14.345	0.044	13.818	0.036	9.966	0.064	7.314	0.085
	J231317.89+631031.3	112.122	2.382	15.272	0.045	13.746	0.035	10.673	0.064	6.822	0.056

Table A.2 (Continued.)

Star-forming molecular cloud	AllWISE source	Coordinate l	b	3.4 μm [mag]	$\sigma_{3.4}$ [mag]	4.6 μm [mag]	$\sigma_{4.6}$ [mag]	12 μm [mag]	σ_{12} [mag]	22 μm [mag]	σ_{22} [mag]
[BKP2003]10841	J000658.92+640134.2	118.087	1.573	14.091	0.032	13.071	0.030	10.255	0.060	7.612	0.120
	J000712.58+635943.6	118.107	1.539	16.419	0.088	14.552	0.056	11.707	0.163	8.071	0.176
	J000712.95+635931.8	118.107	1.536	14.397	0.045	12.641	0.027	8.873	0.025	5.765	0.037
	J000714.56+640004.8	118.111	1.544	14.852	0.034	13.190	0.028	10.340	0.049	6.684	0.049
	J000715.53+640010.4	118.113	1.545	14.908	0.039	13.338	0.034	10.454	0.053	7.304	0.079
	J000717.25+640007.6	118.116	1.544	13.219	0.024	12.064	0.023	9.218	0.025	6.447	0.044
	J000718.37+640155.4	118.123	1.573	13.862	0.025	12.958	0.023	10.266	0.055	7.982	0.122
	J000721.70+640420.9	118.136	1.612	12.393	0.023	11.208	0.021	8.475	0.032	5.685	0.039
	J000724.05+640114.5	118.132	1.560	13.123	0.024	12.046	0.023	9.048	0.025	6.287	0.044
[BKP2003]10844	J231043.38+630230.3	111.802	2.367	15.515	0.042	14.962	0.063	10.298	0.107	8.441	0.238
[BKP2003]10845	J000625.70+635804.3	118.017	1.527	14.882	0.053	13.728	0.040	11.148	0.092	8.180	0.148
	J000626.43+640035.1	118.026	1.568	12.972	0.024	12.139	0.022	8.754	0.026	6.409	0.052
	J000636.77+640033.3	118.045	1.564	15.633	0.043	15.127	0.062	11.213	0.108	9.140	0.361
[BKP2003]10848	J231212.61+624817.0	111.870	2.084	14.102	0.027	13.320	0.028	9.856	0.077	7.208	0.091
	J231217.10+624905.8	111.883	2.093	13.705	0.033	12.164	0.026	8.587	0.029	6.761	0.086
	J231218.40+624911.2	111.885	2.094	12.406	0.025	11.788	0.021	9.326	0.041	6.400	0.071
	J231221.77+624855.1	111.890	2.087	15.352	0.035	14.587	0.045	10.568	0.114	7.578	0.119
[BKP2003]10849	J230033.83+623522.4	110.556	2.413	13.444	0.041	12.681	0.030	8.743	0.049	6.734	0.067
	J230034.77+623436.1	110.553	2.400	11.016	0.023	10.388	0.020	7.787	0.061	5.421	0.089
[BKP2003]10850	J231047.13+625527.8	111.764	2.256	11.910	0.023	11.098	0.022	8.238	0.020	5.986	0.048
	J231048.49+625528.1	111.766	2.255	13.079	0.031	12.058	0.030	9.475	0.042	7.215	0.118
[BKP2003]10851	J010352.97+642448.4	124.276	1.574	12.757	0.024	11.867	0.022	9.420	0.037	6.631	0.075
	J010354.14+642422.3	124.278	1.567	15.019	0.039	14.340	0.053	11.357	0.174	8.318	0.262
	J010426.49+642236.4	124.338	1.541	15.522	0.060	14.856	0.068	11.002	0.143	8.260	null
[BKP2003]10852	J010320.71+645919.6	124.191	2.146	14.225	0.030	13.328	0.034	10.615	0.101	8.301	0.266
[BKP2003]10853	J223955.50+610313.7	107.689	2.136	13.972	0.049	12.559	0.024	9.600	0.036	5.745	0.044
[BKP2003]10855	J225010.87+621257.5	109.310	2.595	14.861	0.034	13.754	0.033	10.829	0.097	9.214	0.456
[BKP2003]10857	J000441.96+633202.7	117.752	1.133	13.936	0.024	12.690	0.024	9.830	0.044	7.238	0.076
	J000442.94+633146.3	117.753	1.129	14.607	0.034	13.863	0.036	11.129	0.090	7.910	0.121
	J000454.36+633002.5	117.769	1.096	13.195	0.042	11.872	0.024	8.927	0.024	5.753	0.032
	J000511.13+632920.8	117.798	1.079	15.724	0.052	14.512	0.049	10.537	0.061	8.042	0.136
[BKP2003]10858	J005325.27+642216.9	123.146	1.501	14.858	0.032	14.073	0.038	11.201	0.193	8.003	0.216
[BKP2003]10859	J004821.04+643039.8	122.600	1.641	14.639	0.111	14.108	0.114	8.945	0.071	3.382	0.019
	J004823.72+643043.4	122.604	1.642	10.300	0.022	9.459	0.018	4.698	0.013	0.899	0.013
[BKP2003]10861	J004735.90+643533.1	122.520	1.724	13.691	0.025	12.569	0.023	9.909	0.055	7.120	0.100
	J004741.38+643531.6	122.530	1.723	14.718	0.028	13.219	0.025	10.211	0.066	7.480	0.138
[BKP2003]10862	J013841.51+642228.8	128.015	1.970	12.341	0.025	10.727	0.021	8.058	0.019	5.443	0.037
[BKP2003]10863	J233230.63+633126.0	114.270	1.987	15.717	0.068	15.104	0.076	10.164	0.048	7.611	0.121
[BKP2003]10864	J000610.04+635759.3	117.989	1.530	15.087	0.055	13.970	0.038	10.844	0.075	7.379	0.084
	J000615.51+640032.2	118.006	1.570	13.991	0.045	12.269	0.024	9.522	0.037	6.785	0.057
	J000625.70+635804.3	118.017	1.527	14.882	0.053	13.728	0.040	11.148	0.092	8.180	0.148
	J000626.43+640035.1	118.026	1.568	12.972	0.024	12.139	0.022	8.754	0.026	6.409	0.052
	J000636.77+640033.3	118.045	1.564	15.633	0.043	15.127	0.062	11.213	0.108	9.140	0.361
[BKP2003]10866	J000425.69+635928.0	117.806	1.588	12.024	0.024	10.760	0.020	8.209	0.027	5.590	0.038
[BKP2003]10867	J011320.20+644848.5	125.260	2.041	12.774	0.020	12.054	0.019	8.228	0.016	5.421	0.022
[BKP2003]10870	J225222.87+622846.8	109.656	2.717	13.979	0.033	13.048	0.033	8.602	0.038	5.661	0.046
[BKP2003]10871	J225314.02+623033.0	109.757	2.700	11.332	0.023	10.391	0.020	8.309	0.030	6.028	0.042
	J225315.97+623321.8	109.781	2.741	12.242	0.037	11.459	0.024	8.745	0.044	6.986	0.069
	J225324.29+623047.6	109.777	2.695	11.915	0.023	11.069	0.021	8.511	0.032	6.241	0.055
	J225326.34+623153.6	109.789	2.710	11.444	0.022	10.781	0.019	7.943	0.029	5.464	0.034
	J225329.22+623020.0	109.782	2.684	13.755	0.029	13.195	0.030	8.801	0.027	6.754	0.062
	J225332.23+623353.7	109.813	2.735	10.432	0.022	9.895	0.020	7.331	0.020	5.144	0.028
	J225333.84+623013.4	109.789	2.679	12.900	0.025	12.266	0.024	10.117	0.064	8.018	0.154

Table A.2 (Continued.)

Star-forming molecular cloud	AllWISE source	Coordinate l	b	3.4 μm [mag]	$\sigma_{3.4}$ [mag]	4.6 μm [mag]	$\sigma_{4.6}$ [mag]	12 μm [mag]	σ_{12} [mag]	22 μm [mag]	σ_{22} [mag]
	J225336.50+623334.3	109.818	2.727	13.376	0.059	12.095	0.038	9.849	0.084	7.230	0.098
	J225340.98+623331.4	109.826	2.722	11.295	0.023	10.469	0.020	8.137	0.024	6.333	0.053
[BKP2003]10872	J233535.42+622542.0	114.281	0.837	10.827	0.021	9.816	0.020	6.995	0.018	4.689	0.025
	J233542.66+622528.5	114.293	0.830	14.065	0.034	12.988	0.028	10.520	0.068	7.775	0.145
	J233600.88+622352.0	114.319	0.794	15.587	0.053	14.810	0.053	10.020	0.045	7.102	0.079
	J233608.23+622346.3	114.332	0.788	10.210	0.022	9.514	0.020	5.475	0.014	3.070	0.018
	J233623.28+622429.7	114.363	0.792	15.568	0.059	14.607	0.060	10.725	0.077	7.920	0.154
	J233624.79+622451.0	114.368	0.797	14.480	0.027	13.639	0.029	10.749	0.074	6.869	0.060
	J233625.51+622503.0	114.370	0.799	13.312	0.030	12.008	0.031	9.610	0.050	5.911	0.061
	J233625.54+622507.6	114.371	0.801	14.732	0.077	13.329	0.077	10.520	0.103	6.597	0.108
[BKP2003]10873	J233512.77+622503.6	114.236	0.840	14.404	0.036	13.342	0.032	10.433	0.057	7.182	0.080
[BKP2003]10874	J013744.37+643509.8	127.875	2.160	13.517	0.027	12.795	0.025	10.381	0.079	7.902	0.210
[BKP2003]10875	J013908.36+644823.7	127.983	2.404	14.422	0.063	13.637	0.038	10.851	0.105	8.148	0.218
	J013909.05+644904.1	127.982	2.415	13.470	0.026	12.696	0.026	9.708	0.047	6.906	0.074
	J013910.54+644650.0	127.991	2.379	15.818	0.072	14.287	0.053	11.607	0.216	8.485	null
[BKP2003]10876	J234938.64+642649.9	116.329	2.371	13.172	0.034	11.889	0.023	9.070	0.027	6.291	0.044
[BKP2003]10877	J020504.94+630314.9	131.163	1.365	13.830	0.030	12.895	0.028	10.340	0.069	7.650	0.168
	J020508.25+630511.5	131.160	1.398	13.692	0.026	12.997	0.029	9.904	0.050	7.505	0.139
	J020508.31+630452.9	131.161	1.393	13.781	0.030	12.462	0.027	9.475	0.044	6.297	0.065
[BKP2003]10878	J225159.26+614328.7	109.280	2.061	13.479	0.029	12.022	0.022	9.533	0.041	6.388	0.049
	J225200.17+614507.9	109.294	2.085	14.011	0.025	11.990	0.021	8.987	0.037	5.859	0.041
	J225200.24+614337.1	109.283	2.062	14.385	0.029	13.150	0.026	10.592	0.084	7.093	0.088
[BKP2003]10883	J005621.64+642108.1	123.465	1.486	15.068	0.044	14.506	0.053	11.351	0.163	8.717	0.428
	J005632.65+642159.0	123.484	1.500	11.494	0.022	10.419	0.020	7.961	0.019	5.476	0.033
[BKP2003]10885	J024825.92+582846.8	137.734	-0.989	14.539	0.033	13.228	0.030	9.903	0.056	7.629	0.139
	J024830.64+582700.5	137.756	-1.011	14.859	0.040	14.356	0.050	10.871	0.110	8.271	0.222
	J024831.69+582639.8	137.761	-1.015	14.996	0.049	14.496	0.058	10.376	0.078	8.235	0.229
	J024838.52+582832.8	137.760	-0.980	15.097	0.045	14.528	0.056	10.562	0.119	7.788	0.170
[BKP2003]10886	J024801.66+582222.8	137.732	-1.108	14.423	0.030	13.028	0.028	9.707	0.042	7.472	0.129
	J024822.19+582249.7	137.770	-1.082	14.037	0.028	12.966	0.027	10.166	0.063	7.960	0.214
	J024826.90+582357.6	137.771	-1.060	13.571	0.033	12.424	0.028	9.812	0.061	7.182	0.155
	J024828.69+582331.9	137.777	-1.065	12.686	0.023	11.495	0.021	8.358	0.026	5.042	0.034
	J024829.02+582414.5	137.773	-1.054	15.489	0.068	14.590	0.052	10.719	0.110	7.624	0.133
	J024835.25+582336.1	137.790	-1.058	12.626	0.025	11.611	0.022	9.124	0.038	6.767	0.085
	J024844.84+582336.1	137.809	-1.049	12.076	0.023	11.062	0.020	8.240	0.022	5.856	0.046
[BKP2003]10888	J004620.92+643807.9	122.387	1.769	14.550	0.030	13.840	0.033	10.080	0.062	7.693	0.191
[BKP2003]10890	J005524.53+643057.4	123.359	1.648	14.098	0.031	13.412	0.032	10.842	0.088	8.434	null
	J005533.21+643141.7	123.375	1.660	15.306	0.041	14.445	0.048	11.276	0.143	8.288	null
[BKP2003]10892	J003955.48+655502.7	121.756	3.072	12.369	0.023	11.238	0.021	8.297	0.022	5.877	0.042
	J004022.86+655655.4	121.804	3.101	16.356	0.067	15.201	0.076	11.689	0.193	8.720	null
	J004029.86+655401.5	121.814	3.053	11.665	0.022	10.860	0.020	7.166	0.015	5.011	0.028
	J004031.66+655425.7	121.817	3.059	15.448	0.045	14.918	0.070	11.595	0.183	8.230	0.233
[BKP2003]10895	J004940.49+652447.3	122.748	2.542	13.165	0.043	12.627	0.036	7.509	0.020	5.516	0.051
	J004942.54+652304.1	122.752	2.513	13.280	0.030	12.739	0.029	10.151	0.122	7.837	0.227
	J004954.92+652513.1	122.773	2.549	10.175	0.023	9.061	0.021	5.670	0.015	3.044	0.025
	J004958.13+652502.3	122.779	2.546	12.471	0.035	11.118	0.026	6.375	0.016	3.459	0.029
[BKP2003]10896	J235754.66+661547.8	117.574	3.950	11.944	0.025	10.984	0.021	7.486	0.021	5.211	0.034
	J235802.21+661721.2	117.591	3.973	10.658	0.023	9.489	0.021	7.113	0.018	4.523	0.026
[BKP2003]10897	J000437.02+655245.9	118.168	3.442	16.810	0.083	15.621	0.095	11.831	0.148	9.062	0.346
[BKP2003]10898	J235039.85+654053.5	116.724	3.545	13.213	0.028	11.813	0.023	8.969	0.041	6.708	0.058
	J235041.21+654014.1	116.724	3.534	14.845	0.051	14.337	0.046	8.424	0.024	5.866	0.039

Appendix B

Image of newly identified star-forming regions and their parental clouds

Example images of newly identified star-forming regions and their parental clouds are shown in this appendix. In the left panels, ^{12}CO distribution of the star-forming molecular clouds are shown. The yellow star marks show the location of newly identified star-forming regions. The white filled circles shows the spatial resolution of the FCRAO data ($100''.88$). The green contours show the ^{12}CO distribution with contour levels of 3σ, 5σ, 7σ, 9σ, 11σ. In the right panels, *WISE* 3.4, 4.6, and 12 μm pseudo-color images of star-forming regions are shown.

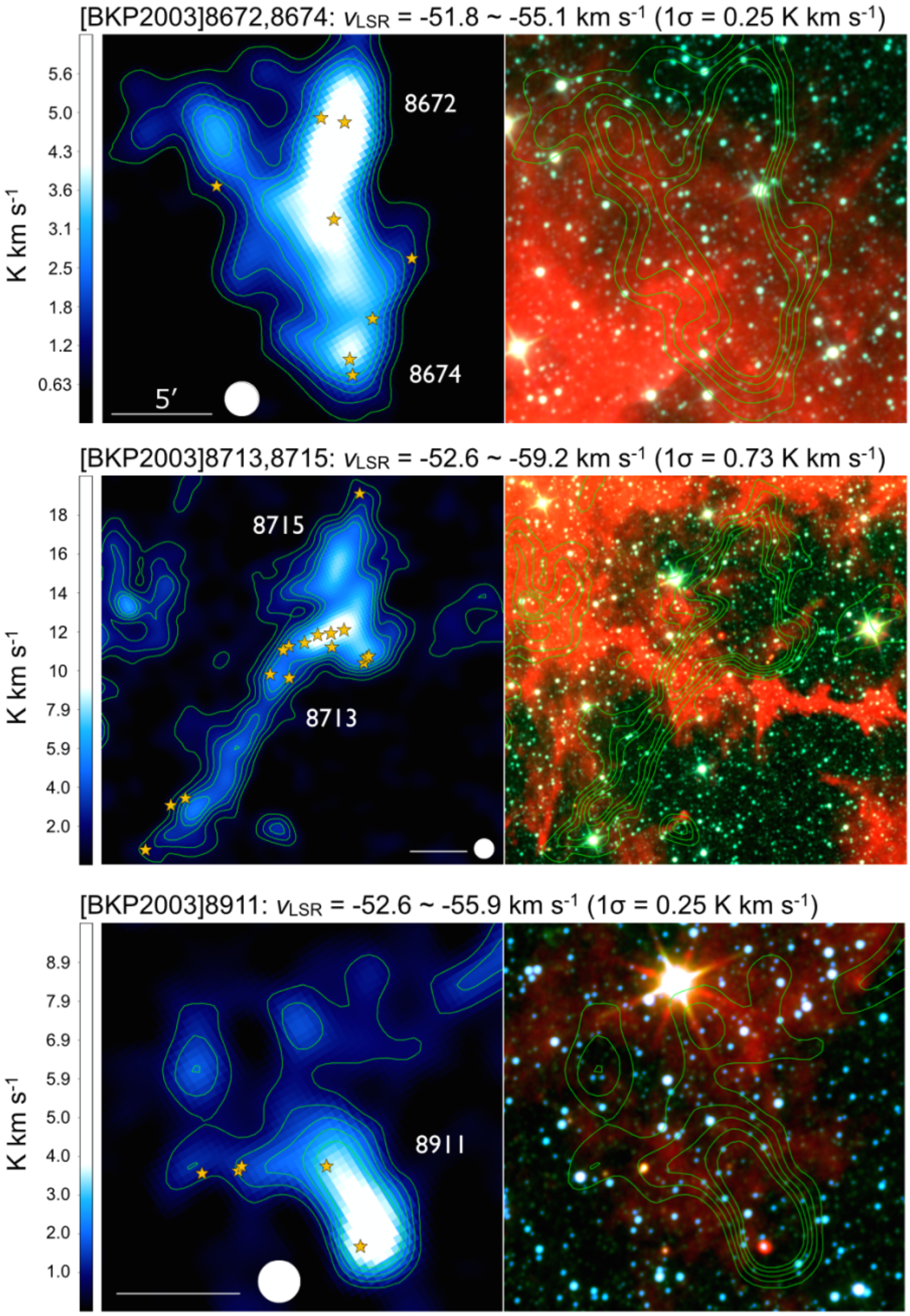
[BKP2003]8672,8674: vLSR = -51.8 ~ -55.1 km s-1 (1σ = 0.25 K km s-1)
K km s-1
5.6
5.0
4.3
3.6
3.1
2.5
1.8
1.2
0.63
8672
8674
5′
[BKP2003]8713,8715: vLSR = -52.6 ~ -59.2 km s-1 (1σ = 0.73 K km s-1)
K km s-1
18
16
14
12
10
7.9
5.9
4.0
2.0
8715
8713
[BKP2003]8911: vLSR = -52.6 ~ -55.9 km s-1 (1σ = 0.25 K km s-1)
K km s-1
8.9
7.9
6.9
5.9
5.0
4.0
3.0
2.0
1.0
8911

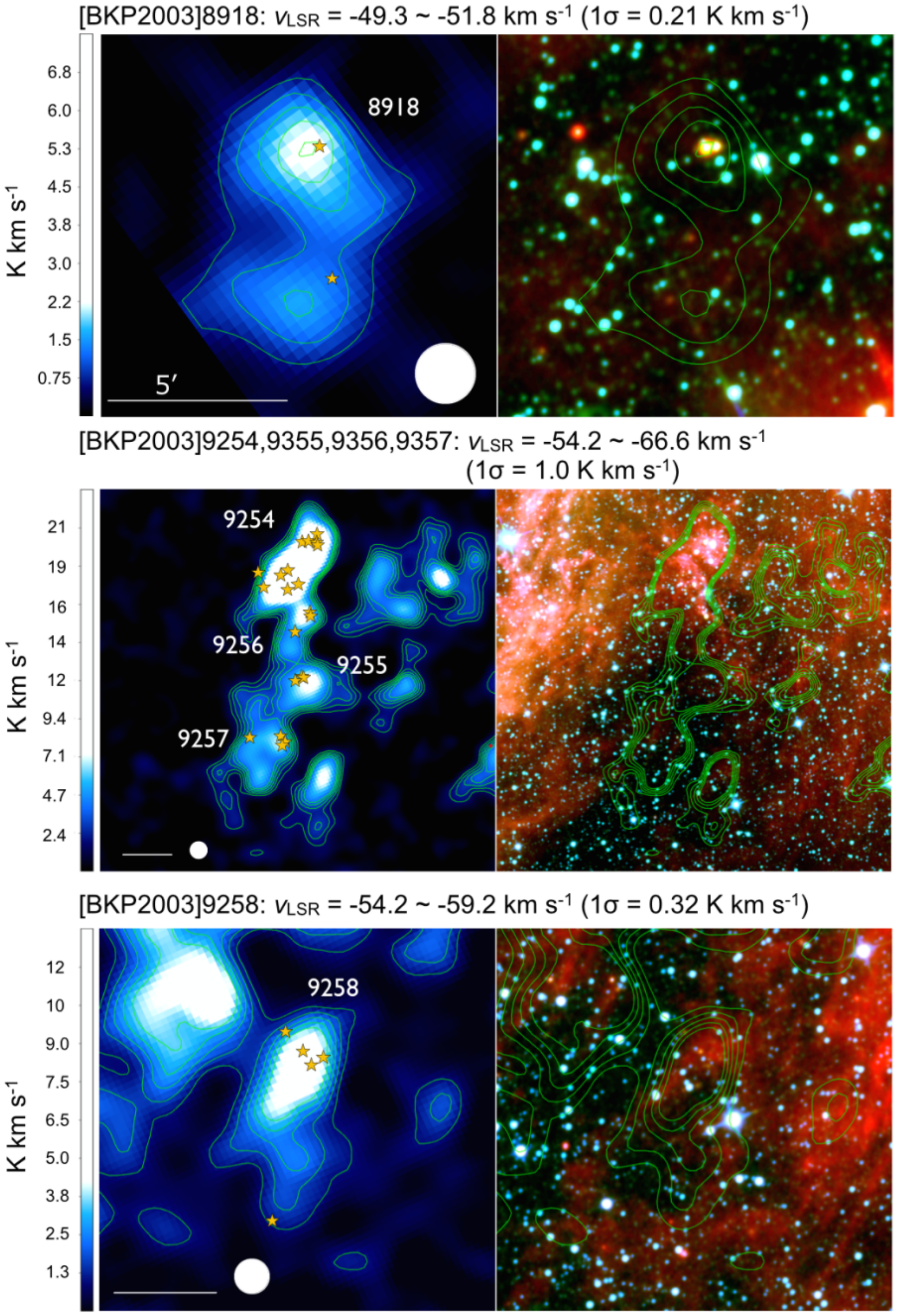
[BKP2003]8918: v_{LSR} = -49.3 ~ -51.8 km s^{-1} (1σ = 0.21 K km s^{-1})
K km s^{-1}
6.8
6.0
5.3
4.5
3.8
3.0
2.2
1.5
0.75
8918
5′
[BKP2003]9254,9355,9356,9357: v_{LSR} = -54.2 ~ -66.6 km s^{-1}
(1σ = 1.0 K km s^{-1})
K km s^{-1}
21
19
16
14
12
9.4
7.1
4.7
2.4
9254
9256
9255
9257
[BKP2003]9258: v_{LSR} = -54.2 ~ -59.2 km s^{-1} (1σ = 0.32 K km s^{-1})
K km s^{-1}
12
10
9.0
7.5
6.5
5.0
3.8
2.5
1.3
9258